

## THESIS / THÈSE

### DOCTOR OF SCIENCES

**Hybrid gold nanoparticles coated with organic polymers and antibodies as platforms for cancer theranostics**

**Investigation of the cytotoxicity mechanisms and feasibility study of radioactive labeling**

DAEMS, Noami

*Award date:*  
2020

*Awarding institution:*  
University of Namur

[Link to publication](#)

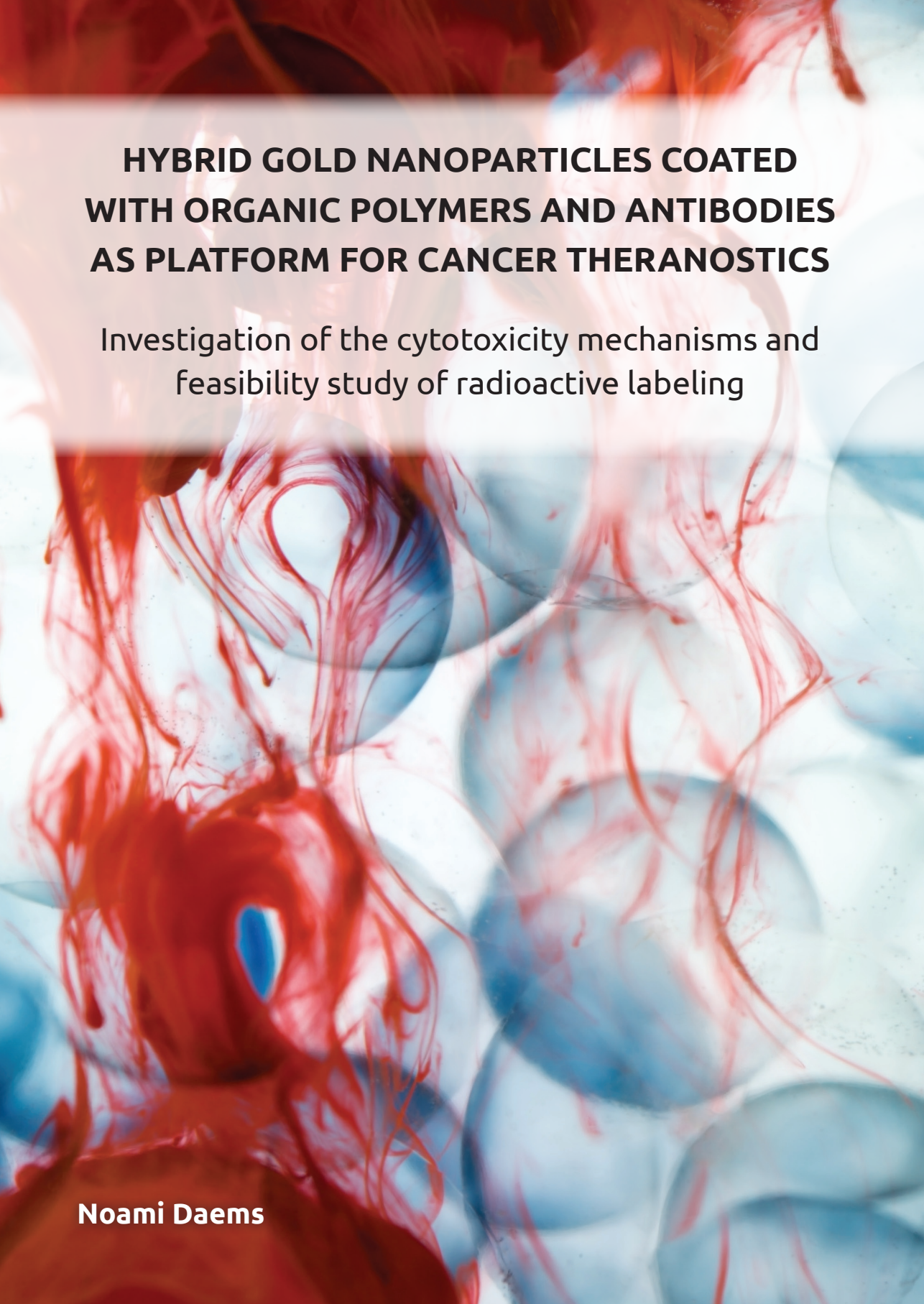
#### General rights

Copyright and moral rights for the publications made accessible in the public portal are retained by the authors and/or other copyright owners and it is a condition of accessing publications that users recognise and abide by the legal requirements associated with these rights.

- Users may download and print one copy of any publication from the public portal for the purpose of private study or research.
- You may not further distribute the material or use it for any profit-making activity or commercial gain
- You may freely distribute the URL identifying the publication in the public portal ?

#### Take down policy

If you believe that this document breaches copyright please contact us providing details, and we will remove access to the work immediately and investigate your claim.



# **HYBRID GOLD NANOPARTICLES COATED WITH ORGANIC POLYMERS AND ANTIBODIES AS PLATFORM FOR CANCER THERANOSTICS**

Investigation of the cytotoxicity mechanisms and  
feasibility study of radioactive labeling

**Noami Daems**



University of Namur – Faculty of Sciences

Namur Research Institute for Life Sciences (NARILIS)

# Hybrid gold nanoparticles coated with organic polymers and antibodies as platforms for cancer theranostics

Investigation of the cytotoxicity mechanisms and  
feasibility study of radioactive labeling

**Noami DAEMS**

Dissertation presented in partial  
fulfilment of the requirements for the  
degree of Doctor of Science (PhD):  
Biology

## **Members of the Jury**

Prof. Dr. Stéphane Lucas (Promoter)  
Prof. Dr. Carine Michiels (Co-promoter)  
Dr. Ir. An Aerts (Co-promoter)  
Dr. Karen Van Hoecke (Co-supervisor)  
Prof. Dr. Sarah Baatout  
Prof. Dr. Bernard Masereel (Chairman)  
Prof. Dr. Nadine Millot



September 2020 Naomi Daems

Hybrid gold nanoparticles coated with organic polymers and antibodies as platform for cancer theranostics: Investigation of the cytotoxicity mechanisms and feasibility study of radioactive labeling

Noami Daems was financially supported by the Fonds de la Recherche Scientifique-FNRS (FRIA)

Printed by ProefschriftMaken || [www.proefschriftmaken.nl](http://www.proefschriftmaken.nl)

## **Members of the Jury**

### **Prof. Stéphane Lucas (Promoter)**

Laboratoire d'Analyse par Réactions Nucléaires (LARN - NARILIS)

Université de Namur, Namur, Belgium

### **Prof. Carine Michiels (Co-promoter)**

Unité de Recherche en Biochimie et Biologie Cellulaire (URBC - NARILIS)

Université de Namur, Namur, Belgium

### **Dr. An Aerts (Co-promoter)**

Radiobiology Unit, Interdisciplinarily Biosciences

Institute for Environment, Health and Safety

Belgian Nuclear Research Center (SCK CEN), Mol, Belgium

### **Dr. Karen Van Hoecke (Co-supervisor)**

Radiochemistry Expert Group

Institute for Nuclear Materials Science

Belgian Nuclear Research Center (SCK CEN), Mol, Belgium

### **Prof. Sarah Baatout**

Radiobiology Unit, Interdisciplinarily Biosciences

Institute for Environment, Health and Safety

Belgian Nuclear Research Center (SCK CEN), Mol, Belgium

### **Prof. Bernard Masereel (Chairman)**

Namur Medicine & Drug Innovation Center (NAMEDIC - NARILIS)

Namur Thrombosis and Hemostasis Center (NTHC - NARILIS)

Université de Namur, Namur, Belgium

### **Prof. Nadine Millot**

Bio-hybrid nanoparticles & nanostructures

Nanosciences department

Laboratoire Interdisciplinaire Carnot de Bourgogne (ICB), Bourgogne, France



# Acknowledgments

It is almost surreal. My PhD journey has come to an end. The past four years have been a very steep learning curve and especially the final year was extra challenging due to the devastating COVID19 crisis. I am most grateful to the many amazing, kind and helpful people who contributed to this research project and who supported me, each in their own way. Furthermore, the multidisciplinary character of this project required scientists with different backgrounds to co-operate, which is not always evident bearing in mind that we 'speak different languages'. Nevertheless, we were able to understand and learn from each other. Therefore, I would like to thank all those people in particular.

First, I would like to thank my daily supervisor and co-promoter, Dr. **An Aerts** and my co-mentor, Dr. **Karen Van Hoecke**. Thank you for your dedication to this project, your scientific knowledge, support and critical input, which guided me through my thesis. You always made time to read and correct my papers and you always welcomed me into your offices when I had questions, when I needed your advice, for an open discussion or just for a friendly talk. I learned a lot from you and maybe one day, I will be able to use this experience to become a mentor for someone else. I would also like to thank Dr. **Simone Cagno**, who was my co-mentor during the first year of my PhD, and who helped me with drafting the project outline.

Second, I would like to thank my university promoters, Prof. **Carine Michiels** and Prof. **Stéphane Lucas**. Although I was not often present at the university, you always welcomed me with a big smile and with great enthusiasm. Furthermore, the distance between Mol and Namur did not stop you to keep in touch regularly and to be open for meetings, both physically and virtually. Thank you to introduce and guide me into the scientific world of nanoparticles and for your valuable time to correct the papers and this thesis. I experienced the collaboration between UNamur and SCK CEN to be very fruitful and positive.

Next to my supervisors and promoters, I would like to show my gratitude to the other members of the examination committee, Prof. **Bernard Masereel**, Prof. **Sarah Baatout** and Prof. **Nadine Millot**. Thank you for taking the time to read this manuscript, for the healthy and positive scientific discussions and for helping me to improve it.

Prof. **Sarah Baatout**, head of the Radiobiology Unit and Prof. **Thomas Cardinaels**, head of the Radiochemistry Expert Group, thank you for warmly embracing me into your research groups, for your continuous support and for the wonderful collaboration between both groups in SCK CEN. In both teams, I would like to show my great appreciation towards the lab technicians, who were always willing to help with the experimental work and with guiding students. **Mieke Neefs** and **Jasmine Buset**, thank you to help me overcome my nerves and shaky hands while handling the animals during my first *in vivo* experience. Thank you **Lisa Daenen** and **Brit Proesmans**, you are both doing a great job in maintaining the animal facility and taking great care of the animals. **Randy Vermeesen**, I very much appreciated your

company during our days in the lab and your help in the Luminex experiment and analysis. Not to forget is **Amelie Coolkens**, you are a great asset to Radiobiology and NURA, thank you for organizing the labs and for your help during the experiments with radioactivity at Radiochemistry. In the Radiochemistry group, I would like to thank **Prisca Verheyen**, **Karolien Van Rompaey** and **Luc Gelens** who worked very hard together with Karen Van Hoecke to optimize the procedure to measure gold concentrations on the ICP-MS. Not to forget are Dr. **Maarten Ooms** and Dr. **Andrew Burgoyne** who greatly guided me with the radiolabeling procedure and the radioactive experimental work. **Yana Dekempeneer**, thank you for being my 'radiolabeling buddy' and for sharing your expertise and knowledge with me.

I always felt very welcome at the University of Namur, where I met the incredibly kind and wonderful people of URBC and of the LARN. I would like to address my gratitude to **Sandra Bouchy**, who taught me new experimental techniques at the start of my PhD and helped me a lot with starting up the project. **Ornella Fichera** and Dr. **Riccardo Marega**, thank you for producing the gold nanoparticles when I needed it and for teaching me the conjugation procedure. Dr. **Sébastien Penninckx**, you were always willing to give me advice on experiments, share your expertise and to answer my many questions. There is no doubt that I learned a lot from you. I also would like to thank **Corry Charlier** and **Carolina de Bona** who helped and taught me to image my samples on the TEM.

Next to the contribution of UNamur and SCK CEN, I would like to mention the collaboration with VITO, where Dr. **Inge Nelissen** and **Diane Van Houtven** performed the zeta potential measurements of the gold nanoparticles.

Of course, I would never forget my lovely students, **Simon Sauvillers**, **Sigrid Vercauteren**, **Ken Kennes** and **Charlemagne Folefac**. Thank you for being very motivated and enthusiastic students who greatly helped me with different aspects of the project. I also learned a lot from you, while guiding your internships. I wish you all the best in your future careers.

Aside from those who were directly involved to the project, I am very thankful for my officemates. Dr. **André Claude Mfossa Mboumbou**, you were always ready to share your life experiences and wisdom with me. I have the greatest respect for you that you managed to successfully perform your PhD away from your family. **Laurens Maertens**, I will definitely miss your jokes and positivity. Thank you for lighting up the office with your beautiful plants. Keep up the good work and bring joy to the other PhDs to come. **Richard Deyhle**, thanks for being a nice friend, always prepared for a good talk and for reminding us about the daily stretch exercises, but most importantly to show us how to enjoy life. **Francisco Javier Giménez del Rey**, we did not share many office moments together because of the lock-down period, but I am sure you will warmly welcome the new PhD students. Next, I would like to thank **Emma Coninx**. After our master thesis, we started this PhD journey together. Your fighting spirit and enthusiasm were very encouraging. I also would like to mention the other PhD students, **Tom**, **Tom**, **Charlotte**, **Shari**, **Magy**, **Auchi**, **Gleb**, **Eline**, **Jessica**, **Lorain** and **Nathalie** who are an

amazing and strong group of young scientists, supporting and helping each other in their projects, but also on a personal level. Working at the RDB-MIC group is even more enjoyable with you people! Finally, I would like to state special thanks to Dr. **Raghda Ramadan**, you are not only a wonderful colleague, but you also became a close friend during the last years of my PhD, supporting me during some stressful and difficult times.

Als laatste zou ik graag de mensen willen bedanken die me het dichtst bij het hart liggen. Mijn ouders en lieve broer, **Danny Daems**, **Ann Vander Eyken** en **Levi Daems**, bedankt voor jullie betrokkenheid, steun, hulp en liefde tijdens al mijn studiejaren. Ik weet dat ik met alles bij jullie terecht kan, en ik ben jullie daarvoor eeuwig dankbaar. Nu we elk onze eigen stek hebben, kijk is des te meer uit naar onze leuke en gezellige familiemomenten samen.

**George Vander Eyken** en **Julia Lievens**, opa en bomma, jullie zijn fantastische grootouders geweest die hun kleinkinderen met veel liefde op handen droegen. Jullie hebben mij steeds vol trots aangemoedigd en hebben altijd interesse getoond in wat ik deed. Ik kijk naar boven en ik glimlach.

Mijn drie fantastische vriendinnen, **Lore Bussé**, **Laura Blockken** en **Sigrid Christiaens**. Na zoveel jaren vormen we nog steeds dezelfde hechte vriendengroep. Bedankt voor jullie vriendschap, luisterend oor en steun. Ik kijk telkens uit naar onze leuke en gezellige bijeenkomsten samen met de jongens. Laten er zo nog veel jaren volgen.

Liefste **Kai Craenen**, woorden schieten te kort om jouw enorme hoeveelheid geduld te omschrijven. Dankzij jou heb ik dit tot een goed einde kunnen brengen. Dankjewel voor je onvoorwaardelijke liefde en steun tijdens de drukke en stressvolle periodes van mijn doctoraat. Maar ook bedankt om zoveel plezierige en mooie momenten met mij te delen. Ik kijk ernaar uit om ons volgende hoofdstuk te beginnen ♥





# Table of Contents

List of Abbreviation .....	13
Summary .....	17
Résumé.....	19
CHAPTER I: General introduction .....	23
1. Nanoparticles: Definition, applications and history .....	24
1.1 Definition and applications .....	24
1.2 History of gold nanoparticles.....	24
2. Cancer.....	25
3. The properties of gold nanoparticles.....	26
3.1 The surface plasmon resonance.....	26
3.2 Surface coating and surface charge .....	26
3.3 Surface area-to-volume ratio .....	28
4. Gold nanoparticles in cancer treatment and detection .....	28
4.1 Cancer targeting.....	29
4.2 Photo-thermal and photodynamic therapy .....	30
4.3 The use of gold nanoparticles in chemotherapy .....	32
4.4 The use of gold nanoparticles as radiosensitizers .....	33
4.4.1 External beam radiotherapy .....	33
4.4.2 AuNPs and photon radiation therapy.....	34
4.4.3 AuNPs and hadron therapy.....	43
4.4.4 Discrepancies between theoretical and experimental data .....	46
4.5 The biological and chemical effects of AuNPs .....	47
4.5.1 Internalization.....	47
4.5.2 Oxidative stress.....	49
4.5.3 Mitochondria .....	50
4.5.4 Cell death .....	50
4.5.5 Cell cycle .....	51
4.5.6 DNA damage and repair.....	52
4.5.7 Others .....	53
4.6 Cancer detection and theranostics .....	54

5. Gold nanoparticles in nuclear medicine .....	57
5.1 Nuclear medicine .....	57
5.2 Radiolabeling of gold nanoparticles .....	60
5.3 The effectiveness of radiolabeled gold nanoparticles in nuclear medicine.....	62
5.3.1 Tumor uptake, retention and distribution .....	62
5.3.2 Imaging.....	65
5.3.3 Treatment .....	68
6. Clinical trials .....	77
7. Challenges of gold nanoparticles in medicine.....	80
7.1 Biocorona formation .....	80
7.2 Sequestration by the reticuloendothelial system .....	81
7.3 Safety evaluation .....	82
7.4 Tumor biology and translatability .....	84
7.5 Regulatory challenges .....	85
CHAPTER II: Aim and outline of the thesis .....	87
CHAPTER III: Gold nanoparticles affect the antioxidant status of selected normal human cells.....	93
1. Abstract .....	94
2. Introduction .....	95
3. Materials and methods .....	96
3.1 Chemicals.....	96
3.2 Production of AuNPs-PAA and Cetuximab conjugation .....	97
3.3 Nanoparticle characterization (Zeta potential and size distribution) .....	97
3.4 Cell culture.....	98
3.5 MTS viability assay .....	98
3.6 Live cell imaging .....	98
3.7 Western blot analysis.....	99
3.8 Transmission electron microscopy and energy dispersive x-ray spectroscopy .....	99
3.9 Inductively coupled plasma mass spectrometry .....	100
3.10 TMRM assay .....	100
3.11 Thioredoxin reductase and glutathione reductase activity measurements .....	101
3.12 Statistical analysis .....	101

4. Results .....	102
4.1 Size distribution and zeta potential of AuNPs-PAA( $\pm$ Ctxb) .....	102
4.2 Cellular internalization of AuNPs-PAA-Ctxb .....	105
4.3 AuNPs-PAA( $\pm$ Ctxb) reduced the cell viability .....	108
4.4 AuNPs-PAA( $\pm$ Ctxb) induced apoptosis .....	110
4.5 AuNPs-PAA( $\pm$ Ctxb) caused mitochondrial dysfunction .....	112
4.6 AuNPs-PAA( $\pm$ Ctxb) inhibited the activity of thioredoxin reductase and glutathione reductase .....	113
4.7 The protective effect of N-acetyl L-cysteine (NAC) .....	114
4.8 Correlation between cell viability, TrxR activity and mitochondrial membrane depolarization .....	116
5. Discussion .....	117
6. Conclusion .....	122
7. Supplemental information .....	122
CHAPTER IV: <i>In vivo</i> pharmacokinetics, biodistribution and toxicity of antibody-conjugated gold nanoparticles .....	129
1. Abstract .....	130
2. Background .....	131
3. Methods .....	132
3.1 Chemicals .....	132
3.2 Gold nanoparticles and antibody conjugation .....	132
3.3 Animal study .....	132
3.4 Inductively coupled plasma mass spectrometry .....	133
3.5 Histological examination .....	133
3.6 Liver enzyme activity measurement and luminex analysis .....	133
3.7 Statistical analysis .....	134
4. Results .....	134
4.1 Blood clearance .....	134
4.2 Tissue distribution .....	135
4.3 Evaluation of liver toxicity .....	137
4.4 Evaluation of immunotoxicity and vascular damage .....	138
4.5 Histological examination .....	139
5. Discussion .....	140

6. Supplemental information .....	146
CHAPTER V: The radiolabeling of antibody-functionalized gold nanoparticles with $^{177}\text{Lu}$ .	149
1. Abstract .....	150
2. Introduction .....	151
3. Materials and methods .....	153
3.1. Chemicals.....	153
3.2. Cell culture.....	153
3.3. DOTA and DTPA conjugation to Cetuximab .....	153
3.4. Conjugation of Ctxb-DTPA to AuNPs-PAA .....	154
3.5. ELISA.....	155
3.6. $^{177}\text{Lu}$ labeling kinetics and stability of Ctxb-DOTA, Ctxb-DTPA and AuNPs-PAA-Ctxb-DTPA .....	155
3.7. Saturation binding of $^{177}\text{Lu}$ -DTPA-Ctxb and $^{177}\text{Lu}$ -DTPA-Ctxb-PAA-AuNPs .....	156
3.8. Specificity of $^{177}\text{Lu}$ -DTPA-Ctxb and $^{177}\text{Lu}$ -DTPA-Ctxb-PAA-AuNPs.....	156
4. Results .....	157
4.1. Immunoreactivity of Ctxb-DOTA and Ctxb-DTPA .....	157
4.2. $^{177}\text{Lu}$ -radiolabeling kinetics and stability .....	158
4.3. Saturation binding of ( $^{177}\text{Lu}$ -)DTPA-Ctxb and ( $^{177}\text{Lu}$ -)DTPA-Ctxb-PAA-AuNPs .....	160
4.4. Specificity of $^{177}\text{Lu}$ -DTPA-Ctxb and $^{177}\text{Lu}$ -DTPA-Ctxb-PAA-AuNPs.....	162
5. Discussion.....	164
6. Future perspectives .....	166
7. Supplemental information .....	166
CHAPTER VI: General discussion and conclusions .....	171
1. Study relevance.....	172
2. The mechanism underlying the cytotoxicity of AuNPs-PAA-Ctxb .....	173
3. The fate and behavior of AuNPs-PAA-Ctxb <i>in vivo</i> .....	179
4. The feasibility of radiolabeled $^{177}\text{Lu}$ -DTPA-Ctxb-PAA-AuNPs as therapeutic agent ....	183
5. General conclusions and future perspectives .....	185
Annex .....	187
References .....	199
List of publications.....	227

## List of Abbreviations

<b>AG</b>	arabic gum	<b>EDTA</b>	ethylenediaminetetraacetic acid
<b>ALP</b>	alkaline phosphatase	<b>EGCg</b>	epigallocatechin-gallate
<b>ALT</b>	alanine transaminase	<b>EGF</b>	epidermal growth factor
<b>AP-1</b>	activator protein-1	<b>EGFR</b>	epidermal growth factor receptor
<b>ASK-1</b>	apoptosis signaling kinase-1	<b>ELISA</b>	enzyme linked immunosorbent assay
<b>AST</b>	aspartate aminotransferase	<b>EMA</b>	European Medicines Agency
<b>AUC</b>	area under the curve	<b>EPR</b>	enhanced permeability and retention
<b>AuNC</b>	gold nanocluster	<b>ER</b>	endoplasmatic reticulum
<b>AuNP</b>	gold nanoparticle	<b>ERAD</b>	Endoplasmic Reticulum Associated Protein Degradation
<b>AuNR</b>	gold nanorod	<b>FA</b>	folic acid
<b>BBB</b>	blood-brain-barrier	<b>FBS</b>	fetal bovine serum
<b>BCA</b>	bicinchoninic acid	<b>FDA</b>	United States Food and Drug Administration
<b>Bcl2L12</b>	Bcl2-like protein 12	<b>FDG</b>	Fluorodeoxyglucose
<b>BmK-CTX</b>	Buthus martensii Karsch chlorotoxin	<b>GA</b>	gum arabic
<b>BSA</b>	bovine serum albumin	<b>GDF-15</b>	growth differentiation factor 15
<b>C<sub>bl</sub></b>	blood clearance	<b>GGT</b>	gamma glutamyl transferase
<b>CCL</b>	C-C motif chemokine ligand	<b>GPx</b>	glutathione peroxidase
<b>CI</b>	confidence interval	<b>GR</b>	glutathione reductase
<b>CLI</b>	Cerenkov luminescent imaging	<b>GRP</b>	gastrin-releasing peptide receptor
<b>C<sub>max</sub></b>	maximal observed concentration	<b>GSH</b>	glutathione
<b>cRGD</b>	cyclic arginine-glycine-aspartic acid	<b>GSSG</b>	glutathione disulfide
<b>CT</b>	computed tomography	<b>H&amp;E</b>	hematoxylin and eosin
<b>CTX</b>	Chlorotoxin	<b>H<sub>2</sub>O<sub>2</sub></b>	hydrogen peroxide
<b>Ctxb</b>	Cetuximab	<b>HAuNS</b>	hollow gold nanoshell;
<b>CXCL</b>	C-X-C motif chemokine ligand	<b>HIF-1<math>\alpha</math></b>	hypoxia inducible factor-1 $\alpha$
<b>CXCR</b>	C-X-C motif chemokine receptor	<b>HR</b>	homologous recombination
<b>DDS</b>	drug delivery system	<b>HU</b>	Hounsfield unit
<b>DEF</b>	dose enhancement factor	<b>HUVECs</b>	human umbilical vein endothelial cells
<b>Den</b>	dendrimer	<b>HYNIC</b>	hydrazinonicotinamide
<b>DMEM</b>	Dulbecco's modified Eagle's medium	<b>ICAM</b>	intercellular adhesion molecule
<b>DOTA</b>	dodecane tetraacetic acid	<b>ICP-MS</b>	inductively coupled plasma-mass spectrometry
<b>DOX</b>	doxorubicin	<b>IFN<math>\gamma</math></b>	interferon $\gamma$
<b>DSB</b>	double strand break	<b>IL</b>	interleukin
<b>DTPA</b>	diethylenetriaminepentaacetic acid	<b>IONP</b>	iron oxide nanoparticle
<b>DTX</b>	docetaxel	<b>IP</b>	intraperitoneal
<b>E</b>	embolization	<b>IRE</b>	irreversible electroporation
<b>EBRT</b>	external beam radiotherapy	<b>IT</b>	intratumoral
<b>EC</b>	electron conversion		
<b>EC<sub>50</sub></b>	half-maximal effect concentrations		
<b>ECM</b>	extracellular matrix		
<b>EDS</b>	energy dispersive X-ray spectroscopy		



## List of Abbreviations

<b>ITLC</b>	instant thin layer chromatography	<b>PDT</b>	photodynamic therapy
<b>IV</b>	intravenous	<b>PE</b>	polyethylenimine
<b>K<sub>d</sub></b>	equilibrium dissociation constant	<b>PEG</b>	polyethylene glycol
<b>KeV</b>	kilo-electron volts	<b>PET</b>	positron emission tomography
<b>kV</b>	kilovolt	<b>PS</b>	photosensitizer
<b>kVp</b>	kilovolt peak	<b>PTEN</b>	phosphatase and tensin homolog
<b>L/M</b>	lung-to-muscle ratio	<b>PTT</b>	photo-thermal therapy
<b>LD<sub>50</sub></b>	lethal dose for 50% of the cells	<b>PVD</b>	plasma vapor deposition
<b>LET</b>	linear energy transfer	<b>RANTES</b>	regulated upon activation, normal T cell expressed and presumably secreted
<b>LITT</b>	laser induced thermal therapy	<b>RBE</b>	relative biological effectiveness RT radiotherapy
<b>LOEC</b>	lowest observed effect concentration	<b>RES</b>	reticuloendothelial system
<b>MALDI-ToF-MS</b>	matrix assisted laser desorption ionization-time of flight-mass spectrometry	<b>RFA</b>	radiofrequency ablation
<b>MC</b>	Monte Carlo	<b>RIT</b>	radio-immunotherapy
<b>MEM</b>	minimal essential medium	<b>ROS</b>	reactive oxygen species
<b>MeV</b>	mega-electron volts	<b>rSIE</b>	relative signal intensity enhancement
<b>MGF</b>	mangiferin	<b>SD</b>	standard deviation
<b>MID</b>	mean inactivation dose	<b>SE</b>	standard error
<b>MIP</b>	macrophage inflammatory protein	<b>SeIP</b>	selenoprotein
<b>MMP</b>	matrix metalloprotease	<b>SER</b>	sensitization enhancement ratio
<b>MRI</b>	magnetic resonance imaging	<b>SERS</b>	surface enhanced Raman scattering
<b>MSRB1</b>	methionine sulfoxide reductase	<b>SF</b>	survival fraction
<b>MTS</b>	3-(4,5-Dimethylthiazol-2-yl)-5-(3-carboxymethoxyphenyl)-2-(4-sulfophenyl)-2H-tetrazolium	<b>SIRT</b>	selective internal radiation therapy
<b>MV</b>	megavolt	<b>SLN</b>	sentinel lymph node
<b>NAC</b>	N-acetyl L-cysteine	<b>SPECT</b>	single photon emission computed tomography
<b>NET</b>	neuroendocrine tumor	<b>SPR</b>	surface plasmon resonance
<b>NF-κβ</b>	nuclear factor-κβ	<b>SPS2</b>	selenophosphate synthetase
<b>NHEJ</b>	non-homologous end joining	<b>SUV</b>	standardized uptake value
<b>NIR</b>	near infrared	<b>T/B</b>	tumor-to-background ratio
<b>NOTA</b>	2-S-(4-isothiocyanatobenzyl)-1, 4, 7-triazacyclononane-1, 4, 7-triacetic acid	<b>T/BI</b>	tumor-to-blood ratio
<b>NS</b>	nanoshell	<b>T/L</b>	tumor-to-lung ratio
<b>OCT</b>	optical coherence tomography	<b>T/Li</b>	Tumor-to-liver ratio
<b>p.i.</b>	post-injection	<b>T/M</b>	tumor-to-muscle ratio
<b>PA</b>	photo-acoustic	<b>T/NT</b>	target-to-non-target ratio
<b>PAA</b>	poly-allylamine	<b>T/S</b>	tumor-to-spleen ratio
<b>PBS</b>	phosphate buffered saline	<b>T<sub>1/2</sub></b>	half-life
<b>PCSK</b>	proprotein convertase subtilisin/kexin	<b>Tat-BN</b>	TAT-bombesin
<b>PDI</b>	protein disulphide isomerase	<b>TCP</b>	tumor control probability
		<b>TEM</b>	transmission electron microscopy
		<b>TGF-α</b>	tumor growth factor α

## List of Abbreviations

<b>TGI</b>	tumor growth index (ratio of the treated tumor volume by the initial tumor volume);	<b>uPAR</b>	urokinase-type plasminogen activator receptor
<b>TIONts</b>	titanate nanotubes	<b>US</b>	ultrasound
<b>T<sub>max</sub></b>	time point of maximal observed concentration	<b>VCAM</b>	vascular cell adhesion molecule
<b>TMRM</b>	tetramethylrhodamine, methyl ester, perchlorate	<b>VEGF</b>	vascular endothelial growth factor
<b>TNF-<math>\alpha</math></b>	tumor necrosis factor- $\alpha$	<b>VEGFR</b>	vascular endothelial growth factor receptor
<b>TPPMS</b>	triphenylphosphine monosulfonate	<b>VL</b>	visible light
<b>TRT</b>	targeted radionuclide therapy	<b>%CS</b>	percentage of cell survival
<b>TrxR</b>	thioredoxin reductase	<b>%ID</b>	percentage injected dose
		<b>3D</b>	three-dimensiona



## Summary

Cancer is the second leading cause of mortality worldwide, responsible for an estimated 9.6 million deaths in 2018. Currently, the conventional therapeutic approaches are surgical removal of the tumor, chemotherapy and/or radiotherapy. However, despite the recent advances in cancer treatment, a significant number of patients still experience tumor recurrence and have serious side effects due to the damage caused to healthy tissues. Therefore, there is a need to further improve the current treatment modalities, or develop new therapeutic strategies, which enhance the cancer cell killing, while sparing the healthy tissues. Thanks to their unique optical and physicochemical properties, gold nanoparticles (AuNPs) have emerged in nanomedicine as promising contrast agents, drug delivery vehicles, photo-thermal agents and radiosensitizers. In order to maximize the concentration of AuNPs into the tumor site, surface modifications with targeting moieties are typically applied onto the AuNP surface.

In this thesis, we used 5 nm AuNPs coated with organic poly-allylamine (AuNPs-PAA) and conjugated to Cetuximab (Cttxb), a commercially available antibody targeting the epidermal growth factor receptor (EGFR). EGFR is overexpressed in numerous cancer types, such as colorectal, head- and neck cancers, breast cancer and prostate cancer. Previously, it has been shown that the resulting AuNPs-PAA-Cttxb are able to selectively target EGFR-overexpressing cancer cells *in vitro* and *in vivo*, and enhance the efficiency of proton therapy in EGFR-overexpressing cancer cells. In nanomedicine, intravenous administration of AuNPs-PAA-Cttxb would be the most realistic exposure scenario. However, following systemic administration, it is inevitable that healthy cells and tissues will be exposed to the AuNPs-PAA-Cttxb as well. The first cells that would encounter the injected AuNPs-PAA-Cttxb are the endothelial cells, lining the inner walls of the vasculature. Furthermore, the hepatobiliary system and the renal system are potential elimination routes to remove AuNPs-PAA-Cttxb from the body. Therefore, we investigated the cytotoxic effects of AuNPs-PAA and AuNPs-PAA-Cttxb in human microvascular endothelial cells, liver cells and kidney cells. After exposure, AuNPs-PAA-Cttxb were internalized in all cell types and were present in intracellular vesicles. Interestingly, the cellular EGFR expression profile was not a prognostic factor to predict the sensitivity of the cells to the effects of AuNPs-PAA-Cttxb. Instead, we reported that AuNPs-PAA and AuNPs-PAA-Cttxb caused mitochondrial dysfunction and significantly suppressed the activity of the antioxidant enzymes, thioredoxin reductase (TrxR) and glutathione reductase (GR), finally resulting in apoptotic cell death. The role of oxidative stress was highlighted by the protective effects of the antioxidant N-acetyl L-cysteine, which prevented mitochondrial dysfunction and considerably reduced apoptosis. Finally, we evidenced that the basal TrxR activity, the extent of TrxR inhibition and the mitochondrial dysfunction are strongly correlated with the sensitivity of the normal cells to AuNPs-PAA and AuNPs-PAA-Cttxb.

## Summary

Since we observed cytotoxic effects of AuNPs-PAA-Ctxb in normal cells *in vitro*, we assessed, the pharmacokinetics, biodistribution and toxicity of the AuNPs-PAA-Ctxb after a single intravenous injection in healthy mice. The AuNPs-PAA-Ctxb were rapidly cleared from the blood circulation, followed by their accumulation and long-term retention in the liver and spleen. However, we did not observe significant morphological changes in the liver, kidney, spleen and lungs up to four weeks post-injection. In addition, there was only a minimal and transient increase in a limited number of serum markers related to the immune response, endothelial activation and liver toxicity.

Finally, since the AuNPs-PAA-Ctxb clearly affected some biological systems involved in the antioxidant defense and cell survival, AuNPs-PAA-Ctxb could predispose cancer cells to apoptosis after exposure to ionizing radiation. The radiosensitizing effects of AuNPs are usually investigated considering external beam radiotherapy (EBRT). However, there are only a limited number of studies investigating the use of AuNPs as radiosensitizing agents in combination with radionuclides. Therefore, in the last part, we radiolabeled the AuNPs-PAA-Ctxb to the theragnostic radionuclide,  $^{177}\text{Lu}$ , using bifunctional chelators conjugated to Ctxb. The bifunctional chelator diethylenetriaminepentaacetic acid (DTPA) was preferred because of the fast radiolabeling reaction under mild conditions and the minimal impact on the Ctxb binding capacity.  $^{177}\text{Lu}$ -DTPA-Ctxb-PAA-AuNPs preserved their ability to recognize EGFR and exhibited a more extensive binding and internalization in cancer cells compared to  $^{177}\text{Lu}$ -DTPA-Ctxb. As a result, together with the biological inhibition,  $^{177}\text{Lu}$ -DTPA-Ctxb-PAA-AuNPs could have the potential to increase the efficacy of targeted radionuclide therapy compared to  $^{177}\text{Lu}$ -DTPA-Ctxb.

In order to assess the radiosensitizing properties of the  $^{177}\text{Lu}$ -DTPA-Ctxb-PAA-AuNPs in targeted radionuclide therapy, future experiments will be conducted, assessing the cell viability and clonogenic potential of various cancer cell types with different EGFR expression and TrxR activity profiles, after exposure to  $^{177}\text{Lu}$ -DTPA-Ctxb-PAA-AuNPs or  $^{177}\text{Lu}$ -DTPA-Ctxb. In addition,  $^{177}\text{Lu}$ -radiolabeling of AuNPs-PAA-Ctxb will enable the real-time imaging of the biodistribution and elimination of the nanoconjugate in mice, bearing EGFR-positive and EGFR-negative tumor xenografts. Finally, *in vivo* preclinical therapy experiments will inform whether  $^{177}\text{Lu}$ -DTPA-Ctxb-PAA-AuNPs bear superior tumor killing capacity.

Altogether,  $^{177}\text{Lu}$ -DTPA-Ctxb-PAA-AuNPs is a potentially superior radiopharmaceutical as compared to  $^{177}\text{Lu}$ -DTPA-Ctxb, because of the (I) mitochondrial dysfunction and suppression of the antioxidant system, (II) the enhanced cancer cell internalization and (III) the delivery of multiple  $^{177}\text{Lu}$  radionuclides per AuNP. However, the rapid sequestration and long-term retention of the AuNPs-PAA-Ctxb in the liver and spleen after intravenous administration might restrict the tumor accumulation and thus the therapeutic potential of  $^{177}\text{Lu}$ -DTPA-Ctxb-PAA-AuNP.

## Résumé

Le cancer est la deuxième cause de mortalité dans le monde, responsable d'environ 9,6 millions de décès en 2018. Actuellement, les approches thérapeutiques classiquement utilisées sont l'ablation chirurgicale de la tumeur, la chimiothérapie et/ou la radiothérapie. Malgré les récents progrès dans le traitement du cancer, d'importants effets secondaires dans les tissus sains et une récurrence de la tumeur sont à déplorer chez un grand nombre de patients. Il est donc nécessaire de continuer à améliorer les modalités de traitement actuelles et de développer de nouvelles stratégies thérapeutiques, qui maximisent les dommages cellulaires créés au sein de la tumeur tout en épargnant les tissus sains. Grâce à leurs propriétés physico-chimiques uniques, les nanoparticules d'or (AuNP) ont révolutionné le domaine de la nanomédecine avec des applications potentielles comme agents de contraste, vecteurs de médicaments, agents photo-thermiques ou encore comme des agents radiosensibilisants prometteurs. Afin de maximiser la concentration des AuNP dans la tumeur, des modifications de la surface des nano-objets avec des biomolécules ciblées sont généralement utilisées.

Dans cette thèse, nous avons utilisé des AuNPs de 5 nm recouverts de poly-allylamine (AuNPs-PAA) et conjugués au Cetuximab (Ctxb), un anticorps commercial ciblant le récepteur du facteur de croissance épidermique (EGFR). L'EGFR est surexprimé dans de nombreux types de cancer, tels que les cancers colorectaux, de la tête et du cou, du sein et de la prostate. Il a été démontré que les AuNPs-PAA-Ctxb sont capables de cibler sélectivement les cellules cancéreuses surexprimant l'EGFR *in vitro* et *in vivo*, et d'améliorer l'efficacité de la protonthérapie dans les cellules cancéreuses surexprimant l'EGFR. En nanomédecine, l'administration intraveineuse d'AuNPs-PAA-Ctxb serait le scénario d'exposition le plus réaliste. Suite à cette administration systémique, il est inévitable que des cellules et des tissus sains soient également exposés aux AuNPs-PAA-Ctxb. Les premières cellules qui rencontrent les AuNPs-PAA-Ctxb sont les cellules endothéliales, qui tapissent les parois internes des vaisseaux sanguins. De plus, le système hépatobiliaire et le système rénal constituent des voies d'élimination potentielles pour l'excrétion des AuNPs-PAA-Ctxb de l'organisme. Ainsi, nous avons étudié les effets cytotoxiques des AuNPs-PAA et des AuNPs-PAA-Ctxb dans des cellules endothéliales microvasculaires humaines, des cellules hépatiques et des cellules rénales. Après incubation, les AuNPs-PAA-Ctxb ont été internalisées dans tous les types cellulaires concentrées dans des vésicules intracellulaires. Il est intéressant de noter que le profil d'expression de l'EGFR dans les divers types cellulaires étudiés n'était pas un facteur de pronostic permettant de prédire la sensibilité des cellules aux effets des AuNPs-PAA-Ctxb. Nous avons plutôt observé que les AuNPs-PAA et les AuNPs-PAA-Ctxb provoquaient un dysfonctionnement mitochondrial et inhibaient de manière significative l'activité d'enzymes antioxydantes comme la thioredoxine réductase (TrxR) et la glutathion réductase (GR), entraînant finalement la mort des cellules par apoptose. Le rôle du stress oxydatif dans ce mécanisme a été mis en évidence par les effets protecteurs de l'antioxydant N-acétyl L-



## Résumé

cystéine, qui empêche l'apparition des dysfonctionnements mitochondriaux et réduit l'apoptose lorsqu'il est présent. Enfin, nous avons démontré que l'activité basale de la TrxR, l'étendue de son inhibition et le dysfonctionnement mitochondrial sont fortement corrélés à la sensibilité des cellules aux AuNPs-PAA et AuNPs-PAA-Ctxb.

Dans la première partie de cette thèse, nous avons observé les effets cytotoxiques des AuNPs-PAA-Ctxb dans des cellules normales *in vitro*. Ainsi, dans la seconde partie, nous avons étudié la pharmacocinétique, la biodistribution et la toxicité des AuNPs-PAA-Ctxb après une injection intraveineuse unique chez des souris saines. Les AuNPs-PAA-Ctxb sont rapidement éliminés de la circulation sanguine mais une accumulation et une rétention à long terme dans le foie et la rate ont été constatées. Cependant, aucun changement morphologique significatif n'a été observé dans le foie, les reins, la rate et les poumons jusqu'à quatre semaines après l'injection des nano-objets. En outre, on n'a observé qu'une faible augmentation transitoire d'un nombre limité de marqueurs sériques liés à la réponse immunitaire, à l'activation endothéliale et à la toxicité hépatique.

Enfin, comme nous avons démontré que les AuNPs-PAA-Ctxb affectent certains systèmes biologiques impliqués dans la défense antioxydante et la survie cellulaire, les AuNPs-PAA-Ctxb pourraient prédisposer les cellules cancéreuses à l'apoptose après exposition aux rayonnements ionisants. Bien que les effets radiosensibilisants des AuNP ont largement été étudiés en envisageant une radiothérapie par faisceau externe (EBRT), il n'existe qu'un nombre limité d'études portant sur l'utilisation des AuNP comme agents radiosensibilisants en combinaison avec des radionucléides. C'est pourquoi, dans la dernière partie de cette thèse, nous avons marqué les AuNPs-PAA-Ctxb avec un radionucléide diagnostique,  $^{177}\text{Lu}$ , en utilisant des chélateurs bifonctionnels conjugués à Ctxb. L'acide diéthylènetriaminépentaacétique (DTPA), chélateur bifonctionnel, a été utilisé pour le couplage en raison de sa réaction de radiomarquage rapide dans des conditions douces et de son impact minimal sur la capacité de liaison du Ctxb. Les  $^{177}\text{Lu}$ -DTPA-Ctxb-PAA-AuNPs ont conservé leur capacité à reconnaître l'EGFR et ont montré une liaison et une internalisation plus importantes dans les cellules cancéreuses par rapport au  $^{177}\text{Lu}$ -DTPA-Ctxb. Par conséquent, en couplant l'inhibition enzymatique des AuNP aux radiations produites par le radionucléide, le  $^{177}\text{Lu}$ -DTPA-Ctxb-PAA-AuNPs pourrait avoir le potentiel d'augmenter l'efficacité de la thérapie radionucléidique ciblée par rapport au  $^{177}\text{Lu}$ -DTPA-Ctxb.

Afin d'évaluer les propriétés radiosensibilisantes du  $^{177}\text{Lu}$ -DTPA-Ctxb-PAA-AuNPs, des expériences seront menées afin d'évaluer la capacité de divers types cellulaires possédant différents profils d'expression de l'EGFR et de la TrxR, à former des colonies après exposition au  $^{177}\text{Lu}$ -DTPA-Ctxb-PAA-AuNPs ou au  $^{177}\text{Lu}$ -DTPA-Ctxb. En outre, le marquage au  $^{177}\text{Lu}$  des AuNPs-PAA-Ctxb permettra l'imagerie en temps réel de la biodistribution et de l'élimination du nanoconjugué chez les souris, portant des xénogreffes tumorales positives et négatives

pour l'EGFR. Enfin, les expériences de thérapie préclinique *in vivo* permettront de déterminer si les  $^{177}\text{Lu}$ -DTPA-Ctxb-PAA-AuNPs ont une capacité supérieure de destruction des tumeurs.

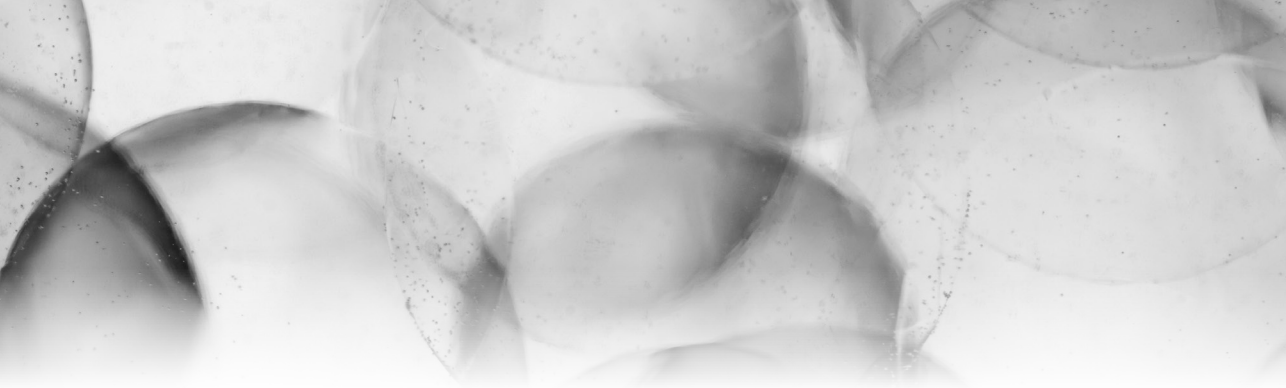
En conclusion, le  $^{177}\text{Lu}$ -DTPA-Ctxb-PAA-AuNPs est un produit radiopharmaceutique potentiellement supérieur au  $^{177}\text{Lu}$ -DTPA-Ctxb, en raison (I) du dysfonctionnement mitochondrial et de la suppression du système antioxydant, (II) de l'internalisation accrue des cellules cancéreuses et (III) de l'administration de plusieurs radionucléides  $^{177}\text{Lu}$  par AuNP. Toutefois, l'accumulation rapide et la rétention à long terme des AuNPs-PAA-Ctxb dans le foie et la rate après administration intraveineuse pourraient limiter la quantité internalisée dans la tumeur et donc le potentiel thérapeutique du  $^{177}\text{Lu}$ -DTPA-Ctxb-PAA-AuNP.



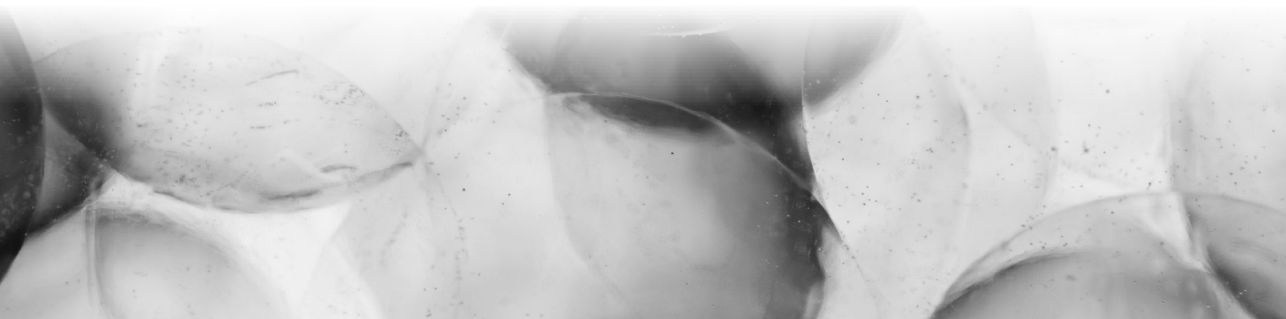
**CHAPTER**

# 1





# General Introduction



## 1. Nanoparticles: Definition, applications and history

### 1.1 Definition and applications

In 2011, the European Commission published a recommendation defining a ‘nanomaterial’ as a natural, incidental or manufactured material with one or more external dimensions in the size range of 1 nm to 100 nm. In this size range, material properties become controllable<sup>1</sup>. Hence, nanoparticles can arise in several shapes, such as spheres, rods, discs, cubes, etc. Typically, nanomaterials consist of many particles of different sizes in a certain distribution. As a result, it would be difficult to determine if a specific material complies with the definition if some particles are below 100 nm while others are not. Therefore, the recommendation specifies that the size distribution must at least consist for 50 % or more of particles having a size between 1 nm and 100 nm (2011/696/EU).

Today, nanomaterials can be found in many consumer products for daily use, such as cosmetics, sunscreen, paints, and even in medication.

### 1.2 History of gold nanoparticles

Although nanotechnology looks like a recent discovery, the use of nanoparticles, such as colloidal gold (i.e. gold nanoparticles (AuNPs) dispersed in liquid) spans many centuries in human history. For example, the Romans used colloidal gold to create ruby-red colored glassware, a process which was further refined by Andreus Cassius and Johann Kunchel in the 17<sup>th</sup> century. Furthermore, during the Middle Ages, colloidal gold was considered to be the ‘drug of longevity’ and was used to treat a number of diseases<sup>2,3</sup>. In 1857, Michael Faraday was the first to present a scientific report describing the formation of colloidal gold by the reduction of gold chloride using phosphorus. Furthermore, he concluded that the intense red color of the fluid was due to the dispersion of gold particles, which were ‘very minute in their dimensions’ and were not visible in any of the microscopes available at that time. Later on, in 1908, Gustav Mie attributed the coloration of AuNPs to their light absorption and scattering. In 1914, Richard Adolf Zsigmondy used ultramicroscopy to make the first observations and size measurements of gold and other nanoparticles<sup>4</sup>. These studies and interpretations marked the starting point of the modern colloid chemistry<sup>3,5,6</sup>. However, the real trigger for strong advances in gold nanoscience and nanotechnology was the development of cluster science and the scanning tunneling microscope<sup>7,8</sup>.

Gold has a significant history in medicine. The benefits of this noble metal in the treatment of rheumatoid arthritis was reported for the first time in 1934, but it was shown to be ineffective to treat tuberculosis<sup>9,10</sup>. Later on, in 1971, two British researchers, Faulk and Taylor, brought a revolution in immunochemistry by describing the conjugation of antibodies to AuNPs to visualize *Salmonellae* using electron microscopy<sup>11</sup>. Thereafter, AuNPs have been receiving increased attention in various biomedical applications, particularly in the field of oncology<sup>12,13</sup>.

## 2. Cancer

According to the World Health Organisation, cancer is the second leading cause of death globally, responsible for an estimated 9.6 million deaths in 2018, a burden that continues to grow. The most common cancer types in men are lung, prostate, colorectal, stomach and liver cancers, while breast, colorectal, lung, cervical and thyroid cancers are the most common types in women. In general, when identified early, patients are more likely to respond to treatment, with a better survival probability<sup>14,15</sup>. There are several imaging methods available to diagnose solid cancers, such as X-ray imaging, computed tomography (CT), magnetic resonance imaging (MRI), ultrasound, positron emission tomography (PET) and single photon emission computed tomography (SPECT). Currently, the main therapeutic approaches involve surgical removal, radiotherapy, chemotherapy or a combination of the above. However, due to the unspecific nature of chemotherapy and radiotherapy, damage is caused to both cancer cells and healthy cells, which often results in several side effects. The probability to develop normal tissue complications limits the maximal therapeutic dose that can be administered to achieve a high tumor control probability. Therefore, a considerable amount of research aims to improve cancer detection, monitoring and treatment. Developing AuNPs that can target and sensitize malignant cells to the applied therapy is one such avenue to maximize the therapeutic window (**Figure 1.1**)<sup>12,16,17</sup>.

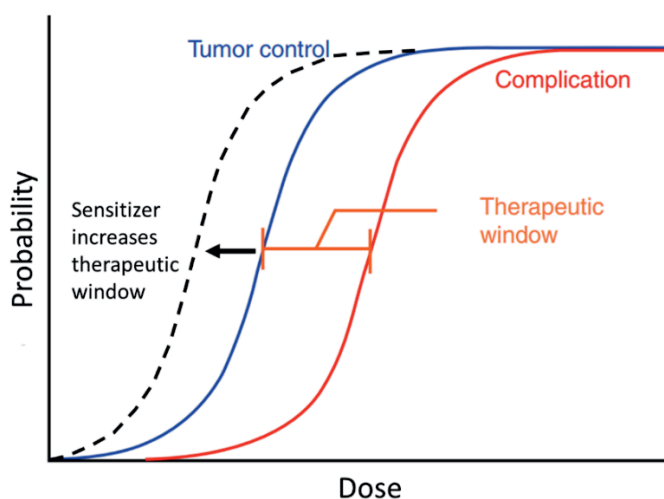


**Figure 1.1** Schematic representation of the relation between the dose, the tumor control probability curve (blue curve) and the normal tissue complication probability curve (red curve). The therapeutic dose should maximize the probability to control the tumor, while minimizing the probability of complications. A sensitizer that specifically targets the cancer cells shifts the tumor control probability curve to the left (dotted black curve), increasing the therapeutic window. Adapted from<sup>18</sup>.

### 3. The properties of gold nanoparticles

Nano-sized gold has properties that are significantly different from those of its bulk counterpart<sup>19</sup>. Today, multiple advanced synthesis methods allow researchers to control the size, shape and functionalization of the AuNPs, influencing their physical, optical and chemical properties<sup>20</sup>.

#### 3.1 The surface plasmon resonance

One of the most important characteristics of AuNPs involves the surface plasmon resonance (SPR), which occurs when incident light of a specific wavelength interacts with the free electrons at the surface of the AuNPs. The interaction causes a collective and coherent oscillation of the electrons and results in the subsequent extinction of light and the generation of heat. The light frequency at which SPR occurs strongly depends on the size of AuNPs. For example, spherical AuNPs smaller than 60 nm typically exhibit a SPR absorption peak around 500-550 nm, which lies in the blue-green portion of the visible light (VL) spectrum, and scatter light in the red portion of the VL spectrum, explaining their red color. Increasing the size of the AuNPs shifts the SPR absorption peak to the red end of the VL spectrum, while blue light is reflected. In addition to the size, altering the shape of the AuNPs can also profoundly affect the SPR absorption peak. For example, gold nanorods (AuNR) exhibit two SPR absorption peaks originating from the oscillation of the electrons along the length and along the width of the AuNR. Changing the length/width ratio of the AuNR will modulate the spectral location of the SPR peaks in the near infrared (NIR) region. The adjustability of AuNPs, with optical properties that can span the broad VL spectrum to the NIR spectrum, makes them interesting tools for cancer detection and certain therapeutic applications, such as photo-imaging and photo-thermal therapy<sup>16,19-21</sup>. In addition, as described in paragraph 4.4, the high atomic number of gold increases the interaction probability of AuNPs with ionizing radiation. Consequently, AuNPs can serve as a potential contrast agent in X-ray based imaging techniques and can exert radiosensitizing properties<sup>17,22</sup>.

#### 3.2 Surface coating and surface charge

In order to produce a stable colloid suspension and to use AuNPs in biological systems, researchers need to modify the particle surface with certain compounds to improve the biocompatibility, solubility and stability in physiological media. Indeed, without such a modification, AuNPs tend to aggregate. The two main strategies to achieve colloid stabilization is (1) through the addition of a stabilizing capping agent during the production of AuNPs, creating a strong surface charge and causing electrostatic repulsion between the particles (e.g. citrate-stabilized AuNPs) or (2) through the generation of a physical barrier by attaching polymers to the AuNP surface (i.e. steric stabilization)<sup>23</sup>. The polymer coating of AuNPs is frequently applied post-production during a second modification step, using thiol-

functionalized molecules, which directly graft onto the AuNP surface via the thiol-gold affinity interaction, progressively replacing the stabilizing capping agent. The main disadvantage of electrostatic-stabilized AuNPs is their tendency to aggregate when they are dispersed in biological media with a high ionic strength or with unfavorable pH values. A charged particle in suspension affects the ion distribution in its near environment, forming an electrical double layer. In more detail, the electrical double layer consists of (I) an inner stationary layer of counterions strongly adsorbed onto the charged surface of the nanoparticle (Stern layer), and (II) an outer, diffuse layer of free ions, with a gradually decreased density of the counterions further away from the nanoparticle surface (**Figure 1.2**)<sup>24,25</sup>. The ionic strength and pH cause this diffuse layer around the AuNPs to compress and neutralize, which results in aggregation due to the Van der Waals forces. In contrast, steric-stabilized AuNPs are more resistant to aggregation, thanks to the physical barrier. Furthermore, the hydrophilic nature of the coating molecules creates an extra stabilization through the repulsive hydration forces<sup>23,26</sup>. Importantly, depending on the applied functionalized coating, the net surface charge of the AuNPs can be positive, negative or neutral and it strongly influences the fate and the biological effects of the AuNPs. For instance, one of the most commonly used steric-stabilizing polymers for AuNP coating is polyethylene glycol (PEG), which neutralizes the surface charge of electrostatic-stabilized AuNPs and gives the AuNPs a stealth character, preventing their recognition and subsequent removal by the phagocytic cells of the reticuloendothelial system (RES), and prolonging their blood circulation time. Other coating options next to polymers include citrate, cetyltrimethylammonium bromide (CTAB), proteins, peptides, glycans and zwitterionic ligands<sup>16,19,23,27</sup>.

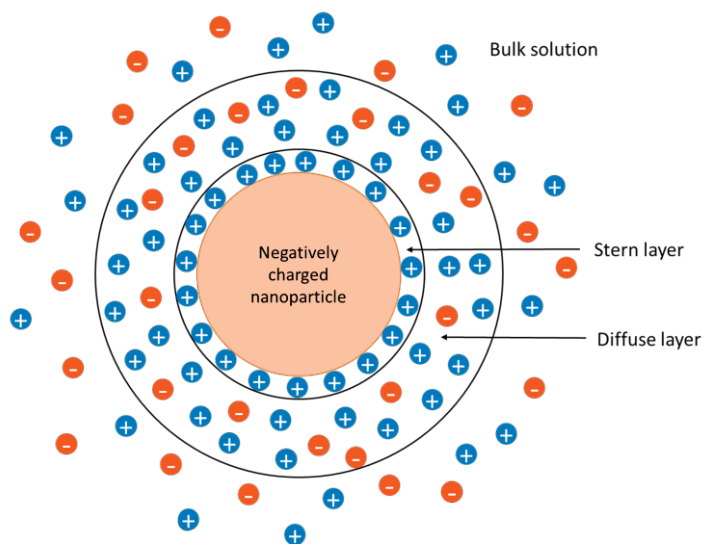


**Figure 1.2** The electrical double layer surrounding a negatively charged nanoparticle in suspension. Adapted from <sup>28</sup>.



### 3.3 Surface area-to-volume ratio

The high surface area-to-volume ratio is an important physical property of nanoparticles. When the size of the nanoparticles decreases, a higher proportion of their atoms or molecules are displayed on the particle's surface, rather than in the particle's interior. For example: a 5 nm AuNP has a surface area-to-volume ratio of 1.2 and exhibits a total surface area of 62 m<sup>2</sup>/g of AuNPs, whereas a 200 nm AuNP has a surface area-to-volume ratio of 0.03 and a total surface area of 1.6 m<sup>2</sup>/g of AuNPs. This determines the biological profile and reactivity of the nanoparticles, which is distinct from their bulk counterparts <sup>29</sup>. As a result, this large surface area-to-volume ratio, together with the functional groups offered by the coatings, facilitate the incorporation of multiple moieties onto the AuNP surface. As a result, anti-cancer drugs, imaging agents and molecules that 'actively' target cancer cells can be conjugated to AuNPs, hence supporting the assembly of multifunctional platforms and further increasing the diagnostic and therapeutic potential of AuNPs <sup>30,31</sup>.

## 4. Gold nanoparticles in cancer treatment and detection

Thanks to their optical and physicochemical properties described above, AuNPs can serve as multifunctional platforms, combining different cancer targeting, therapy and detection modalities, which will be discussed in the following sections and are summarized in **Figure 1.3**.

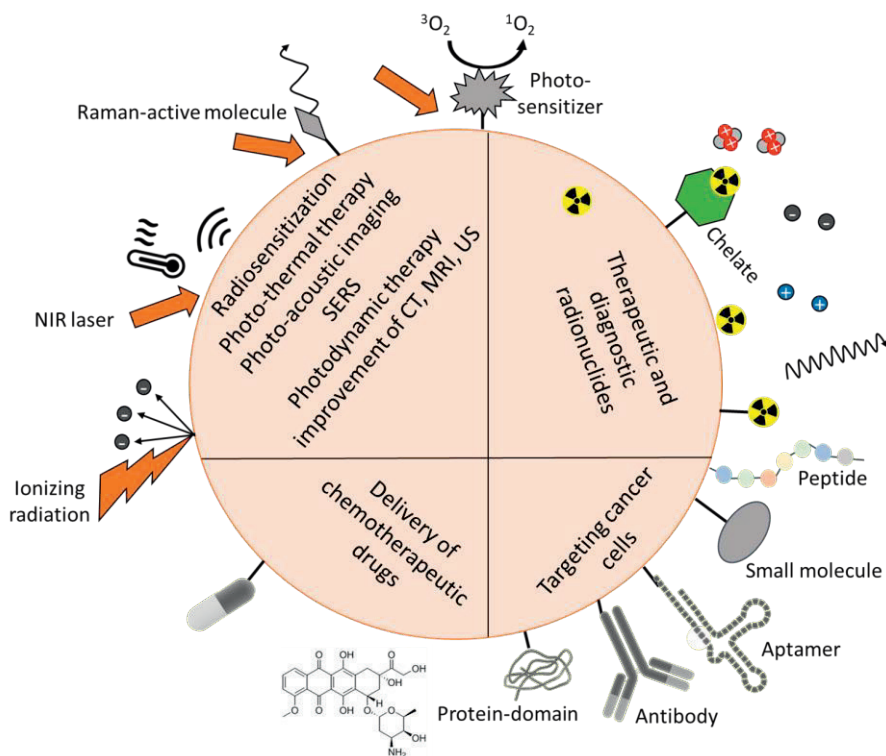


**Figure 1.3** Multifunctional AuNPs and their potential applications in the diagnosis and treatment of cancer.

**Abbreviations:** CT: computed tomography; MRI: magnetic resonance imaging; SERS: surface-enhanced Raman scattering; US: ultrasound.

## 4.1 Cancer targeting

In order to use AuNPs in cancer remediation applications, AuNPs need to reach and accumulate in the tumor tissue. Thanks to their small size, AuNPs can efficiently pass through the leaky and immature blood vessels within the tumor mass. Furthermore, the decreased level of lymphatic drainage and a reduced uptake of the interstitial fluid within the tumor microenvironment promote their subsequent tumor retention. This 'passive' process is known as the enhanced permeability and retention (EPR) effect (**Figure 1.4**)<sup>19,32</sup>. However, the efficacy of passive targeting can be limited due to the heterogeneity of the vasculature and thus of the EPR effect within a tumor, at different tumor stages and between different tumor types. Therefore, additional functionalization with cancer-specific ligands can increase the targeting capacity of the AuNPs<sup>33</sup>. Cancer targeting ligands are often specific for factors that are unique or upregulated in cancer cells and that are mostly involved in processes such as tumor progression, invasion, metastasis and angiogenesis. In general, these targeting ligands can be categorized in five main classes: small molecules, peptides, protein domains,

antibodies and nucleic-acid based aptamers<sup>34</sup>. Some of the most widely used cancer-specific targeting ligands for AuNP conjugation are folic acid (FA) (essential for DNA synthesis), cyclic arginine-glycine-aspartic acid (cRGD) peptide (a cell adhesion motif with a high affinity for  $\alpha\beta$ -integrins), and targeting ligands that can bind to the epidermal growth factor receptor (EGFR) 1 and 2, or to the vascular endothelial growth factor receptor (VEGFR)<sup>34-46</sup>. However, it should be nuanced that ‘active’ delivery does not make the AuNPs act as a guided missile acquiring its own power. In reality, the targeted AuNPs are carried through the body by the circulatory system. Therefore, the AuNPs will need to circulate several times before encountering the tumor and thus remain in the blood circulation for a sufficient amount of time. Nevertheless, the targeting ligands on the AuNP surface increase the probability of the AuNPs to interact with the tumor site and to become internalized<sup>47</sup>.

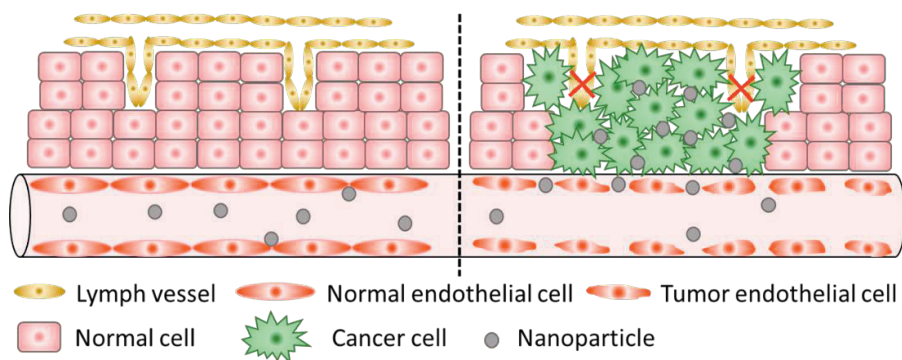


**Figure 1.4** Schematic representation of gold nanoparticles accumulating in the tumor site due to the enhanced permeability and retention effect. Adapted from<sup>48</sup>.

Besides a distinct vasculature structure, the extracellular environment of cancer tissue tends to have a lower pH value (pH = 6.5) than that of the surrounding healthy tissue (pH = 7.5). Furthermore, cancer cells can exhibit a higher redox potential (e.g. high glutathione levels) and a higher activity of specific enzymes, such as phosphatases and metalloproteases<sup>49</sup>. These cancer-specific features can be exploited as stimuli to boost the diagnostic and therapeutic potentials of AuNPs, as described below.

## 4.2 Photo-thermal and photodynamic therapy

Hyperthermia can help in tumor control thanks to its effects on the tumor vasculature and on cancer cells. In more detail, the appropriate physiological response of healthy vasculature to hyperthermia is vasodilation, which helps to efficiently dissipate the heat and to avoid tissue damage. In contrast, the tumor vasculature is characterized by an aberrant organization and structure, consisting of blood vessels that are immature, tortuous and hyperpermeable. When hyperthermia is applied, the blood flow and oxygen supply to the tumor tissue initially increases, which enhances the delivery and efficacy of chemotherapeutic drugs and sensitizes the cancer cells to radiotherapy. However, when the

heat accumulates in the tumor tissue, reaching a temperature of 42°C, the tumoral blood vessels collapse, aggravating the acidic, hypoxic and nutrient-poor tumor conditions and promoting cancer cell death. In contrast, normal tissues show a different vascular response to heat, characterized by an increased blood flow even at temperatures that cause vascular occlusion in tumors. Nevertheless, there is no consensus about the difference in heat sensitivity between normal and tumor cells *in vitro*<sup>50</sup>. At the microscopic level, hyperthermia mainly causes protein denaturation and aggregation, which results in cell cycle arrest, inactivation of protein synthesis and inhibition of DNA damage repair. Other cellular effects are DNA disruption, damage to cell structures, increased membrane permeability and cell death<sup>51</sup>. Therefore, it is important to localize hyperthermia to the tumor tissue, while avoiding prolonged exposure of healthy cells to elevated temperatures.

Thanks to their SPR characteristics, AuNPs can efficiently convert light of a specific wavelength into thermal energy. This, together with the ability to conjugate cancer-specific ligands to AuNPs, makes AuNPs attractive tools to localize heat generation in cancer cells. This therapeutic strategy is called photo-thermal therapy (PTT). A comparison of the light-to-heat conversion efficiency of different AuNPs demonstrated that AuNPs with a smaller size are better transducers<sup>52</sup>. However, in order to use AuNPs for PTT *in vivo*, it is desirable that the spectral location of the SPR peak is tuned beyond the visible and into the NIR region of the spectrum, since NIR light provides deep tissue penetration able to reach the tumor site. In fact, lasers are used in two specific ‘treatment windows’ ranging from 650 nm-850 nm with a tissue penetration of 2-3 cm, and from 950 nm- 1350 nm with a tissue penetration up to 10 cm<sup>27</sup>. As discussed earlier, tuning the SPR peak to the NIR region can be achieved by controlling the physical parameters of AuNPs, such as the size and the shape. In this regard, configurations such as AuNRs, gold nanostars, gold nanoshells and gold nanoprisms are recently being assessed for their application as PTT agent, because of their optical resonance in the NIR region<sup>21,53,54</sup>. In addition, several studies used a strategy based on stimulus-sensitive AuNPs, which aggregate in response to light or when internalized by cancer cells due to the acidic pH, upregulated enzymes or an upregulated redox activity. The stimulus-induced aggregation increases the size of the AuNPs in the cancer cells to > 600 nm and shifts the SPR peak to the NIR region, which enhances the efficacy of PTT. Furthermore, the aggregation of the AuNPs when entering the tumor site leads to a better tumor retention<sup>55-59</sup>.

There are several advantages associated with the use of AuNPs for PTT. First, the much higher absorption coefficient of AuNPs compared to the conventional dyes reduces the laser power needed to achieve a thermo-therapeutic effect. Second, thanks to the selective loading of targeted AuNPs in cancer cells, the laser power required to kill cancer cells is below that required to kill healthy cells. This is supported by several *in vitro* studies demonstrating that the higher uptake of AuNPs in cancer cells leads to a higher PTT efficiency and toxicity than in normal cells<sup>60,61</sup>. Finally, the required laser irradiation time is much shorter (3 minutes),

compared to that in conventional hyperthermia (60 minutes)<sup>62</sup>. Indeed, several *in vivo* studies demonstrated that a tumor loaded with AuNPs could reach a temperature of 44°C-62°C in only 2-10 minutes time when irradiated with a low-intermediate power laser (0.5-5 W/cm<sup>2</sup>) in the NIR range (633-980 nm). These temperatures exceed the threshold temperature needed to induce irreversible tissue damage and thus result in a better tumor growth inhibition, tumor regression, and a longer survival of the mice, as compared to treatment with NIR irradiation or AuNPs alone<sup>56,57,59,63-69</sup>.

Another phototherapy next to PTT is the photodynamic therapy (PDT). PDT causes cell death based on the light absorption by a photosensitizer (PS), which transfers its energy to molecular oxygen, generating reactive oxygen species (ROS), such as singlet oxygen. However, the use of PS is often limited due to their non-selectivity and their hydrophobic nature, leading to aggregation in aqueous media. Besides, a lack of oxygen in tumor hypoxic microenvironments can limit the therapeutic efficacy of the oxygen-reliable PDT. Conjugation of PS to AuNPs can help to overcome these limitations by improving the PS solubility and targeted delivery. Furthermore, it creates the opportunity to enhance the photo-therapeutic effect by combining PDT and PTT. Indeed, the photo-thermal ability of AuNPs under NIR irradiation enables heat generation, which improves tumoral blood flow *in vivo* and increases the oxygen supply required for PDT<sup>70-74</sup>. In addition, the photoluminescence arising from NIR-irradiated AuNPs can activate the PS via energy transfer, enhancing singlet oxygen formation<sup>75,76</sup>. This has inspired research to design dual PTT/PDT therapy approaches, which can be activated by a double or single NIR wavelength, resulting in a synergistic cancer cell death *in vitro* and *in vivo*, as compared to PTT or PDT alone<sup>66,69,71,77-91</sup>.

### 4.3 The use of gold nanoparticles in chemotherapy

Chemotherapy uses toxic agents that kill rapidly dividing cells by directly or indirectly inducing DNA damage<sup>92</sup>. However, the conventional chemotherapeutic approaches are limited due to the systemic administration and nonspecific distribution of the agent through the body, leading to poor pharmacokinetics, a low therapeutic index and damage to healthy cells, which causes serious side effects. AuNPs have the potential to improve these aspects by acting as targeted nanocarrier drug delivery systems (DDS). AuNPs as nanocarriers can improve the solubility and stability of a free drug. In addition, they can efficiently hold and transport a high payload of the drug to the tumor, improving its biodistribution profile and efficacy, while minimizing the side effects<sup>16,93,94</sup>.

Next to targeting, gold nanocarriers enable the release of chemotherapeutic drugs in a controlled and sustained manner. A commonly used strategy is the engineering of stimulus-sensitive DDS, which are based on the abnormalities of the tumor microenvironment. For example, a pH sensitive DDS allows chemotherapeutic drugs to circulate through the neutral healthy tissues, until the DDS reaches the slightly acidic cancer cell environment and is

internalized into lysosomes where it is triggered to release the drug. In this way, drug distribution is restricted in cancerous tissues, while nonspecific drug leakage is prevented in the healthy tissues<sup>95</sup>. This approach has been assessed by several studies to regulate the delivery of effective, but toxic anticancer drugs, such as cisplatin, 5-fluorouracil and doxorubicin. In more detail, AuNPs can be conjugated to the drug by pH-sensitive hydrazone bonds, *cis*-aconityl bonds or by electrostatic interactions with surface conjugated peptides or anionic polymers. When entering an acidic environment, these coupling agents become protonated, abolishing the interaction between the nanocarrier and the biologically active compound<sup>41,45,96-99</sup>. In addition, chitosan, a natural polysaccharide, is an attractive polymer coating for AuNPs that are used in drug delivery applications, thanks to its biocompatibility and biodegradability. When modified, the chitosan polymers can form a gel-like structure thanks to the inter-chain hydrogen bonds at neutral pH, encapsulating anti-cancer drugs. In an acidic environment, swelling and gel-sol transition of the chitosan takes place, releasing the drug<sup>38,100-104</sup>. Besides an acidic pH, the higher redox activity or upregulated enzymes in cancer cells can be exploited to trigger drug release as well as the disassembly or aggregation of gold nanocarriers, hence promoting a better tumor penetration or retention, respectively<sup>41,98,105-108</sup>.

The development of gold nanocarriers sensitive for exogenous stimuli such as light and heat enables an 'on-demand' drug delivery. As a result, tremendous research has been performed on AuNPs as photo-thermal responsive DDS, combining NIR-induced PTT and targeted chemotherapeutic delivery. PTT sensitizes the cancer cells to the chemotherapeutic drug, allowing it to be administered in smaller doses or reverse multidrug resistance<sup>37,109-116</sup>. In addition, the NIR irradiation of plasmonic AuNPs and the subsequent thermal effect can boost drug uptake and drug unloading in cancer cells, for example by favoring drug diffusion and by destabilizing the drug-holding material<sup>117-126</sup>.

## 4.4 The use of gold nanoparticles as radiosensitizers

### 4.4.1 External beam radiotherapy

Currently, approximately 50% of all cancer patients receive radiation therapy at some point during the course of their disease<sup>127</sup>. External beam radiotherapy (EBRT) is the most common form of radiotherapy, where ionizing radiation energy is delivered to the tumor cells using externally generated photons (X-rays or  $\gamma$ -rays) or charged particles (protons, electrons or ions)<sup>128</sup>.

When passing through a medium, ionizing radiation can interact with atoms, losing energy along their track. The average energy deposited per unit length is called the linear energy transfer (LET). Alpha particles, ions and protons are considered as high-LET radiation inducing dense ionizations along their track. Therefore, high-LET radiation is likely to cause damage through the direct interaction with essential cellular target structures, such as the DNA, which makes it highly destructive to biological tissues. Indeed, high-LET radiation causes

complex genetic lesions such as clustered DNA double strand breaks (DSBs). The cells will respond to DNA damage by arresting the cell cycle and activating the DNA damage response mechanisms. However, the severe genetic lesions caused by high-LET radiation are typically difficult to repair and are likely to activate apoptotic cell death. On the other hand, X-rays,  $\gamma$ -rays and electrons are classified as low-LET radiation. Low-LET radiation sparsely and randomly causes ionizations along the length of its track. As a result, this type of radiation primarily acts indirectly through the interaction with the abundant water molecules inside the cell. This results in the generation of a variety of ROS, including hydroxyl radicals, superoxide, singlet oxygen, and hydrogen peroxide ( $H_2O_2$ ). The generated ROS diffuse over a distance, which is usually very short, and in turn interact with critical cellular components, such as the DNA, proteins and lipids. The damage to the genomic DNA is usually less complex and severe than that caused by high-LET radiation, including single strand breaks and base damages. Therefore, DNA damage is repaired more easily and thus a higher radiation dose is needed to cause cell death. In other words, high-LET radiation has a higher relative biological effectiveness. The latter represents the ratio of the dose of the reference radiation (usually X-rays) to the dose of the test radiation to achieve the same biological effects<sup>129,130</sup>.

The goal of radiotherapy is to deliver a lethal radiation dose to the tumor, while keeping the dose in the surrounding healthy tissues to a minimum. Therefore, accurate treatment planning and dose calculations are required. In the context of ERBT, this is based on CT imaging or MRI, creating a three-dimensional (3D) image to precisely match the radiation beams to the tumor volume in the treatment position using multi-leaf collimators. Furthermore, the surrounding organs at risk are spared as much as possible by modulating the intensity of the radiotherapy. Despite these significant technological advancements in ERBT, successful tumor control can still be challenging, due to the heterogeneity of the tumor, the presence of radio-resistant cancer cells and the risk for normal tissue toxicity<sup>131</sup>. Gold nanoparticles with good biocompatibility profiles have been proposed as favorable radiosensitizing agents, which can improve the efficacy of radiotherapy<sup>132-134</sup>.

### 4.4.2 AuNPs and photon radiation therapy

#### 4.4.2.1 Physical interactions between AuNPs and radiation

Hainfeld, et al performed a pioneering study where they intravenously injected a high dose of 1.9 nm AuNPs (2.7 g Au/kg) in mice bearing subcutaneous EMT-6 mammary carcinomas. Subsequently, the tumors were irradiated with 250 kVp<sup>1</sup> X-rays. Their results showed a longer survival of the AuNPs-injected mice compared to the mice that received X-rays or AuNPs alone. This radiosensitizing effect was attributed to the high atomic number ( $Z = 79$ ) of gold,

---

<sup>1</sup> Kilovolts (kV) and megavolts (MV) refers to the electron-accelerating potential and equals the maximum energy of the generated spectrum of **poly-energetic photons**. kVp is the peak potential applied across an X-ray tube. Kilo-electron volts (KeV) and mega-electron volts (MeV) denotes the energy of **mono-energetic** particles or photons.

resulting in the preferential absorption of X-rays by the AuNPs as compared to soft tissue<sup>135</sup>. This property enables AuNPs to increase the radiation dose deposition in cancer cells when accumulated in the tumor site, enhancing cancer cell death. In more detail, when X-rays interfere with matter such as AuNPs, a number of interaction processes can occur<sup>132</sup> (**Figure 1.5**).

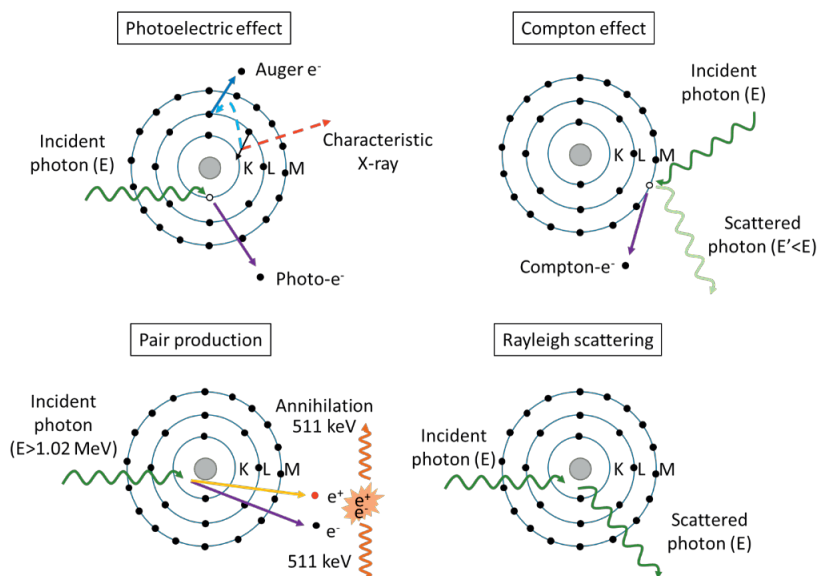


**Figure 1.5** Overview of the interaction mechanisms of photons with matter leading to attenuation and secondary emissions. Adapted from<sup>136</sup>.

In the keV energy range, photons interact with the AuNPs mainly through the Compton effect and the photoelectric effect. In the Compton (inelastic) effect, the incident photon collides to a free or a weakly bound electron, ejecting it from the outer shell of the atom. The photon loses a part of its energy and can continue its course or it can be involved in other interaction processes. The ejected electron travels through the surrounding material, losing its energy by atom excitations or ionizations. In case of Rayleigh (elastic) scattering, the incident photon collides with the entire atom, resulting in a negligible energy deposition. Therefore, this kind of scattering is not useful for therapy<sup>132,137</sup>.

In the photoelectric effect, the incident photon collides with an electron belonging to one of the inner shells of the atom. The photon energy is completely absorbed and the ejected 'photoelectron' acquires kinetic energy, which equals the energy of the incident photon minus the electron binding energy. As a result, the photoelectron can travel over a distance of several cell diameters ( $\mu\text{m}$ -range). The ejection of the photoelectron creates a vacancy, which can be refilled by an electron from a higher level. This transition usually occurs together with the emission of characteristic X-rays or is accompanied by the ejection of an



'Auger electron'. Auger electrons can only travel short distances (nm-range), but can produce a very high ionization density. In contrast to the Compton effect, the cross-section of the photoelectric effect (i.e. the probability for the interaction to occur) and the subsequent Auger cascade strongly increases with an increasing atomic number of the material. Since soft tissues consist mostly out of low Z organic material, there is only a very small contribution of the photoelectric effect. In fact, in soft tissues and water, Compton scattering is the primary mechanism by which photons (>20 keV) lose their energy (**Figure 1.6A**). In contrast, gold has a high Z number, resulting in the photoelectric effect being the most prominent mechanism (**Figure 1.6B**). Therefore, gold is much more effective in the absorption of energy per unit mass (more than 100 times) than soft tissues or water (**Figure 1.6C**). As a result, the secondary electron emission from many gold atoms in an AuNP (and from multiple AuNPs in the biological tissue) translates into a considerable increase in the local dose deposition<sup>134,137</sup>. The abundant secondary electrons in turn can directly damage biomolecules in their close proximity or they can interact with the water molecules inside the cell, producing hydroxyl radicals, which cause indirect damage to biomolecules<sup>138</sup>.

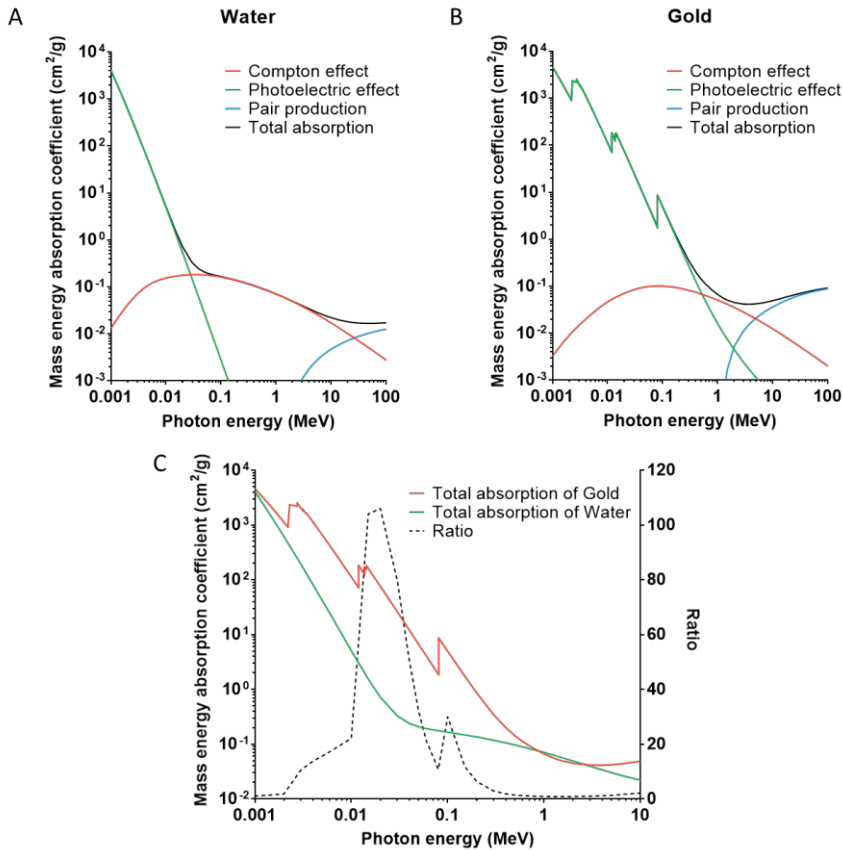


**Figure 1.6** The total absorption cross-section and the absorption cross-section of the Compton effect, the photo-electric effect and pair production in function of the photon energy in (A) water and (B) gold. (C) A comparison of the total absorption cross-section in water and gold in function of the photon energy, represented as the ratio of the total absorption cross-section in gold to that in water. The data was retrieved from the NIST photon cross sections database <sup>139</sup>.

Pair production occurs when high-energy photons (> 1.02 MeV) pass near the nucleus of the atom, where the energy of the incident photon is converted into an electron and a positron. The positron can annihilate with a free electron, emitting two photons, each having an energy of 511 keV and traveling in the opposite direction. The pair production cross-section in gold is slightly higher than in water. However, using such high beam energy levels (>10 MeV), the photoelectric effect, which is the main advantage of gold, is negligible (**Figure 1.6B**)

<sup>132</sup>.

#### 4.4.2.2 *In vitro*, *in vivo* and Monte Carlo results

After the promising findings of Hainfeld, a large number of studies followed, focusing on the radiosensitizing effects of AuNPs using photon irradiation *in vitro* and *in vivo* (**Table 1.1**). In

addition, Monte Carlo (MC) simulations are able to model the radiation passage through a virtual environment mimicking different biological systems, while taking into account the presence of AuNPs and their interaction probability with the incident radiation. MC simulations performing macrodosimetry predict the energy deposition induced by randomly distributed AuNPs, averaged over a millimeter- or centimeter-scaled phantom representing the tumor site. On the other hand, microdosimetry and nanodosimetry estimate the dose deposition on a cellular or molecular level and focus more on the ionizing particle track originating from the AuNP surface. Such calculation-based tools are helpful in determining a promising combination of parameters, which could lead to a strong radiosensitizing effect in experimental studies. The contribution of the AuNPs to the radiotherapeutic effect is usually quantified by the 'dose enhancement factor' (DEF), which represents the dose deposited in the tumor region with AuNPs divided by the dose deposited in the tumor region without AuNPs. Alternatively, the 'sensitization enhancement ratio' (SER) is defined as the ratio of the radiation doses required to elicit the same biological effect without and with AuNPs. If these ratios are larger than one, then the AuNPs are functioning as radiosensitizers. Importantly, DEF or SER varies depending on several parameters related to the radiation quality, the cell model, AuNP characteristics (such as the size and coating), AuNP concentration and AuNP localization <sup>136</sup>:

- Radiation energy

As previously explained, the photoelectric effect is an important physical interaction mechanism that contributes to the radiosensitizing properties of AuNPs through the strong production of photoelectrons, Auger cascades, characteristic X-rays and free radicals during low-energy photon irradiation <sup>140</sup>. As a result, large dose enhancement factors were observed in cells and animals exposed to AuNPs and irradiated with kilovoltage photons (**Table 1.1**). Unfortunately, kilovoltage X-rays have a limited clinical utility due to their shallow tissue penetration. Therefore, megavoltage (MV) radiation is used to treat deep-seated tumors. Irradiation of AuNPs with clinical MV photons is not expected to elicit significant AuNPs-mediated radiosensitization, because the photoelectric absorption in gold during high-energy MV photon irradiation is negligible, while Compton electron scattering and pair production in gold and in soft tissue are comparable (**Figure 1.6**) <sup>141,142</sup>. Nevertheless, although the DEF consistently reduces when the radiation energy increases as observed by Chithrani, et al, several *in vitro* and *in vivo* experimental studies, listed in **Table 1.1**, still showed a significant radiosensitization effect when AuNPs are irradiated with MV photons <sup>143-153</sup>.

These experimental results are not in agreement with multiple macroscopic MC simulations, which usually take into account high AuNP concentrations and estimate little or no dose enhancement using high-energy MV photons <sup>134,154-157</sup>. This discrepancy between experimental and theoretical studies could partly be related to a limited resemblance of the

experimental situation in the MC simulations. For instance, MC simulations usually assume a homogenous distribution of AuNPs inside a phantom, whereas AuNPs are typically clustered together inside lysosomes and display a heterogeneous intracellular distribution. In fact, Rudek, et al showed that the total dose enhancement decreases with an increasing degree of AuNP clustering<sup>158</sup>. Nevertheless, dose enhancement hot spots are observed within the spaces between the AuNPs in the cluster and are much greater than the peripheral dose enhancement around a single AuNPs or around a cluster of AuNPs<sup>159</sup>. Besides cluster formation, AuNPs are mainly found in the perivascular areas of a tumor. As a result, it is more realistic that a considerable, AuNPs-mediated dose enhancement within cells and tumors occurs in a heterogeneous fashion<sup>160</sup>.

In order to better understand the radiosensitization effects of AuNPs observed after exposure to MV photons, McMahon, et al used the 'Local Effect Model' to estimate the energy deposition close to the AuNP surface. The authors found significant, but heterogeneous dose enhancement peaks on the nanoscale level in close proximity of the AuNPs. The dose enhancement peaks are caused by cascading secondary electrons following an ionization event and are considerably greater than the average macroscopic dose estimation over the entire cell. In fact, these microscopic dose enhancements around the AuNPs are similar to those seen after low-energy photon exposure and thus could contribute to the radiosensitization observed in the MV experimental studies. However, the dose enhancements drop off quickly with an increasing distance from the AuNPs<sup>161,162</sup>.

**Table 1.1** Overview of the *in vitro* and *in vivo* studies focusing on the radiosensitization effects of AuNPs using photon radiotherapy.

<i>In vitro</i> experiments						
Author	Size (nm)	Concentration	Surface functionality	Cell model	Source energy	Effect/SER (survival/dose)
Bobyk, et al <sup>163</sup>	1.9 15	10 mg/ml	thiol	F98	50 keV	1.92 (SF 10%) 1.40
Butterworth, et al <sup>164</sup>	1.9	10 µg/ml 100 µg/ml	thiol	AGO-1522B L132 Astro T98G MDA-MB-231 MCF-7 PC3 DU145	160 kVp	1.16-1.97 (2 Gy) 0.86-0.87 1.04-0.96 1.30-1.91 1.67-1.11 1.41-1.09 1.07-1.02 0.98-0.81
Chattopadhyay, et al <sup>165</sup>	30	2.4 mg/ml	PEG Trastuzumab	MDA-MB-361	100 kVp	1.30 (PEG) (SF 10%) 1.60 (Trastuzumab)
Chen, et al <sup>166</sup>	28	36 µg/ml	BSA	U87	160 kVp	1.37 (2 Gy)

## Chapter I

Chithran i, et al 144	14 <sup>+</sup> 50* 74	7 x 10 <sup>9</sup> NP/ml	Citrate	HeLa	150 kVp 220 kVp 660 keV 6 MV	1.66* (SF 10%) 1.20 <sup>†</sup> - 1.43*- 1.26 1.18* 1.17*
Coulter et al. 167	1.9	12 µM (500 µg/ml)	Thiol	MDA-MB-231 DU-145 L132	160 kVp	~1.87 (3 Gy) for MDA-MB- 231 only
Cui et al. 168	2.7	0.5 mg/ml	Tiopronin	MDA-MB-231	225 kVp	1.04 - 1.44 (SF 10%)
Cui et al. 168	2.7	0.5 mg/ml (EC/IC/EC+IC)	Tiopronin	MDA-MB-231	225 kVp	1.09 - 1.39 - 1.41 (SF 10%)
Geng et al. 169	14	5 nM	Glucose	SKOV-3	90 kVp 6 MV	1.30 (5 Gy) 1.20
Guo, et al 170	14.4 30.5	0.05 mM	PEG	H22 HepG2	662 keV ( <sup>137</sup> Cs)	1.20 (SF 50%) 1.30
Jain et al. 145	1.9	12 µM (500 µg/ml)	Thiol	MDA-MB-231 DU145 L132	160 kVp* 6 MV 15 MV	1.41* - 1.29 - 1.16 (4 Gy) 0.92 - 1.13 1.05 - 1.08
Jain et al. 171	1.9	12 µM (500 µg/ml)	Thiol	MDA-MB-231	160 kVp	1.10 [0.1% O <sub>2</sub> ] (4 Gy) 1.39 [1% O <sub>2</sub> ] 1.41 [21% O <sub>2</sub> ]
Jeynes, et al 172	50	5.5 µg/ml	FBS	RT112	250 kVp	1.6 (SF 50%)
Joh et al. 173	23	1 mM	PEG	U251	150 kVp	1.30
Kaur et al. 174	5–9	5.5 µM	Glucose	HeLa	1.17-1.33 MeV ( <sup>60</sup> Co)	1.52 (SF 10%)
Kazmi, et al 147	42	100 µg/ml	Citrate	U87	6 MV	1.45 (2 Gy)
Khoshga rd et al. 152	47- 52	50 µM	PEG Folic acid	HeLa	120-250 kVp  1.17-1.33 MeV ( <sup>60</sup> Co)	1.35 (PEG) (2 Gy) 1.64 (FA) 1.03 (PEG) 1.05 (FA)
Kong et al. 153	10.8	15 µM	Cysteamine Glucose	MCF-7	200 kVp  662 keV ( <sup>137</sup> Cs) 1.17-1.33 MeV ( <sup>60</sup> Co)	1.30 (cysteamine) 1.60 (glucose) 1.13 ( <sup>137</sup> Cs and <sup>60</sup> Co)
Liu, et al 175	4.7		PEG	CT26	6 MV	1.33-1.59
Liu et al. 157	14.8	1.5-7.5-15 µg/ml	Citrate	HeLa	50 kVp	1.14–2.88-1.86 (SF 50%)

Liu, et al <sup>176</sup>	40 38	10 µg/ml	PEG Tirapazamine	HepG2	50 kVp	1.05 (PEG) (SF 10%) 1.25 (Tirapazamine)
Pennink kx, et al <sup>177</sup>	10	50 µg/ml	PEG	A549	225 kV	1.22 (SF 10%)
Roa et al. <sup>178</sup>	10.8	15 nM	Glucose	DU-145	662 keV ( <sup>137</sup> Cs)	1.24–1.38 (2 Gy)
Saberi, et al <sup>148</sup>	50	20-100 µM	/	HT-29	9 MV	1.4 (MID)
Shi, et al <sup>179</sup>	2.77	0.1 mg/ml 0.25 mg/ml	Tiopronin	HCT116	26 keV	1.48 (MID) 1.69
Taggart et al. <sup>180</sup>	1.9	12 µM (500 µg/ml)	Thiol	MDA-MB-231 T98G DU-145	225 kVp	1.23-1.20-1.17 (2-4-8 Gy) 1.90-1.57-1.35 1.20-1.06-1.10
Wang et al. <sup>181</sup>	13	20 nM	Glucose	A549	6 MV	1.49 (MID)
Wang et al. <sup>182</sup>	16 49	20 nM	Glucose	MDA-MB-231	6 MV	1.49 (MID) 1.86
Wolfe et al. <sup>143</sup>	31x9	0.3 OD	PEG Goserelin	PC-3	6 MV	1.09 (PEG) (SF 10%) 1.35 (Goserelin)
Zhang, et al <sup>183</sup>	4.8 12.1 27.3 46.6	0.05-0.1 mM	PEG	HeLa	662 keV ( <sup>137</sup> Cs)	1.41-1.46 (SF 50%) 1.65-2.07 1.58-1.86 1.42-1.52
Zhang, et al <sup>184</sup>	< 2	50 µg/ml	Glutathione BSA	HeLa	662 keV ( <sup>137</sup> Cs)	1.30 (SF 50%) 1.21
Zhang, et al <sup>151</sup>	20 28	400 nM	PEG Octaarginine	LS180	6 MV	1.21 (Average lethal dose) 1.59

***In vivo experiments***

Author	Size (nm)	Dose	Surface functionality	Cell model	Therapy	Effect
Chattop adhyay, et al <sup>165</sup>	30	0.8 mg Au, IT	Trastuzumab	MDA-MB-361	100 kVp, 11 Gy	Tumor growth: RT + Au: 46% Regression RT- Au: 16% Growth
Chen, et al <sup>185</sup>	28	325 µg Au, IV	BSA	U87	160 kVp, 3 Gy (2h p.i.) + 2 Gy (24 p.i.)	Tumor regression
Hainfeld , et al <sup>135</sup>	1.9	1.35 g Au/kg, IV 2.7 g Au/kg, IV	Thiol	EMT-6	250 kVp, 26 Gy	Long-term survival: 1.35 g/kg: 50% 2.7 g/kg: 86% RT alone: 20%
Hainfeld , et al <sup>186</sup>	1.9	1.9 g Au/kg, IV	Thiol	SCCVII	68 keV, 42 Gy,	Tumor doubling time: 68 keV: 53 <sup>(-)</sup> vs 76 <sup>(+)</sup> days

					157 keV, 50.6 Gy	157 keV: 31 <sup>(-)</sup> vs 49 <sup>(+)</sup> days Long-term survival: 68 keV: 67% <sup>(-)</sup> vs 25% <sup>(+)</sup> 157 keV: 0% <sup>(-)</sup> vs 38% <sup>(+)</sup>
Hainfeld , et al <sup>187</sup>	1.9	4 g Au/kg, IV	Thiol	Tu-2449	100 kVp, 30 Gy	long-term survival: RT + Au: 50% (tumor-free) RT - Au: 0%
Joh, et al <sup>173</sup>	23	1.25 g Au/kg, IV	PEG	U251	175 kVp, 20 Gy	Increased median survival RT + Au: 28 days RT - Au: 14 days
Shi, et al <sup>179</sup>	2.77	732.6 µg Au, IV 366.3 µg Au, IT	Tiopronin	HCT-116	26 keV 10 Gy	Time to increase tumor size 4x after IT injection: RT + Au: 54 days RT - Au: 37 days
Wolfe, et al <sup>143</sup>	31x9	10 mg/kg (100 µl), IV	Goserelin	PC-3	6 MV, 5 Gy	Tumor growth delay: RT + Au: 17 days RT - Au: 3 days
Zhang, et al <sup>183</sup>	4.8 12.1 27.3 46.6	4 mg Au/kg, IV	PEG	HeLa	662 keV ( <sup>137</sup> Cs), 5 Gy	Tumor growth inhibition Most effect = 12.1 nm
Zhang, et al <sup>184</sup>	<2	10 mg Au/kg, IP	BSA Glutathione (GSH)	U14	662 keV ( <sup>137</sup> Cs), 5 Gy	Decrease in tumor volume compared to RT: BSA: 10% GSH: 35%

**Abbreviations:** BSA: bovine serum albumin; DEF: dose enhancement factor; EC: extracellular; FA: folic acid; GSH: glutathione; IP: intraperitoneal; IC: intracellular; IT: intratumoral; IV: intravenous; MID: mean inactivation dose; p.i.: post-injection; RT: radiotherapy; SER: sensitization enhancement ratio; SER: sensitization enhancement ratio; SF: survival fraction.

- AuNP concentration and localization

The concentration and localization of AuNPs in cancer cells can also have an impact on the achievable DEF. Multiple MC simulations proposed that a high concentration of AuNPs inside a tumor phantom increases the radiation interaction probability <sup>156,188-191</sup>. This was further demonstrated by conjugating AuNPs to targeting ligands, which promotes the uptake of AuNPs in cancer cells. As a result, functionalized AuNPs significantly increase the DEF *in vitro* and the effectiveness of MV radiotherapy *in vivo* as compared to untargeted AuNPs <sup>143,151-153,192-194</sup>. Similarly, the intratumoral administration of AuNPs in tumor-bearing mice results in a much higher AuNP tumor concentration and a significant improvement of tumor response after 26 keV irradiation as compared to intravenous (IV) administration <sup>179</sup>. In terms of localization, AuNPs that are present within or in close proximity to the cell nucleus achieve a more pronounced radiosensitizing effect as compared to AuNPs that reside solely extracellularly or are attached to the cell membrane <sup>153,168,195-199</sup>. According to MC

simulations, the sub-cellular localization was suggested to be especially important for AuNPs-mediated enhancement of MV photon irradiation, due to the short range of the sensitization effects as compared to kV photon irradiation<sup>141,162</sup>. However, it is important to note that the vast majority of the experimental studies observed AuNPs in the cell cytoplasm, rather than in the cell nucleus<sup>143-145,153,157,163,167,168,171,172,177,179,181,200-202</sup>.

#### - AuNPs and tumor cell characteristics

The characteristics of AuNPs can also strongly affect the dose enhancement after irradiation. In fact, spherical AuNPs achieve higher DEF values in HeLa cells after irradiation with 6 MV X-rays as compared to gold nanospikes and AuNRs, thanks to their higher uptake efficiency<sup>203</sup>. Another important factor that can influence the radiosensitization effect is the size of the AuNPs. For instance, in large AuNPs or AuNP clusters, the ionizing events and formation of secondary Auger electrons after irradiation of the AuNPs can occur within their bulk. As a result, larger AuNPs could mitigate the kinetic energy of the electrons, preventing them from reaching the AuNP surface. Consequently, this would result in a rapid loss of dose-enhancement when AuNP size increases<sup>162,204</sup>. Besides, the coating of the AuNPs can also attenuate secondary electrons and scavenge hydroxyl radicals that would otherwise contribute to the radio-enhancement<sup>205,206</sup>. Furthermore, small AuNPs can penetrate deeper inside tumor cells or the tumor tissue, achieving a more homogenous distribution, which could promote a higher radiation-induced cell killing<sup>183,199,204</sup>. Accordingly, Luo, et al reported a higher dose enhancement ratio in X-ray irradiated PC3 cells exposed to 2 nm AuNPs as compared to 5 nm or 19 nm AuNPs<sup>204</sup>. This is in contrast with the results of Chithrani, et al showing a higher uptake efficiency of 50 nm AuNPs in HeLa cancer cells, compared to the 14 nm AuNPs and 74 nm AuNPs<sup>144</sup>. They further highlighted that the radiosensitizing effects of AuNPs are not dependent on the mass of gold inside the cells, but on the number of internalized AuNPs. As a result, the 50 nm AuNPs exhibit the highest radiosensitizing effect after irradiation with 220 kVp X-rays<sup>144</sup>. Similarly, Zhang, et al reported that 12.1 nm and 27.3 nm AuNPs show a higher tumor accumulation *in vivo* compared to 4.8 nm and 46.6 nm. Consequently, the 12.1 nm and 27.3 nm AuNPs show a better tumor control after gamma irradiation<sup>183</sup>. Finally, the cell type and certain tumor-related properties, such as hypoxia, could affect the level of AuNPs-induced dose enhancement. In fact, hypoxia diminishes the AuNP uptake and free radical production<sup>164,167,171</sup>.

#### 4.4.3 AuNPs and hadron therapy

The majority of the studies have focused on the radiosensitization effects of AuNPs in conjunction with external photon radiotherapy<sup>140</sup>. However, lately there has been a growing interest in expanding their application to other radiation sources, such as hadron therapy. Hadron therapy uses charged particles, such as protons or carbon ions, as radiation source instead of photons. The main advantage of this radiation technique is its depth dose distribution. The depth dose distribution of photons is characterized by the gradual energy



deposition when entering the tissue, which results in an undesired off-target irradiation of healthy tissue located upstream and downstream the tumor site. Unlike photons, charged particles slow down when travelling through the tissue and display a maximal dose deposition near the end of their track, the so-called Bragg peak. In this view, the healthy tissue in front of the tumor receives a small part of the dose deposition, whereas the tissue downstream the tumor site is completely preserved. Hadron therapy is especially useful in the treatment of pediatric tumors and tumors located in or in proximity of organs at risk.

A large proportion of the studies on AuNPs-mediated proton irradiation enhancement are theoretical assessments. Nanometric simulations demonstrated considerable dose escalations in the immediate vicinity of the AuNPs (<100 nm) <sup>155,207-209</sup>. For instance, the MC simulation of Heuskin, et al reported an energy-dependent emission of proto-electrons and Auger electrons from AuNPs that were exposed to 1.3 MeV (25 keV/μm) and 4 MeV (10 keV/μm) protons. The secondary electron yield is higher for 4 MeV protons and large 50 nm AuNPs than for 1.3 MeV protons and small AuNPs. On the other hand, the LET of the secondary electrons is lower after 4 MeV proton irradiation than after 1.3 MeV proton irradiation<sup>210</sup>. Besides the AuNP size, the proton LET and the proton energy, the AuNP coating also influence the microscopic dose escalation. In fact, the implementation of an organic coating of 2 nm introduces a significant increase in the production of very low-energy electrons, whereas a thicker coating results in a large loss of enhancement <sup>210,211</sup>.

Although MC simulations demonstrated significant nanoscale dose escalations in the close proximity of the AuNP surface during proton irradiation, the average macroscopic dose enhancement is negligible. Furthermore, Heuskin, et al reported that the hit probability between AuNPs and protons is very low <sup>210</sup>. The authors also highlighted that the low energy of the secondary electrons makes them susceptible for self-absorbance in the AuNPs. As a result, the dose enhancement efficiency strongly decreases as the AuNP size increases, despite the increasing secondary electron yield <sup>210,211</sup>. The secondary electrons that do escape from the AuNPs after proton irradiation have a much shorter range as compared to those produced after kV photon irradiation. As a result, cellular uptake of the AuNPs is suggested to be essential during proton therapy, since no enhancement effect is expected, unless the AuNPs are located close to the nucleus <sup>141,212,213</sup>. Consistent with this, the theoretical simulation of Sotiropoulos, et al did not detect any significant increase in DNA strand breaks or damage complexity in the presence of AuNPs under proton irradiation <sup>214</sup>. Despite these theoretical predictions, several *in vitro* studies did report a significant radiosensitization of cancer cells exposed to protons and carbon ions in the presence of AuNPs. These studies are summarized in **Table 1.2**. The *in vitro* studies were further supported by *in vivo* evidence demonstrating tumor regression and a prolonged survival of CT26 colorectal carcinoma-bearing mice following intravenous injection with 1.9 nm or 14 nm AuNPs and irradiation of the tumors with 40 MeV protons (41 Gy and 100 Gy, respectively) <sup>215,216</sup>.

**Table 1.2** *In vitro* studies focusing on the radiosensitization effects of AuNPs during proton or carbon ion radiation therapy

Author	Size (nm)	Concentration	Coating	Cell model	Source energy (LET)	Effect/SER <sub>% survival</sub>
Enferadi, et al <sup>200</sup>	2.6	45-90 µg/ml	cRGD	ALTS1C1	200 MeV protons	1.17 <sub>10%</sub>
Polf, et al <sup>217</sup>	44	/	phage-nanoscaffold	DU145	160 MeV protons	15-20% increased RBE
Rashid, et al <sup>218</sup>	1.9	1 mM	Thiol	HCT-116	150 MeV protons	2.64 <sub>50%</sub>
Liu, et al <sup>146</sup>	6.1	0.5 mM	PEG	EMT-6	3 MeV protons	Cell survival rate decreased by 2-11.9%
Li, et al <sup>201</sup>	5	5 µg/ml	Cetuximab	A431	1.3 MeV (25 keV/µm) protons	1.22 <sub>10%</sub>
Li, et al <sup>202</sup>	5 10	50 µg/ml	PEG	A431	1.3 MeV (25 keV/µm) protons	1.08 <sub>10%</sub> 1.14 <sub>10%</sub>
Li, et al <sup>202</sup>	5 10	50 µg/ml	PEG	A431	4 MeV (10 keV/µm) protons	No significant enhancement
Jeynes, et al <sup>172</sup>	50	5.5 µg/ml	TAT-peptide	RT-112	3 MeV (12 keV/µm) protons	No significant enhancement
Liu et al. <sup>219</sup>	15	0.1-10 µg/ml	Citrate	HeLa	165 MeV (70 keV/µm) Carbon ions	5.5x enhanced OH• production; 20% increased RBE at 50% survival
Liu et al. <sup>157</sup>	15	1.5-7.5-15 µg/ml	Citrate	HeLa	165 MeV (30 keV/µm) Carbon ions	1.27-1.44-1.33 <sub>50%</sub>
Kaur, et al <sup>174</sup>	5-9	5.5 µM/ml	Glucose	HeLa	62 MeV (290 keV/µm) Carbon ions	1.39 <sub>10%</sub> and 41% increased RBE

**Abbreviations:** LET: Linear energy transfer; PEG: polyethylene glycol; RBE: relative biological effectiveness; SER: sensitization enhancement ratio.

Although the macroscopic physical effects between AuNPs and protons are limited, the LET enhancement and dose escalation closely around the AuNP surface could generate detrimental effects in the cell. For instance, Li, et al demonstrated that the ROS scavenger, dimethyl sulfoxide (DMSO), could remarkably reduce the contribution of AuNPs to the

decrease in cell survival after proton irradiation. This highlights the role of AuNPs in enhancing the ROS generation in combination with protons<sup>202</sup>. In addition, it was postulated that the energy absorbed in AuNPs could result in a thermal effect in the cells, which in turn could lead to detrimental biological effects<sup>210</sup>.

#### 4.4.4 Discrepancies between theoretical and experimental data

To recapitulate, from the above described literature investigating the radiosensitization effects of AuNPs in combination with MV photon energies and charged particles, it is clear that there are certain discrepancies between the theoretical MC simulations and the experimental data<sup>133,134</sup>:

- There is a very weak correlation between the predicted dose enhancement and the observed radiosensitization (**Figure 1.7**). Despite the low absorption cross section of AuNPs with MV photons and the low hit probability between AuNPs and charged particles, experimental studies report significant radiosensitization effects, where little or no increase in overall dose deposition is expected.

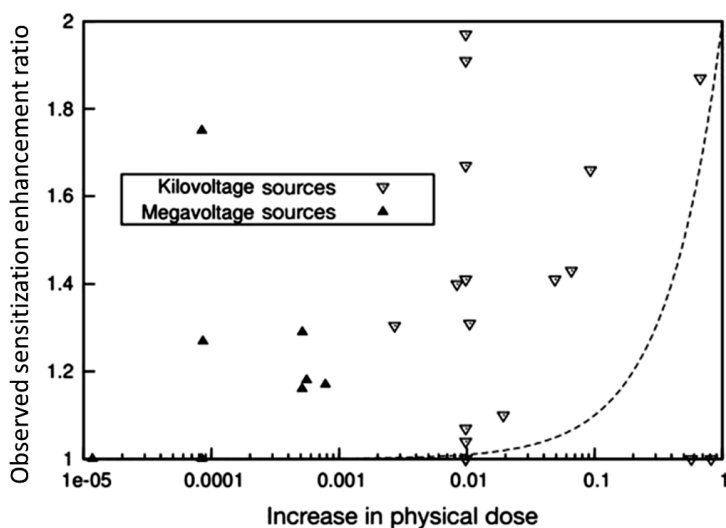


**Figure 1.7** Comparison of the observed experimental radiosensitization and the predicted physical dose enhancement for AuNPs at both megavoltage and kilovoltage energies. The absolute increase in physical dose refers to the additional dose deposition by X-rays in the presence of AuNPs relative to the dose that would be deposited in the absence of gold minus one (an absolute increase of 1 equals a doubled dose deposition). The dashed line shows the trend that would be followed if the observed sensitizations were caused by the predicted increases in physical dose. Adapted from<sup>133</sup>.

- The higher experimental radiosensitization effects are obtained with AuNP concentrations that are far less than the 0.1-1 weight percentage of gold, which is typically associated to the simulation studies.

- MC simulations conclude that AuNPs should be internalized and reside inside or in very close proximity to the nucleus, in order to elicit a radiosensitizing effect. In contrast, AuNPs are mainly observed in intracellular vesicles, in the cytoplasm of cells.

These conflicts described above raise the assumption that the physical interaction between AuNPs and radiation, increasing the dose delivered to the cancer cells, is not the only mechanism responsible for the observed radiosensitization properties of AuNPs. Therefore, several studies focused on revealing other mechanisms contributing to the radiosensitization, such as biological and chemical effects of AuNPs, which are discussed in the next section.

## 4.5 The biological and chemical effects of AuNPs

### 4.5.1 Internalization

When AuNPs reach the surface of the cells, they can interact with several components of the plasma membrane, resulting in cellular uptake, mainly via endocytosis. Endocytosis is the engulfment of AuNPs via internal invagination of the plasma membrane, followed by their budding and pinching-off to form intracellular vesicles. Endocytosis can be categorized into two main mechanisms: phagocytosis and pinocytosis. Phagocytosis is usually mediated by the opsonization of the cargo and occurs in specialized cells such as monocytes, macrophages, dendritic cells and neutrophils, which are responsible for the clearance of pathogens, debris and foreign particles. On the other hand, pinocytosis occurs in all cell types. An important aspect affecting the uptake mechanism and intracellular trafficking is the AuNP size, shape, surface charge and surface functionalization <sup>220,221</sup>:

AuNPs with a size of 50 nm show a higher cellular uptake compared to larger and smaller sized AuNPs. This is likely because of the better interaction efficiency of 50 nm particles with multiple membrane receptors, creating sufficient energy to drive the endocytosis with a beneficial balance between the fast membrane wrapping time and the receptor recycling time (**Figure 1.8A**). Small AuNPs first need to cluster together in order to produce enough energy to initiate the uptake process (**Figure 1.8B**), or they might be able to directly cross the plasma membrane via diffusion and freely enter into the cell. Regarding the shape, several studies demonstrated that rod-shaped AuNPs, especially those with a high aspect ratio, are internalized less efficiently than spherical AuNPs. A possible reason could be the larger contact area of the longitudinal axis of the rods with a high number of cell membrane receptors, leading to an undesirable, slow wrapping time and a reduced number of available receptors at the plasma membrane surface (**Figure 1.8C**) <sup>221-223</sup>. This is in contrast to the findings of Bartneck, et al who demonstrated a more efficient uptake of rod-shaped AuNPs compared to spherical AuNPs, which was attributed to the resemblance of rod-shaped AuNPs to viral protein capsules <sup>224</sup>. In addition, the rod-shaped particles with a higher surface area-to-volume ratio than spherical particles also show a higher uptake efficiency <sup>221,225</sup>.

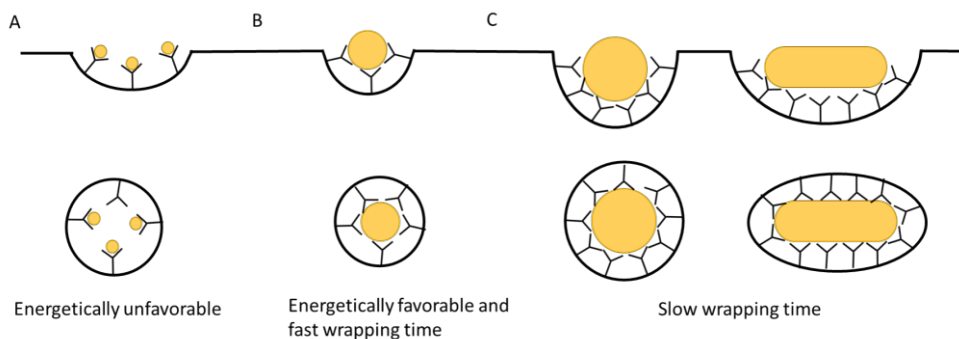


**Figure 1.8** Schematic representation of the size-dependent uptake efficiency by endocytosis. Adapted from <sup>222</sup>.

The charge of the AuNPs also influences the AuNP cellular interaction and internalization. In general, cationic AuNPs bind more effectively to the cell surface than neutral and anionic AuNPs, due to their electrostatic attraction to the negatively charged cell membrane, increasing the extent of internalization <sup>226,227</sup>. However, the cell surface adhesion of cationic AuNPs can depolarize the plasma membrane and disrupt the membrane integrity, increasing the cytotoxicity <sup>228</sup>. Nevertheless, negatively charged AuNPs are still capable of overcoming the anionic cell membrane and of accumulating within the cells via endocytosis <sup>220,223,229</sup>. Finally, functionalization of AuNPs can strongly promote receptor interaction and subsequent uptake of the particles.

After endocytosis, the AuNPs are confined within intracellular vesicles and are shielded from the cell cytoplasm and organelles. The vesicles are sent to an early endosome, which undergoes several transformations. The ageing of an early endosome is typically accompanied by a gradual decrease in the intra-vesicular pH. These early maturing endosomes are able to recycle vesicles to the Golgi apparatus or the plasma membrane, resulting in exocytosis or transcytosis. Eventually, late endosomes fuse with lysosomes, enabling enzymatic degradation of the content. This endosomal pathway is often a barrier for nanomedicine, hindering its biological or therapeutic functions <sup>230</sup>. Nevertheless, several studies reported on the biological effects of AuNPs. Therefore, it is suggested that AuNPs are able to escape the endosomal transport system, accessing the cytoplasm and organelles. A potential strategy is the destabilization of the endosomal membrane by cationic AuNPs, which can create pores or induce leakage of the content to the cytoplasmic environment. Another well-known mechanism for endosomal escape is the ‘proton sponge effect’, based on AuNPs coated with polymers containing uncharged amino groups. These amino functionalities could buffer the protons during the acidification of the endosome, promoting the continuous influx of protons, together with counter-ions to balance the endosomal transmembrane voltage difference. Eventually, this process would induce osmotic swelling, membrane rupture and release of the endosomal content <sup>231,232</sup>. Alternatively, AuNPs could

passively cross the plasma membrane or the endosomal membrane, particularly escaping from macropinosomes, which have been reported to be leaky. Finally, Sabella, et al suggested that lysosomal entrapment of AuNPs results in the release of toxic gold ions, which in turn could exhibit biological effects<sup>233</sup>.

#### 4.5.2 Oxidative stress

In physiological conditions, ROS are produced as byproducts of the cellular oxidative metabolism, which occurs in the mitochondria. Furthermore, ROS act as signaling modulators and play a significant role in the antimicrobial defense. Nevertheless, it is essential that there exists an equilibrium between the cellular antioxidant defense system and the ROS production. Indeed, In case the production of ROS exceeds the detoxification capacity of the antioxidants, the cells experience 'oxidative stress', which causes damage to the cellular biomolecules and affect cellular signaling pathways that control proliferation and cell death. Oxidative stress is considered as a major contributor to the AuNPs-mediated cytotoxicity, even in the absence of ionizing radiation<sup>167,234-237</sup>. AuNPs can induce oxidative stress via two different strategies.

Firstly, although gold is an inert metal in its bulk form, multiple studies suggest that the surface of AuNPs is electronically active, thus catalyzing chemical reactions and promoting ROS production. The amount of ROS produced usually increases with decreasing AuNP size. In fact, a large area-to-volume ratio allows a greater proportion of gold atoms to be available at the surface of the AuNPs, compared to the interior of the AuNPs. Furthermore, the high surface curvature of small AuNPs causes defects in the crystal structure and disrupts the normally continuous electronic configuration. This creates specific sites that are available for electron donation and acceptance. As a result, AuNPs would be able to transfer electrons from donor groups to molecular oxygen, creating superoxide radicals<sup>238-240</sup>. In addition, the catalytic properties of the AuNPs could chemically enhance the effects of ionizing radiation by interacting with superoxide radicals that are generated by the irradiation. The formed reactive AuNPs-O<sub>2</sub> could then catalyze reactions between radical intermediates and other biomolecules, generating super oxide radicals, H<sub>2</sub>O<sub>2</sub> and hydroxyl radicals<sup>137,138,241,242</sup>. The results from these studies demonstrate that the chemical reactivity of AuNPs is oxygen dependent. Interestingly, under hypoxic conditions, the sensitizing effects of AuNPs upon irradiation is significantly diminished. This indirectly indicates that chemical reactivity of AuNPs can enhance the effects of radiation<sup>168,171</sup>.

Secondly, besides chemically generated ROS, AuNPs can also interact and inhibit biomolecules, which are involved in the regulation of the antioxidant defense system. AuNPs show a very high affinity and a fast binding reaction to thiol-containing cysteine and selenocysteine residues, which are present in antioxidant enzymes, such as thioredoxin reductase (TrxR) and glutathione reductase (GR), respectively<sup>243</sup>. TrxR and GR catalyze the reduction of thioredoxin and glutathione, respectively, which in turn are used by peroxidases

to detoxify  $\text{H}_2\text{O}_2$ . Furthermore, TrxR1 is involved in cell viability and proliferation. Consequently, multiple studies linked oxidative stress in AuNPs-exposed cancer cells to the inhibited activity of TrxR1 enzyme and the interaction between AuNPs and glutathione<sup>177,235,244-246</sup>. In addition, thiolated AuNPs could oxidize the protein disulphide isomerase (PDI). PDI catalyzes the creation and cleavage of disulphide bonds in folding proteins and is found in the endoplasmic reticulum, the cytosol, mitochondria, the nucleus and on the cell surface. It has been proposed that oxidation of glutathione is required to reduce PDI (which has been oxidized by the thiolated AuNPs)<sup>247</sup>. Eventually, these interactions between AuNPs and the antioxidant system result in the depletion of the endogenous pool of reduced glutathione and thioredoxin, disturbing the redox capacity of the cells. This was further confirmed by the protective effects of the thiol-containing N-acetyl L-cysteine (NAC), which abolished the cytotoxic effects of AuNPs<sup>235</sup>. As a result, the cellular defense against ROS production is suppressed and oxidative stress is created, sensitizing the cells for additional stresses such as ionizing radiation.

### 4.5.3 Mitochondria

Mitochondria are responsible for the energy production of the cell. A series of multiprotein complexes transfer electrons to oxygen in the mitochondrial matrix, while pumping protons across the inner mitochondrial membrane into the intermembrane space. This creates an electrochemical membrane potential, which drives the synthesis of ATP, a process called oxidative phosphorylation. Under physiological conditions, mitochondria are a main source of cellular ROS generation, since electrons can occasionally leak out of the electron transport chain, interacting with oxygen to produce superoxide or  $\text{H}_2\text{O}_2$ <sup>248</sup>. Internalized AuNPs and the oxidative stress promoted by the AuNPs can impair the mitochondrial functions in the cell. For instance, transmission electron microscopy (TEM) showed that small, positively charged AuNPs are internalized in the mitochondria, resulting in profound morphological changes, such as swelling and enlargement<sup>249-251</sup>. In addition, multiple studies demonstrated that AuNPs cause mitochondrial membrane depolarization, which has been associated with an impaired ATP production and an exacerbated ROS generation<sup>151,180,249,251-254</sup>. The generated ROS in turn may cause damage to the mitochondrial DNA and the respiratory chain, increase the mitochondrial membrane permeability and disrupt the  $\text{Ca}^{2+}$  homeostasis. These effects are often cellular events known to precede the induction of cell death<sup>180</sup>.

### 4.5.4 Cell death

Mitochondria are key regulators of autophagy and apoptosis. Autophagy, also called 'self-eating', is initially a protective response of cells aimed at coping with stresses, notably because it generates energy through the degradation of cytosolic components. As mentioned before, AuNPs can induce mitochondrial membrane depolarization, leading to a reduced ATP level and an increased mitochondrial  $\text{H}_2\text{O}_2$  level, which are both stimulants to induce autophagy. In fact, Gallud, et al demonstrated that exposure of monocytic THP-1 cells

to 5 nm and 20 nm cationic AuNPs upregulated the expression mTOR and prohibitin, proteins involved in the regulation of autophagic and mitophagic degradation, respectively. Furthermore, autophagosomes were visible in the cells using TEM<sup>194,249</sup>. In order to break down the intracellular components and to generate energy, the autophagosomes need to fuse with lysosomes. However, AuNPs can impair the functionality of the lysosomal system through alkalization and membrane instability, resulting in the intracellular accumulation of autophagosomes and thus reducing the degradative capacity of the cell<sup>255-259</sup>. Since autophagy and apoptosis are partly regulated by the same proteins, there exists a strong interplay between the two mechanisms. Therefore, autophagic cells can succumb to mitochondrial-dependent apoptosis when the cellular stress and damage are too extensive and overwhelm the pro-survival autophagy pathway<sup>260</sup>. Thus, severe mitochondrial dysfunction and oxidative stress caused by AuNP exposure can lead to mitochondrial membrane permeabilization and to the release of pro-apoptotic molecules into the cytosol, including cytochrome C, a component of the electron transport chain. These pro-apoptotic elements, in turn, activate caspase proteins and apoptotic cell death, which is characterized by the formation of membrane-enclosed apoptotic bodies<sup>249,261</sup>. Due to the important role of mitochondria in the generation of ROS and in the regulation of different cell death mechanisms, mitochondrial dysfunction has been proposed as a key player in the AuNPs-mediated radiosensitization<sup>180</sup>. Besides autophagy and apoptosis, extensive stress and damage to cells, such as a complete ATP depletion, can also induce necrosis, characterized by cell swelling and disruption of the plasma membrane. Necrosis of cells has been demonstrated after exposure to high concentrations of cationic AuNPs (50 µg/ml)<sup>249</sup>.

#### 4.5.5 Cell cycle

Besides ROS generation and mitochondrial dysfunction, AuNP exposure may cause cell cycle disruption. The cell cycle is a series of events, in which cellular DNA and components are doubled and segregated into two daughter cells. Replication of the DNA occurs during the S phase, while chromosome segregation and cell division occur during the M phase. Two gap phases separate the S phase and the M phase: G<sub>1</sub> before the S phase, followed by G<sub>2</sub> before the M phase. The two gap phases allow the cells to grow and monitor the environment to ensure that conditions are suitable and preparations are complete before committing to the S phase or the M phase. Finally, G<sub>0</sub> is known as the resting phase, in which the cell can reside for a prolonged time before resuming the cell cycle<sup>262</sup>. Importantly, the radiosensitivity of cells varies depending on the cell cycle phase. Cells in the late G<sub>2</sub> and mitosis (G<sub>2</sub>/M) phases are the most sensitive, presumably because condensed chromatin in mitotic cells is more susceptible to radiation-induced DSBs, which are commonly repaired by the error-prone non-homologous end joining (NHEJ) mechanism. On the other hand, cells in the late S phase are the most radioresistant, since there are more diffused chromatin regions. In addition, during the S phase, DNA damage is usually repaired by the accurate homologous recombination (HR) mechanism<sup>263,264</sup>.



Interestingly, Roa, et al demonstrated that glucose-conjugated AuNPs alone and in combination with  $^{137}\text{Cs}$  irradiation cause acceleration of the  $\text{G}_0/\text{G}_1$  phase and accumulation of DU-145 prostate cancer cells arrested in the  $\text{G}_2/\text{M}$  phase. This cell cycle change is not observed after irradiation alone. Furthermore, the cell cycle results are supported by an increased expression of cyclin E and B1 and a reduced expression of p53 and cyclin A. As a result, the radiosensitizing effects of the glucose-AuNPs are attributed to stalling of the cell cycle in the radiosensitive  $\text{G}_2/\text{M}$  phase <sup>178</sup>. Similarly, multiple other groups reported an elevated proportion of cells in the  $\text{G}_2/\text{M}$  phase and a decreased cell number in the  $\text{G}_0/\text{G}_1$  phase after AuNP exposure, but without irradiation <sup>150,151,194,252,265</sup>. On the other hand, a substantial amount of studies demonstrated a significant arrest of cells in the  $\text{G}_0/\text{G}_1$  phase after AuNP exposure, which is associated to the induction of apoptosis <sup>164,249,266-269</sup>. In addition, Jiang, et al found that a combinational use of apigenin-stabilized AuNPs and 40 kV X-ray irradiation greatly enhances the ratio of A549 cells in the  $\text{G}_0/\text{G}_1$  phase, compared to AuNPs or X-ray irradiation alone <sup>270</sup>. A potential explanation for these distinct results was provided by Li, et al: BSA-AuNPs accumulated in lysosomes could stabilize the microtubules in the cells by promoting the tubulin polymerization. This effect blocks the chromosome segregation, causing a  $\text{G}_2/\text{M}$  arrest. In contrast, AuNPs-CTAB disrupt the lysosomes, which result in damage of the microtubules, promoting  $\text{G}_0/\text{G}_1$  arrest and apoptosis <sup>268,269</sup>. Besides the AuNP coating, the differences in cell cycle arrest induced by AuNPs was shown to be dependent from the cell type and the AuNP size and charge <sup>164,182,249,267</sup>. Finally, 30 nm nuclear-targeted AuNPs affect the cell cycle of HSC-3 cells by inducing the accumulation of cells in the S phase and the depletion of cells in the  $\text{G}_2/\text{M}$  phase. This significantly increased the efficacy of the chemotherapeutic drug, 5- fluorouracil, which interferes with the DNA replication and repair during the S-phase of the cell cycle, leading to cytotoxicity and cell death <sup>271</sup>. In contrast, other groups reported no change in cell cycle progression after AuNP exposure <sup>145,148,272,273</sup>.

#### 4.5.6 DNA damage and repair

As mentioned earlier, the primary target of ionizing radiation is DNA. Therefore, radiosensitization could be achieved by increasing the formation of complex DSBs or by inhibition of the DNA damage repair response. In fact, some groups demonstrated an enhanced induction of  $\gamma\text{H2AX}$  and 53BP1 foci when cells are incubated with AuNPs, without exposure to radiation <sup>164,180,194,274</sup>. Furthermore, early after irradiation, AuNPs-exposed cells exhibit a significantly higher number of DSBs compared to the cells exposed to kV or MV X-ray irradiation alone <sup>185,194</sup>. These AuNP effects are usually linked to the excessive ROS production in the cells <sup>164,194,274</sup>. In contrast, Cui, et al could not observe an increase in the number of initial  $\gamma\text{H2AX}$  foci in 2.7 nm AuNPs-exposed MDA-MB-231 breast cancer cells, 30 minutes after 225 kVp X-ray irradiation. However, at 24 hours post-irradiation, the number of residual DSBs in the irradiated cells was significantly higher in the presence of AuNPs, indicating a delayed DNA damage repair <sup>168</sup>. These results were also observed by several

other studies<sup>144,177,180,273</sup>. In addition, it was shown that 1.8 nm cationic, anionic and neutral AuNPs could down-regulate the expression of several genes involved in DNA repair mechanisms in HaCaT cells, including RAD21 and ATM<sup>254</sup>. Moreover, PEGylated nanogels containing AuNPs decrease the protein expression of RAD51 and Ku70, which are key regulators of the NHEJ and HR DNA damage repair pathways, respectively<sup>275</sup>. Since non-resolved DSBs are an important cause of radiation-induced cell death, the DNA damage repair inhibition by AuNPs was suggested to be a key mode of radiosensitization. However, conflicting results were obtained by Chen, et al who demonstrated that BSA-capped AuNPs enhance the DSBs induction 2-4 hours post-irradiation with 160 kVp X-rays, but they did not observe a difference in the number of DNA DSBs after 4–24 hours<sup>185</sup>. Furthermore, Jain, et al did not observe any effect of 1.9 nm AuNPs on the amount of DSBs in prostate, breast and lung cancer cells after 160 kVp X-ray irradiation, nor on DNA repair mechanisms<sup>145</sup>.

#### 4.5.7 Others

Another biological effect of AuNPs is the inhibition of the lysosome functionality. Lysosomes are responsible for the removal of misfolded or aggregated proteins from the ER. As a result, cellular exposure to AuNPs also increased the expression of endoplasmatic reticulum (ER) stress markers<sup>258</sup>. In addition, AuNPs are observed within the ER using TEM imaging<sup>276</sup>. The resulting ER stress, in turn, can trigger the induction of mitochondrial-dependent apoptosis<sup>276 275</sup>. Besides ER stress, AuNPs may induce Golgi fragmentation, causing abnormal protein processing and a decreased cellular adhesion<sup>277</sup>.

Moreover, AuNPs markedly inhibit different matrix metalloproteases (MMPs) in RAW264 macrophages, L929 fibroblasts and SW579 thyroid cancer cells<sup>267,278,279</sup>. MMPs are able to degrade the extracellular matrix (ECM) components and facilitate cancer metastases by increasing the access of cancer cells to the vasculature and the lymphatic system. Consequently, due to the downregulation of MMP-2 and MMP-9 by 5-10 nm AuNPs, the invasion capacity of the thyroid cancer cells is significantly suppressed<sup>267</sup>.

### Overview: Radiosensitization mechanisms of gold nanoparticles

#### *Physical radiosensitization*

- Emission of low-energy secondary electrons

#### *Chemical radiosensitization*

- Catalyzation of ROS generation

#### *Biological radiosensitization:*

- Suppression of antioxidant enzymes
- Mitochondria:
  - Increased permeability of mitochondrial membrane
  - Insufficient energy supply
  - Release of cytochrome C
  - Autophagy/apoptosis
- Cell cycle
  - Altered cyclin/cyclin dependent kinase levels
  - Cell cycle synchronization into G<sub>2</sub>/M phase
- Increased DNA damage and impaired DNA repair
- Inhibition of lysosome functionality resulting in accumulation of misfolded protein and ER stress
- Inhibition of MMPs reducing the cancer cell evasion capacity

The chemical and biological effects summarized above could explain the discrepancy regarding the radiosensitization effects of AuNPs between the MC simulation data and the experimental studies.

## 4.6 Cancer detection and theranostics

An early diagnosis of cancer is often related to a better prognosis. Therefore, next to SPECT and PET, the conventional, non-invasive imaging systems, such as CT, MRI and ultrasound are essential in the clinic. AuNPs have the potential to improve the quality of CT, MRI and ultrasound by acting as imaging probes and thus could improve the accuracy of the diagnosis.

The contrast in X-ray and CT images originates from the differences in mass X-ray attenuation between tissues. For instance, the calcium and phosphorus-rich bone tissue has a higher electron density or a higher atomic number as compared to soft tissues and thus absorbs more X-rays. As a result, bone tissue appears as white (radiopaque) areas on X-ray or CT images, while soft tissues, such as skin and muscles, appear as darker (radiolucent) areas. Introducing media with a high atomic number into the body increases the contrast of the X-ray based images. Currently, iodine-based compounds are the most frequently used contrast agents. However, their rapid renal clearance requires short imaging times and potential catheterisation. Furthermore, the increased kidney retention of the contrast media can increase the risk on renal injury<sup>280</sup>. An additional shortcoming of the iodine-based compounds is the relatively high viscosity and high osmolality, due to the presence of only 3-

6 iodine atoms per molecule, which potentially causes a poor patient tolerance. In contrast, 1.9 nm sized AuNPs contain 250 gold atoms per particle, and thus exhibit a much lower osmolality and viscosity at the same elemental concentration as the iodine agents. Furthermore, the higher molecular weight of the AuNPs causes a slower blood clearance as compared to the iodine agents, permitting longer imaging times after IV injection. Finally, gold has a higher atomic number and absorption coefficient (79 and  $5.16 \text{ cm}^2/\text{g}$  at 100 keV, respectively) as compared to iodine (53 and  $1.94 \text{ cm}^2/\text{g}$  at 100 keV, respectively). As a result, a clinical mammographic image could reveal a small 5 mm murine tumor after IV injection of a high dose of 1.9 nm sized AuNPs (2.7 g Au/kg) thanks to the high tumoral vascularization and gold content. Strikingly, even blood vessels as fine as  $100 \mu\text{m}$  in diameter and a remarkably detailed anatomical and functional kidney morphology could be distinguished, which was not possible after injection of an equal weight of iodine contrast agent (**Figure 1.9**)<sup>22</sup>. Comparable results were obtained with 13 nm AuNPs revealing a small tumor in nude mice, which was undetectable with CT imaging only<sup>281</sup>. Furthermore, 30 nm AuNPs show an X-ray attenuation, which is approximately 5.7 times higher than the current iodine-based contrast media. Here again, the blood circulation of the AuNPs is much longer, resulting in the clear delineation of the blood vessels on the CT image. However, the larger size of the AuNPs promotes the accumulation in liver and spleen, instead of kidney clearance<sup>280,282,283</sup>.

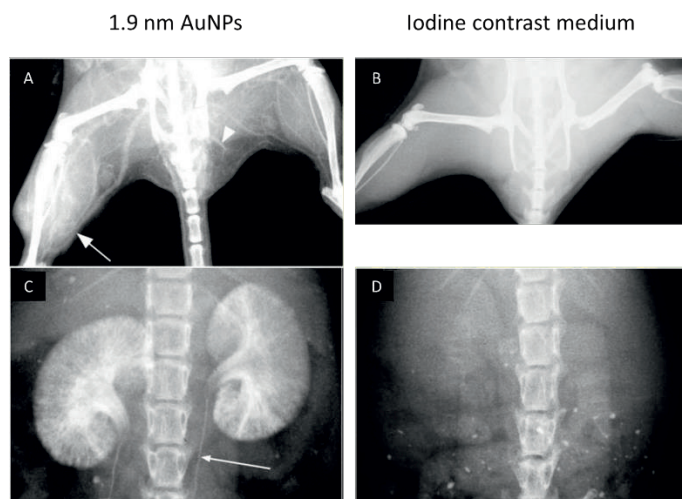


**Figure 1.9** X-ray images of mice intravenously injected with (A, C) 1.9 nm AuNPs or with iodine contrast agent (B, D). Arrows indicate detailed vascularization and kidney morphology. Images are acquired at (A, B) 2 minutes post-injection and (C, D) 60 minutes post-injection. Adapted from <sup>22</sup>.

MRI is also a common clinical imaging modality offering anatomical information in high-spatial resolution, with a high contrast in soft tissue. This is based on the relaxation of hydrogen protons and their electromagnetic energy emission after a radiofrequency pulse, under the influence of a strong external magnetic field. MRI contrast agents,  $T_1$ -positive or

$T_2$ -negative, affect the rate of the proton relaxation and enhance the sensitivity and quality of the images<sup>284</sup>. Thus, in order to exploit AuNPs as a contrast agent for MRI, they need to be complexed with MRI contrast materials. For instance, multicomponent nanoparticles have been produced by surrounding a magnetic core of iron oxide with a gold shell, or by coupling iron-oxide nanoparticles to AuNPs. Iron oxide is a superparamagnetic material exhibiting a strong magnetization under the influence of an external magnetic field, creating microscopic field heterogeneity. This accelerates the dephasing of the proton spins or the  $T_2$  relaxation process. As a result, IV injection of these multicomponent NPs in tumor-bearing mice significantly decreases the signal intensity in the tumors using  $T_2$ -weighted MRI<sup>118,285-287</sup>. On the other hand, coupling AuNPs to paramagnetic metals, such as gadolinium or manganese, accelerates the  $T_1$ -relaxation process. As a result, administration of these nanomaterials increases the signal intensity in the murine tumors, creating bright  $T_1$ -weighted images<sup>288-293</sup>.

Finally, thanks to the unique optical properties, including strong optical absorption and scattering, AuNPs are promising candidates to enhance high-resolution optical imaging modalities, such as fluorescent imaging, surface enhanced Raman scattering (SERS), photo-acoustic (PA) imaging and optical coherence tomography (OCT). Raman scattering is the inelastic and specific scattering of photons when they interact with molecules. The SPR of AuNPs during photon irradiation locally increases the electromagnetic field in the proximity of the nanoparticle surface, which can dramatically enhance the Raman scattering of adjacent molecules. In this regard, AuNPs are often coupled to strong Raman-active reporters. This effect enhances the sensitivity to detect the AuNPs in the pM range<sup>294,295</sup>. AuNPs can also enhance PA imaging based on their strong absorption of photons. The absorbed photons are converted to heat, resulting in a thermo-elastic expansion and the subsequent emission of acoustic transients. The latter can be probed by a transducer to construct photo-acoustic images<sup>296,297</sup>. On the other hand, the enhancement of OCT by AuNPs relies on their effective backscattering of photons<sup>298</sup>. As discussed earlier, in order for optical modalities to detect or treat *in vivo* tumors, the use of NIR light is recommended, because of the deeper tissue penetration. Therefore, AuNPs need to be tuned to absorb or scatter NIR light, depending on their application.

The characteristics of AuNPs and their utility in cancer detection and treatment as discussed thoroughly in the sections above, allow researchers to create highly complex and multimodal nanoplatforms. Indeed, AuNPs can be tuned to absorb NIR light supporting phototherapy and optical imaging. Furthermore, they can be easily functionalized with several imaging agents, biological targeting moieties and chemotherapeutic drugs. This concept of combining multiple therapeutic and diagnostic functions is called ‘theranostics’. Theranostic AuNPs allow a non-invasive and real-time tracking of the *in vivo* distribution of the nanomaterials and can facilitate the dose and toxicity management<sup>286</sup>. In addition, combining multiple treatment modalities, such as phototherapy, drug delivery or radiosensitization, can

synergize the efficacy of the anticancer therapy, which is useful to combat radio-resistant and/or chemo-resistant cancer cells <sup>299</sup>. On the other hand, combining multiple imaging modalities, such as optical imaging, MRI and CT imaging, merges the high spatial resolution and 3D reconstruction of CT and MRI, and the high temporal resolution and sensitivity of optical imaging <sup>289-291</sup>. An example of a theranostic application is the design of 43.5 nm, cubic iron oxide nanoparticles, which are decorated with multiple smaller 3.4 nm AuNPs. MRI imaging showed a maximal tumor contrast, 24 hours post-injection. At this time point, the NPs in the tumor were irradiated with NIR light, which caused a temperature rise in the tumor to 56 °C. The AuNPs also radiosensitized the cancer cells after irradiation of the tumor with 160 keV X-rays. As a result, the tumor volume exposed to photo-thermal and radiotherapy is significantly smaller compared to those exposed to unimodal AuNPs-mediated treatments <sup>286</sup>. Similarly, photo-acoustic imaging demonstrated a maximal uptake of 50 nm hyaluronic acid conjugated gold nanoclusters (AuNCs) in the tumor at 24 hours post-injection, after which irradiation with NIR light and 6 MV X-rays exhibits an efficient tumor growth inhibition <sup>300</sup>. PA imaging can also be used to monitor the temperature rise and temperature distribution in the tumor tissue during photo-thermal therapy, because the volume expansion and the speed of sound are both temperature-dependent <sup>301</sup>. Besides MRI and optical imaging, CT imaging has also been used to perform image-guided AuNPs-mediated photo-thermal therapy and drug delivery <sup>302-305</sup>.

Next to improving CT, MRI, ultrasound and optical imaging, conjugation of AuNPs to radionuclides enables the delivery of radiation to the tumor site and the use of SPECT and PET imaging. The combination of AuNPs and nuclear medicine paves the way to the development of even more advanced multimodal imaging, therapeutic and theranostic applications, which are discussed in detail in the following section (Paragraph 5.3).

## 5. Gold nanoparticles in nuclear medicine

### 5.1 Nuclear medicine

Nuclear medicine involves the internal administration of radionuclides into the body to diagnose, stage and treat diseases, including cancer. In this rapidly growing field, radiopharmaceuticals are developed by linking a radionuclide to a carrier molecule (also referred to as targeting molecule), which is directed against a cancer-specific antigen or process. In this regard, it is essential that the physical half-life of the radionuclide matches the biological half-life of the carrier molecule. Furthermore, the selection of the suitable radionuclide depends on its specific emission and the intended application <sup>306</sup>. In more detail, positron ( $\beta^+$  particles) and gamma emitting radionuclides enable 3D PET and SPECT imaging, respectively. Consequently, the radiopharmaceutical can be traced inside the body providing functional information about specific molecular and cellular processes in the tumor depending on the carrier molecule, such as the blood flow, metabolism, receptor expression, tumor metastatic capacity, inflammation, programmed cell death, etc. Usually, the highly

sensitive PET and SPECT imaging is combined with CT or MRI to locate the functional processes in anatomical structures with high spatial resolution. This improves the interpretation of the nuclear images, leading to a better accuracy of cancer detection and treatment follow-up<sup>307,308</sup>.

Radionuclides emitting  $\beta^-$  particles,  $\alpha$ -particles or Auger electrons have the potential to be used for cancer treatment. These particles exhibit different LET abilities and tissue penetration depths (**Figure 1.10**). Alpha particles possess a high LET, causing a dense track of ionizations, which are likely to induce complex DNA damage, such as double strand breaks. Consequently,  $\alpha$ -emitting radiopharmaceuticals can be applied in low concentrations, since only 1-4 hits are needed to induce cell death. However, their large mass and high LET cause  $\alpha$ -particles to have a poor tissue penetration of a few cell diameters (50-100  $\mu\text{m}$ ). For this reason,  $\alpha$ -emitting radiopharmaceuticals are suitable to treat small lesions, like micro-metastasis without causing considerable damage to the surrounding healthy tissue, if an accurate targeting is provided. Likewise, since Auger electrons have the shortest tissue path length (1-10 nm), they only exhibit a potent cell killing effect when they are in close proximity to cellular DNA. In contrast to high-LET  $\alpha$ -particles and Auger electrons,  $\beta^-$  particles have a low LET, resulting in a deeper tissue penetration of 0.05-12 mm. As a result, they are able to induce damage in multiple neighboring cells. This crossfire effect overcomes the need to target each cancer cell individually and has the potential to treat small, heterogeneous and residual tumors. However, the less destructive character of  $\beta^-$  particles asks for a higher concentration of the radiopharmaceutical inside the target tissue. In addition, there is a higher risk to affect the healthy neighboring cells<sup>309,310</sup>.

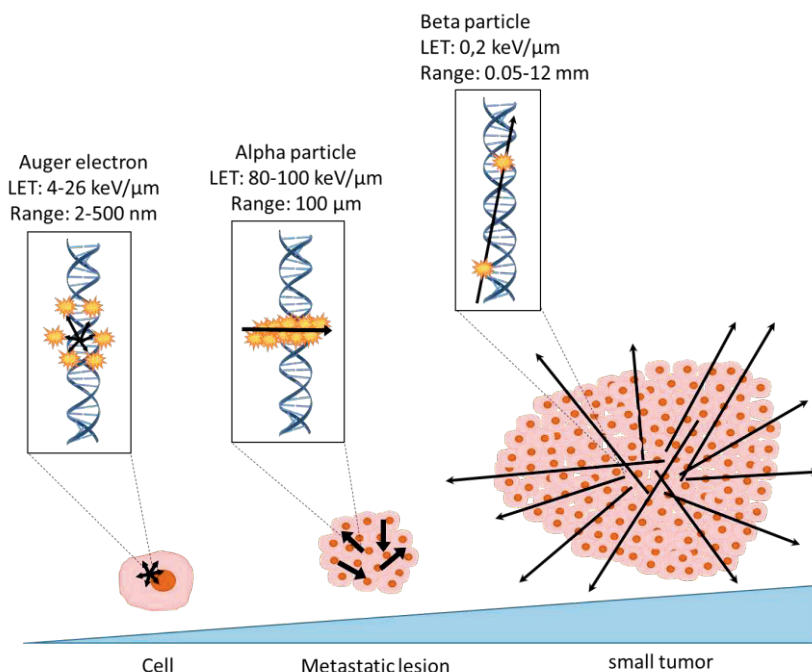


**Figure 1.10** Schematic representation of the range, DNA damage trajectory and cancer therapy application of Auger, alpha and beta particles. Adapted from <sup>136</sup>.

Currently, <sup>99m</sup>Tc and <sup>18</sup>F are the two most commonly used radionuclides for routine diagnostic purposes in nuclear medicine. Other radioisotopes intended for clinical use or under investigation to diagnose or treat cancer-related diseases are presented, but not limited to those included in **Annex Table 1**. Thanks to their specific properties, nanoparticles can offer a significant contribution to nuclear medicine. First, a major advantage is the potential of a single nanoparticle to hold multiple radionuclides, achieving much higher payloads as compared to a radiopharmaceutical agent that carries only one or a few radionuclides. In fact, Lucas, et al calculated that a much higher absorbed radiation dose could be delivered to a solid, non-small-cell lung carcinoma model using nanoparticles containing several  $\beta^-$ -emitters compared to antibodies that were each conjugated to a single radionuclide. The number of radionuclides needed per nanoparticle to achieve 100% tumor control strongly depends on the physical properties of the radionuclide (physical half-life and radiation energy) and on the biological properties of the nano-object (intra-tumoral distribution and biological half-life) <sup>311</sup>. Second, multiple targeting ligands can be conjugated to the nanoparticle surface, creating a multivalent effect, which promotes efficient binding to the tumor cells. As a result, the introduction of nanoparticles could increase the delivery of radioactivity to the tumor, which in turn leads to an improved imaging quality and therapeutic efficacy <sup>311-313</sup>. Finally, the ability to load a combination of different types of



radionuclides and/or chemotherapeutic drugs raises the opportunity to develop targeted, multimodal diagnostic and therapeutic nanoparticles. Thanks to their ease of synthesis and functionalization, AuNPs are often selected to hold a variety of radionuclides<sup>308,314</sup>.

## 5.2 Radiolabeling of gold nanoparticles

A stable association between the radionuclide and the nanoparticle is essential for the successful implementation of radiolabeled nanoparticles in cancer diagnosis and therapy. Loss of the radionuclide can result in its accumulation in non-targeted tissues<sup>315</sup>. In literature, several methods for nanoparticle radiolabeling have been described (**Figure 1.11**).

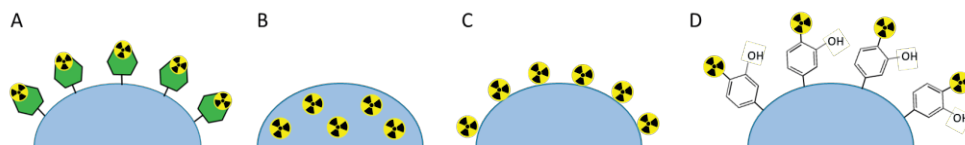


**Figure 1.11** Radiolabeling of nanoparticles by (A) chelation, (B) incorporation, (C) chemisorption and (D) covalent binding. Adapted from<sup>315</sup>.

A frequently used strategy is the use of bifunctional chelators, which are covalently attached to the nanoparticle coating or to the vector molecule, and strongly complex radiometals. In the development of radiopharmaceuticals, a successful bifunctional chelator minimizes the dissociation of the radionuclide from the chelator *in vivo*. This depends on the thermodynamic stability and the kinetic inertness of the bifunction chelator. The thermodynamic stability reflects the direction of the dissociation reaction, while the kinetic inertness reflects the rate of the dissociation reaction. Two well-known bifunctional chelators are diethylenetriaminepentaacetic acid (DTPA) (**Figure 1.12A**) and dodecane tetraacetic acid (DOTA) (**Figure 1.12B**). Generally, DOTA shows a higher thermodynamic stability to form a complex with most metal ions than DTPA<sup>316</sup>. Furthermore, due to their ‘open-chain’, acyclic structure, radiometal-DTPA complexes are characterized by fast dissociation kinetics. As a result, DTPA analogs rapidly achieve a high radiolabeling efficiency and yield under mild reaction conditions. However, a fast dissociation rate and a lower thermodynamic stability might result in the release of the radionuclide from DTPA when applied in biological solutions. Conversely, due to their ‘caged’, macrocyclic construction, DOTA analogs have a higher thermodynamic stability and are much more kinetically inert compared to DTPA analogs, creating radiometal-DOTA complexes that are more likely to retain their chemical integrity in the presence of natural chelators. However, the radiolabeling kinetics of DOTA analogs are much slower, requiring elevated temperatures to achieve a high yield, which might affect the integrity of the biomolecules<sup>310</sup>. DOTA and DTPA analogs are often used to chelate  $^{177}\text{Lu}$ ,  $^{111}\text{In}$ ,  $^{64}\text{Cu}$  and  $^{90}\text{Y}$ <sup>314,317-320</sup>. On the other hand, hydrazinonicotinamide (HYNIC) is a typical chelator for  $^{99\text{m}}\text{Tc}$ <sup>321,322</sup>. The stability of radionuclides chelated to AuNPs can vary from 80% to >95% when incubated in serum during 24-72h<sup>314,317-319,321-326</sup>.

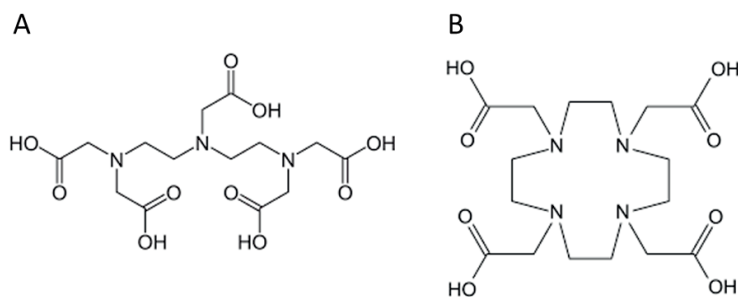


**Figure 1.12:** Molecular structures of (A) diethylenetriaminepentaacetic acid (DTPA) and (B) dodecane tetraacetic acid (DOTA).

In order to avoid harsh radiolabeling conditions, possible instability and trans-chelation of the radionuclide, several studies preferred a chelator-free radiolabeling method, embedding  $^{64}\text{Cu}$  and radioactive gold ( $^{198}\text{Au}$  and  $^{199}\text{Au}$ ) into the AuNPs during the production process<sup>327-334</sup>. These  $^{64}\text{Cu}$ -doped AuNPs are reported with a radiochemical stability of 95% when challenged with ethylenediaminetetraacetic acid (EDTA). They show no degradation or trans-chelation in serum up to 48h, while the stability of  $^{64}\text{Cu}$ -DOTA is less stable<sup>328,330</sup>. Similarly,  $^{198}\text{Au}$ -doped AuNCs show no dissociation of  $^{198}\text{Au}$  in serum during a week<sup>335</sup>. For radioiodination and radiofluorination of AuNPs, it is possible to covalently attach radioactive iodine ( $^{124}\text{I}$ ,  $^{125}\text{I}$  and  $^{131}\text{I}$ ) and  $^{18}\text{F}$  to an aromatic phenol group via in situ oxidation and substitution<sup>136</sup>. In case of direct radiolabeling, the phenol group is present into the organic coating of the AuNPs or is provided by a tyrosine residue being part of an AuNPs-conjugated peptide or antibody<sup>336-342</sup>. Indirect radiolabeling involves a linker molecule, which already carries the radiolabeled phenol group and facilitates its coupling to the AuNPs<sup>343,344</sup>. On the other hand, the phenol-free prosthetic probes silicon- $^{18}\text{F}$  and  $^{18}\text{F}$ -bicyclononyne also effectively attached  $^{18}\text{F}$  to AuNPs<sup>345,346</sup>. Iodination and fluorination are both rapid radiolabeling methods. However, various studies observed some degree of radioiodine release resulting in a serum stability of the conjugate of 49-76.3% after 48-72h<sup>341,342</sup>. As a result, the free radionuclides can accumulate in different organs and increase the dose in healthy tissues, such as in the thyroid, the stomach and the bladder<sup>340</sup>. To address this issue, Lee, et al constructed a protective Au-shell around  $^{124}\text{I}$ -labeled AuNPs and showed that more than 98 % of  $^{124}\text{I}$  remained on the AuNPs for 48h in human serum, while ‘unprotected’ AuNPs released 20% or more of  $^{124}\text{I}$ <sup>336-338,347,348</sup>. Alternatively, the halogens iodine and astatine possess a strong affinity for the AuNP surface. As a result, radioactive iodine and the  $\alpha$ -emitter  $^{211}\text{At}$  could be attached to the AuNP surface via chemisorption<sup>349-353</sup>. Interestingly, Dziawer, et al demonstrated that 15 nm astatinated AuNPs exhibit a better *in vitro* stability than their  $^{131}\text{I}$ -iodinated analogues in serum (99.3% vs 92.8%) and in cerebrospinal fluid (99.5% vs 82.1%) during 24h<sup>352,353</sup>. Furthermore, it has been shown that the radioiodine adsorption strength onto the AuNP surface depends on the AuNP surface modifications and the incubation medium, which could lead to detachment of the radionuclides and hinder

their applications *in vivo* <sup>354</sup>. In order to reduce iodine detachment from <sup>131</sup>I-radiolabeled AuNRs *in vitro* and *in vivo*, Wang, et al pre-oxidized radioactive Na<sup>131</sup>I via chloramine T or the iodogen as oxidizing agents to convert sodium iodide to iodine. They demonstrated that the valence state of iodine significantly affects the adsorption strength of the radioiodine to AuNRs. Indeed, <sup>131</sup>I(0)AuNRs exhibits a much higher radiochemical stability *in vitro* and *in vivo*, with only negligible uptake of radioiodine in the thyroid of treated mice, compared to <sup>131</sup>I(-1)AuNRs. To explain this result, the authors hypothesized that <sup>131</sup>I(-1) simply adsorbs onto the AuNRs, while <sup>131</sup>I(0) reacts with the AuNRs, forming a stronger bond <sup>355</sup>.

## 5.3 The effectiveness of radiolabeled gold nanoparticles in nuclear medicine

### 5.3.1 Tumor uptake, retention and distribution

The inherent AuNP characteristics, such as their size, shape, and coating are determining factors that can affect the AuNP pharmacokinetics, biodistribution and tumor uptake. Therefore, these properties have to be carefully tuned in order to maximize the tumor uptake, the tumor-to-background ratio (T/B), and thus the effectiveness of radiolabeled AuNPs as diagnostic and therapeutic nano-radiopharmaceuticals. For this purpose, SPECT-CT and PET-CT are useful imaging tools to better understand the *in vivo* behavior of radiolabeled AuNPs in real-time. In addition, *ex vivo* inductively coupled plasma-mass spectrometry (ICP-MS),  $\gamma$ -imaging, Raman scattering imaging and fluorescence imaging are often used to complement the *in vivo* nuclear imaging and to verify the amount of AuNPs in the major organs and in the tumor.

#### - Pharmacokinetics and biodistribution

Following administration *in vivo*, the pharmacokinetics and biodistribution profile of targeted AuNP-based radiopharmaceuticals, carrying multiple targeting molecules, substantially differ from the monomeric radiopharmaceuticals lacking AuNPs. For instance, the radiolabeled low-molecular weight monomers, <sup>99m</sup>Tc-RGD and <sup>64</sup>Cu-DOTA-PEG are cleared from the blood pool shortly after IV administration ( $T_{1/2} < 10$  min and 30 min, respectively), whereas <sup>99m</sup>Tc-AuNPs-RGD and <sup>64</sup>Cu-gold nanoshells exhibit a blood circulation  $T_{1/2}$  of 47 min and 12.8 hours, respectively. The blood clearance of the small monomeric radiotracers is followed by early excretion, mainly via the kidneys and to a lesser extent via the hepatobiliary pathway, 0-20h post-injection <sup>356-359</sup>. Unlike small molecules, high molecular weight targeting agents, such as antibodies, are not excreted via the renal system, but accumulate in the liver <sup>323,360</sup>. The most important difference in biodistribution pattern is the significantly higher uptake of the colloidal radiolabeled AuNP analogs in the liver, spleen and lungs, compared to the low- and high-molecular weight monomeric systems <sup>321,323,357,360,361</sup>. Excretion of the radiolabeled AuNPs can take place via both the renal system and the hepatobiliary system, depending on their size <sup>321,327,357,358,361</sup>. However, Xie, et al concluded that <sup>64</sup>Cu-gold nanoshells were

excreted via the hepatobiliary system at a slower pace than the monomeric controls<sup>357</sup>. This is potentially due to the sequestration of the AuNPs by the phagocytic cells of the RES, which prevents their efficient hepatobiliary elimination<sup>362</sup>. Intraperitoneal administration of <sup>99m</sup>Tc-AuNP-RGD and <sup>111</sup>In-AuNP@Albumin significantly reduces the nanoparticle sequestration by the RES, compared to IV administration<sup>317,321,363</sup>. Nevertheless, the tumor uptake of <sup>99m</sup>Tc-AuNP-RGD is faster after IV injection (maximal after 1 hour) than after IP administration (maximal after 3 hours). Therefore, IV administration is probably more convenient for diagnostic purposes<sup>321</sup>.

Importantly, active targeting of AuNPs significantly improves the tumoral uptake compared to untargeted AuNPs. However, certain targeting moieties can also increase the exposure of healthy tissues to the radiolabeled AuNPs. For example, a high accumulation of radiolabeled AuNPs is observed in the pancreas when the AuNPs are conjugated to the peptides bombesin or octreotide<sup>358,361,363,364</sup>. Bombesin and octreotide target the gastrin-releasing peptide receptor (GRP) and the somatostatin receptor, which are both highly expressed in the pancreas, but are also overexpressed on prostate cancer cells and neuroendocrine cancer cells, respectively. Orocio-Rodriguez, et al demonstrated a higher uptake of <sup>99m</sup>Tc-AuNPs-Tyr3-Octreotide in the pancreas compared to the monomeric <sup>99m</sup>Tc-Tyr3-Octreotide<sup>361</sup>. Furthermore, the pancreas-to-blood ratio of <sup>99m</sup>Tc-AuNP-Lys3-bombesin is higher than that of monomeric <sup>99m</sup>Tc-Lys3-Bombesin<sup>358</sup>. Both observations were explained by the faster renal excretion of the monomeric systems compared to the nanoconjugates. Another example is the higher liver and spleen uptake of AMD3100-conjugated <sup>64</sup>CuAuNCs compared to untargeted <sup>64</sup>CuAuNCs. AMD3100 is an antagonist of the chemokine receptor CXCR4, which is expressed on metastatic breast cancer cells. However, CXCR4 is also present on immune cells residing in the spleen and liver<sup>327</sup>. Similarly, conjugation of <sup>111</sup>In-AuNPs to Trastuzumab exhibit a faster blood clearance and a higher uptake in the liver and spleen compared to untargeted <sup>111</sup>In-AuNPs, which is explained partly by the Fc-mediated recognition and uptake of the <sup>111</sup>In-AuNPs-Trastuzumab by the RES<sup>365</sup>. Despite the off-target uptake of these targeted, radiolabeled AuNPs, the studies did not assess the toxic effects in the healthy organs.

#### - Enhanced tumor uptake and retention

Despite the higher RES sequestration after IV injection, the average tumor uptake of <sup>99m</sup>Tc-AuNPs-RGD (3.65 %ID/g), <sup>99m</sup>Tc-AuNPs-Tyr<sup>3</sup>-Octreotide (≈3.4 %ID/g), <sup>64</sup>CuAuNCs-AMD3100 (7.15 %ID/g) and <sup>64</sup>Cu-nanoshells (0.77 %ID/g) is considerably higher than that of <sup>99m</sup>Tc-RGD (≈2.5 %ID/g), <sup>99m</sup>Tc-Tyr<sup>3</sup>-Octreotide (≈2 %ID/g), <sup>64</sup>Cu-AMD3100 (2.98 %ID/g) and <sup>64</sup>Cu-DOTA-PEG (0.09 %ID/g), respectively<sup>321,356,357,361</sup>. In addition, the early stage of 4T1 lung metastasis, which is currently difficult to detect, is successfully highlighted by <sup>99m</sup>Tc-AuNPs-RGD (≈14 %ID/g) and <sup>64</sup>CuAuNCs-AMD3100 (7.36 %ID/g), whereas the small <sup>99m</sup>Tc-RGD and <sup>64</sup>Cu-AMD3100 radiotracers show a significantly lower uptake in these micro-metastatic lesions

( $\approx 2.7$  %ID/g and 0.65 %ID/g, respectively)<sup>327,356</sup>. Importantly, the extent of tumor uptake of radiolabeled AuNPs depends on the properties of the AuNPs, such as the size and the coating. In size-comparing studies, the smaller radiolabeled AuNPs, including 20 nm <sup>111</sup>In-PEG-AuNPs, 29 nm Gd/<sup>99m</sup>Tc-AuNPs-RGD and 30 nm <sup>64</sup>Cu-DOTA-PEG-AuNPs, consistently exhibit a longer blood circulation time, a higher tumor uptake and/or a lower RES sequestration compared to their larger counterparts (40 nm, 80 nm and 55 nm, respectively)<sup>319,325,366</sup>. Furthermore, a PEG coating on <sup>64</sup>Cu-AuNPs performs better in terms of a prolonged blood circulation, delayed RES sequestration and increased tumoral uptake compared to a zwitterionic coating or stabilization by Tween 20<sup>328</sup>. The functionalization and the length of the PEG molecules have an influence on the stability and the *in vivo* behavior of the radiolabeled AuNPs. For instance, the immobilization of the PEG molecules on the AuNP surface via thioctic acid or lipoic acid providing two or more gold-sulfur bonds results in a higher stability and a longer blood circulation time of <sup>177</sup>Lu-labeled AuNPs and <sup>111</sup>In-labeled AuNPs compared to PEG immobilization via a single gold-sulfur bond<sup>359,366</sup>. In addition, longer PEG molecules (1000 and 5000 Da) prolongs the blood circulation time of <sup>64</sup>CuAuNCs and <sup>111</sup>In-AuNPs, compared to 350 and 2000 Da PEG molecules, respectively<sup>366,367</sup>. However, increasing the length of the PEG molecules from 800 to 6000 Da also reduces the cancer cell uptake of the <sup>111</sup>In-EGF-AuNPs<sup>368</sup>.

Next to an increased tumor uptake, AuNPs increase the tumor retention of the radionuclide. For instance, the residence time of <sup>177</sup>Lu-Tyr<sup>3</sup>-octreotate-AuNPs in a 3D-multilayered culture of HeLa cells (17.10h) is significantly higher than that of monomeric <sup>177</sup>Lu-Tyr<sup>3</sup>-octreotate (5.13h)<sup>369</sup>. Other studies confirmed the enhanced tumor retention of AuNP-based radiopharmaceuticals *in vivo*. In fact, <sup>177</sup>Lu-AuNPs-RGD show a tumor residence time of 61.6h after four intratumoral injections, whereas <sup>177</sup>Lu-RGD remains in the tumor site for approximately 17.3h<sup>370</sup>. In addition, the accumulation of <sup>64</sup>Cu-gold nanoshells in the tumor achieves a plateau 20h after IV injection. At 44h after IV injection, the majority of accumulated <sup>64</sup>Cu-gold nanoshells are still present in the tumor, which is not the case for the monomeric <sup>64</sup>Cu-DOTA-PEG<sup>357</sup>. Altogether, the enhanced tumor uptake and retention of targeted, radiolabeled AuNPs contribute to a high T/B ratio and are mainly attributed to the EPR effect, the multivalent targeting avidity and the high radionuclide cargo of the targeted, radiolabeled AuNPs, compared to the small monomeric radiotracers<sup>321,327,356,357,369</sup>.

#### - Intratumoral distribution

Once within the tumor matrix, the most beneficial scenario is that the radiolabeled AuNPs diffuse and spread uniformly throughout the tumor tissue<sup>311</sup>. Several studies assessed the local intratumoral distribution of the radiolabeled AuNPs using nuclear imaging, microscopic examination or autoradiography. The latter blots the emission of the radionuclides in the tissues to a 2D-image by means of a photographic imaging plate. Unfortunately, in the majority of the studies, AuNPs were usually observed in the periphery of the tumor mass

close to the vasculature and displayed a general heterogeneous distribution<sup>328,329,340,348,356,365-367,371,372</sup>. The intratumoral diffusion of AuNPs depends on the characteristics of both the AuNPs and the tumor tissue. For instance, <sup>198</sup>Au-nanospheres and <sup>198</sup>Au-nanodisks were found in the tumor periphery, whereas <sup>198</sup>Au-nanorods and <sup>198</sup>Au-nanocages were detected throughout the tumor after IV injection<sup>334</sup>. Similar results were obtained with 30 nm <sup>64</sup>Cu-DOTA-PEG-AuNCs, which accumulated in the central region of the tumor 24h after IV administration. This is attributed to their small size and neutral charge as well as to the uniform blood flow and the low interstitial pressure of the EMT-6 tumor model<sup>319</sup>. In addition, the heterogeneous intratumoral distribution observed for Trastuzumab-targeted and Cetuximab-targeted <sup>111</sup>In-AuNPs is partly attributed to the 'binding-site barrier effect' by which the strong binding of the antibodies to their target facilitates extravasation of the AuNPs into the tumor, but also limits the intra-tumoral diffusion of the AuNPs<sup>365,371,373</sup>. Finally, in an advanced cancer stage, the presence of substantial necrotic foci limits the delivery of AuNPs or other anti-cancer pharmaceuticals<sup>327</sup>. Since <sup>177</sup>Lu-AuNP-RGD significantly suppress the tumor progression and thus prevent the formation of necrotic foci, <sup>177</sup>Lu-AuNP-RGD display a more uniform intratumoral distribution as compared to <sup>177</sup>Lu-AuNPs or <sup>177</sup>Lu-RGD<sup>370</sup>.

Intratumoral penetration of radiolabeled AuNPs can also be promoted by the application of external stimuli. For example, the intratumoral uptake of <sup>64</sup>Cu-PEG-HAuNS-DOX is enhanced when injection into the hepatic artery (i.e. liver embolization) is followed by electroporation, radiofrequency ablation, or laser-induced thermal therapy. Electroporation causes cell membrane permeabilisation via the use of electrical pulses, while radiofrequency ablation and laser-induced thermal therapy both generate heat via the delivery of an alternating electrical current and via laser irradiation, respectively. As a result, the <sup>64</sup>Cu-PEG-HAuNS-DOX are localized both in and around the tumor, whereas embolization alone results in a predominant peripheral tumor uptake<sup>318</sup>. Another strategy is the co-injection of an adjuvant such as lipiodol, which selectively enters liver tumors after liver embolization. It boosts the uptake of <sup>64</sup>Cu-PEG-HAuNS throughout the tumor achieving a high tumor-to-normal liver ratio of 4.17. Conversely, embolization of <sup>64</sup>Cu-PEG-HAuNS without lipiodol leads to a perivascular distribution and a lower tumor-to-normal liver ratio of 0.81<sup>374</sup>. Similarly, intratumoral co-injection of the <sup>103</sup>Pd/<sup>198</sup>Au-dual radiolabeled AuNPs with the biocompatible polymer alginate sequesters them in the tumor<sup>375</sup>.

### 5.3.2 Imaging

A detailed overview of radiolabeled AuNPs used for imaging purposes is presented in **Annex Table 2**. Hereunder, we describe the use of AuNPs in multimodal nuclear imaging and dual radiolabeling.

- MRI/SPECT-CT and MRI/PET dual imaging

The radiolabeling of AuNPs offers the opportunity to combine multiple imaging modalities to visualize tumor tissues *in vivo*. As discussed in paragraph 4.6, the high X-ray attenuation of AuNPs increases the contrast of X-ray-based imaging techniques, such as of CT imaging. The radiolabeling of AuNPs enables the further advancement of the CT imaging application. For instance, dendrimer-entrapped and polyethylenimine-entrapped AuNPs, radiolabeled with  $^{99m}\text{Tc}$  or with  $^{131}\text{I}$ , enhance the CT contrast on one hand and enable SPECT imaging of tumor cells, both *in vitro* and *in vivo*, on the other hand. The X-ray attenuation property of the nanocarriers is exceeding that of Omnipaque, a clinically used iodine-based CT contrast agent. Furthermore, the increase in SPECT-CT signal intensity is related to the concentration of gold and the radionuclide in the tumor cells. As a result, the imaging contrast enhancement significantly improves when anti-cancer targeting probes, such as chlorotoxin, chlorotoxin-like peptides, duramycin, cRGD, folic acid or pH-responsive moieties are linked to the nanocarriers as compared to their untargeted analogues <sup>324,339,376-381</sup>.

Another imaging modality discussed in paragraph 4.6 is the combination of AuNPs with MRI contrast agents. This imaging application is further advanced by Yang, et al, who conjugated 29 nm cRGD-AuNPs to  $^{99m}\text{Tc}$  and Gd. As a result, the radiolabeled nanoconjugate can specifically target and visualize the tumor site by means of SPECT-CT imaging, while taking advantage of complementary high-resolution MRI images. Indeed, the authors found hyper-intense MR signals in the tumor region of tumor-bearing mice, 30 minutes post-injection, after which the signal intensity gradually increased to values that were 2.4 times higher than the baseline signal, reaching a plateau 2h after injection. In addition, the MR signal enhancement is much less pronounced in mice that received the untargeted AuNP probes or free cRGD to block the tumor binding sites. The SPECT-CT images confirm the MRI observation, demonstrating high tumor accumulation (14.6% ID/g) after 2h, which strongly reduces after blocking (6.2% ID/g) or after administration of the untargeted AuNP probe (4.0 %ID/g). However, SPECT-CT also reveals that the  $^{99m}\text{Tc}$ /Gd-cRGD-AuNPs are present in the liver ( $\approx 20\%$  ID/g) and spleen ( $\approx 55\%$  ID/g). Furthermore, *ex vivo* studies demonstrate an increased  $^{99m}\text{Tc}$  content in urine ( $>60\%$  ID/g) compared to the amount of gold ( $\approx 10\%$  ID/g), which is attributed to the detachment of  $^{99m}\text{Tc}$  from the AuNPs. Importantly, the presence of 29 nm sized AuNPs in the urine may be an indication of kidney damage. Nevertheless, the  $^{99m}\text{Tc}$ /Gd-cRGD-AuNPs are suitable for image-guided therapy as the authors were able to define the optimal time point post-injection at which the AuNP content in the tumor site was maximal to perform radiotherapy and benefit from the radiosensitization effect <sup>325</sup>. Alternatively, a targeted PET/MRI imaging probe was created by developing a multicomponent system consisting out of (I) an AuNP, which was radiolabeled with  $^{64}\text{Cu}$ , and (II) an iron-oxide nanoparticle (IONP), which acted as a MRI reporter and was conjugated to anti-EGFR affibodies. The Au-IONP shows a similar  $T_2$  relaxation rate of water as Feridex, a colloidal superparamagnetic iron oxide MRI contrast agent, and reduces the MR signal

intensity at the tumor site by 44% on T<sub>2</sub>-weighted MRI images, 48h after IV injection. Next to RES accumulation, the PET images shows high tumor uptake (4.6% ID/g, 24h p.i.) and a good tumor-to-muscle ratio of approximately 6. Blocking the tumor binding sites reduces the tumor uptake (1.9% ID/g, 24h p.i.), resulting in a tumor-to-muscle ratio of approximately 2 and abolishes the effect on the MR signal intensity in the tumor region <sup>287</sup>.

Another multimodal imaging possibility was demonstrated by coupling and embedding the positron-emitting <sup>124</sup>I in PEGylated AuNPs (<sup>124</sup>I-PEG-Au@AuCBs), which allowed *in vivo* PET-CT scanning and optical Cerenkov luminescence imaging (CLI). CLI is based on the detection of Cerenkov photons, which arise from charged particles originating from the radionuclide decay and traveling through a dielectric medium with a velocity exceeding the speed of light in the given medium. Particle deceleration polarizes the electrons of water molecules, which relax back to the equilibrium by emitting photons <sup>382</sup>. CLI can compensate for the relatively low spatial resolution of PET imaging, while PET overcomes the penetration depth limitation of the optical CLI imaging. Furthermore, CLI provides the opportunity to utilize existing clinical radiotracers for image-guided surgery. Despite the significant uptake in the liver and spleen, the PET-CT imaging shows a rapid accumulation of PEG-<sup>124</sup>I-Au@AuCBs in the breast tumor lesion as early as 1h post-injection (5.38% ID/g). The signal remains detectable at 24h post-injection (1.81% ID/g) with a desirable tumor-to-muscle (T/M) ratio of approximately 5. Consistent with the PET-CT results, *in vivo* CLI imaging clearly visualizes the uptake of the PEG-<sup>124</sup>I-Au@AuCBs in the tumor at 24h post-injection. As a result, there is a good linearity between the PET-CT and CLI imaging at 24h ( $R^2 = 0.85$ ). <sup>348</sup>. In addition, PET-CLI imaging is useful to detect sentinel lymph nodes (SLNs) after sub-cutaneous injection of PEG-<sup>124</sup>I-AuNP. Indeed, the images show PEG-<sup>124</sup>I-AuNP uptake in the SLNs as early as 1h post-injection ( $\approx 30\%$  ID/g). The signal intensity increases to a maximum after 6h and remains evident after 24h ( $\approx 10\%$  ID/g) <sup>336</sup>. As a result, PET/CLI could facilitate the clinical staging of cancer.

#### - Dual radiolabeling

Alternative to multimodal imaging, dual radiolabeling of AuNPs with <sup>111</sup>In and <sup>125</sup>I enables multispectral SPECT imaging, in which the emissions from <sup>125</sup>I and <sup>111</sup>In are independently tracked at a window centered around 28 keV and 200 keV, respectively. Multispectral imaging helps to study the radiolabeling stability, the radionuclide anchor stability and biological parameters, such as enzyme activity. In this case, <sup>111</sup>In is specifically linked to a MMP9-cleavable peptide, which is conjugated to the AuNPs. Four hours after IV injection, <sup>125</sup>I is detected in the thyroid, stomach and bladder due to the lack of *in vivo* stability, whereas <sup>111</sup>In remains chelated to the AuNPs, circulating in the blood pool. Tumor uptake was clearly visible 24h post-injection in both MMP9-high A431 and MMP9-low 4T1Luc tumors, leading to a high T/M of 8, after 48h. However, due to the high MMP9 expression in the A431 tumor, the <sup>111</sup>In-labeled peptide is cleaved from the AuNPs, facilitating its tissue clearance and reducing the <sup>111</sup>In signal intensity between 24h and 48h (from 7.25 to 6.23 %ID/g). In



contrast, the signal intensity in the MMP9-low 4T1Luc tumor continues to increase (from 6.41 to 10.2 %ID/g) <sup>340</sup>. Dual radiolabeling is also useful to establish the biodistribution of multi-component AuNPs. This was proven by administration of <sup>198</sup>Au-AuNPs with a [<sup>4</sup>C]citrate surface coating to rats. Gamma spectrometry and liquid scintigraphy were used to detect and quantify the <sup>198</sup>Au and <sup>4</sup>C activity in the ex-vivo organs, respectively. Interestingly, the biodistribution profile of the gold core and the citrate coating were different from each other and thus the authors concluded that the different components of the AuNPs separated one from each other and that the AuNPs did not remain intact <sup>383</sup>.

### 5.3.3 Treatment

For therapeutic purposes, the goal of radiolabeled AuNPs is to deliver a lethal radiation dose to the tumor site, while minimizing the radiation damage to healthy tissue. The effectiveness of radiolabeled AuNPs for targeted radionuclide therapy (TRT) and as multimodal therapeutic agents has been investigated *in vitro* and *in vivo*. These studies are presented in detail in **Table 1.3**.

- In vitro experiments

Radiolabeled AuNPs can potentially increase the effectiveness of TRT. For instance, *In vitro*, AuNPs conjugated to Lys<sup>3</sup>-bombesin (Tat-BN) and radiolabeled with <sup>99m</sup>Tc are stronger inhibitors of PC-3 cell proliferation (cell proliferation of <10%) than the monomeric <sup>99m</sup>Tc-Tat-BN without AuNPs (cell proliferation of ≈37%) <sup>384</sup>. Similarly, the <sup>177</sup>Lu-AuNPs-RGD inhibited C6 cell proliferation (cell proliferation of 3.62%) significantly more as compared to the monomeric <sup>177</sup>Lu-RGD (cell proliferation of 29.67%) <sup>370</sup>.

Various *in vitro* studies demonstrate that the conjugation of targeting ligands directed against EGFR1 (Cetuximab or EGF) or EGFR2 (Trastuzumab or Panitumumab) increases the effectiveness of AuNPs, radiolabeled with <sup>131</sup>I, <sup>111</sup>In, <sup>177</sup>Lu, <sup>198</sup>Au or <sup>211</sup>At, to reduce the viability of EGFR1- or EGFR2-expressing cancer cells, respectively <sup>314,320,342,353,385,386</sup>. First, <sup>111</sup>In-AuNPs-Trastuzumab, <sup>177</sup>Lu-Panitumumab-AuNP, <sup>177</sup>Lu-AuNPs-Trastuzumab and <sup>211</sup>At-AuNP-PEG-Trastuzumab show a higher cytotoxic effect than their untargeted, radiolabeled AuNPs analogs <sup>320,353,385,386</sup>. Second, increasing the EGF load on <sup>111</sup>In-EGF-AuNPs increases its cytotoxic efficacy <sup>314</sup>. Third, cancer cells with a low or intermediate HER1/HER2 expression profile are less affected by the targeted radiopharmaceuticals as compared to the cells with a high receptor expression <sup>314,320,385,386</sup>. Finally, pre-blocking the binding sites on A549 cells diminishes the cytotoxic effect of <sup>131</sup>I-Cetuximab-AuNPs <sup>342</sup>.

- Intravenous injection in tumor-bearing mice

There are a limited number of *in vivo* studies, which intravenously inject radiolabeled AuNPs to investigate their use as potential agents for TRT. For instance, IV administration of 7 doses of polyethylenimine-entrapped AuNPs, radiolabeled to <sup>131</sup>I and conjugated to chlorotoxin

( $^{131}\text{I}$ -Au PENPs-BmK CTX and  $^{131}\text{I}$ -Au PENPs-CTX) in glioma-bearing mice significantly slows down the tumor growth and prolongs the survival after 3 weeks as compared to the saline control, the untargeted AuNP analogs or the non-radioactive AuNP analogs<sup>339,377</sup>. Next to the delivery of radionuclides to the tumor site, radiolabeled AuNPs can also act as radiosensitizers. This was investigated *in vivo*, where SPECT-CT imaging was used to define the maximal tumor delivery of  $^{125}\text{I}$  after IV administration of  $^{125}\text{I}$ -cRGD-AuNPs, which was then followed by EBRT. Combined  $^{125}\text{I}$ -cRGD-AuNPs and RT suppressed the tumor growth more effectively during 21 days as compared to no treatment, IR alone, AuNPs+RT and cRGD-AuNPs+RT. However, there was no significant difference in the apoptotic degree caused by  $^{125}\text{I}$ -cRGD-AuNPs and cRGD-AuNPs, 2 days after RT. The authors suggested that a significant increase in therapeutic efficacy might be possible if  $^{125}\text{I}$  was exchanged by  $^{131}\text{I}$ , which has a higher therapeutic potency<sup>341</sup>. Alternatively, TRT could be combined with photothermal therapy. This approach was studied *in vitro*, showing the radiotoxicity of  $^{99\text{m}}\text{Tc}/^{177}\text{Lu}$ -AuNP-Tat-BN and dendrimer-entrapped  $^{177}\text{Lu}$ -AuNP conjugated to folate and bombesin ( $^{177}\text{Lu}$ -DenAuNPs-folate-bombesin) in cancer cells, while the corresponding unlabeled analogs, DenAuNP-folate-bombesin and AuNPs-Tat-BN, exhibited thermo-ablative properties following laser irradiation at 532 nm for 6 min ( $0.65\text{W}/\text{cm}^2$ ). It is important to note that laser irradiation at 532 nm, close to the SPR peaks of the respective AuNPs, has a limited clinical application, due to its poor tissue penetration<sup>384,387</sup>. Nevertheless, the studies highlight a proof-of-principle for future research on the TRT/photothermal combination therapy. Furthermore, the research group also demonstrates an enhanced cytotoxic effect of the dual-radiolabeled AuNPs as compared to the single radiolabeled  $^{177}\text{Lu}$ -AuNP-Tat-BN or  $^{99\text{m}}\text{Tc}$ -AuNP-Tat-BN, which is attributed to the biological effects of Auger electrons and low-energy internal conversion of  $^{99\text{m}}\text{Tc}$ <sup>384</sup>.

#### - Intratumoral injection in tumor-bearing mice

The majority of the research assessing the effectiveness of radionuclide therapy using radiolabeled AuNPs *in vivo* chose for an intratumoral route of administration, usually with the aim to improve the therapy of localized prostate cancer or breast cancer<sup>359,370,375,385,386,388-392</sup>. Intratumoral administration maximizes the tumor concentration of the radiolabeled AuNPs and minimizes the sequestration by the liver and spleen, which is associated with IV injection<sup>365,385,393</sup>. Conjugation of targeting molecules, such as Trastuzumab, Panitumumab, cRGD, pigallicocatechin-gallate (EGCg) to the AuNPs result in a more than 2 times prolonged tumor retention, compared to their untargeted radiolabeled AuNPs counterparts, which show a gradual tissue redistribution to the liver and spleen over time<sup>370,386,388,389,394</sup>. Furthermore, due to their relatively large size, 150 nm non-functionalized  $^{103}\text{Pd}@$ Au nanoseeds show a tumor xenograft retention of 5 weeks<sup>392</sup>. The significantly longer retention of  $^{198}\text{Au}$ NPs-EGCg (75% ID/g after 24h) within the tumor compared to  $^{198}\text{Au}$ NPs-gum arabic (GA) (200% ID/g after 24h) allows to inject only one third

of the activity, without compromising the tumor response (5 MBq for  $^{198}\text{AuNP-EGCg}$  vs 15 MBq for  $^{198}\text{AuNP-GA}$ )<sup>388,389</sup>.

A longer tumor retention leads to a higher radiation dose delivered to the tumor. For instance, 48h after injection of 10 MBq  $^{111}\text{In-AuNPs-Trastuzumab}$  in a breast cancer xenograft, the cumulative absorbed radiation dose is estimated to be 60.5 Gy, compared to 28.4 Gy for untargeted  $^{111}\text{In-AuNPs}$ <sup>385</sup>. Comparably, 48h after injection of 4.5 MBq  $^{177}\text{Lu-AuNPs-Panitumumab}$  in a breast cancer xenograft, the cumulative absorbed radiation dose is estimated to be 30.37 Gy, compared to 21.86 Gy for untargeted  $^{177}\text{Lu-AuNPs}$ <sup>394</sup>. Finally, intratumoral injection of 8 MBq of  $^{177}\text{Lu-cRGD-AuNPs}$  results in a cumulative absorbed radiation dose of 63.8 Gy after 23 days, compared to 38.3 Gy and 16.6 Gy for  $^{177}\text{Lu-AuNPs}$  and  $^{177}\text{Lu-cRGD}$ , respectively<sup>370</sup>. As a result, treatment of tumor xenografts with radiolabeled, targeted AuNPs inhibits the tumor growth after more than 2 weeks post-treatment and prolongs the survival of the treated mice, compared to the saline control<sup>385,386,388,389,391,394</sup>. In addition,  $^{177}\text{Lu-cRGD-AuNPs}$  significantly reduces the tumor metabolic activity, the intratumoral blood vessels formation and the VEGF tumoral gene expression, compared to the saline control group,  $^{177}\text{Lu-AuNPs}$  and  $^{177}\text{Lu-cRGD}$ <sup>370</sup>. Due to the non-systemic, highly localized administration of the radiolabeled AuNPs into the tumor, the radiation doses in the healthy organs was lower than 1.5 Gy<sup>370,385,394</sup>. Furthermore, the studies did not reveal significant differences in serum ALT, creatinine and urea, and caused no decrease in blood cell counts<sup>385,386,388,389,391,394</sup>.

The intratumoral administration strategy of radiolabeled AuNPs is seen as a potential alternative for the implantation of radioactive seeds during interstitial brachytherapy<sup>375,392</sup>. Interstitial brachytherapy is based on the, often permanent, implantation of millimeter-sized radioactive seeds in or near the tumor, providing a continuous dose delivery. Although successful, there are certain limitations associated to this mode of therapy, such as discomfort and a heterogeneous intratumoral dose distribution<sup>375</sup>. Injection of colloidal nanoseeds using much smaller needles could reduce the trauma caused by implantation. Furthermore, the delivered radiation dose would be easily controllable by adjusting the injection volume in contrast to the millimeter seeds, which are each 18.5-74 MBq. In addition, injection of nanoseeds would enable the treatment of smaller tumors<sup>375,392</sup>. Finally, experimental studies show that the presence of gold nanoparticles in cancer cells during exposure to  $^{125}\text{I}$  or  $^{131}\text{I}$  results in significant radiosensitization of the tumor *in vitro* and *in vivo*<sup>395,396</sup>.

One of the radionuclides used during low-dose brachytherapy is  $^{103}\text{Pd}$ . Laprise-Pelletier produced core-shell nanoparticles (<50 nm) consisting of a core of radioactive  $^{103}\text{Pd}$ , surrounded by a shell of gold, which needed to provide dose enhancement ( $^{103}\text{Pd:Pd@AuNPs-PEG}$ ). In addition, similar nanoparticles were co-labeled with the high-energy emitter  $^{198}\text{Au}$  ( $^{103}\text{Pd:Pd@}^{198}\text{Au:AuNPs-PEG}$ ). Four weeks after a single injection of 60

MBq of  $^{103}\text{Pd}:\text{Pd}@\text{AuNPs-PEG}$  or  $^{103}\text{Pd}:\text{Pd}@^{198}\text{Au}:\text{AuNPs-PEG}$ , the tumor volume decreases with 56% and 75%, respectively, as compared to the controls. However, the tumor growth inhibition of  $^{103}\text{Pd}:\text{Pd}@^{198}\text{Au}:\text{AuNPs-PEG}$  is associated with severe necrosis at the skin of the treated animals. This observation is attributed to the emission of high-energy electrons and the long-range high-energy photons by  $^{198}\text{Au}$ , which could be a limitation of  $^{198}\text{Au}$  when used for short-range nanobrachytherapy<sup>375</sup>. Alternatively, Moeendarbari, et al produced  $^{103}\text{Pd}$ -coated gold nanoseeds, consisting of an 100 nm inner gold core and an outer shell of  $^{103}\text{Pd}$ . Due to the large size of the gold core, the secondary electrons produced by the interaction between the  $^{103}\text{Pd}$  emission and the gold are expected to be trapped inside the gold core. Nevertheless, the  $^{103}\text{Pd}@\text{Au}$  nanoseeds significantly inhibit the tumor growth and reduce the tumor metabolic activity, 5 weeks after treatment, compared to the saline controls<sup>392</sup>.

**Table 1.3** An overview of radiolabeled gold nanoparticles under investigation for their therapeutic potentials.

Isotope	Particle name	Size (nm)	Functionalization	Labeling method	Cell model, administration	Purpose	Therapeutic effect	Author
<sup>131</sup> I	<sup>131</sup> I-C225-AuNPs-PEG	52.9	Cetuximab (C225)	Covalent	A549, IV 18.5 MBq	TRT <i>in vitro</i> SPECT-CT <i>in vivo</i>	%CS: <sup>131</sup> I-C225-AuNPs: 37 (2h) %CS after blocking: >82. T/M: 3.9 (2h) – 5.5 (4h)	Kao, et al <sup>342</sup>
	<sup>131</sup> I-Au PENP-BmK CTX	147	Chlorotoxin-like peptide (T) Untargeted (UT)	Covalent	C6, IV 7x 9.25 MBq, 100 µl	Targeted SPECT-CT and TRT	Tumor volume increased 17-22x (controls), 20x (UT) and 7x (T) after 3 weeks. Treatment with T results in prolonged survival compared to UT. Higher tumor SPECT (2x) and CT (1.67x) signal intensities compared to UT-form, 6-8h p.i.	Sun, et al <sup>339</sup>
	<sup>131</sup> I-Au PENPs-CTX	151	Chlorotoxin (T) Untargeted (UT)	Covalent	C6, IV 7x 7.4 MBq, 100 µl	Targeted SPECT-CT and TRT	Treatment with T leads to higher tumor SPECT (2.2-2.4x) and CT (1.7x) signal intensities compared to treatment with UT, 6-8h p.i. Tumor volume increased 18.2x (UT), 9.7x (T) and 19.6-21.9x (controls). Survival time after treatment with T was significantly longer than after treatment with UT.	Zhao, et al <sup>377</sup>
<sup>125</sup> I	<sup>125</sup> I-cRGD-AuNPs	45.2	Cyclic RGD	Covalent	NCI-H466, IV 37 MBq, 100 µl	RT and TRT. SPECT-CT	T/NT tumor uptake ratio: 2.07 (1h) - 4.76 (2h) - 4.25 (4h). T/NT apoptosis ratio (2 days after RT): RT+cRGD-AuNPs- <sup>125</sup> I: 11.2   RT+cRGD-AuNPs: 9.8   RT+AuNPs: 5.5   RT alone: ≈ 5   no treatment: ≈ 3 % increase in tumor vol. (grams) (after 21d): Control: 312 (0.538)   RT: 137 (0.209)   RT+AuNPs: 85.5 (0.171)   RT+cRGD-AuNPs: 33.1 (0.113)   RT+ <sup>125</sup> I-cRGD-AuNPs: 15.2 (0.116) → Therapeutic effect of <sup>125</sup> I-cRGD-AuNPs+RT not significantly improved compared to cRGD-AuNPs+RT.	Su, et al <sup>341</sup>
<sup>111</sup> In	<sup>111</sup> In-EGF-Au NPs	14	EGF	Chelation	MDA-MB-468 MCF-7	TRT <i>in vitro</i>	SF MDA-MB-453: 42.8%. Increasing the EGF loading on the AuNP, reduces the SF to 17.1%. Not toxic to MCF-7	Song, et al <sup>314</sup>

<sup>177</sup> Lu	<sup>111</sup> In-AuNPs- Trastuzumab	30	Trastuzumab (T) Untargeted (UT)	Chelation	MDA-MB-361 (intermediate) IT, 10 MBq, 100 μL  SK-BR-3 (high)	TRT <i>in vitro</i> and <i>in vivo</i>	T form was internalized more efficiently in the perinuclear region, lead to more DSBs and cell death in both cell types than the UT form. The uptake and cell death is higher in SK-BR-3 cells than in MDA-MB-361 cells treated with T form. T form arrested tumor growth over 70 days.  Control: 8x tumor volume increase over 70 days Absorbed dose: T: 60.5 Gy – UT: 28.4 Gy (48h)	Cai, et al <sup>385</sup>
	<sup>177</sup> Lu-AuNPs- cRGD	26.6 25.6	Cyclic RGD (T) Untargeted (UT)	Chelation	C6 IT, 4 x 2 MBq, 50 μl	Radionuclide therapy	Inhibited C6 cell proliferation (3.6%) compared to UT form (6.3%) and <sup>177</sup> Lu-cRGD (29.7%). %ID/g (T): 68.1 (3h) - 34.7 (96h)   SUV <sub>18F-FDG</sub> : 0.335 (23d) %ID/g (UT): 48.2 (3h) - 25.5 (96h)   SUV <sub>18F-FDG</sub> : 0.584 (23d) %ID/g ( <sup>177</sup> Lu-cRGD): 26.8 (3h) - 5.7 (96h)   SUV <sub>18F-FDG</sub> : 2.740 (23d)  Absorbed dose: T: 63.8 Gy - UT : 38.3 Gy - <sup>177</sup> Lu-RGD : 16.6 Gy (23d)  T treatment: Tumor size was 27x smaller than control, 12x smaller than <sup>177</sup> Lu-cRGD and 3x smaller than UT treatment (23d).	Vilchis-Juarez, et al <sup>370</sup>
	<sup>177</sup> Lu-T-AuNPs	67.3 45.8	Panitumumab (T) Untargeted (UT)	Chelation	MDA-MB-468 (high) MDA-MB-231 (moderate) MCF-7 (low)	TRT <i>in vitro</i>	%CS (high) T: 21.7 (1.5MBq) - 0.1 (3MBq) - <0.001 (4.5MBq) %CS (high) UT: 43.1 (1.5MBq) - 22.5 (3MBq) - 8.4 (4.5MBq) %CS (mod) T: 58.1 (1.5MBq) - 46.4 (3MBq) - 33.8 (4.5MBq) %CS (mod) UT: 84.2 (1.5MBq) - 64.8 (3MBq) - 51.6 (4.5MBq) %CS (low) T: 64.1 (1.5MBq) - 30.3 (3MBq) - 25.8 (4.5 MBq) %CS (low) UT: 54.3 (1.5MBq) - 31.9 (3MBq) - 32.3 (4.5 MBq)  %ID/g (T): 465.7 (1h) and 196.6 (48h) %ID/g (UT): 341.1 (1h) and 99.0 (48h)  TGI of T was 35X lower (0.3) than TGI of control (11.1) (90d).  No difference in TGI of T (0.3) and UT form (0.8). Mice	Yook, et al <sup>320</sup>
	<sup>177</sup> Lu-T-AuNPs	67.3 45.8	Panitumumab (T) Untargeted (UT)	Chelation	MDA-MB-468 IT, 4.5 MBq, 30 μL	Radionuclide therapy		Yook, et al <sup>394</sup>

<sup>177</sup> Lu/ <sup>99m</sup> Tc	<sup>177</sup> Lu-DenAuNPs-folate-bombesin	1-2.9	Folate – bombesin (T) Untargeted (UT)	Chelation	T47D	Optical imaging, PTT and TRT <i>in vitro</i>	treated with T and UT survived for 75-86d. Absorbed dose: T: 30.37 Gy - UT: 21.86 (48h) Absorbed dose: T: 15.1 Gy – UT: 63.2 Gy (72h, 14.8 Bq/cell) Cell lethality 4 times higher after exposure to T form, compared to UT form.	Mendoza-Nava <sup>387</sup>
	<sup>177</sup> Lu-AuNPs-Trastuzumab	30	Trastuzumab (T) Untargeted (UT)	Chelation	MDA-MB-361 (intermediate), IT, 3 MBq, 30 µL BT-474 (high) SK-BR-3 (high)	TRT <i>in vitro</i> and <i>in vivo</i>	T form was internalized more in BT-474 and SK-BR-3 cells than in MDA-MB-361 cells. The T form was internalized and retained more efficiently than the UT form in SK-BR-3 cells, and lead to more DSBs and cell death. TGI after 16 days: (T) = 2.5   (UT) = 4.2   (saline) = 5.6	Cai, et al <sup>386</sup>
	<sup>99m</sup> Tc/ <sup>177</sup> Lu-AuNPs-Tat-BN	8.07	Bombesin/TAT (49-57) (T) Untargeted (UT)	Chelation	PC-3	PTT and TRT <i>in vitro</i>	52% more internalization than UT form. Significantly inhibited cell proliferation compared to UT form or <sup>99m</sup> Tc-Tat-BN.	Jimenez-Mancilla, et al <sup>384</sup>
<sup>198</sup> Au	<sup>198</sup> AuNPs-GA	85	Gum arabic	Incorporation	PC-3 IT, 15 MBq, 30 µL	Radionuclide therapy	3 weeks after treatment, tumor volume of treated group was 82% smaller (0.17 cm <sup>3</sup> ) as compared to the control group (0.86 cm <sup>3</sup> ). After 31 days: %ID: 19.9	Chanda, et al <sup>388</sup>
	<sup>198</sup> AuNPs-EGCg	80	epigallocatechin-gallate	Incorporation	PC-3 IT, 5 MBq, 30 µL	Radionuclide therapy	72% tumor retention (24h) - %ID: 37.4 (42d) 80% tumor volume reduction after 28 d (reduced by 0.28 cm <sup>3</sup> ) compared to controls (reduced by 0.05 cm <sup>3</sup> )	Shukla, et al <sup>389</sup>
	<sup>198</sup> AuNPs-GA	85	Gum arabic	Incorporation	Naturally occurring prostate cancer, IT, 111-666 MBq, 100-200 µl	Radionuclide therapy	%ID: 53 (30 min). Tumor volume was stable (n=6) or reduced by 30-50% (n=2). One dog had a tumor volume increase of 26%.	Axiak-Bechtel, et al <sup>390</sup>
	<sup>198</sup> AuNPs-MGF	35	Mangiferin	Incorporation	PC-3 IT, 6 MBq, 30 µL	Radionuclide therapy	%ID: 80.98 (0.5h) - 79.82 (24h) – 60.96-69.7 (24d) Tumor volume treated group: 0.18-0.22 cm <sup>3</sup> (stable) (24d) Tumor volume control group: 1.31 cm <sup>3</sup> (6.5x increase) (24d)	Al-Yasiri, et al <sup>391</sup>

<sup>198</sup> Au_LACT	3.7	N.A.		Incorporation	MCF7 CRL-1790	Radionuclide therapy <i>in vitro</i>	The viability of MCF-7 cancer cells decreased (50 µg/ml – 72h). The effect on normal cells (CRL-1790) was considerably smaller.	Wojtowicz, et al <sup>397</sup>
<sup>198</sup> Au/ <sup>103</sup> Pd	<sup>103</sup> Pd: Pd@ Au-PEG NPs (group 1) <sup>103</sup> Pd: Pd@ <sup>198</sup> Au: Au-PEG (group 2)	36-48	PEG	Encapsulation	PC-3 IT, 59-63 MBq, 4 µL	Low-dose radionuclide therapy	After 4 weeks: Control group reached endpoint Tumor volumes of treated group 1 were 56% smaller Tumor volumes of treated group 2 were 75% smaller, but severe skin necrosis. Prolonged survival compared to control: 38-62d or >80d.	Laprise-Pelletier, et al <sup>375</sup>
<sup>103</sup> Pd	<sup>103</sup> Pd@Au nanoseeds	140	N.A.	Shell	PC-3 IT, 55.5 MBq, 40 µL	radionuclide therapy	%ID/g: 101.5 (24h) – 274.5 (5w) Tumor control mm <sup>3</sup> : ( <sup>103</sup> Pd@Au): 82.7 to 19.8 (5w) Metabolic activity decreased with 62% (5w) Tumor control mm <sup>3</sup> : (PBS): 67.1 to 187, (cold Au): 58.7 to 122 (5w)	Moenda rbari, et al <sup>392</sup>
<sup>211</sup> At	<sup>211</sup> At-AuNPs- PEG- trastuzumab	45.8 16.1	Trastuzumab (T) Untargeted (UT)	Adsorption	SKOV-3	TRT <i>in vitro</i>	LD <sub>50</sub> (T): 0.55 MBq/mL (24h) LD <sub>50</sub> (UT): 1.3 MBq/ mL (24h) Bioconjugates successfully penetrate SKOV-3 cells and were localized in the nuclear envelope area	Dziawer, et al <sup>353</sup>
<sup>211</sup> At	<sup>211</sup> At-AuNPs- S-PEG-SP(5- 11)	24.6	Substance P(5- 11) (T) Untargeted (UT)	Adsorption	T98G, 0.6 MBq	TRT <i>in vitro</i>	metabolic activity: non-radiolabeled AuNP-S-PEG-SP(5-11): 88% (24h) metab. act.: UT: ≈55% (24h) metab. act.: T: ≈38% (24h)	Dziawer, et al <sup>352</sup>

**Abbreviations:** AuNP: gold nanoparticle; Au-PENPs: polyethylenimine-entrapped gold nanoparticles; BmK-CTX: Buthus martensii Karsch chlorotoxin; CT: computed tomography; DenAuNPs: dendrimer conjugated gold nanoparticles; DSBs: double strand breaks; EGCG: epigallocatechin-gallate; EGF: epidermal growth factor receptor; FDG: Fluorodeoxyglucose; GA: gum Arabic; IT: intratumoral; IV: intravenous; LACT: *Lactobacillus rhamnosus*; LD<sub>50</sub>: lethal dose for 50% of the cells; MGF: Mangiferin; PEG: polyethylene glycol; p.i.: post-injection; PTT: photothermal therapy; RT: radiotherapy; SF: survival fraction; SPECT: single photon emission computed tomography; SP(5-11): substance P(5-11); SUV: standardized uptake value; T: targeted; TAT-Bn: TAT-bombesin; TGI: tumor growth index (ratio of the treated tumor volume by the initial tumor volume); T/M: tumor-to-muscle ratio; T/NT: target-to-non-target ratio; TRT: targeted radionuclide therapy; UT: untargeted; %CS: percentage of cell survival; %ID: percentage injected dose



---

**Overview: Gold nanoparticles in nuclear medicine**

---

*Combining AuNPs in nuclear medicine enables:*

- Conjugation of multiple radionuclides per AuNP
- Prolonged blood circulation time
- Multivalent targeting
  - Increased tumor uptake
  - increased intratumoral retention time

*In diagnostics:*

- Increased SPECT and PET signal intensity
- Detection of micro-metastatic lesions
- Multi-modal imaging platform:
  - increased CT contrast due to X-ray absorption coefficient
  - MRI via conjugation of MRI contrast agents
  - SPECT or PET imaging
- Monitoring the tumor uptake to ensure maximal X-ray radiosensitization or PTT effect (theranostics)

*In therapy:*

- Potential multi-modal therapeutic platform: radionuclide therapy and PTT
  - Main application is intratumoral injection
    - Maximized intratumoral concentration
    - Less invasive than brachytherapy
    - Minimized RES sequestration
    - Minimized radiotoxicity in healthy tissue (well-tolerable)
  - Increased estimated absorbed dose in the tumor
  - Reduced tumoral metabolic activity
  - Suppressed tumor growth
  - Prolonged survival of treated mice
-

## 6. Clinical trials

Liposomes were the first class of nanoparticles to receive approval for cancer treatment. Currently, they still represent a large proportion of clinical-stage nanotherapeutics. This is thanks to their biostability, safety and biodegradability. In addition, they can transport both hydrophobic and hydrophilic drugs in the lipid bilayer and vesicle lumen compartments, respectively. In contrast, although well represented in research, only a few AuNPs were investigated in clinical trials (**Table 1.4**).

**Table 1.4** Overview of the clinical trials using AuNPs

Name	Formulation	Admin. Route Dose	Size (nm)	Status Enrollment	Indication	ID
AuroLase therapy (AuroShell) (Nanospectra Biosciences)	Silica core coated with gold shell	IV, single dose of 21-35 mg/kg, 12-24h prior to 3.5-5W/cm <sup>2</sup> NIR laser (808 nm) irradiation.	150	Completed pilot study (2008-2014) 11 participants	Photo-thermal ablation of head and neck cancers: <i>adverse effects* and tumor response.</i>	NCT00848042
		IV, single dose, 12-36h prior to MRI/US guided laser irradiation.		Active, not recruiting pilot study (2016-2020) 45 participants	MRI/US guided photo-thermal ablation of prostate neoplasm: <i>efficacy* and adverse effects</i>	NCT02680535
				Recruiting pilot study (2020-2023) est. 60 participants	Extension: MRI/US guided photo-thermal ablation of prostate neoplasm: <i>efficacy* and adverse effects</i>	NCT04240639
AurImmune (CYT-6091) (CytImmune Sciences)	Tumor necrosis factor (TNF) - AuNPs	IV, single dose 12-78h prior to surgery.	27	Completed early Phase I (2006-2009) 84 participants	Patient with primary or metastatic cancer undergoing surgery: <i>Tumor and normal tissue distribution*, acute anti-tumor activity and long-term toxicity.</i>	NCT00436410
		IV, 50-600 µg/m <sup>2</sup> , on days 1 and 15 (course 1). Up to 3 re-treatment courses.		Completed Phase I (2006-2009) 60 participants	Advanced solid tumors: <i>maximum tolerated dose*, toxicity*, pharmacokinetics, tumor and normal tissue distribution, antitumor effect.</i>	NCT00356980

NU-0129	siRNA-AuNPs	IV, single dose of 0.04mg/kg, 8-48 hours prior to tumor resection.	13	Active, not recruiting early phase 1 (2017-2022) 8 participants	Targeting BCL2L12 in recurrent glioblastoma or gliosarcoma: <i>safety*</i> , <i>pharmacokinetics</i> , <i>tumor tissue distribution</i> , <i>treatment feasibility</i>	NCT03020017
C19-A3 GNP	human C19A3 pro-insulin peptide-AuNPs	Intradermal, 10 µg of C19A3 peptide every 28 days for 8 weeks (3 doses)	5	Active, not recruiting phase 1 (2016-2020) 8 participants	Type 1 Diabetes: <i>safety*</i> , <i>feasibility</i> , <i>immune response</i>	NCT02837094
NANOM FIM	Silica-gold NPs	Transplantation, 39-45 nM, NIR laser (821 nm, 35-44 W/cm <sup>2</sup> , 7 days after intervention	60/15-70/40 nm core/shell	Completed Phase I (2007-2016) 180 participants	Plasmonic photo-thermal therapy of atherosclerotic lesions: <i>plaque volume*</i> , <i>Major adverse cardiovascular events-free survival*</i>	NCT01270139

**Abbreviations:** \* Primary objectives; BCL2L12: Bcl2-like protein 12; IV: intravenous; MRI: magnetic resonance imaging; NIR: near-infrared; TNF: tumor necrosis factor; US: ultrasound

One of the first studies investigating AuNPs in modern medicine was performed by Guy Abraham and Peter Himmel in 1997. They evidenced that the oral administration of 20 nm AuNPs (daily doses of 30 mg for 4 weeks, followed by one dose per month for 5 months) significantly decreased the tenderness and the swelling of the joints in 10 patients with rheumatoid arthritis. Although no signs of toxicities were noted, no follow-up studies were conducted<sup>398</sup>. Later on, a novel nanomedicine, CYT-6091 or Aurlmmune was tested in a phase I clinical trial in advanced-stage cancer patients (**Table 1.4**). CYT-6091 consisted out of a 27 nm PEGylated AuNP which was conjugated to recombinant human tumor necrosis factor alpha (TNF- $\alpha$ ). TNF- $\alpha$  is a cytokine that exerts anti-tumor effects and induces hyper-permeability of the tumor vasculature<sup>399,400</sup>. As a result, TNF- $\alpha$  could enhance the efficacy of subsequently administered chemotherapy, improving the tumor response rate. However, the cytokine has a limited clinical value due to unfavorable pharmacokinetics, poor tumor delivery and toxic side effects, such as hypotension, hepatotoxicity, general malaise and fatigue<sup>401,402</sup>. Conjugation of TNF- $\alpha$  to AuNPs resulted in a 5-fold longer half-life of TNF- $\alpha$  and enabled the delivery of the cytokine to the tumor as was confirmed by core biopsies. The dose of TNF- $\alpha$  could be increased from 225 µg/m<sup>2</sup> to 600 µg/m<sup>2</sup>, without serious dose-limiting toxicity or immunogenicity<sup>403</sup>.

Besides drug delivery, the ability of AuNPs to absorb NIR light promoted the development of 120 nm silica nanoparticles, surrounded by a 12-15 nm gold shell and coated with PEG molecules for the photo-thermal ablation of solid tumors. A pilot study was performed in 22 patients with prostate cancer, receiving an intravenously administered dose of 35 mg/kg of AuroShell NPs, one day prior to laser irradiation (AuroLase therapy) (**Table 1.4**). The chemical,

hematological, immunological and urinalysis evaluations identified no sign of toxicity, lack of tolerance, or immunological effects in the patients until 6 months after AuroShell NP treatment. Furthermore, there was no change in temperature of the anterior rectal wall after laser irradiation. However, two adverse effects were attributed to the AuroLase therapy. One patient showed an allergic reaction and one patient experienced a transient burning sensation of the epigastrium at the time of infusion. Nevertheless, the authors concluded that systemic infusion of AuroShell NPs is clinically safe to use for the focal ablation of prostate cancer <sup>404</sup>. Similarly, no adverse effects were related to the AuroLase therapy in patients with head-and neck cancers <sup>405</sup>. Following these promising results, a recent clinical study evaluated the efficacy of the AuroLase therapy protocol in 15 patients with low-or intermediate risk prostate cancer. The authors combined AuroShell NPs with MRI-ultrasound fusion imaging to achieve high-precision, transperineal laser ablation of the prostate cancer. There were no serious adverse events (grade 3) during the procedure and within 90 days post-treatment. Furthermore, no significant difference in the International Prostate Symptom Score, Urinary Quality of Life or Sexual Health Inventory for Men was reported after treatment. The biopsies taken after three and 12 months post-treatment showed that the ablation zones were cancer free in 60% (9/15) and 86.7% (13/15) of the patients, respectively. As a result, the clinical study reported that the treatment protocol is technically feasible and safe for the targeted destruction of prostate tumors <sup>406</sup>.

Glioblastoma is difficult to treat due to the limited ability of chemotherapeutics to cross the blood-brain-barrier (BBB). Therefore, researchers developed the NU-0129 nanodrug, a 13 nm AuNP densely packed with a siRNA oligonucleotide, which targets the oncogene Bcl2-like protein 12 (Bcl2L12) mRNA. Bcl2L12 is overexpressed in glioblastoma, preventing tumor cell apoptosis and promoting tumor growth. An early phase I clinical trial is ongoing with 8 glioblastoma patients treated with NU-0129 IV infusion, followed by tumor resection (**Table 1.4**). In six patients, sufficient tumor tissue was available for element analysis. This analysis demonstrated gold accumulation, evidencing the ability of NU-0129 to cross the BBB. However, two patients showed severe hypophosphatemia and/or lymphopenia (> grade 3), which were possibly related to the infusion. No significant treatment-related toxicities were observed in the other six patients. Pharmacokinetic studies and the immunohistochemical analysis of the tumor tissue to determine the expression of Bcl2L12 and apoptotic markers are pending <sup>407</sup>.

Finally, besides tumor treatment, AuNPs were evaluated in clinical trials for their use in non-cancer diseases. For instance, transfer of silica-AuNPs to atherosclerotic lesions, followed by NIR laser excitation is a promising technique for atherodestruction, with a possibility to reverse atherosclerosis. After 12 months, patients treated with silica-AuNPs and NIR irradiation showed a mean plaque volume reduction of 43.2-44.8%, compared to a 22.7% reduction in patients treated with a conventional stent. In addition, the prevalence of major adverse cardiovascular events within 12 months and 60 months demonstrated that the

treatment with silica-AuNPs resulted in a lower risk on cardiovascular death compared to the stent-treatment. No nanotoxicity, clinical complications or thrombosis were recorded at the site of intervention up to 60 months after treatment <sup>408,409</sup>. Besides the treatment of atherosclerosis, AuNPs were recently investigated as therapeutic agents for diabetes type I and as sensors to detect gastric lesions and pulmonary arterial hypertension in exhaled breath.

## 7. Challenges of gold nanoparticles in medicine

### 7.1 Biocorona formation

As mentioned before, despite the increasing number of promising reports on the use of AuNPs in nanomedicine, clinical translation has been limited. The preferred route of nanoparticle administration in a clinical view is via IV injection. However, a meta-analytical review about nanoparticle delivery revealed that only 0.7% (median) of the injected dose of nanoparticles reached the tumor <sup>410</sup>. This could be explained by some major physical and biological barriers that AuNPs encounter once applied *in vivo*. Indeed, AuNPs must endure an extensive journey, traveling through the circulatory system multiple times in order to reach the tumor site and to perform their therapeutic function <sup>47</sup>. First, AuNPs are almost immediately and inevitably coated with proteins, lipids, carbohydrates and nucleic acids, which are present in the biological environment, forming the 'biocorona'. The major part of the studies have focused on the protein part of the biocorona. The formation of a biocorona is a dynamic and complex process. Initially, low-affinity, but highly abundant proteins, such as albumin, interact with the AuNPs, followed by the gradual replacement with high-affinity, but lower abundant proteins. Eventually, two layers are created around the AuNPs, an inner 'hard' layer of irreversibly attached proteins and an outer 'soft' layer of loosely bound proteins. The biocorona gives the AuNPs a 'biological identity', which is presented to the body and which is distinct from the intended 'synthetic identity'. Important factors determining the biocorona are the size, shape and surface charge of the AuNPs as well as the biological environment <sup>411</sup>. Larger AuNPs are found to be covered with a larger amount of proteins having a higher molecular weight, as compared to smaller AuNPs. This is due to the higher surface area of the larger particles. However, smaller AuNPs show a more complex biocorona composition and consisted more out of low molecular weight proteins than their larger sized counterparts <sup>412,413</sup>.

The biological effects arising from this new AuNP interface on the AuNP biological behavior can be both beneficial or unfavorable. For instance, adherence of proteins to the AuNP surface can induce protein unfolding, exposing epitopes that bind to macrophage receptors or activate the immune response <sup>414,415</sup>. Furthermore, Kuschnerus, et al showed that the formation of a biocorona in the presence of bovine serum or fibrinogen reduces the colloid stability of the AuNPs and induces oxidative stress in microglial cells, respectively. The AuNP agglomeration increases the AuNP size and consequently facilitates the cellular uptake by

endocytosis<sup>416</sup>. Comparably, the adherence of negatively charged BSA proteins to cationic CTAB-AuNPs neutralizes the surface charge and induces aggregation, while anionic AuNPs are more stable<sup>417</sup>. In addition, the formation of a biocorona diminishes the targeting capabilities of transferrin-conjugated AuNRs and cRGD-AuNPs to human cancer cells, potentially due to shielding of the targeting ligands by proteins of the biocorona<sup>418-420</sup>. In this view, Su, et al found that the absorbed proteins interfere in particularly with the binding of small functionalized AuNPs as compared to large AuNPs, since small sized AuNPs show less multivalent receptor interactions<sup>421</sup>. In contrast to the above, there are also studies demonstrating that the biocorona helps to stabilize nanoparticles, reduces the cytotoxicity and does not have detrimental effects on the targeting capabilities of functionalized nanoparticles<sup>422-424</sup>.

## 7.2 Sequestration by the reticuloendothelial system

The adsorbed surface proteins are recognized by the phagocytic macrophages of the RES, leading to a fast clearance of AuNPs from the blood. This is in particular true if ‘opsonins’ such as immunoglobulins, complement proteins and coagulation factors are included in the biocorona<sup>425</sup>. On the other hand, ‘dysopsonins’ like albumin and apolipoproteins reduce the phagocytic uptake and increase the blood circulation time<sup>411</sup>. Usually, the nanoparticles are sequestered by the liver, since the Kupffer cells make up 80-90% of all macrophages in the body. Furthermore, the specialized liver endothelial cells exhibit fenestrae allowing particulate matter to be trapped in a similar manner as the EPR effect describing the accumulation of AuNPs in the tumor tissue<sup>426</sup>.

In order to reduce the effects associated to the biocorona formation and liver sequestration, researchers often modify the nanoparticles with PEG. PEG grafting suppresses protein adsorption by blocking the protein binding sites on the AuNP surface and by creating a barrier against protein diffusion. In case of targeted AuNPs, suppression of the protein adsorption preserves the binding efficiency of the targeting ligand to the cancer cells<sup>427</sup>. Although PEGylation cannot completely eliminate corona formation, PEG molecules give the AuNPs a stealth character, slowing down the phagocytic uptake and increasing the blood circulation time<sup>425,428,429</sup>. However, PEGylation also brings the ‘PEG dilemma’: an excessive PEGylation strongly inhibits the interaction efficiency of the AuNPs to cancer cells and hinders endosomal escape, reducing the AuNPs targeting and delivery capabilities<sup>430</sup>. Another approach to minimize RES uptake is by tuning the size and shape of the nanoparticles. For instance, multiple researchers demonstrated that rod-shaped NPs and worm-like NPs with very high aspect ratio exhibited a lower macrophage uptake and an increased blood circulation time compared to spherical NPs, due to a limited interaction between the NPs and the macrophages under flow conditions<sup>431-434</sup>. In addition, macrophages prefer to take up rigid NPs compared to softer NPs, such as hydrogels<sup>435</sup>.

Instead of changing the nanoparticle properties, a few selected number of studies aimed to reversibly block the RES sequestration by pre-injecting tumor-bearing mice with liposomes. It was suggested that the liposomes would saturate the macrophage receptors and/or would deplete the opsonins. 1.5-5 hours later, the injection of AuNRs or paclitaxel-encapsulated nanoparticles followed. Interestingly, these studies demonstrated a significantly prolonged blood circulation time of the nanoparticles, an increased tumor uptake and an improved tumor treatment efficacy using the paclitaxel-encapsulated nanoparticles<sup>436-438</sup>. However, Sun, et al demonstrated that the extent of tumor uptake enhancement was not as large as the extent to which the liver and spleen uptake decreased. Therefore, they suggested that the lipids released by destabilized liposomes could potentially influence the tumor microenvironment and the biological identity of the nanomaterials<sup>437</sup>. A more aggressive approach is the pre-injection of dichloromethylene-bisphosphonate or clodronate-encapsulated liposomes, which trigger macrophage apoptosis<sup>439-441</sup>. Similarly, gadolinium chloride suppresses the phagocytic activity and promotes macrophage elimination<sup>442</sup>. Comparably to macrophage saturation, these studies reported an increased blood circulation time and an improved tumor accumulation of their respective NPs, resulting in an inhibited tumor growth. However, macrophages play an important role in the innate immune response. Inhibition of these cells may affect the integrity of the immune system and could possibly lead to an increased susceptibility to infection. Therefore, although blocking the RES system through macrophage saturation or depletion shows promising results, further research is essential regarding the safety of such approaches<sup>443</sup>.

### 7.3 Safety evaluation

The accurate safety evaluation of nanomedicine is an important key point for their translation to the clinic. Acute toxicity of nanomedicine compounds is usually related to complement activation, inflammation, hemolysis and/or oxidative stress<sup>444</sup>. This was confirmed by Senguputa, et al demonstrating a dose-dependent acute increase in white blood cell count and red blood cell count 6-72 hours after IV injection (1-2-10 mg/kg) of 50 nm citrate-stabilized AuNPs<sup>445</sup>. In addition, IV injection of 13 nm PEGylated AuNPs (4.26 mg/kg) causes inflammation and cell death in the liver of healthy mice 5 minutes and one week after administration<sup>446</sup>. Similarly, transient pathological abnormalities and increased expression of inflammatory cytokines are observed in the liver, spleen and kidney, one day after intraperitoneal injection of differently sized AuNPs (5-170 µg/kg) in rats and mice<sup>447-450</sup>. In contrast, other studies showed no signs of *in vivo* AuNP toxicity at all<sup>405,451-455</sup>. The conflicting results in literature clearly illustrate that drawing conclusions on AuNP safety is a complicated matter due to the great variety in AuNP design, which strongly determines the *in vivo* fate, behavior and performance. In general, AuNPs with a small size, spherical shape and a positive surface charge are considered more likely to induce hazardous effects than large, rod-shaped and negatively charged AuNPs. This is due to the extravasation into normal tissues, the high reactivity related to the large surface area-to-volume ratio, and the

extensive interactions and uptake in the cells <sup>456-459</sup>. Furthermore, the surface stabilizing agents also exhibit a significant impact on the toxicity profile of the AuNPs. A well-known example is CTAB, the most common and convenient surfactant for the synthesis and stabilization of AuNRs, but with a high cytotoxicity <sup>460</sup>. Besides the high variety in AuNP parameters, the differences in the experimental design, such as the administered doses, the administration mode, single or multiple injections, the evaluation at certain time points after injection and the type of assays make it difficult to compare results between studies <sup>461</sup>.

Another important aspect to take into account during the safety evaluation of AuNPs is the high stability and the low biodegradability of the inorganic AuNPs. After sequestration by the RES organs, AuNPs can persist in RES macrophages up to 6 months after administration <sup>462</sup>. As a result, this long-term AuNP exposure raises concerns about potential delayed or chronic toxicological effects. The long-term studies in literature usually consider a follow-up of 30 to 90 days after injection. Here again, conflicting results were found. For instance, Senguputa, et al demonstrated significant histo-pathological changes, such as nuclear infiltration, nuclear proliferation and loss in structural integrity in the liver, kidneys, lungs, spleen and testis of mice that received daily intraperitoneal injections of 50 nm AuNPs for 30, 60 and 90 days (1-2 mg/kg). Furthermore, after 30 days, they observed a strongly increased white blood cell count <sup>445</sup>. A single intravenous injection of pentapeptide CALNN-coated AuNPs (0.7 mg/kg) caused spleen atrophy and hematological findings indicating anaemia in rats at 28 days post-injection <sup>463</sup>. In contrast, a single intravenous injection of 2, 5 or 10 nm AuNPs (1.25 mg/kg) in mice were found to be non-toxic in terms of inflammatory responses, histopathological changes, blood and serum biochemistry or any physiological aspects for a period of 90 days <sup>451</sup>. Similarly, accumulation of gold in tissues after weekly repeated administrations of 14 nm AuNPs (90 µg) during 7 weeks caused no observable overt toxicity, kidney or liver damage <sup>454</sup>. Interestingly, one study assessed the toxicity of AuroShell particles, which are currently under clinical investigation to ablate prostate cancers (**Table 1.4**). The safety of the gold-silica nanoshells after a single IV infusion of clinically expected doses was evaluated in mice, rats and dogs for time durations of up to 404 days. Apart from brown-black pigmentation in the macrophages of the liver and spleen and in the medulla of the lymph nodes, no other clinically relevant signs of toxicity were observed according to histopathology, blood chemistry, hematology, urinalysis, electrocardiography, ophthalmology, body weights, and general health of the animals <sup>405</sup>. Promising results regarding the toxicity of gold-silica nanoshells was also demonstrated in 22 human prostate cancer patients. In fact, an intravenous infusion of 35 mg/kg AuNPs was not associated with any adverse effects regarding clinical symptoms, chemical analysis, hematological analysis, immunological analysis, and urinalysis at 2, 8, 15, 30, 60, 90, 120, 150, and 180 days post-infusion <sup>404</sup>. In another clinical study, a functional follow-up was performed at one and five years after implantation of silica-gold NPs in a bioengineered on-artery patch and photo-thermal therapy of atherosclerotic plaques. At both time points, the authors did not observe



detrimental effects regarding biochemical serum analysis (e.g. plasma concentrations of hemoglobin, cholesterol, glucose, creatinine, etc.)<sup>409</sup>. Nevertheless, the pre-clinical GLP-certified *in vivo* study demonstrated that after more than 1 year, the quantity of gold in the liver and spleen of the mice and dogs were similar to the initial infused dose of silica-gold nanoshells, which indicated that the body was unable to break down the particles. This raises the concern that AuNPs that are too large to be eliminated via standard excretion pathways could perhaps reside permanently inside the body<sup>405</sup>.

### 7.4 Tumor biology and translatability

Other important challenges impeding tumor accumulation that AuNPs encounter, besides fast clearance, protein corona formation or RES sequestration, are related to the tumor and tumor environment. For instance, the Starling forces are usually disrupted in tumor tissues, which can counteract the efficiency of the EPR effect. The immature and permeable vasculature at the tumor site allows small and large solutes to diffuse freely from the blood vessels to the tumor tissue, reducing the high intravascular osmotic pressure. Furthermore, the poor lymphatic drainage at the tumor site elevates the interstitial tumor pressure, approaching the intra-arterial pressure<sup>464</sup>. As a result, the extravasation of the NPs depends more on encountering and diffusion through the fenestrae into the tumor than on convective transport. Once extravasated, nanoparticles might be impaired in their intratumoral diffusion due to the high interstitial tumor pressure, the dense ECM and tightly packed cells, pushing the nanoparticles toward the tumor's periphery. In addition, tumors exhibit an uneven distribution of blood vessels, which results in inaccessible tumor regions. As a result, the distribution of AuNPs is highly heterogeneous, concentrated around the tumor blood vessels, rather than reaching internal tumor cells<sup>47</sup>.

Another potential reason for the poor translation of promising AuNPs to the clinic is the limited translatability between animal models and clinical patients. In fact, animal tumors differ from human tumors. The tumor growth rate has a substantial impact on the tissue organization. The limited amount of time in pre-clinical studies asks for the inoculation of xenografted human tumor cells, which develop quickly. As a result, angiogenesis rapidly follows, resulting in a more profound disorganization of the tumor vasculature than in human tumors, which usually grow at a slower pace. This could overestimate the EPR effect. Furthermore, the xenografted tumor size can increase up to 10% of the animal's body weight before treatment is administered. Consequently, it is more likely that AuNPs will encounter the xenografted tumor while circulating through the vasculature as compared to a clinical tumor, which might comprise approximately 0.005% of the human body weight. Furthermore, AuNPs holding a targeting agent that is specifically directed against a human cancer antigen is more likely to bind to the human xenografted tumor cells than to normal animal cells. Besides the above described differences in tumor biology between pre-clinical *in vivo* models and human patients, a substantial tumor heterogeneity between patients

exists as well, decreasing the predictability of the patient response and requiring a personalized approach <sup>47</sup>. It should be noted that many of these challenges are also applicable for the delivery of other anti-cancer drugs.

## 7.5 Regulatory challenges

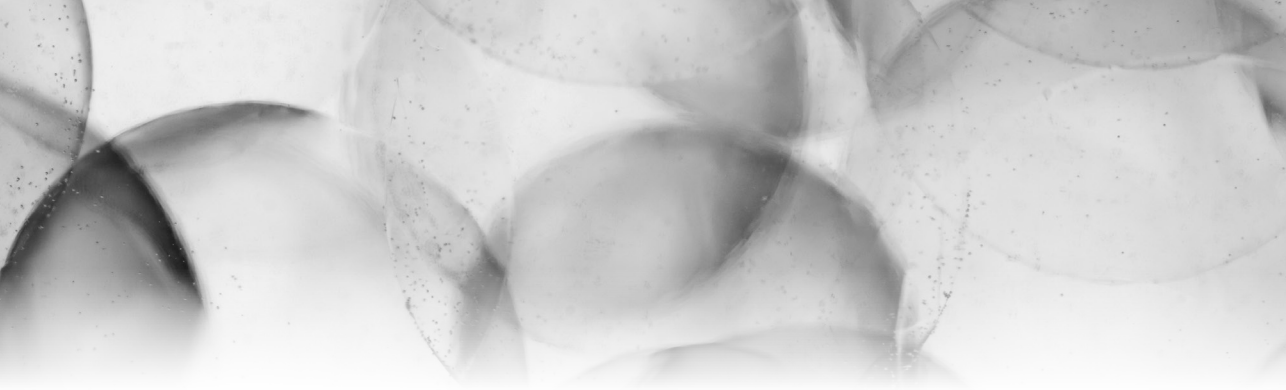
Next to the various biological challenges described above, the slow pace of clinical translation of nanomedicine also depends on certain technological and regulatory hurdles. For instance, the amount of nanomaterials required for pre-clinical studies is small. In order to proceed to clinical studies, large-scale production is needed. This requires a demanding chemistry, manufacturing, and control process, with proper quality standards and a strict analysis of reproducibility on a batch-to-batch basis. In addition, due to the complex and diverse nature of nanomedicine, regulatory decisions to obtain market authorization of nanotherapeutics and their follow-on products are based on individual case-by-case analyses, which is a complex and time-consuming process <sup>465,466</sup>. Therefore, regulatory bodies have recognized the importance to establish clear guidelines and recommendations for medicinal products containing nanomaterials. Currently, the European Medicines Agency (EMA) released reflection papers regarding IV iron-based nano-colloidal products <sup>467</sup>, IV liposomal products <sup>468</sup>, the development of block-copolymer-micelle medicinal products <sup>469</sup> and surface coatings <sup>470</sup>.



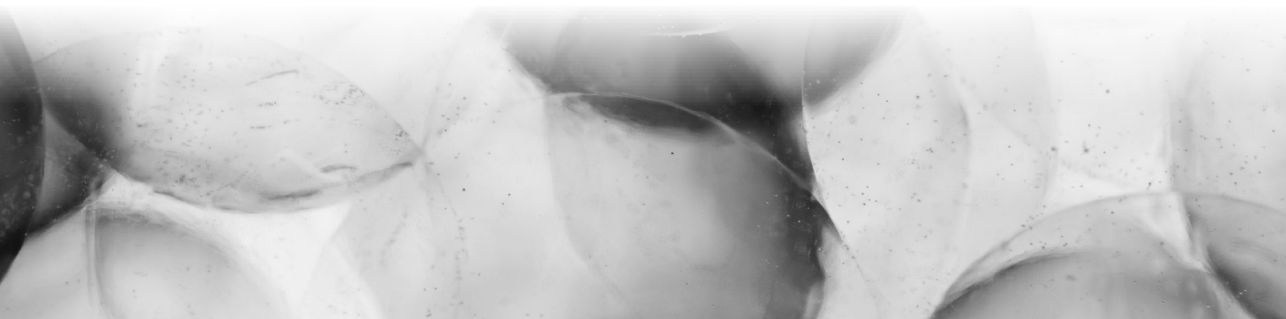
# 2

**CHAPTER**





## Aim and outline of the thesis



The literature discussed in the introduction gives a broad overview on the promising potentials of AuNPs to facilitate cancer diagnosis and enhance the efficacy of cancer therapy, including EBRT and targeted radionuclide therapy (TRT). However, it is also clear that the strong variety in AuNP design, such as the size, shape, zeta potential, coating, functionalization, etc. has a considerable impact on the effects of AuNPs *in vitro* and *in vivo*, determining the biological response and outcome. The research included in this thesis aims to evaluate the *in vitro* cytotoxicity and the *in vivo* fate of unique poly-allylamine coated, Cetuximab-conjugated gold nanoparticles (AuNPs-PAA-Ctxb). Furthermore, the thesis describes the radiolabeling of AuNPs-PAA-Ctxb in order to investigate their potential as radiosensitizing agents in TRT.

The AuNPs-PAA used in this work are produced by means of plasma vapor deposition (PVD)<sup>2</sup>. This technique uses a vacuum chamber filled with argon gas and is equipped with two magnetron sputtering cathodes, one mounted with NaCl and the other with 99.99% gold. The application of an electric field generates a gaseous plasma condition ionizing the argon atoms. Then, the Ar ions accelerate from the plasma to the cathode and eject atoms from the target material, which in turn are deposited on the substrate (**Figure 2.1A**). Typically, one cycle includes a single layer of NaCl deposition, followed by the deposition of a discontinuous layer of gold and eventually ends with the poly-allylamine modification of the AuNP surface, achieved through the plasma polymerization of the monomer. Repeating this cycle results in the generation of multi-layered samples (**Figure 2.1B**). The NaCl layers are dissolved in water-based solutions, obtaining a suspension of AuNPs-PAA<sup>471</sup>. Polyelectrolytic PAA has a hydrophilic character and a coating of at least 1.7 nm is required to stabilize the AuNPs in suspension<sup>472</sup>. The PVD synthesis method allows the AuNP production process and surface coating to occur in one step, which results in a good adhesion of the coating to the AuNPs, provides a good control over the AuNP size and coating thickness, and offers a high production rate.

---

<sup>2</sup> PVD was performed at l'Unité de Recherche Laboratoire d'Analyse par Reaction Nucléaire (LARN), University of Namur.

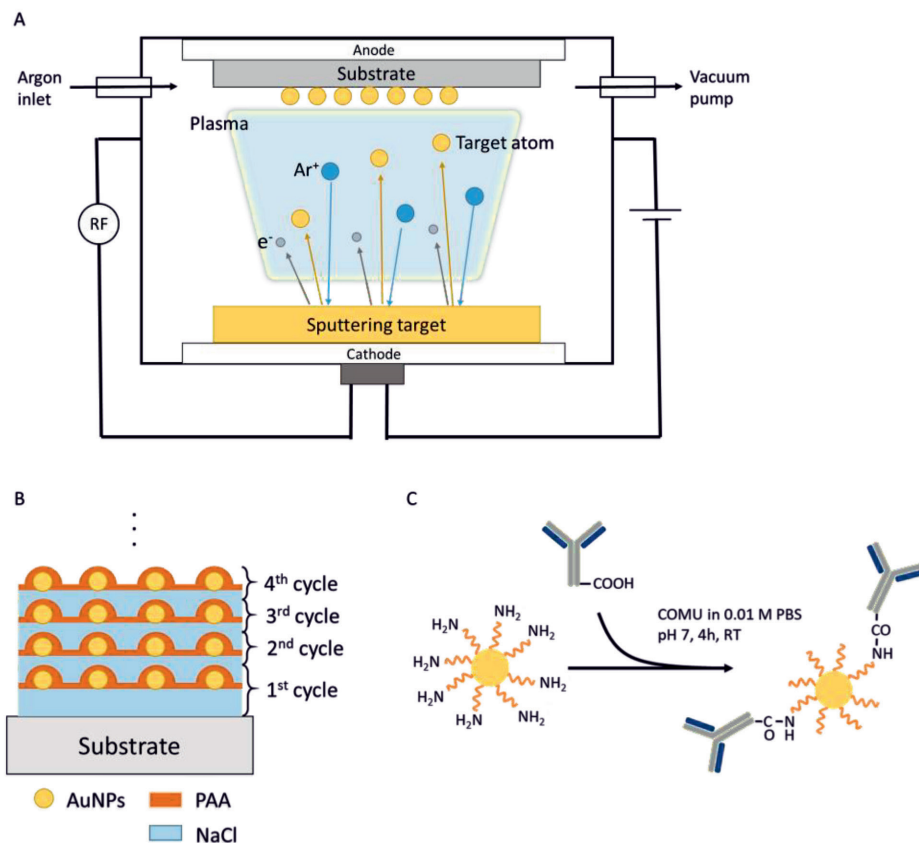


**Figure 2.1** A schematic representation of (A) the plasma vapor deposition mechanism (adapted from <sup>473</sup>), (B) the repeating deposition cycles to produce AuNPs-PAA, obtaining a multilayered sample and (C) antibody-conjugated, PAA-coated AuNPs (adapted from <sup>472,474</sup>).

**Abbreviations:** AuNPs: gold nanoparticles; Ar<sup>+</sup>: argon ion; e<sup>-</sup>: electron; PAA: polyallyl-amine.

After suspending the AuNPs-PAA in acetate buffer (pH 5), excess of PAA and NaCl is removed by filtration. Subsequently, the AuNPs-PAA are conjugated to the antibody Cetuximab (Ct<sub>xb</sub>) in the presence of the coupling reagent, COMU<sup>3</sup>. COMU activates the carboxylic acid groups of Ct<sub>xb</sub>, promoting the formation of an amide bond with the amino groups of the external PAA coating on the AuNPs (**Figure 2.1C**) <sup>472</sup>. Following removal of COMU and unreacted Ct<sub>xb</sub> by filtration, AuNPs-PAA and AuNPs-PAA-Ct<sub>xb</sub> are freeze-dried in order to improve long-term storage and colloid stability. For this purpose, 3% of arabic gum is added to the AuNPs-PAA and AuNPs-PAA-Ct<sub>xb</sub> as stabilizer and cryoprotectant.

<sup>3</sup> 1-Cyano-2-ethoxy-2-oxoethylidenaminooxy)dimethylamino-morpholino-carbenium hexafluorophosphate

Ctxb is a human-mouse chimeric monoclonal antibody and is directed against the accessible extracellular domain of the epidermal growth factor receptor (EGFR) or the HER1 receptor. EGFR is a member of the ErbB family of tyrosine kinase receptors, including four receptor subtypes (HER1 to HER4). When inactive, EGFR is a monomer. Upon interaction with the epidermal growth factor (EGF) or the transforming growth factor- $\alpha$  (TGF- $\alpha$ ), EGFR forms a homodimer or a heterodimer with another member of the ErbB family. Dimerization activates the intracellular tyrosine kinase region of the EGFR, causing autophosphorylation and initiation of the downstream pathway. Eventually it results in the transcription of genes stimulating cell proliferation, survival, migration and angiogenesis<sup>475,476</sup>. Since sustained proliferation and survival of cells, metastasis and angiogenesis are all hallmarks of cancer, the ErbB receptors are considered as proto-oncogenes. In fact, the overexpression of EGFR is observed in a wide range of cancer types. Examples include lung cancer, colorectal cancer, head-and neck cancers, glioblastoma, breast cancer, prostate cancer, ovarian cancer and renal cancer<sup>477,478</sup>. Currently, Ctxb is used to treat advanced metastatic colorectal cancer or squamous-cell head-and-neck cancer as a monotherapy or in combination with chemotherapy or radiotherapy<sup>475,476</sup>. Ctxb prevents endogenous ligand binding to EGFR and sterically inhibits the EGFR dimerization. Furthermore, internalization of the Ctxb/EGFR complex withstands the low pH environment of the endosome, resulting in the lysosomal degradation of the complex, instead of receptor recycling, which happens after internalization of EGF/EGFR complexes. As a result, EGFR expression is downregulated and the receptor-dependent signal transduction pathways are blocked. An additional mechanism of action is the antibody-dependent cellular cytotoxicity, in which the Fc region of Ctxb recruits immune cells to destroy the tumor cells<sup>479</sup>. Although Ctxb has its own anti-cancer properties, in this research, Ctxb is primarily conjugated to the AuNPs to act as a targeting vector, promoting the interaction of the AuNPs to the EGFR-overexpressing cancer cells.

Intravenous injection of AuNPs is a realistic exposure scenario when used as nanomedicine in a clinical setting. However, such a systemic administration leads to the inevitable exposure of healthy cells and tissues to AuNPs. The first cells that encounter the injected AuNPs are the endothelial cells, lining the inner walls of the vasculature and responsible for the exchange of oxygen, nutrients and waste products with the tissues. Furthermore, AuNPs are prone to sequestration by the reticuloendothelial system (RES), while both the hepatobiliary system and the renal system are potential elimination routes to remove AuNPs from the body. AuNPs-PAA-Ctxb have previously been shown to specifically bind cancer cells overexpressing EGFR in comparison to EGFR negative cells, with an *in vivo* biodistribution profile similar to that of unconjugated Ctxb<sup>360,474</sup>. However, the effects on healthy cells have not yet been investigated before.

Furthermore, AuNPs-PAA-Ctxb were previously shown to enhance the efficiency of proton therapy in the EGFR-overexpressing A431 cancer cells<sup>201</sup>. It has been suggested that the radiosensitization mechanism of AuNPs does not solely depend on the physical interactions

of the AuNPs with the radiation. Instead, there is a growing interest in the biological effects of AuNPs as radiosensitization mechanism<sup>177</sup>. In addition, since AuNPs are interesting platforms to hold multiple radionuclides, it would be interesting to investigate the potential of our targeted AuNPs-PAA-Ctxb to sensitize cancer cells to TRT. For this purpose, <sup>177</sup>Lu is a promising radionuclide thanks to its physical half-life of 6.67 days, which is compatible with the biological half-life of antibodies. Furthermore, the mean tissue penetration range of the  $\beta^-$  particles is proficient to eradicate small, residual tumors with a minimized damage to the surrounding healthy tissue, while the emission of low-energy gamma photons enables SPECT imaging<sup>480</sup>.

Therefore, **the aim of this thesis** is to evaluate the biological toxicity effects of the AuNPs-PAA and AuNPs-PAA-Ctxb in normal healthy cells and tissues, and to assess the potential of <sup>177</sup>Lu-radiolabeled AuNPs-PAA-Ctxb as a radiopharmaceutical and radiosensitizing agent:

In the first part of this thesis (**Chapter 3**), normal human kidney (HK-2) cells, human liver (THLE-2) cells and human microvascular endothelial (TIME) cells are exposed to AuNPs-PAA and AuNPs-PAA-Ctxb. The mechanism of AuNP cytotoxicity is unraveled by investigating the cellular uptake of the nanoparticles and their effects on cell viability, apoptosis, mitochondrial function and the antioxidant defense system. In addition, the role of oxidative stress is revealed by assessing the protective effects of the antioxidant N-acetyl L-cysteine.

In the next chapter (**Chapter 4**), the pharmacokinetics and the biodistribution of AuNPs-PAA-Ctxb is evaluated in healthy mice, upto 6 months after IV injection. AuNPs-PAA-Ctxb are prone to rapid sequestration by the RES. Therefore, we assessed the potential liver damage by evaluating the serum activity of several liver enzymes. In addition, since the *in vitro* study demonstrated that endothelial cells are particularly sensitive to the effects of AuNPs-PAA-Ctxb, we measured the serum levels of specific cytokines related to endothelial cell activation. Furthermore, possible inflammatory response was also assessed by measuring the serum levels of cytokines related to the immune response. Finally, we evaluated the morphological appearance of the liver, spleen, kidney and lungs.

In the last part, since we demonstrated that AuNPs-PAA-Ctxb inhibit the antioxidant system, induce oxidative stress and cause mitochondrial dysfunction in cells (Chapter 3), we hypothesized that these biological effects could sensitize cancer cells to TRT. Therefore, in **Chapter 5**, we optimized the radiolabeling of AuNPs-PAA-Ctxb with <sup>177</sup>Lu and evaluated the binding and specificity of the radiolabeled nanoconjugate *in vitro*. This chapter also describes the future research required to test our hypothesis and to demonstrate the potential of the radiolabeled AuNPs-PAA-Ctxb to be used as a radiopharmaceutical *in vivo*.

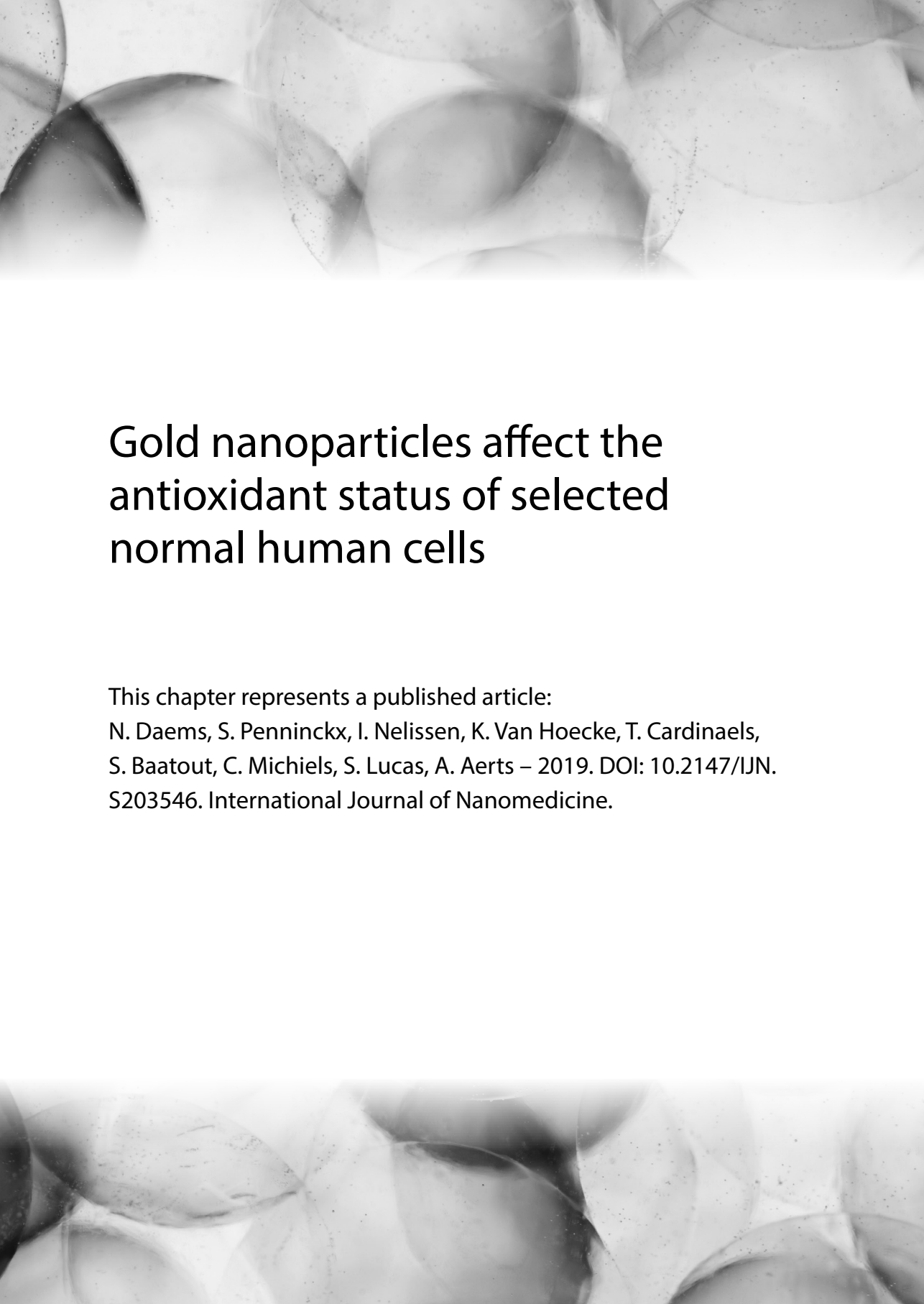




# 3

**CHAPTER**





# Gold nanoparticles affect the antioxidant status of selected normal human cells

This chapter represents a published article:

N. Daems, S. Penninckx, I. Nelissen, K. Van Hoecke, T. Cardinaels, S. Baatout, C. Michiels, S. Lucas, A. Aerts – 2019. DOI: 10.2147/IJN.S203546. International Journal of Nanomedicine.

## 1. Abstract

**Purpose:** This study evaluates the cytotoxicity of AuNPs coated with polyallylamine (AuNPs-PAA) and conjugated or not to the epidermal growth factor receptor (EGFR)-targeting antibody Cetuximab (AuNPs-PAA-Ctxb) in normal human kidney (HK-2), liver (THLE-2) and microvascular endothelial (TIME) cells, and compares it with two cancer cell lines that are EGFR-overexpressing (A431) or EGFR-negative (MDA-MB-453).

**Results:** Conjugation of Cetuximab to AuNPs-PAA increased the AuNPs-PAA-Ctxb interactions with cells, but reduced their cytotoxicity. TIME cells exhibited the strongest reduction in viability after exposure to AuNPs-PAA( $\pm$ Ctxb), followed by THLE-2, MDA-MB-453, HK-2 and A431 cells. This cell type-dependent sensitivity was strongly correlated to the inhibition of thioredoxin reductase (TrxR) and glutathione reductase (GR), and to the depolarization of the mitochondrial membrane potential. Both are suggested to initiate apoptosis, which was indeed detected in a concentration- and time-dependent manner. The role of oxidative stress in AuNPs-PAA( $\pm$ Ctxb)-induced cytotoxicity was demonstrated by coincubation of the cells with N-acetyl L-cysteine (NAC), which significantly decreased apoptosis and mitochondrial membrane depolarization.

**Conclusion:** This study helps to identify the cells and tissues that could be sensitive to AuNPs and deepens the understanding of the risks associated with the use of AuNPs *in vivo*.

## 2. Introduction

In order to improve cancer detection and therapy efficiency, gold nanoparticles (AuNPs) are emerging as promising contrast agents, drug delivery vehicles, photo-thermal agents and radiosensitizers <sup>22,169,186,202,481-485</sup>. Functional surface modifications are typically applied to actively target the cancer cells <sup>486-489</sup>. In our team, 5 nm AuNPs are synthesized and coated with organic polyallylamine (AuNPs-PAA) by plasma vapor deposition. AuNPs-PAA are subsequently conjugated to Cetuximab (AuNPs-PAA-Ctxb), a commercially available antibody targeting the epidermal growth factor receptor (EGFR), which is overexpressed in numerous tumor types <sup>471</sup>. The resulting nanoconjugates are able to selectively target EGFR-overexpressing cancer cells *in vitro* and *in vivo*, and exhibit an *in vivo* pharmacokinetic profile similar to that of unconjugated Cetuximab. However, the reticuloendothelial system (RES) in the liver and spleen rapidly sequesters AuNPs-PAA-Ctxb <sup>360,474</sup>. This phenomenon has been demonstrated by several other *in vivo* biodistribution studies and is the main reason why clinical success of AuNPs remains, in general, elusive <sup>360,490-495</sup>. In addition, accumulation of AuNPs-PAA-Ctxb and other AuNPs has been demonstrated in the kidneys, which are particularly sensitive to xenobiotics due to their high degree of vascularization and their ability to concentrate toxins <sup>360,451,455,474,490,496,497</sup>. In conclusion, since AuNPs accumulate in several non-target organs *in vivo*, it is essential to assess the potential toxicity of AuNPs in these healthy cells and tissues before AuNPs can be used in a clinical setting <sup>498</sup>.

Due to their small size, nanoparticles generally exhibit different characteristics and have a higher reactivity compared to their bulk counterparts. Various studies have reported that AuNPs are able to induce formation of reactive oxygen species (ROS) in cells, which would be the major cause of cellular damage, genotoxicity and cell death <sup>253,499,500</sup>. In addition, abnormalities in tissue morphology of the kidney, the liver and the spleen and a minor increase in lung inflammation were detected in rodents after exposure to AuNPs <sup>497,501-504</sup>. However, these findings contradict to those of other research groups that have demonstrated that AuNPs exhibit no toxic health effects at all *in vitro* and *in vivo* <sup>505-507</sup>. These conflicting results in the literature indicate that it is difficult to predict the toxicity of AuNPs in different biological systems, and that this depends strongly on their physicochemical properties including particle size, shape, surface coating, surface charge and adsorbed protein corona <sup>506,508-512</sup>.

In this study, we characterized our in-house produced AuNPs-PAA and AuNPs-PAA-Ctxb in terms of their size and surface charge. Furthermore, we evaluated and compared the cellular uptake and cytotoxic effects of the AuNPs-PAA and AuNPs-PAA-Ctxb on human microvascular endothelial (TIME) cells, human proximal tubular kidney (HK-2) cells and human liver (THLE-2) cells. These three cell types were chosen because they originate from normal human primary cells, retaining their phenotypic and functional characteristics. Furthermore, since these cell types are exposed to a significant amount of AuNPs *in vivo*, they are suitable *in*

*vitro* models for the estimation and understanding of the nanoparticle toxicity on human health, such as vascular toxicity, nephrotoxicity and hepatotoxicity<sup>360,490-495</sup>. Indeed, microvascular endothelial cells are the first cells to encounter the AuNPs after intravenous injections and are responsible for the transport and exchange of the AuNPs from the bloodstream to the tissues. Renal tubular cells are exposed to AuNPs after their filtration through the glomerular capillary wall during renal excretion. Finally, although Kupffer cells in the liver have a high phagocytic capacity to sequester AuNPs, the hepatocytes are part of the hepatobiliary system, which represents an important pathway for nanoparticle processing and thus forms a potential site for toxicity<sup>513</sup>. In addition to these non-cancerous cell types, EGFR-overexpressing A431 cells and EGFR-negative MDA-MB-453 cancer cell lines were used as positive and negative controls, respectively, for antibody targeting. Cytotoxicity was assessed by following the number of viable cells and measuring the mitochondrial membrane potential, the thioredoxin reductase and glutathione reductase activity, and the extent of apoptotic cell death. In order to explore the role of oxidative stress, the possible protective effect of N-acetyl L-cysteine (NAC) was studied. If a situation applies for both AuNPs-PAA and AuNPs-PAA-Ctxb, we will refer to them as AuNPs-PAA( $\pm$ Ctxb) in the remainder of the chapter. This work contributes to a better estimation of the potential negative effects of therapeutic AuNPs formulations on human health.

### 3. Materials and methods

#### 3.1 Chemicals

Polyallylamine, (1-Cyano-2-ethoxy-2-oxoethylidenaminoxy) dimethylamino-morpholino-carbenium hexafluorophosphate (COMU), Arabic gum, NAC, CellTiter M, the bicinchoninic acid (BCA) protein assay kit, the Thioredoxin reductase assay kit, bovine serum albumin (BSA), non-fat dry milk, phosphatase inhibitor tablets (PhosStop) and the Complete Mini EDTA-free Protease Inhibitor Cocktail were purchased from Sigma-Aldrich (Diegem, Belgium). Cetuximab (Erbix<sup>®</sup> 5 mg/ml) was kindly provided by the Sint-Dimpna Hospital (Geel, Belgium). Vivaspin<sup>®</sup> centrifugal concentrators and cacodylate buffer were obtained from Merck (Overijse, Belgium). All cell lines, the Microvascular Endothelial Cell Growth Kit-VEGF and EGF were obtained from ATCC (Molsheim Cedex, France). Fetal bovine serum (FBS), Dulbecco's modified Eagle's medium (DMEM), DMEM:F12, phosphate buffered saline (PBS) tablets and penicillin-streptomycin were purchased from Gibco (Aalst, Belgium). The BEGM Bullet Kit was received from Lonza (Verviers, Belgium). The CellTiter 96 Aqueous One Solution Cell Proliferation Assay was purchased from Promega (Leiden, The Netherlands). The IncuCyte Caspase 3/7 Green Reagent and the IncuCyte Annexin V Red Reagent were obtained from Essen BioScience (Hertfordshire, UK). TGX Stain-free Precast Protein Gels, Trans-Blot Turbo Mini Nitrocellulose Transfer Packs and the Clarity Western ECL substrate kit were provided by Bio-Rad Laboratories (Temse, Belgium). The rabbit anti-EGFR antibody was purchased from Cell Signaling Technology (Leiden, The Netherlands). The mouse anti- $\beta$  actin

antibody was purchased from Santa Cruz Biotechnology (Heidelberg, Germany). HRP-labeled goat anti-rabbit antibody, goat-anti mouse antibody and tetramethylrhodamine, methyl ester, perchlorate (TMRM) were obtained from Invitrogen (Merelbeke, Belgium). Glutaraldehyde and osmic acid were received from Agar Scientific (Essex, UK). The Eponate 12 Embedding Kit with BDMA was purchased from Ted Pella (Paris, France). The Glutathione Reductase Assay kit was obtained from Abcam (Cambridge, UK). Nitric acid ( $\text{HNO}_3$ ), hydrochloric acid (HCl), hydrogen peroxide ( $\text{H}_2\text{O}_2$ ) and hydrofluoric acid (HF) were of trace metal grade and purchased from Fisher Scientific (Merelbeke, Belgium). SPEX Certiprep certified standard solutions (Boom B.V., Meppel, The Netherlands) were used to prepare the calibration standards and internal standards.

### 3.2 Production of AuNPs-PAA and Cetuximab conjugation

The AuNPs were produced and coated with PAA by physical plasma vapor deposition as described previously<sup>471</sup>. The resulting PAA-coated AuNPs (AuNPs-PAA) were dispersed in acetate buffer (pH 5) under pulsed sonication (50W, 30 kHz, 20% amplitude, 0.5 sec pulses), and were subsequently purified from excess PAA and NaCl by filtration in a centrifugal filter unit with a molecular cut-off of 10 kDa. Cetuximab was purified by filtration in a centrifugal filter unit with a molecular cut-off of 10 kDa, after which it was lyophilized (LABCONCO, Osterode, Germany). Lyophilized Cetuximab and COMU were dissolved in 0.01 M PBS to a concentration of 1 mg/ml and 1.5 mg/ml, respectively. The Cetuximab and COMU solutions were mixed and the pH was adjusted to 7 with 0.1 M HCl. Then, the AuNPs-PAA were added to the Cetuximab-COMU mixture to achieve a final concentration of 0.24 mg/ml, 0.43 mg/ml and 0.17 mg/ml of Cetuximab, COMU and gold, respectively. The mixture was stirred for 4h at room temperature, after which it was purified with a centrifugal filter unit with a molecular cut-off of 300 kDa. The AuNPs-PAA-Ctxb were lyophilized for long-term storage after the addition of 3% arabic gum as stabilizer, which also causes steric repulsion between the nanoparticles when they are re-suspended after the freeze-drying process.

### 3.3 Nanoparticle characterization (Zeta potential and size distribution)

Lyophilized AuNPs-PAA( $\pm$ Ctxb) were dispersed in Class 1 water, DMEM or DMEM with 10% (v/v) FBS to a gold concentration of 80  $\mu\text{g/ml}$ . The size distribution of the nanoparticles was characterized by means of CPS Disc Centrifugation (Benelux Scientific, Eke, Belgium). A rotational speed of 22 000r.p.m., a sucrose density gradient of 2–8% with a fluid density of 1.017 g/ml and a refractive index of 1.341 were employed. The measurement range of the instrument was set from 3.5 nm to 50  $\mu\text{m}$ . The particle density was set to 10.05 g/ml and the particle refractive index to 0.47. Each measurement was calibrated with certified PVC microparticles provided by CPS Instruments, having a peak diameter of 0.263  $\mu\text{m}$  and a particle density of 1.386 g/ml. The peak particle sizes and the 5<sup>th</sup> and 95<sup>th</sup> percentiles were extracted from relative number size distributions. The zeta potential was determined with

the Nanosizer Nano ZSP (Malvern P analytical, Brussels, Belgium) with a temperature equilibration time of 2 min at 25°C. A dispersant refractive index of 1.330, a viscosity of 0.8872 cP and a dispersant dielectric constant of 78.5 were used. UV-Vis spectra were recorded on the CLARIOstar microplate reader (BMS Labtech, De Meern, Netherlands). Conjugation of Cetuximab to AuNPs-PAA was also confirmed by SDS-PAGE. 10 µg of Cetuximab, Cetuximab + AuNPs-PAA and AuNPs-PAA-Ctxb were loaded on a TGX Stain-free Precast Protein Gel. Migrated Cetuximab was detected with UV light by using the Fusion FX Imager (Vilber Lourmat, Eberhardzell, Germany).

### 3.4 Cell culture

A431 cells and MDA-MB-453 cells were grown in DMEM High Glucose medium. HK-2 cells were grown in DMEM:F12 High Glucose medium. TIME cells were grown in Vascular Cell Basal Medium supplemented with the Microvascular Endothelial Cell Growth Kit-VEGF. Finally, THLE-2 cells were cultured by using the BEGM Bullet kit without gentamycin/amphotericin and epinephrine, but supplemented with 5 ng/ml EGF. All the cultured cells were supplemented with 10% FBS and 100 u/ml penicillin-streptomycin and were maintained in a humidified 37°C incubator with 5% CO<sub>2</sub>.

### 3.5 MTS viability assay

The cell viability after exposure to AuNPs-PAA(±Ctxb) was tested with the CellTiter 96 AQueous One Solution Cell Proliferation Assay. Cells were seeded into a 96-well plate (25 000 cells/cm<sup>2</sup> for HK-2 and TIME cells; 28 125 cells/cm<sup>2</sup> for A431 cells; 31 250 cells/cm<sup>2</sup> for THLE-2 cells; and 43 750 cells/cm<sup>2</sup> for MDA-MB-453 cells). After 24h, the medium was replaced by fresh medium containing increasing concentrations of nanoparticles (1.56-50.00 µg Au/ml) for incubation periods of 3h or 24h. After the exposure period, the medium was discarded and cells were washed twice with DMEM + 10% FBS to avoid the interference of the AuNPs at 490 nm. The MTS reagent, prepared according to the manufacturer's instructions, was added to the cells. The plate was incubated at 37°C for 1.5h and the absorbance was measured at 490 nm with the CLARIOstar microplate reader (BMS Labtech, De Meern, Netherlands). The cell viability was calculated as the ratio of the absorbance of the sample well to the average of the unexposed control wells, after subtraction of the background signal of wells that contained AuNPs-PAA(±Ctxb) but no cells. The results, expressed as percentages, were obtained from at least three independent experiments with a minimum of three replicates per condition. Curve fitting of the concentration-response data was performed with Origin 2017 software, by using a log-logistic function and a modified log-logistic function (**Equation S3.1** and **Equation S3.2**, respectively).

### 3.6 Live cell imaging

The effect of AuNPs-PAA(±Ctxb) on cell apoptosis was investigated by recording time-lapse images of the cells every 2h during 3 days with the IncuCyte ZOOM system (Essen BioScience,

Hertfordshire, UK). Approximately 15 000-45 000 cells/cm<sup>2</sup> were seeded into 96-well plates. After 24h, the medium was replaced by fresh medium containing increasing concentrations of nanoparticles (1.56-50.00 µg Au/ml). To assess the presence of oxidative stress, cells were also co-incubated with 2 nM NAC. The IncuCyte Caspase 3/7 Green Reagent and the IncuCyte Annexin V Red Reagent were added to the cell media to monitor apoptosis according to the manufacturer's instructions<sup>514,515</sup>. Built-in software was used to analyze the images in order to generate the annexin V and caspase 3/7 area data (µm<sup>2</sup>/well), which was normalized to cell confluency data (%). The results were obtained from at least three replicates per condition.

### 3.7 Western blot analysis

To determine EGFR expression, cells were cultured in T25 flasks until 80% confluency. Briefly, cells were rinsed with ice cold PBS and lysed with lysis buffer (20 mM Tris, 150 mM NaCl, 1 mM EDTA, 1 mM EGTA, 1% sodium deoxycholate, 1% Nonidet P40, 10% glycerol, pH 7.5) containing a protease and phosphatase inhibitor tablet. The protein concentrations were quantified with the BCA kit according to the manufacturer's instructions. 15 µg of proteins were separated on a 4TGX Stain-free Precast Protein Gel. After protein transfer onto a nitrocellulose membrane, the membranes were blocked with 5% non-fat dry milk in PBS-0.1% Tween (PBS-T) for 2h at room temperature. Next, membranes were incubated with rabbit anti-EGFR antibody diluted 1:1000 in 5% BSA, or with mouse anti-β-actin antibody diluted 1:5000 in 5% non-fat dry milk, overnight at 4°C. After washing in PBS-T, the membranes were incubated with HRP-labeled goat anti-rabbit antibody diluted 1:10 000 in 5% BSA or HRP-labeled goat anti-mouse antibody diluted 1:50 000 in 5% non-fat dry milk for 1h at room temperature. Protein detection was performed with the Clarity Western ECL substrate kit and the Fusion FX Imager (Vilber Lourmat, Eberhardzell, Germany). Protein bands were quantified with Bio1D analysis software (Vilber Lourmat, Eberhardzell, Germany). The EGFR protein level was normalized to the level of the housekeeping protein, β-actin. The results are expressed as mean EGFR expression relative to the EGFR expression in A431 cells and were obtained from at least 4 independent replicates.

### 3.8 Transmission electron microscopy and energy dispersive x-ray spectroscopy

Transmission electron microscopy (TEM) was used to determine the subcellular localization of the AuNPs-PAA-Ctxb. Approximately 25 000-45 000 cells/cm<sup>2</sup> were seeded in T175 flasks. After 24h, the medium was replaced by fresh medium containing 5.0 µg Au/ml of AuNPs-PAA-Ctxb for incubation periods of 3h or 24h. After the exposure period, the cells were washed twice with DMEM + 10% FBS, once with PBS, and collected by trypsinization. Cells were fixed with 2.5% (w/v) glutaraldehyde in 0.1 M cacodylate buffer (pH 7.4) at 4°C during 2.5h. Next, the cells were washed with 0.2 M cacodylate buffer and subsequently post-fixed in 1% (v/w) osmic acid in 0.1 M cacodylate buffer. Finally, samples were dehydrated by



successive passages in increasing concentrations of ethanol (30%, 50%, 70%, 85% and 100%), and were embedded in resin. Ultra-thin sections for TEM analysis were prepared with an 8800 ultratome III (LKB, Sollentuna, Sweden), after which the cells were visualized with a FEI Tecnai 10 TEM (Thermo Fisher Scientific, Zaventem, Belgium) and iTEM software (Olympus, Soft Imaging Solutions, Muenster, Germany). Energy dispersive X-ray spectroscopy (EDS) was performed on representative cells with the scanning electron microscope JEOL 7500F and Jeol JED2300 software (Jeol Benelux, Zaventem, Belgium).

### 3.9 Inductively coupled plasma mass spectrometry

Inductively coupled plasma mass spectrometry (ICP-MS) was used to quantify the cellular gold content after interaction of AuNPs-PAA( $\pm$ Ctxb) with the cells. Approximately 20 000–40 000 cells/cm<sup>2</sup> were seeded in T25 flasks. After 24h, the medium was replaced by fresh medium containing 5.0  $\mu$ g Au/ml of AuNPs-PAA( $\pm$ Ctxb) for incubation periods of 3h, 6h, 12h or 24h. After exposure, the cells were rinsed twice with DMEM + 10% FBS, once with PBS, and collected by trypsinization. Detached cells were washed twice with DMEM + 10% FBS by successive centrifugation. The cells were counted and re-suspended in 1 ml of Class 1 water. Next, samples were digested with 0.5 ml aqua regia for 2h at 110°C in PFA Savillex® digestion vessels (VWR, Leuven, Belgium). The samples were evaporated to incipient dryness, redissolved in 5% HNO<sub>3</sub> and then exposed to UV light in a 705 UV-digester (Metrohm, Zwijndrecht, Belgium) for 2h. Beforehand, 100  $\mu$ L of 30% H<sub>2</sub>O<sub>2</sub> was added as initiator for the UV digestion. Finally, 0.05% HF was added to reduce Au memory effects. The Au content in the samples was determined with an XSeriesII quadrupole ICP-MS instrument (ThermoFisher Scientific, Bremen, Germany). Data was acquired from 20 ms dwell time per isotope, 200 sweeps per reading, and 5 readings per sample, resulting in 20 s of measurement time per isotope. A rinsing time of 150 s was included between each sample. The elements Re, Ir, Tl were used as internal standards. An external calibration curve based on 0.5 – 1 – 2 – 5 ng/ml of Au standards permitted quantification of the gold content in the samples. The results are expressed as mean pg Au/cell calculated from three replicates per condition obtained from one experiment.

### 3.10 TMRM assay

The effect of AuNPs-PAA( $\pm$ Ctxb) on the mitochondrial membrane potential was assessed by measuring the mitochondrial retention of the TMRM dye. Approximately 25 000 cells/cm<sup>2</sup> were seeded in 24-well plates. After 24h, the medium was replaced by fresh medium containing a non-lethal concentration of nanoparticles (ie 3.0  $\mu$ g Au/ml for TIME cells, and 5.0  $\mu$ g Au/ml for THLE-2 and HK-2 cells) for incubation periods of 30 min, 3h, 6h, 12h or 24h. The non-lethal concentration was estimated on the basis of IncuCyte apoptosis data acquired from cells exposed to AuNPs-PAA. To assess the presence of oxidative stress after 12h of exposure, cells were also co-incubated with 2 nM NAC. After the exposure period, the cells were washed twice with DMEM + 10% FBS, once with PBS, and collected by trypsinization.

Subsequently, cells were re-suspended in full medium containing 100 nM TMRM dye, and incubated for 20 min at 37°C. After centrifugation, cells were re-suspended in PBS, and the TMRM intensity was measured in the FL2-channel of the BD Accuri C6 flow cytometer (BD Biosciences, Erembodegem, Belgium). The relative average TMRM intensity was calculated as the ratio of the TMRM intensity of the sample wells to the average TMRM intensity of the unexposed control wells, after subtraction of the background signal from unlabeled cells. The results were obtained from at least three independent experiments with a minimum of three replicates per condition.

### 3.11 Thioredoxin reductase and glutathione reductase activity measurements

Approximately 25 000-45 000 cells/cm<sup>2</sup> cells were seeded in 175 cm<sup>2</sup> flasks. After 24h, the medium was replaced by fresh medium containing a non-lethal concentration of nanoparticles (ie 3.0 µg Au/ml for TIME cells and 5.0 µg Au/ml for THLE-2 and HK-2 cells) for an incubation period of 12h. The non-lethal concentration was estimated on the basis of IncuCyte apoptosis data acquired from cells exposed to AuNPs-PAA. After the exposure period, cells were washed twice with DMEM + 10% FBS, once with PBS, and collected by trypsinization. Subsequently, the cell pellets were re-suspended in ice cold PBS. Next, the cells were centrifuged and lysed by CelLytic M (100 µl per 10<sup>7</sup> cells), supplemented with a protease inhibitor tablet. After centrifugation of the samples (14 000 g, 10 min, 4°C), protein concentrations were quantified with the BCA protein assay kit. Next, the thioredoxin reductase activity and the glutathione reductase activity in 100 µg of protein were measured according to the manufacturer's instructions<sup>516,517</sup>. Results are expressed as the average change in absorbance per minute and are obtained from at least three independent experiments with a minimum of two replicates per condition.

### 3.12 Statistical analysis

Results are reported as mean ± standard error (SE). A parametric one-way ANOVA was performed when more than two cell groups needed to be compared to the unexposed control group. In this case, the cell groups were exposed to only one variable, such as different concentrations of AuNPs-PAA(±Ct<sub>xb</sub>) in the MTS assays or for different incubation time periods in the TMRM assay. The one-way ANOVA was then followed by a Dunnett post-hoc test to identify which pairs were significantly different. A parametric two-way ANOVA was used to analyze the IncuCyte data, since the treated cell groups were exposed to two independent variables, both different concentrations of AuNPs-PAA(±Ct<sub>xb</sub>) and for different incubation times and were compared to the unexposed control group. The two-way ANOVA was followed by a Dunnett post-hoc test to identify which pairs were significantly different. A parametric Student's t-test was used to compare the means of AuNPs-PAA and AuNPs-PAA-Ct<sub>xb</sub> treated cells for the MTS assay and the TMRM assay or between the treated and untreated groups for the enzyme activity assay. Finally, since the ICP-MS data is based on a

single experiment, a non-parametric Kruskal-Wallis test and a Dunn's post-hoc test were performed in order to compare cell groups exposed for different incubation time periods. A non-parametric Mann-Whitney test was used to compare the means between AuNPs-PAA and AuNPs-PAA-Ctxb. The statistical analyses were performed by using Prism 7.02 software. The level of statistical significance is depicted by the number of asterisks as follows: \* $p < 0.05$ , \*\* $p < 0.01$ , \*\*\* $p < 0.001$ , \*\*\*\* $p < 0.0001$ .

## 4. Results

### 4.1 Size distribution and zeta potential of AuNPs-PAA( $\pm$ Ctxb)

First, UV-Vis spectra showed surface plasmon resonance peaks between 522 and 526 nm, which is characteristic for nano-sized AuNPs (**Figure S3.1A**). The composition of the AuNPs-PAA-Ctxb and the preserved functionality of Cetuximab after conjugation were described previously<sup>201,474</sup>. Successful conjugation of Cetuximab was also demonstrated by gel electrophoresis showing that Cetuximab was unable to migrate when conjugated to AuNPs-PAA, unlike uncoupled Cetuximab incubated with AuNPs-PAA (**Figure S3.1B**). Next, the AuNPs-PAA( $\pm$ Ctxb) were characterized in terms of their size distribution and nanoparticle surface charge. Both these parameters were determined for the AuNPs-PAA( $\pm$ Ctxb) dispersed in Class 1 water, DMEM and DMEM supplemented with 10% FBS (**Table 3.1**). Size measurements demonstrated peak particle diameters of 4-5 nm for AuNPs-PAA when dispersed in Class 1 water, DMEM and DMEM with 10% FBS. Conjugation of AuNPs-PAA to Cetuximab increased the peak particle diameter to 26 nm, 25 nm and 19 nm when dispersed in Class 1 water, DMEM and DMEM with 10% FBS, respectively. The 5<sup>th</sup> and 95<sup>th</sup> percentiles indicate nanoparticle suspensions that are mainly monodispersed. The size distribution curves are presented in **Figure S3.1C**.

The zeta potential values of the AuNPs-PAA and the AuNPs-PAA-Ctxb dispersed in Class 1 water were -30.53 mV and -29.27 mV, respectively. The zeta potential values shifted significantly towards less negative values when AuNPs-PAA and AuNPs-PAA-Ctxb were dispersed in DMEM (-8.03 mV and -7.59 mV, respectively) or in DMEM with 10% FBS (-8.37 mV and -7.04 mV, respectively).

**Table 3.1** Characterization of the AuNPs-PAA and AuNPs-PAACtxb dispersed in different media

Nanoparticle type		
Suspension medium	AuNPs-PAA	AuNPs-PAA-Ctxb
Modus size (nm) [5 <sup>th</sup> and 95 <sup>th</sup> percentile]		
Class 1 water	4 [4-14]	26 [13-53]
DMEM	5 [4-11]	25 [13-66]
DMEM + 10% FBS	5 [4-11]	19 [12-62]
Zeta potential (mV) + SD		
Class 1 water	-30.53 ± 0.25	-29.27 ± 0.15
DMEM	-8.03 ± 0.27	-7.59 ± 0.45
DMEM + 10% FBS	-8.37 ± 0.25	-7.04 ± 0.22

**Notes:** The size was measured with disc centrifugation. The values represent the modus particle size, the 5th and 95th percentile (nm). The zeta potential values were assessed with the Nanosizer Nano ZSP and are expressed as the mean nanoparticle surface charge ± standard deviation (n=3).

**Abbreviations:** AuNPs, gold nanoparticles; Ctxb, Cetuximab; DMEM, Dulbecco's modified Eagle's medium; FBS, fetal bovine serum; mV, millivolts; PAA, polyallylamine; SD, standard deviation.

The AuNPs-PAA(±Ctxb) used in the following experiments involving cell culture were dispersed in full medium containing 10% FBS. **Table 3.2** presents a summary of the experiments, the exposure conditions and a short description of the results.

**Table 3.2** Overview of the performed cell assays, exposure conditions and results.

Cell type	Endpoint	Assay	Incubation time	Concentration	Results
A431, MDA-MB-453, HK-2, THLE-2, TIME	EGFR expression	Western blot	N.A.	N.A.	Relative EGFR expression compared to A431: HK-2 $\pm$ 26%; THLE-2 $\pm$ 3%; TIME $\pm$ 2%; MDA-MB-453 $\pm$ 0.14%.
	AuNPs internalization	TEM	3h, 24h	5.0 $\mu$ g Au/ml (Only AuNPs-PAA-Ctxb)	AuNPs-PAA-Ctxb in intracellular vesicles. AuNPs-PAA-Ctxb clusters in TIME cells.
		ICP-MS	3h, 6h, 12h, 24h	5.0 $\mu$ g Au/ml	Fast AuNPs-PAA-Ctxb interaction in A431 and HK-2 cells followed by a decrease. AuNPs-PAA( $\pm$ Ctxb) interaction progressively increased in TIME, THLE-2 and MDA-MB-453 cells. Overall, AuNPs-PAA-Ctxb interaction was higher than AuNPs-PAA interaction.
	Cell viability	MTS assay	3h, 24h	0-50.0 $\mu$ g Au/ml	Conjugation of Ctxb to AuNPs-PAA reduced cytotoxicity. TIME cells were the most sensitive cells followed by THLE-2, MDA-MB-453, HK-2 and A431 cells.
	Apoptosis	Live cell imaging	0-72h	0-50.0 $\mu$ g Au/ml	AuNPs-PAA( $\pm$ Ctxb) caused apoptosis, which increased with an increasing concentration and exposure period.
		<b>+ 2 nM NAC</b>	0-72h	0-50.0 $\mu$ g Au/ml	Annexin V and caspase 3/7 activity reduced when cells were co-exposed to NAC.
HK-2, THLE-2, TIME	Mitochondrial membrane depolarization	TMRM	3h, 6h, 12h, 24h	3.0-5.0 $\mu$ g Au/ml	Mitochondrial membrane potential decreased most profoundly in TIME cells followed by THLE-2 cells and HK-2 cells after 12h. Mitochondrial membrane potential recovers after 24h.
		<b>+ 2 nM NAC</b>	12h	3.0-5.0 $\mu$ g Au/ml	NAC prevented mitochondrial membrane depolarization.
	Enzyme activity	GR and TrxR	12h	3.0-5.0 $\mu$ g Au/ml	GR and TrxR enzyme activity decreased most profoundly in TIME cells followed by THLE-2 cells and HK-2 cells.

**Abbreviations:** A431: human epidermoid cancer cells; AuNPs-PAA: polyallylamine-coated gold nanoparticles; Ctxb: Cetuximab, EGFR: epidermal growth factor receptor; HK-2: human kidney cells; ICP-MS: inductively coupled plasma mass spectrometry; MDA-MB-453: human breast cancer cells; N.A.: not applicable; NAC: N-acetyl L-cysteine; THLE-2: human liver cells; TIME: human telomerase immortalized microvascular endothelial cells; GR: glutathione reductase; TrxR: thioredoxin reductase; TEM: transmission electron microscopy.

## 4.2 Cellular internalization of AuNPs-PAA-Ctxb

Cetuximab targets EGFR and thus can influence the interaction of AuNPs-PAA-Ctxb with the cells depending on their EGFR expression. Therefore, we verified the overexpression of EGFR in A431 cells by means of western blot. Compared to A431 cells, HK-2 cells, THLE-2 cells and TIME cells displayed an EGFR expression of 26%, 3% and 2%, respectively. MDA-MB-453 cells had the lowest EGFR expression (0.14%) of all (**Figure 3.1**). TEM demonstrated the internalization of AuNPs-PAA-Ctxb in all cell types when exposed to 5.0  $\mu\text{g Au/ml}$  of AuNPs-PAA-Ctxb for 3h or 24h (**Figure 3.2**). After an exposure period of 3h, the nanoparticles were present in small intracellular membrane-bound vesicles, which were localized mostly in the peri-nuclear region of A431 cells (**Figure 3.2A**), HK-2 cells (**Figure 3.2E**) and THLE-2 cells (**Figure 3.2G**). In the EGFR-negative MDA-MB-453 cells, only a minimal uptake of nanoparticles was observed (**Figure 3.2C**). When the exposure period was increased to 24h, the number of nanoparticle-containing vesicles and the amount of AuNPs-PAA-Ctxb in the vesicles appeared to increase in all cell types. The nanoparticle uptake by the TIME cells was characterized mainly by large clusters of AuNPs-PAA-Ctxb, which could be observed at both 3h (**Figure 3.2I**) and 24h of exposure (**Figure 3.2J**). EDS analysis on representative cells confirmed the presence of intracellular gold (**Supplemental Figure S3.2**).

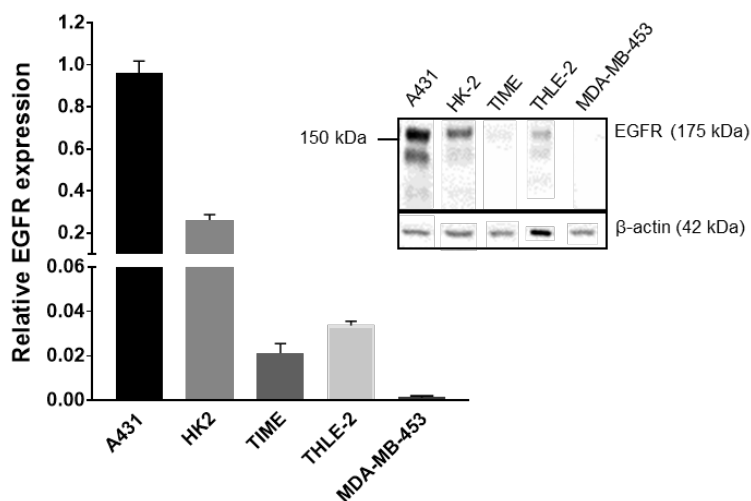


**Figure 3.1** EGFR expression in HK-2 cells, THLE-2 cells, TIME cells and MDA-MB-453 cells relative to EGFR expression in A431 cells, determined by Western blot. Results are expressed as mean  $\pm$  SE and are obtained from at least 4 independent replicates. Protein bands were normalized against  $\beta$ -actin.

**Abbreviations:** A431: human epidermoid cancer cells; EGFR: epidermal growth factor receptor; HK-2: human kidney cells; MDA-MB-453: human breast cancer cells; SE: standard error; THLE-2: human liver cells; TIME: human telomerase immortalized microvascular endothelial cells.

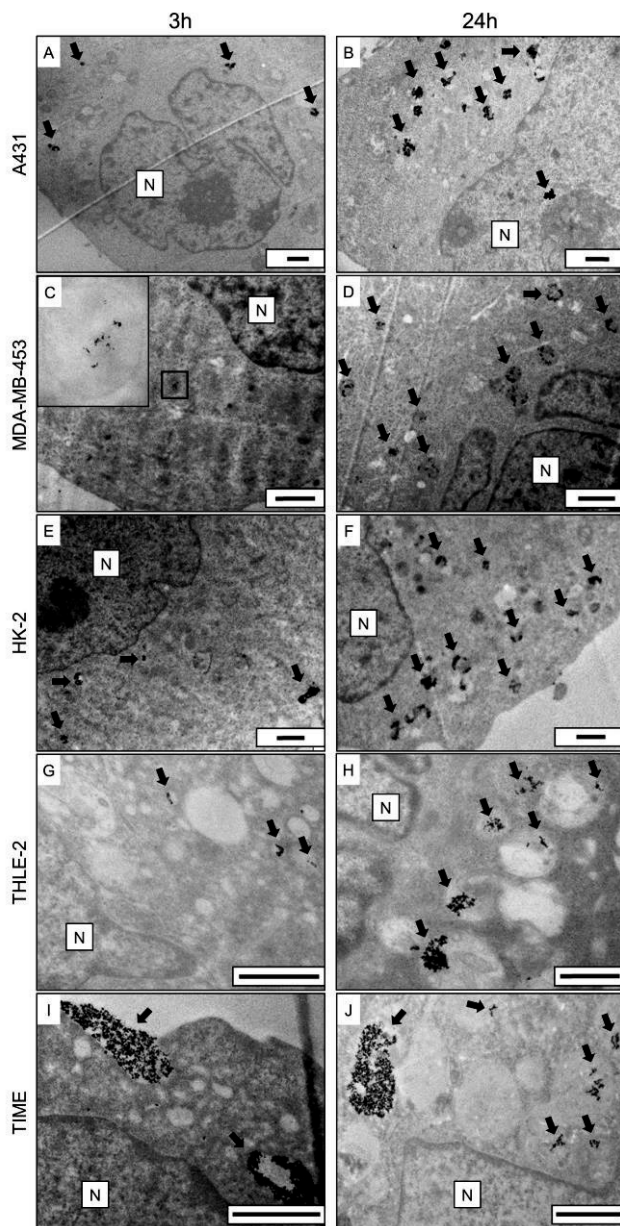


**Figure 3.2** Transmission electron microscopy images demonstrating the internalization of AuNPs-PAA-Ctxb in A431 cells (A and B), MDA-MB-453 cells (C and D), HK-2 cells (E and F), THLE-2 cells (G and H) and TIME cells (I and J). The cells were exposed to 5.0  $\mu\text{g Au/mL}$  of AuNPs-PAA-Ctxb for 3h (left column) or 24h (right column). Arrows indicate AuNPs-PAA-Ctxb. Images were acquired at different magnifications. Size bar = 1  $\mu\text{m}$ , N = Nucleus.

**Abbreviations:** AuNPs-PAA-Ctxb, polyallylamine-coated gold nanoparticles conjugated to Cetuximab; A431, human epidermoid cancer cells; HK-2, human kidney cells; MDA-MB-453, human breast cancer cells, THLE-2, human liver cells; TIME, human telomerase immortalized microvascular endothelial cells.

We also quantified the gold content of the cells by means of ICP-MS after incubation with  $5.0 \mu\text{g Au/ml}$  of AuNPs-PAA( $\pm$ Ctxb) for 3h, 6h, 12h and 24h (**Figure 3.3**). It is important to note that the ICP-MS data represents the interaction of AuNPs with the cell surface as well as the uptake of AuNPs by the cells. The results demonstrated maximum interaction of AuNPs-PAA-Ctxb with A431 cells after 3h ( $1.09 \pm 0.07 \text{ pg Au/cell}$ ). Then, the AuNPs-PAA-Ctxb content decreased to a plateau phase after 6h, which continued until 24h of exposure. During the plateau phase, there was no significant difference between AuNPs-PAA and AuNPs-PAA-Ctxb content (**Figure 3.3A**). The MDA-MB-453 cells showed a small, but significant increase in AuNPs-PAA content after 24h ( $0.62 \pm 0.11 \text{ pg Au/cell}$ ) compared to 3h of exposure ( $0.27 \pm 0.01 \text{ pg Au/cell}$ ) (**Figure 3.3B**). In HK-2 cells, the AuNPs-PAA( $\pm$ Ctxb) content increased and peaked after 6h of incubation ( $0.69 \pm 0.15 \text{ pg Au/cell}$  for AuNPs-PAA and  $0.98 \pm 0.07 \text{ pg Au/cell}$  for AuNPs-PAA-Ctxb), after which it decreased gradually (**Figure 3.3C**). The THLE-2 cells demonstrated an increased AuNPs-PAA( $\pm$ Ctxb) interaction after 24h of exposure ( $0.51 \pm 0.02 \text{ pg Au/cell}$  for AuNPs-PAA and  $1.59 \pm 0.14 \text{ pg Au/cell}$  for AuNPs-PAA-Ctxb) (**Figure 3.3D**). Finally, the TIME cells showed a trend of increasing AuNPs-PAA-Ctxb content after 12h ( $0.38 \pm 0.07 \text{ pg Au/cell}$ ) (**Figure 3.3E**). Overall, the cellular AuNPs-PAA-Ctxb interaction was higher than the AuNPs-PAA interaction in TIME cells, in THLE-2 cells, in A431 cells after 3h, in MDA-MB-453 cells after 3h, and in HK-2 cells after 3h and 6h (exact p-values of 0.1).

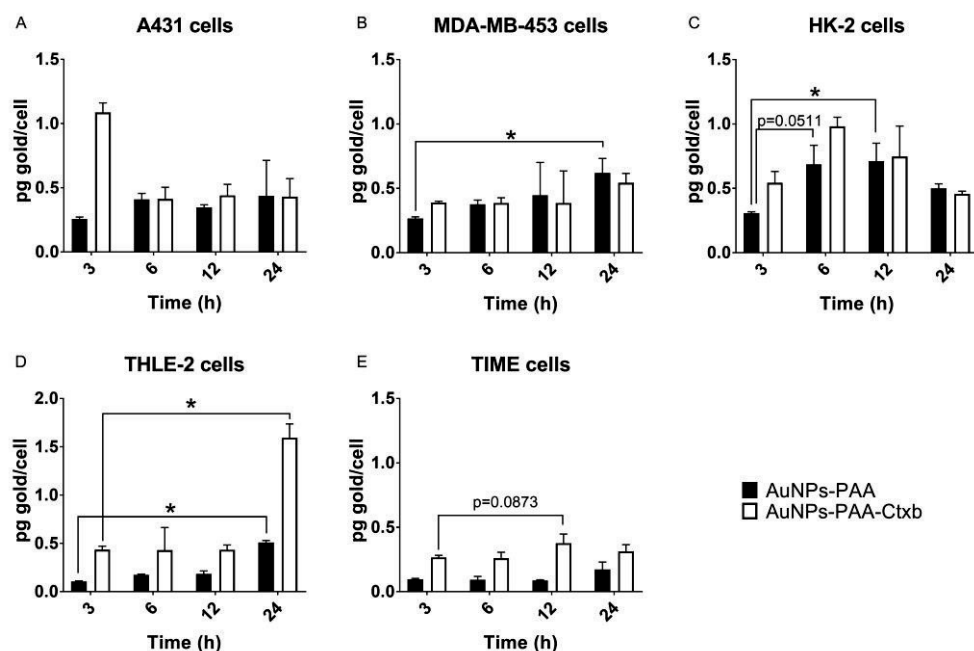


**Figure 3.3** Interaction of AuNPs-PAA( $\pm$ Ctxb) with A431 cells (A), MDA-MB-453 cells (B), HK-2 cells (C), THLE-2 cells (D) and TIME cells (E) quantified with ICP-MS. The cells were exposed to  $5.0 \mu\text{g Au/mL}$  of AuNPs-PAA( $\pm$ Ctxb) for 3h, 6h, 12h or 24h. Results are expressed as mean pg gold per cell  $\pm$  SD calculated



from 3 replicates per condition obtained from one experiment. A significant difference compared to 3h of exposure was calculated by a Kruskal-Wallis test and a Dunn's post-hoc test (\* $p < 0.05$ ).

**Abbreviations:** A431: human epidermoid cancer cells; Ctxb: Cetuximab; Au: gold; AuNPs-PAA: polyallylamine-coated gold nanoparticles; HK-2: human kidney cells; ICP-MS: inductively coupled plasma mass spectrometry; MDA-MB-453: human breast cancer cells; SD: standard deviation; THLE-2: human liver cells; TIME: human telomerase immortalized microvascular endothelial cells.

### 4.3 AuNPs-PAA( $\pm$ Ctxb) reduced the cell viability

TEM and ICP-MS results clearly showed interactions and uptake of AuNPs by the cells. Therefore, we assessed the cell viability after exposure to increasing concentrations of AuNPs-PAA( $\pm$ Ctxb) for 3h and 24h. MTS assays revealed that AuNPs-PAA( $\pm$ Ctxb) reduced cell viability in a concentration- and time-dependent manner (**Figure 3.4**). The lowest observed effect concentration (LOEC) presents the lowest tested concentration causing a significantly reduced cell viability. The LOEC of AuNPs-PAA after 3h of exposure is 25.0  $\mu$ g Au/ml for the A431 cells and 12.5  $\mu$ g Au/ml for the MDA-MB-453 cells (**Figure 3.4C**), the THLE-2 cells (**Figure 3.4G**) and the TIME cells (**Figure 3.4I**). The HK-2 cells showed no significant reduction in cell viability (**Figure 3.4E**) at the maximum exposure concentration of 50.0  $\mu$ g/ml. However, when the exposure period was increased to 24h, the LOEC values decreased for all cell types (**Table 3.3**). Although exposure to AuNPs-PAA-Ctxb demonstrated a concentration- and time-dependent cytotoxicity profile comparable to that described for unconjugated AuNPs, they were significantly less cytotoxic. This difference in cytotoxic effect was generally observable from exposure to a nanoparticle concentration of 6.25  $\mu$ g Au/ml for 24h for A431 cells (**Figure 3.4B**), MDA-MB-453 cells (**Figure 3.4D**), HK-2 cells (**Figure 3.4F**) and THLE-2 cells (**Figure 3.4H**). Indeed, the calculated half maximal effect concentrations ( $EC_{50}$ ) of AuNPs-PAA-Ctxb were significantly higher than the  $EC_{50}$  concentrations of AuNPs-PAA in all cell types, except for the TIME cells (**Table 3.3**). In addition, these  $EC_{50}$  values demonstrated that the sensitivity to the cytotoxic effects of the nanoparticles were also cell type-dependent. Interestingly, the EGFR-overexpressing A431 cancer cells were the least sensitive cells. Amongst the healthy cells, the TIME cells were the most vulnerable for the cytotoxic effects of the AuNPs-PAA( $\pm$ Ctxb), whereas the HK-2 cells were the most resistant.

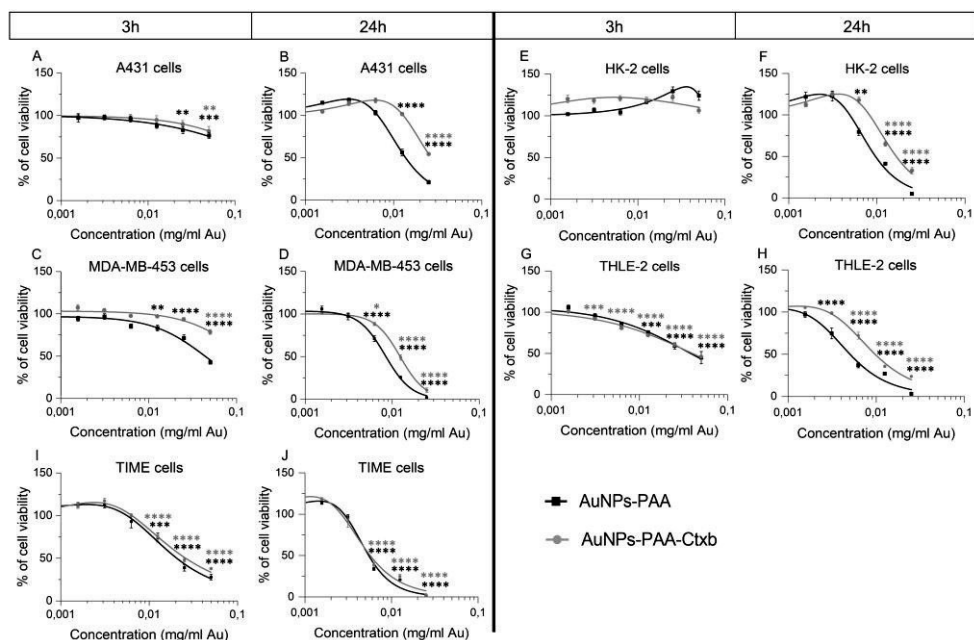


**Figure 3.4** Cell viability after exposure to AuNPs-PAA (black curves) and AuNPs-PAA-Ctxb (gray curves) of A431 cells (A and B), MDA-MB-453 cells (C and D), HK-2 cells (E and F), THLE-2 cells (G and H) and TIME cells (I and J). Cells were exposed to increasing concentrations of AuNPs-PAA or AuNPs-PAA-Ctxb for 3h or 24h. The number of viable cells was assessed by MTS assay. The results are expressed as the mean percentage of viable cells relative to the unexposed cells  $\pm$  SE and are obtained from at least three independent experiments with a minimum of three replicates per condition. A significantly reduced viability compared to the unexposed control was calculated by a one-way ANOVA and a Dunnett post hoc test (\* $p < 0.05$ , \*\* $p < 0.01$ , \*\*\* $p < 0.001$ , \*\*\*\* $p < 0.0001$ ).

**Abbreviations:** A431: human epidermoid cancer cells; ANOVA: analysis of variance; AuNPs-PAA: polyallylamine-coated gold nanoparticles; Ctxb: Cetuximab; HK-2: human kidney cells; MDA-MB-453: human breast cancer cells; SE: standard error; THLE-2: human liver cells; TIME: human telomerase immortalized microvascular endothelial cells.

**Table 3.3** EC<sub>50</sub> values (μg Au/ml) after 24h of cell exposure and LOEC (μg Au/ml) after 3h and 24h of exposure to AuNPs-PAA and AuNPs-PAA-Ctxb.

Cell type	AuNPs-PAA			AuNPs-PAA-Ctxb		
	LOEC (3h)	LOEC (24h)	EC <sub>50</sub> + 95% CI (24h)	LOEC (3h)	LOEC (24h)	EC <sub>50</sub> + 95% CI (24h)
A431	25.0	12.5	13.7 [12.8 – 14.6]	50.0	25.0	26.9 [24.8 – 29.1]
MDA-MB-453	12.5	6.25	8.31 [7.67 – 8.96]	50.0	6.25	12.3 [11.6 – 13.0]
HK-2	>50	6.25	9.65 [8.60 – 10.7]	>50	12.5	16.7 [15.3 – 18.2]
THLE-2	12.5	3.12	5.08 [4.36 – 5.79]	3.12	6.25	9.75 [9.04 – 10.5]
TIME	12.5	6.25	5.47 [5.18 – 5.75]	12.5	6.25	5.67 [5.08 – 6.26]

**Note:** Values were calculated from the MTS viability assays and expressed as μg Au/mL (**Figure 3.4**).

**Abbreviations:** A431: human epidermoid cancer cells; AuNPs: gold nanoparticles; CI: confidence interval; EC<sub>50</sub>: Half maximal effect concentration; HK-2: human kidney cells; LOEC: lowest observed effect concentration; MDA-MB-453: human breast cancer cells, THLE-2: human liver cells; TIME: human telomerase immortalized microvascular endothelial cells; Ctxb: cetuximab.

#### 4.4 AuNPs-PAA(±Ctxb) induced apoptosis

The MTS viability assays demonstrated reduced cell viability after exposure to AuNPs-PAA(±Ctxb). However, the assay is based on the metabolic activity of the cells and gives no further information about the process of cell death. Therefore, we performed live cell imaging measuring the caspase 3/7 activity and annexin V labeling, two markers of apoptosis. The results demonstrated that exposure to AuNPs-PAA(±Ctxb) caused apoptotic cell death in a concentration- and time-dependent manner (**Figure 3.5**). In the first 24h, 50.0 μg Au/ml (red line) and 25.0 μg Au/ml (purple line) of AuNPs-PAA(±Ctxb) resulted in a significant increase in caspase 3/7 activity and annexin V labeling in all cell types. TIME cells, in addition, showed a significant increase in the apoptotic parameters after exposure to 12.5 μg Au/ml of nanoparticles (**Figure 3.5I-T**, yellow line). Extending the exposure period to 48h, 12.5 μg Au/ml of AuNPs-PAA (yellow line) significantly increased apoptosis in MDA-MB-453 (**Figure 3.5C-D**) cells, HK-2 cells (**Figure 3.5E-F**) and THLE-2 cells (**Figure 3.5G-H**), whereas 6.25 μg Au/ml (brown line) also induced significant apoptosis in the TIME cells (**Figure 3.5I-J**) and HK-2 cells (**Figure 3.5E-F**). Finally, from 48h to 72h, 6.25 μg Au/ml of AuNPs-PAA (brown line) led to a significant number of apoptotic cells in MDA-MB-453 cells (**Figure 3.5C-D**), whereas 3.12 μg Au/ml of AuNPs-PAA (green line) increased apoptosis significantly in the TIME cells (**Figure 3.5I-J**). Similar to the MTS assay, the live cell imaging data demonstrated that AuNPs-PAA-Ctxb are less cytotoxic than the AuNPs-PAA. Exposure to AuNPs-PAA-Ctxb reduced or delayed the increase in caspase 3/7 activity and annexin V labeling compared to exposure to AuNPs-PAA.

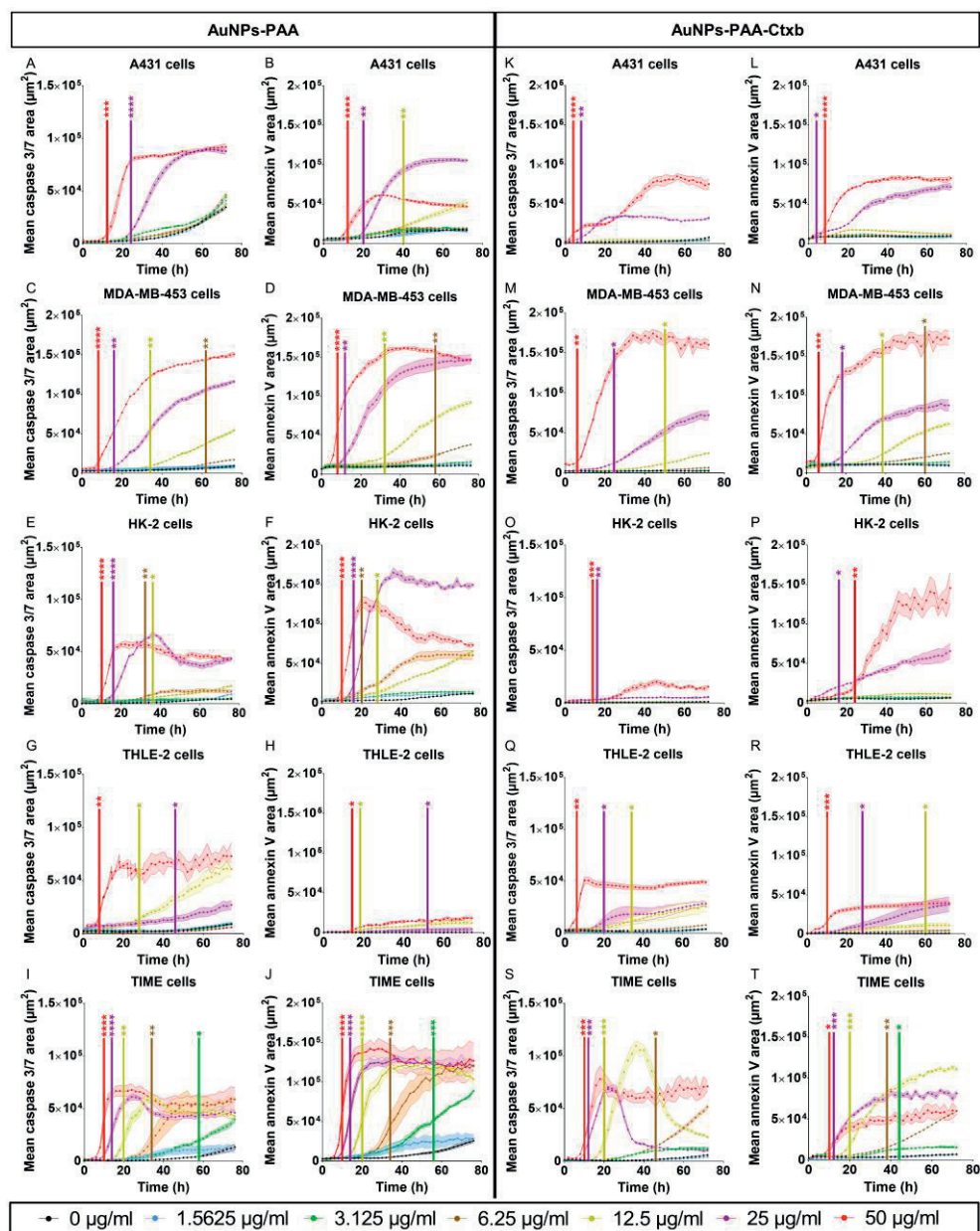


**Figure 3.5** Live cell imaging for caspase 3/7 activation (left lanes) and annexin V labeling (right lanes) in A431 cells (A and B, K and L), MDA-MB-453 cells (C and D, M and N), HK-2 cells (E and F, O and P), THLE-2 cells (G and H, Q and R) and TIME cells (I and J, S and T). The cell lines were exposed to increasing concentrations of AuNPs-PAA or AuNPs-PAA-Ctxb. Time-lapse pictures were taken every 2h for 72h. The results are expressed as the mean area of caspase 3/7 or annexin V per well  $\pm$  SE and are obtained from at least three replicates. A significant increase in caspase 3/7 activity and annexin V labeling

compared to unexposed control cells was calculated by a two-way ANOVA and a Dunnett post-hoc test. The start of significance is visualized by vertical bars (\* $p < 0.05$ , \*\* $p < 0.01$ , \*\*\* $p < 0.001$ , \*\*\*\* $p < 0.0001$ ).

**Abbreviations:** A431: human epidermoid cancer cells; ANOVA: analysis of variance; AuNPs-PAA: polyallylamine-coated gold nanoparticles; Ctxb: Cetuximab; HK-2: human kidney cells; MDA-MB-453: human breast cancer cells; SE: standard error; THLE-2: human liver cells; TIME: human telomerase immortalized microvascular endothelial cells.

## 4.5 AuNPs-PAA( $\pm$ Ctxb) caused mitochondrial dysfunction

Live cell imaging identified apoptosis as the cell death mechanism after exposure to AuNPs-PAA( $\pm$ Ctxb). Since mitochondria are key players in activating apoptosis, we assessed mitochondrial dysfunction by measuring the mitochondrial membrane potential after exposure of the cells to a sub-lethal concentration of AuNPs-PAA( $\pm$ Ctxb) (Figure 3.6). A temporary hyperpolarization of the mitochondrial membrane potential was observed in HK-2 cells exposed to AuNPs-PAA-Ctxb (Figure 3.6A) and in TIME cells exposed to AuNPs-PAA( $\pm$ Ctxb) (Figure 3.6C) for 3h. Following 6h of exposure to AuNPs-PAA( $\pm$ Ctxb), the mitochondrial membrane potential of THLE-2 cells (Figure 3.6B) was reduced by approximately 11-14%, and of TIME cells (Figure 3.6C) by approximately 6-10%, compared to the unexposed controls. After extending the exposure period to 12h, the mitochondrial membrane potentials of the THLE-2 cells and TIME cells were further depolarized to 80% and 60%, respectively. Only exposure to AuNPs-PAA could temporarily reduce the mitochondrial membrane potential of the HK-2 cells by 15% (Figure 3.6A). Finally, after 24h of exposure, the mitochondrial membrane potential of the THLE-2 cells and the TIME cells was repolarized to more than 90% compared to the unexposed control cells. HK-2 cells exposed to AuNPs-PAA-Ctxb exhibited a significant hyperpolarization. Although AuNPs-PAA-Ctxb led to less cell death than AuNPs-PAA, no strong differences were observed in the mitochondrial membrane depolarization of cells exposed to AuNPs-PAA and those exposed to AuNPs-PAA-Ctxb.

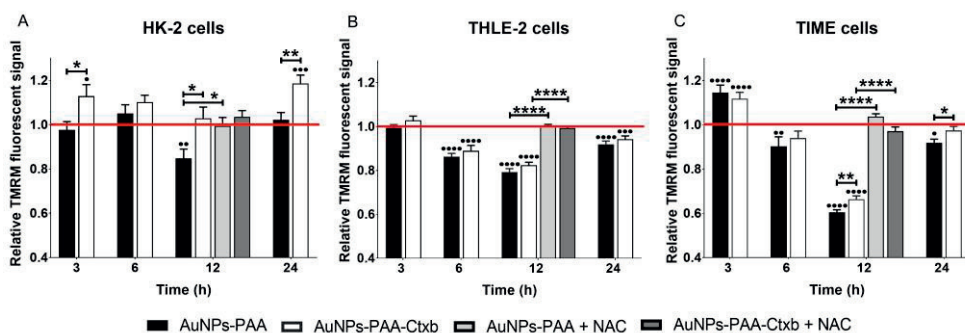


**Figure 3.6** Mitochondrial membrane potential measurements of the HK-2 cells (A), THLE-2 cells (B) and TIME cells (C) after exposure to AuNPs-PAA or AuNPs-PAA-Ctxb. TIME cells were exposed to 3.0  $\mu$ g Au/mL, THLE-2 and HK-2 cells were exposed to 5.0  $\mu$ g Au/mL of AuNPs-PAA or AuNPs-PAA-Ctxb. During the 12h exposure, 2 nM NAC was added to assess oxidative stress. The mitochondrial membrane

potential was measured with TMRM fluorescence, detected by flow cytometry. The results are expressed as mean TMRM fluorescent signal relative to the unexposed control cells (red line)  $\pm$  SE and are obtained from at least three independent experiments with a minimum of three replicates per condition. Significant difference in TMRM signal compared to the unexposed control was calculated by a one-way ANOVA and a Dunnett post-hoc test (bullets). Significant difference in TMRM fluorescent signal between AuNPs-PAA and AuNPs-PAA-Ctxb exposed cells, or between nanoparticle-exposed cells and NAC co-exposed cells, was calculated by a Student's t-test (asterisks) (\* $p < 0.05$ , \*\* $p < 0.01$ , \*\*\* $p < 0.001$  \*\*\*\* $p < 0.0001$ ).

**Abbreviations:** ANOVA: analysis of variance; AuNPs-PAA: polyallylamine-coated gold nanoparticles; Ctxb: Cetuximab; HK-2: human kidney cells; NAC: N-acetyl L-cysteine; SE: standard error; THLE-2: human liver cells; TIME: human telomerase immortalized microvascular endothelial cells.

#### 4.6 AuNPs-PAA( $\pm$ Ctxb) inhibited the activity of thioredoxin reductase and glutathione reductase

Thioredoxin reductase (TrxR) and glutathione reductase (GR) are enzymes involved in the antioxidant defense mechanism of the cell. TrxR and GR both use NADPH to reduce thioredoxin (Trx) and glutathione (GSH), respectively, which are in turn used by peroxidases to eliminate  $H_2O_2$ . Oxidative stress can have a negative effect on mitochondrial function. Since an exposure period of 12h resulted in the most pronounced mitochondrial membrane depolarization (**Figure 3.6**), we measured the TrxR and GR activity in the cells after exposure to a non-lethal concentration of AuNPs-PAA( $\pm$ Ctxb) for 12h (**Figure 3.7**). Incubation with AuNPs-PAA( $\pm$ Ctxb) strongly inhibited the TrxR activity in HK-2 cells (**Figure 3.7A**), THLE-2 cells (**Figure 3.7B**) and TIME cells (**Figure 3.7C**) with residual activities of 22.8%, 15.3% and 6.3%, respectively. In addition, a decrease of the GR activity was observed, but to a lesser extent than was the case for TrxR inhibition (with residual activities of 61.2%, 69.2% and 37.9% for HK-2 cells, THLE-2 cells and TIME cells, respectively). In general, the inhibitory effects on TrxR and GR were most profound in TIME cells, followed by THLE-2 cells and HK-2 cells.

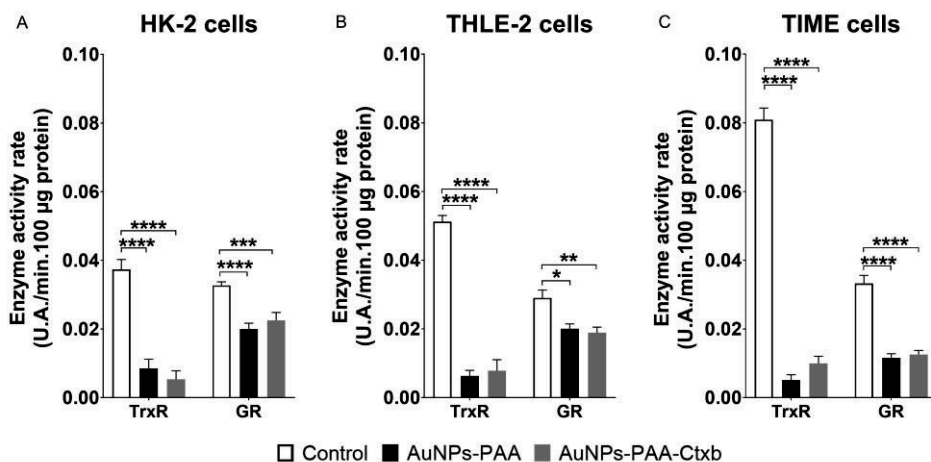


**Figure 3.7** Thioredoxin reductase and glutathione reductase activity in the HK-2 cells (A), THLE-2 cells (B) and TIME cells (C) after exposure to AuNPs-PAA or AuNPs-PAA-Ctxb. TIME cells were exposed to 3.0  $\mu\text{g Au/mL}$ , THLE-2 and HK-2 cells were exposed to 5.0  $\mu\text{g Au/mL}$  of AuNPs-PAA or AuNPs-PAA-Ctxb for 12h. The enzyme activity rate per minute was measured by the increase in absorbance at 405 nm for GR and at 412 nm for TrxR. The results are expressed as mean enzyme activity rate per minute per 100  $\mu\text{g}$  of protein  $\pm$  SE and are obtained from at least three independent experiments with a minimum of two replicates per condition. Significant difference in enzyme activity rate compared to the unexposed control was calculated by a Student's t-test (\* $p < 0.05$ , \*\* $p < 0.01$ , \*\*\* $p < 0.001$  \*\*\*\* $p < 0.0001$ ).

**Abbreviations:** AuNPs-PAA: polyallylamine-coated gold nanoparticles; Ctxb: Cetuximab; GR: glutathione reductase; HK-2: human kidney cells; SE: standard error; THLE-2: human liver cells; TIME: human telomerase immortalized microvascular endothelial cells; TrxR: Thioredoxin reductase.

#### 4.7 The protective effect of N-acetyl L-cysteine (NAC)

Finally, we investigated the ability of NAC to counteract the cytotoxicity caused by AuNPs-PAA( $\pm$ Ctxb). NAC is a potent thiol-containing anti-oxidant, which can interact with ROS such as  $\text{OH}^\cdot$  and  $\text{H}_2\text{O}_2$  through the reducing capacity of its thiol-disulfide exchange activity. Furthermore, NAC acts as a precursor of reduced glutathione<sup>518,519</sup>. Since an exposure period of 12h resulted in the most pronounced mitochondrial membrane depolarization, the potential protective effect of NAC was assessed after exposure to a non-lethal concentration of AuNPs-PAA( $\pm$ Ctxb) for 12h. Co-incubation of the cells with AuNPs-PAA( $\pm$ Ctxb) and NAC prevented mitochondrial membrane depolarization in all cell types after 12h of exposure (Figure 3.6). Furthermore, the increases in caspase 3/7 activity and annexin V labeling were remarkably reduced (Figure 3.8) compared to AuNPs-PAA( $\pm$ Ctxb) exposure without NAC (Figure 3.5). Indeed, during co-exposure with NAC, only exposure to the highest AuNPs-PAA( $\pm$ Ctxb) concentrations of 50.0  $\mu\text{g Au/mL}$  (red line) and 25.0  $\mu\text{g Au/mL}$  (purple line) resulted in a significant increase in annexin V and caspase 3/7 labeling in most cell types. In addition, a concentration of 12.5  $\mu\text{g Au/mL}$  (yellow line) of AuNPs-PAA resulted in a significant

increase in annexin V and caspase 3/7 labeling in MDA-MB-453 cells (**Figure 3.8C-D**) and TIME cells (**Figure 3.8I-J**).

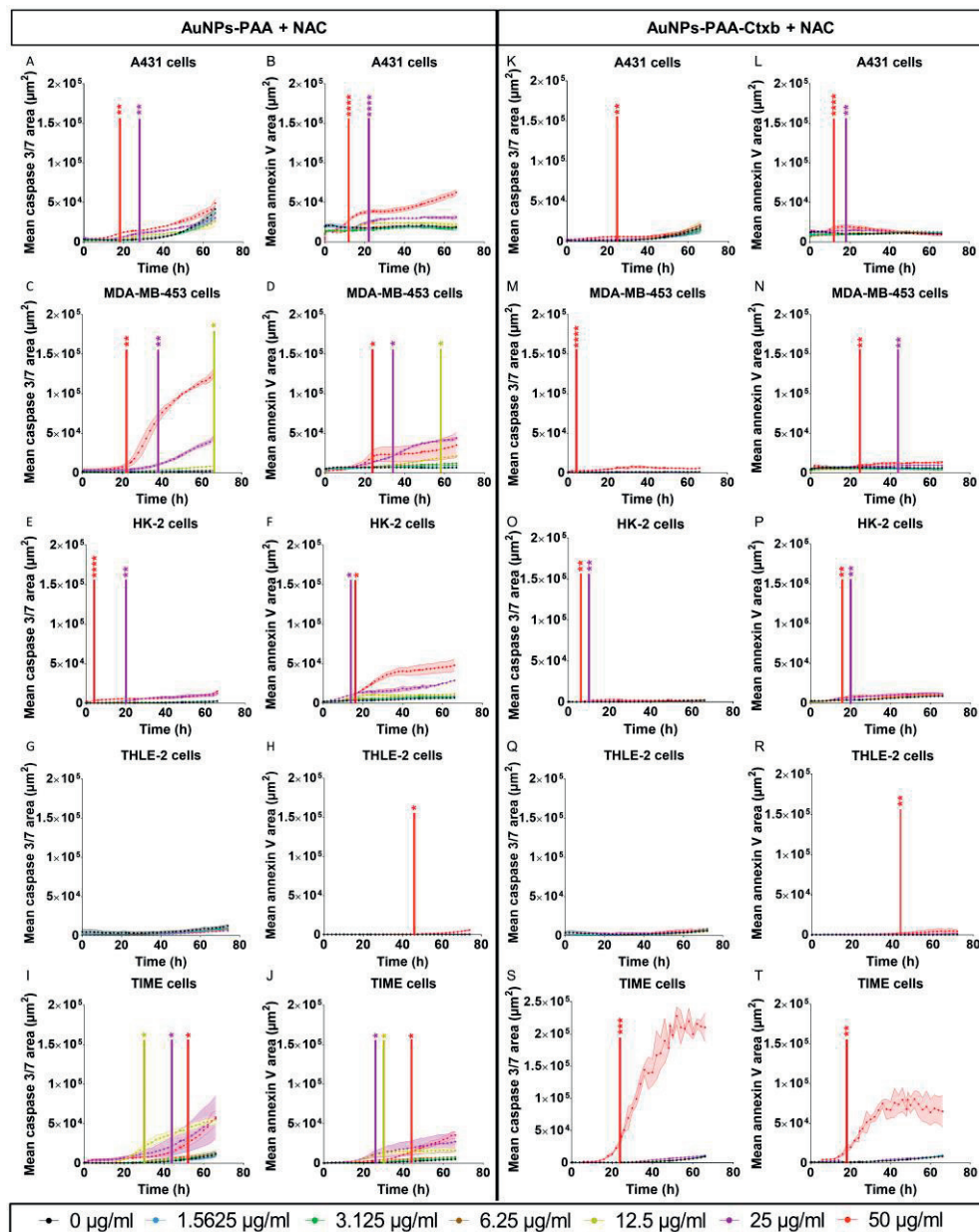


**Figure 3.8** Live cell imaging for caspase 3/7 activation (left panels) and annexin V labeling (right panels) in A431 cells (A and B, K and L), MDA-MB-453 cells (C and D, M and N), HK-2 cells (E and F, O and P), THLE-2 cells (G and H, Q and R) and TIME cells (I and J, S and T). The cell lines were co-exposed to increasing concentrations of AuNPs-PAA or AuNPs-PAA-Ctxb and 2 nM of NAC. Time-lapse pictures



were taken every 2h for 72h. The results are expressed as the mean area of caspase 3/7 or annexin V per well  $\pm$  SE and are obtained from at least three replicates. A significant increase in caspase 3/7 activity and annexin V labeling compared to unexposed control cells was calculated by a two-way ANOVA and a Dunnett post-hoc test. The start of significance is visualized by vertical bars (\* $p < 0.05$ , \*\* $p < 0.01$ , \*\*\* $p < 0.001$  \*\*\*\* $p < 0.0001$ ).

**Abbreviations:** A431: human epidermoid cancer cells; ANOVA: analysis of variance; AuNPs-PAA: polyallylamine-coated gold nanoparticles; Ctxb: Cetuximab; HK-2: human kidney cells; MDA-MB-453: human breast cancer cells; SE: standard error; NAC: N-acetyl L-cysteine; THLE-2: human liver cells; TIME: human telomerase immortalized microvascular endothelial cells.

### 4.8 Correlation between cell viability, TrxR activity and mitochondrial membrane depolarization

The previous results demonstrated that the most sensitive TIME cells exhibited the strongest mitochondrial membrane depolarization, the highest basal TrxR activity and the strongest TrxR inhibition. Alternatively, the more resistant HK-2 cells showed a mild mitochondrial membrane depolarization, the lowest basal TrxR activity and the least TrxR inhibition. In order to interpret the relation between the cell viability, the TrxR activity and the mitochondrial membrane potential, correlation studies were performed. The results highlighted a clear correlation between: (I) the residual mitochondrial membrane potential and the cell viability (**Figure 3.9A**, Pearson's  $r = 0.995$ ), (II) basal TrxR activity and the cell viability (**Figure 3.9B**, Pearson's  $r = -0.929$ ), (III) the extent of TrxR inhibition and the cell viability (**Figure 3.9C**, Pearson's  $r = -0.920$ ), and (IV) the extent of TrxR inhibition and the residual mitochondrial membrane potential (**Figure 3.9D**, Pearson's  $r = -0.997$  for AuNPs-PAA and  $r = -0.969$  for AuNPs-PAA-Ctxb).

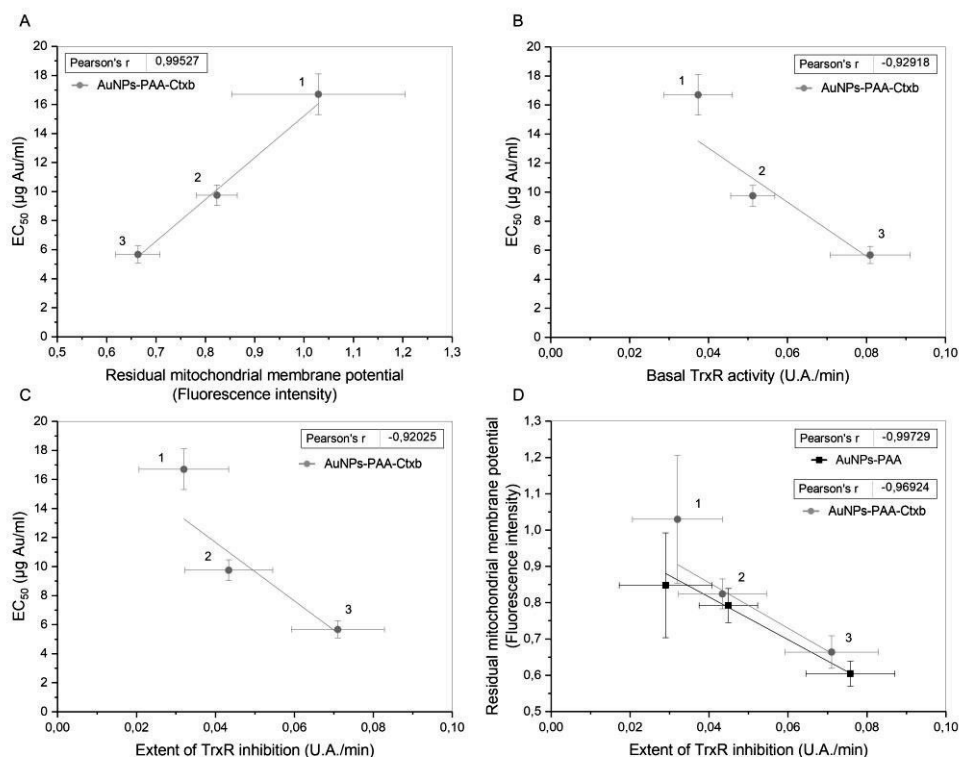


**Figure 3.9** Correlation analyses showing the relation between the residual mitochondrial membrane potential and cell viability (A); the basal TrxR activity and cell viability (B); the extent of TrxR activity and cell viability (C); and the extent of TrxR inhibition and the residual mitochondrial potential (D). Data are presented as mean  $\pm$  SD (for mitochondrial membrane potential and TrxR activity) or 95% CI (for  $EC_{50}$ ). 1= HK-2 cells, 2= THLE-2 cells and 3= TIME cells.

**Abbreviations:** CI, confidence interval; HK-2, human kidney cells; SD, standard deviation; THLE-2, human liver cells; TIME, human telomerase immortalized microvascular endothelial cells; TrxR, thioredoxin reductase; AuNPs-PAA, polyallylamine-coated gold nanoparticles; Ctxb, cetuximab;  $EC_{50}$ , half maximal effect concentration

## 5. Discussion

Only a limited number of reports have been published investigating the toxicity of AuNPs on non-cancerous human cells that were expected to be significantly exposed to AuNPs after *in vivo* administration. In this study, we presented a comprehensive evaluation of the cytotoxicity of polyallylamine-coated AuNPs conjugated to Cetuximab (AuNPs-PAA-Ctxb) in normal human kidney, liver and microvascular endothelial cells, and compared the toxicity profile with their unconjugated counterparts (AuNPs-PAA).

TEM images demonstrated that the AuNPs-PAA-Ctxb were present in intracellular vesicles and thus suggested that AuNPs-PAA-Ctxb uptake was mediated by endocytosis. The extent of nanoparticle internalization depends on the AuNPs surface modifications as well as on the cell type and the incubation time. Indeed, quantitative ICP-MS data showed that conjugation of the AuNPs-PAA with Cetuximab resulted in an overall increased cellular interaction. This was observed in the THLE-2 cells and TIME cells, but less so in the EGFR-negative MDA-MB-453 cells, which potentially use non-specific uptake routes. Furthermore, A431 cells and HK-2 cells, with high expression levels of EGFR, exhibited this higher AuNPs-PAA-Ctxb interaction, especially after short incubation times of 3h and 6h. This observation could be attributed to Cetuximab, since it promotes a fast receptor-mediated internalization of AuNPs in A431 cells and in pancreatic cancer cells after 30 min-2h<sup>486,520</sup>. Furthermore, it has been demonstrated that intermediate-sized nanoparticles (20-60 nm) are endocytosed more efficiently than smaller nanoparticles<sup>222,521</sup>. Thus, in addition to receptor targeting, the overall increased size of the AuNPs-PAA-Ctxb compared to AuNPs-PAA could have facilitated their cellular uptake. However, we noticed a subsequent decrease in the gold content in the A431 and HK-2 cells. This could potentially be related to a reduced cell surface number of EGFR and/or exocytosis of the AuNPs. In fact, Cetuximab-conjugated AuNPs inhibit the recycling of EGFR from endosomes to the cell surface more efficiently than free Cetuximab<sup>486,520</sup>. This would lead to a prolonged reduction in the number of docking sites for Cetuximab and therefore less uptake of the AuNPs-PAA-Ctxb over time. Furthermore, it has been reported that macropinosomes in A431 cells diffuse with difficulty to lysosomes and travel back to the extracellular fluid<sup>522,523</sup>. No exocytosis processes were reported yet for HK-2 cells. In contrast to the aforementioned interaction kinetics, the MDA-MB-453 cells, the TIME cells and the THLE-2 cells showed a more gradual and progressive increase in AuNPs-PAA( $\pm$ Ctxb) content with increasing incubation periods, which could indicate a less efficient and specific AuNPs uptake. Interestingly, despite the relatively low interactions of AuNPs-PAA( $\pm$ Ctxb) with the TIME cells, as shown by ICP-MS (maximum  $0.38 \pm 0.07$  pg Au/cell), the TEM images demonstrated large intracellular nanoparticle clustering. Nanoparticle clustering was also observed in human umbilical vein endothelial cells (HUVECs) incubated with  $10^{12}$  citrate-capped AuNPs/ml for 24h under static conditions<sup>524</sup>. A possible hypothesis for this observation is that nanoparticles can be trapped and clustered within the glycocalyx coating of the endothelial cells<sup>525</sup>. Furthermore, the microvascular endothelial cells control the continuous passage of macromolecules and fluid from the blood to the extravascular tissue. Therefore, endothelial cells are rich in cell surface invaginations to engulf proteins, lipids and nanoparticles<sup>526</sup>.

Since we demonstrated clear, but different interactions of the AuNPs-PAA( $\pm$ Ctxb) with the cells, we performed cell viability assays to investigate the effects of AuNPs-PAA( $\pm$ Ctxb) on the different cell types. Our results showed that the AuNPs-PAA( $\pm$ Ctxb) toxicity was increased in a concentration- and time-dependent manner. In addition, the EC<sub>50</sub> values, based on the MTS

assays after 24h of exposure, demonstrated that various cell types are differentially sensitive to the effects of the AuNPs. Interestingly, EGFR-overexpressing A431 cells exhibited the highest resistance to AuNPs-PAA-Ctxb-induced toxicity ( $EC_{50} = 26.9 \mu\text{g Au/ml}$ ), followed by HK-2 cells ( $EC_{50} = 16.7 \mu\text{g Au/ml}$ ), MDA-MB-453 cells ( $EC_{50} = 12.3 \mu\text{g Au/ml}$ ), THLE-2 cells ( $EC_{50} = 9.75 \mu\text{g Au/ml}$ ) and TIME cells ( $EC_{50} = 5.67 \mu\text{g Au/ml}$ ). These findings are not consistent with several other toxicity studies demonstrating that cancer cells are more sensitive to nanoparticle-induced toxicity than normal cells and that antibody-conjugated AuNPs enhance cell death in antigen-overexpressing cancer cells<sup>251,252,489,527-529</sup>. In fact, we showed that conjugation of AuNPs-PAA to Cetuximab even reduced nanoparticle-induced cytotoxicity, leading to  $EC_{50}$  values that are 1.5-2 times higher than the  $EC_{50}$  values of the cells incubated with AuNPs-PAA. This observation could be attributed to the change in surface coating of AuNPs-PAA after antibody conjugation, which could reduce the interaction of gold with biological components<sup>506,530</sup>.

The calculated  $EC_{50}$  values allow comparison of the sensitivity of the (normal) cells and the toxicity of our unique AuNPs-PAA( $\pm$ Ctxb) with other reports in literature. As such, the  $EC_{50}$  value of A431 cells after 24h of exposure to AuNPs-PAA-Ctxb is 2.5 times lower than the  $EC_{50}$  value calculated for 30 nm citrate-reduced AuNPs on A431 cells<sup>531</sup>. As a result, our AuNPs-PAA-Ctxb have a much higher capacity to induce cell death in the tumor cells, whereas the reduced cytotoxicity of the AuNPs-PAA-Ctxb compared to AuNPs-PAA is advantageous for the normal healthy cells. Focusing on the kidney cells, incubation of normal human proximal tubular cells with 40 nm polyethylenimine-coated AuNPs has shown to activate pathways involved in apoptosis and DNA damage repair. An  $EC_{50}$  value of  $72.18 \mu\text{g/ml}$  was calculated after 24h of exposure, which is approximately 4-7 times higher than the  $EC_{50}$  value of the HK-2 cells in this study<sup>508</sup>. In the liver tissue, the RES is the main cause of rapid sequestration of AuNPs. Uptake of 5 nm polyvinylpyrrolidone-coated AuNPs ( $98 \mu\text{g/ml}$ ) in endocytic vesicles was observed in hepatocytes of rat liver precision-cut slices<sup>532</sup>. This uptake did not translate into significant cytotoxicity after 24h of exposure. The latter is consistent with 3.2 nm dihydrolipoic-coated gold nanoclusters ( $24.5 \mu\text{g/ml}$ ) causing no toxicity in the normal human liver L02 cell line after 72h of exposure<sup>532,533</sup>. In contrast, production of pro-inflammatory cytokines has been demonstrated in primary rat hepatocytes after 4h of incubation with 20 nm AuNPs ( $211.2 \mu\text{g/ml}$ ), showing a higher sensitivity than liver macrophages<sup>534</sup>. Furthermore, a time- and concentration-dependent uptake of 40 nm polyethylenimine-coated AuNPs in normal human hepatocytes resulted in oxidative stress. However, the calculated  $EC_{50}$  value of  $170 \mu\text{g/ml}$  after 24h of exposure is still 30 times higher than the  $EC_{50}$  value for the THLE-2 cells in this study<sup>509</sup>. Finally, we showed that TIME cells exhibit the highest sensitivity to AuNPs-PAA( $\pm$ Ctxb), which could be related to their clustered nanoparticle uptake observed by TEM imaging. It is noteworthy that the experiments were performed under static conditions, whereas the endothelial cell layer in particular is subjected to a continuous blood flow and shear stress *in vivo*. Fede et al (2015) revealed that

the cytotoxicity of PEG-coated AuNPs in HUVECs was significantly lower under flow-conditions than under static conditions. However, the toxicity increased with increasing concentrations and incubation times, which is consistent with our data<sup>524</sup>. Altogether, our results regarding cell viability and the above-mentioned reports demonstrate that the sensitivity to AuNPs-induced cytotoxicity depends on the cell type as well as on the nanoparticle size, coating, concentration and incubation time.

Multiple hypotheses have been proposed regarding how AuNPs interact with cellular components after endocytosis. For example, endosomal escape could lead to physical interaction between the AuNPs and biological components<sup>535,536</sup>. Others have reported on gold ion release due to particle degradation caused by the acidic lysosomal environment<sup>177,233,537</sup>. In order to gain knowledge regarding the underlying mechanisms of our AuNPs-PAA( $\pm$ Ctxb) cytotoxicity, we assessed apoptosis, mitochondrial dysfunction and measured antioxidant enzyme activities. Our results demonstrated that AuNPs-PAA( $\pm$ Ctxb) were able to decrease the TrxR and GR activity in normal cell types. Generally, the AuNPs-PAA( $\pm$ Ctxb) inhibited TrxR more effectively than GR, which may be ascribed to the high affinity of gold for the selenocysteine residue present in the active site of TrxR, but lacking in GR<sup>243</sup>. TIME cells showed the highest basal TrxR and GR activity, followed by THLE-2 cells and HK-2 cells. The abundance of TrxR in TIME cells could be related to the Trx system modulating angiogenic activities, such as endothelial migration, proliferation and vascular network formation<sup>538,539</sup>. Consequently, AuNPs-PAA( $\pm$ Ctxb) were able to exert a considerable stronger inhibitory effect on the TrxR (and GR) of TIME cells than on THLE-2 and HK-2 cells (6.3% of residual TrxR activity in TIME cells versus 15.3% in THLE-2 cells and 22.8% in HK-2 cells). Similar cell type-dependent differences in TrxR inhibition were reported in 5 cancer cell lines with A431 cells, the most resistant cell type in our experiments, having the lowest basal TrxR activity<sup>177,537</sup>. Inhibition of TrxR and GR creates a lack of reduced Trx and GSH, which are needed as substrates for peroxidases to eliminate H<sub>2</sub>O<sub>2</sub>. The disturbance in the thiol redox balance can lead to oxidative stress causing mitochondrial dysfunction<sup>540</sup>. Indeed, our results demonstrated a substantial depolarization of the mitochondrial membrane potential after 12h of AuNPs incubation, especially in TIME cells (60.4% of control fluorescence), in THLE-2 cells (79.2% of control fluorescence) and to a lesser extent in HK-2 cells (84.8% of control fluorescence). Furthermore, a strong correlation was observed between the extent of TrxR inhibition and the mitochondrial membrane depolarization (**Figure 3.9D**). The correlation analyses including EC<sub>50</sub> values (**Figure 3.9A-C**) indicate that the sensitivity of the cells to AuNPs-PAA( $\pm$ Ctxb) was strongly associated with the basal TrxR activity, the extent of TrxR inhibition and the mitochondrial membrane depolarization. Alternatively, EGFR expression and cellular AuNPs-PAA( $\pm$ Ctxb) interaction were less decisive, as shown by ICP-MS (maximum gold content of 0.98 pg/cell in HK-2 cells compared to 0.38 pg/cell in TIME cells).

Notably, the mitochondrial membrane depolarization recovered almost completely after 24h of exposure to a sub-lethal concentration of AuNPs-PAA( $\pm$ Ctxb). A possible explanation is given by Penninckx et al, who demonstrated a substantial increase of autophagic activity in A549 after 12-18h of AuNPs incubation, but no longer after 24h<sup>177</sup>. In addition, exposure to 50 nm citrate-capped AuNPs caused autophagy in HK-2 cells, promoting their cell survival<sup>261</sup>. This suggests that autophagy could be responsible for the observed cell recovery by providing energy through the lysosomal degradation of cytoplasmic constituents. However, next to serving as a cell survival mechanism, autophagy can also mediate the induction of apoptosis after exposure to AuNPs<sup>261</sup>. Furthermore, a link exists between apoptosis and the Trx system. More specifically, reduced Trx interacts with the apoptosis signaling kinase-1 (ASK-1) and prevents its homodimerization and activation. As Trx becomes oxidized, it dissociates from the complex and ASK1 induces the mitochondrial-dependent apoptotic pathway<sup>538,539</sup>. Since AuNPs-PAA( $\pm$ Ctxb) caused a strong TrxR inhibition, it can lead to a lack of reduced Trx and a pro-apoptotic status. The live cell imaging results showed that exposure to AuNPs-PAA( $\pm$ Ctxb) provoked a concentration- and time-dependent activation of caspase 3/7 and annexin V labeling, identifying apoptosis as a major mechanism of cell death.

We further verified the central role of oxidative stress in AuNPs-induced cytotoxicity by co-incubation of the cells with AuNPs-PAA( $\pm$ Ctxb) and NAC. In addition to its antioxidant function, NAC acts as a precursor for reduced glutathione and can replenish the depleted intracellular glutathione content. The latter has been observed in human leukemia cells, human hepatoma cells and normal human fibroblasts following exposure to AuNPs<sup>235,541</sup>. The results showed that co-incubation of the cells with NAC avoided the mitochondrial membrane depolarization and significantly reduced apoptotic cell death. This is consistent with results demonstrating that pre-exposure of HeLa cells and MCF-7 cells with NAC, glutathione, and triphenylphosphine monosulfonate (TPPMS) increased cell survival during exposure to 1.4 nm TPPMS-coated AuNPs and 3-10 nm chitosan-coated AuNPs<sup>253,527</sup>. However, pre-exposure with ascorbic acid, a non-thiol containing antioxidant, did not significantly reduce the toxicity of the AuNPs. Therefore, Pan et al suggested that thiol-containing antioxidants not only reduced the oxidative stress caused by the nanoparticles, but also could neutralize the AuNPs interactions with vital biological targets<sup>253</sup>.

Altogether, our findings in normal cells complement other studies demonstrating that AuNPs disturb the cellular redox balance, trigger mitochondrial dysfunction and could lead to apoptosis in various cancer cells<sup>177,180,233,244,246,251-253,528,537,542</sup>. In fact, the inhibition of TrxR and the mitochondrial dysfunction have been identified as important biological aspects of the AuNPs radiosensitization mechanism in therapeutic radiotherapy<sup>180,537</sup>. Consequently, basal TrxR activity could possibly be used as a tool to estimate the sensitivity of normal cells to AuNPs when a significant accumulated dose of AuNPs is expected after administration. It should be noted that the results of this study are based on one specific cell line originating from either the kidney, the liver or the microvasculature, and therefore warrants further *in*

*vivo* testing. Furthermore, this study stimulates future research to investigate AuNPs toxicity in normal human cells and tissues that encounter a significant dose of AuNPs after *in vivo* administration.

## 6. Conclusion

Since only a limited number of reports have been published investigating the toxicity of AuNPs on normal human cells, the present study complements the literature on the inhibitory effects of AuNPs investigated in cancer cells. The results of this study point out a general mechanism of cytotoxicity induced by AuNPs-PAA( $\pm$ Ctxb). However, the sensitivity to AuNPs-PAA( $\pm$ Ctxb) is cell-type dependent according to the cell type characteristics. More specifically, basal TrxR activity, TrxR inhibition and mitochondrial membrane depolarization were clearly correlated with the sensitivity of the cells to AuNPs-PAA( $\pm$ Ctxb). In contrast, EGFR expression and the subsequent cellular interactions with AuNPs-PAA( $\pm$ Ctxb) were less clear cut. Furthermore, we demonstrated that conjugation to Cetuximab reduced the cytotoxicity of the AuNPs-PAA, potentially due to the change in surface coating. This study paves the way to investigate basal TrxR activity as a potential tool to predict which healthy cells and tissues could exhibit a high sensitivity to AuNPs after administration. This supports the understanding of the risks associated with the use of AuNPs *in vivo*.

## 7. Supplemental information

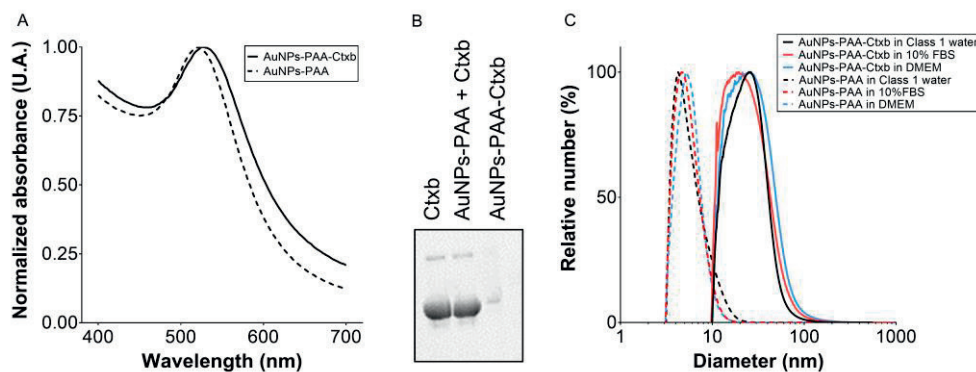


**Figure S3.1** UV-Vis spectrum of AuNPs-PAA and AuNPs-PAA-Ctxb (A). Gel electrophoresis of Ctxb, AuNPs-PAA + Ctxb and AuNPs-PAA-Ctxb (B). Size distribution curves (relative number) of AuNPs-PAA and AuNPs-PAA-Ctxb in MilliQ water, DMEM and DMEM + 10% FBS obtained from CPS Disk Centrifugation (C).

**Abbreviations:** AuNPs-PAA, polyallylamine-coated gold nanoparticles; Ctxb, Cetuximab; FBS, Fetal bovine serum; DMEM, Dulbecco's Modified Eagle Medium

$$y = \frac{k}{1 + \left(\frac{x}{x_{50}}\right)^s}$$

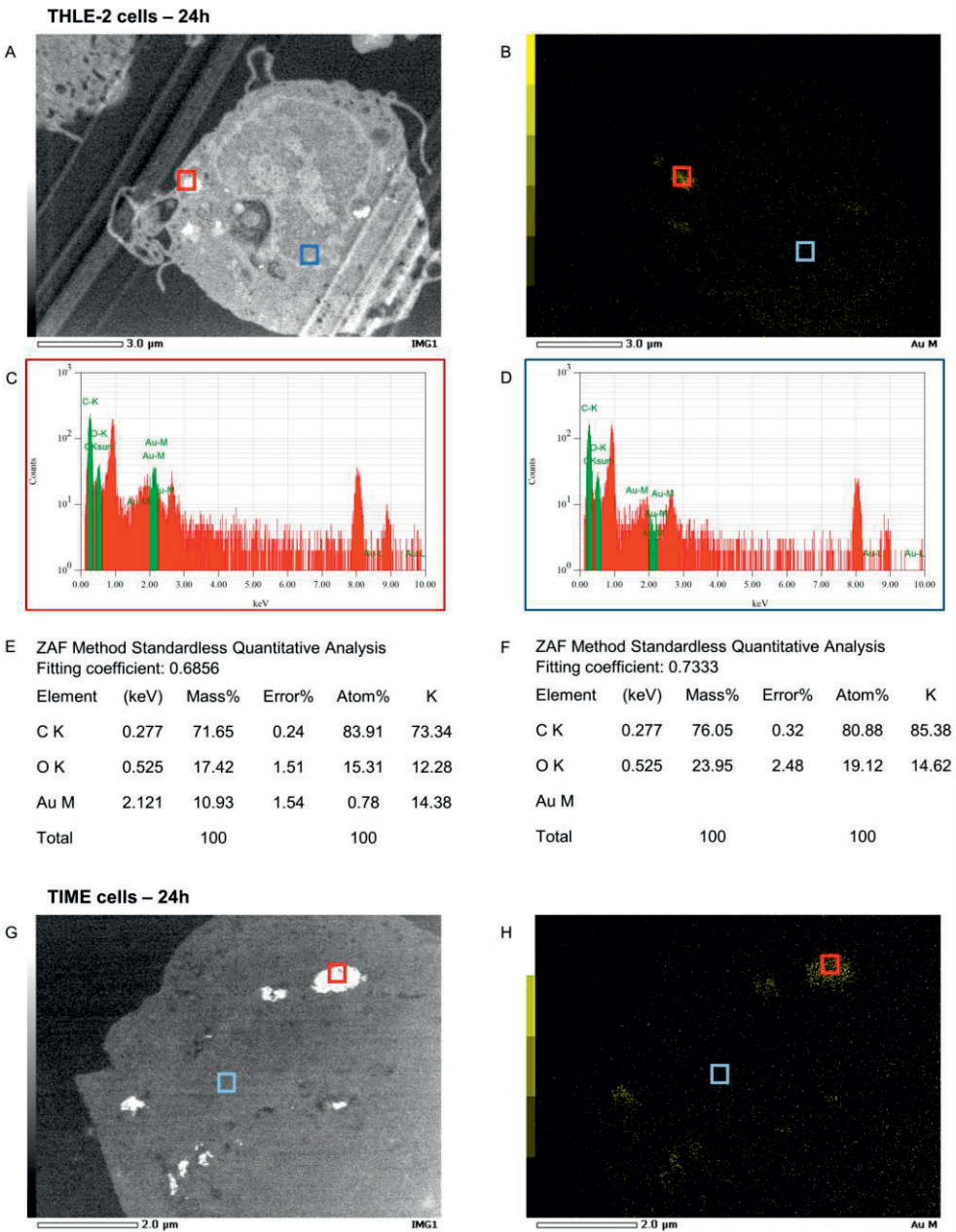
**Equation S3.1** Log-logistic function for curve fitting of the MTS viability data.

$$y = \frac{k (1 + gx)}{1 + (1 + 2gx_{50}) \left(\frac{x}{x_{50}}\right)^s}$$

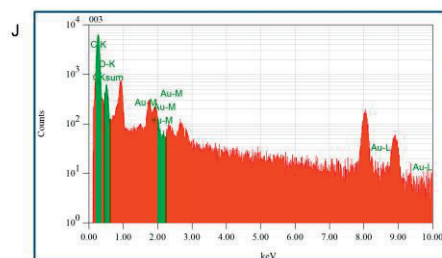
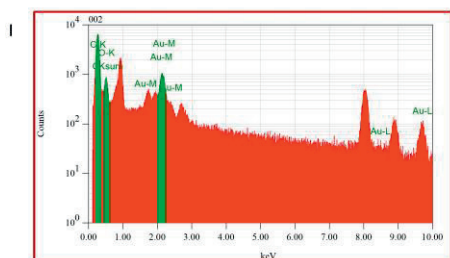
**Equation S3.2** Modified log-logistic function for curve fitting of the MTS viability data.

In both equations,  $y$  represents the experimental cell viability,  $x$  is the gold concentration and  $S$  defines the slope parameter. Moreover,  $k$  is the response at  $x = 0$  and  $x_{50}$  is the gold concentration at which the cell viability is reduced by 50% compared to control response. Finally, in the second equation,  $g$  represents the hormesis parameter, modelling a potential stimulatory effect of low gold concentrations.





# Gold nanoparticles affect the antioxidant status of selected normal human cells



K

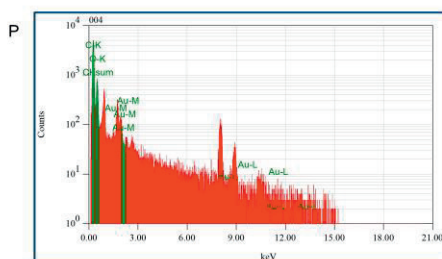
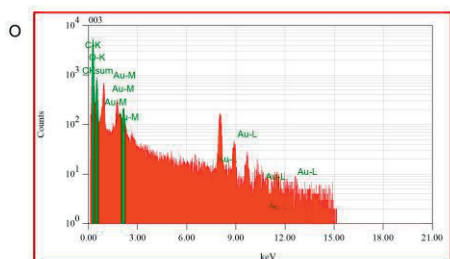
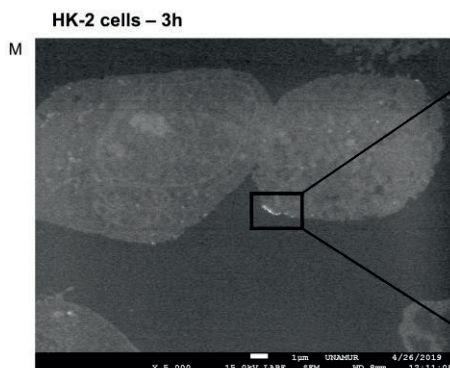
ZAF Method Standardless Quantitative Analysis  
Fitting coefficient: 0.4868

Element	(keV)	Mass%	Error%	Atom%	K
C K	0.277	73.77	0.12	86.31	75.00
O K	0.525	14.65	0.78	12.86	9.86
Au M	2.121	11.58	0.76	0.83	15.14
Total		100		100	

L

ZAF Method Standardless Quantitative Analysis  
Fitting coefficient: 0.4286

Element	(keV)	Mass%	Error%	Atom%	K
C K	0.277	79.47	0.09	83.75	88.56
O K	0.525	20.53	0.74	16.25	11.44
Au M					
Total		100		100	



Q

ZAF Method Standardless Quantitative Analysis  
Fitting coefficient: 0.4868

Element	(keV)	Mass%	Error%	Atom%	K
C K	0.277	73.04	0.07	79.75	80.72
O K	0.525	24.51	0.50	20.09	16.40
Au M	2.121	2.45	0.54	0.16	2.88
Total		100		100	

R

ZAF Method Standardless Quantitative Analysis  
Fitting coefficient: 0.4286

Element	(keV)	Mass%	Error%	Atom%	K
C K	0.277	73.36	0.06	78.58	82.58
O K	0.525	26.64	0.47	21.42	17.42
Au M					
Total		100		100	

**< Figure S3.2** Energy dispersive X-ray spectroscopy analysis on a representative THLE-2 cell (A), a TIME cell (G) and a HK-2 cell (M-N), which were treated with 5  $\mu\text{g Au/ml}$  of AuNPs-PAA-Ctxb for 3h or 24h. Gold mapping was performed on the THLE-2 cell (B) and the TIME cell (H). Bright signal zones (red squares) were analyzed resulting in specific X-ray spectra (C-I-O) and quantification of gold, carbon and oxygen (E-K-Q). No-signal zones (blue squares) were analyzed resulting in specific X-ray spectra (D-J-P) and the detection of only carbon and oxygen (F-L-R).

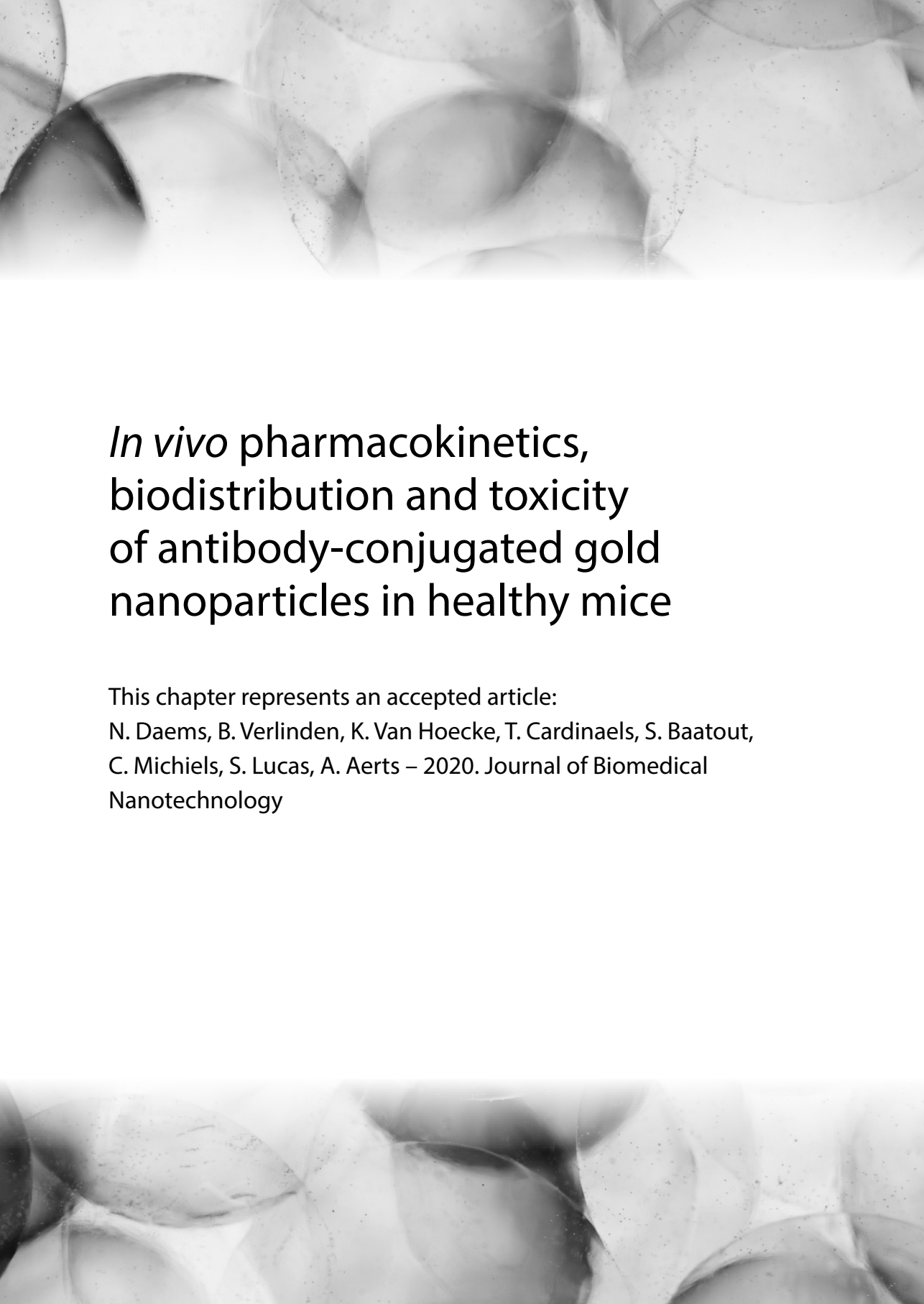




**CHAPTER**

# 4





# *In vivo* pharmacokinetics, biodistribution and toxicity of antibody-conjugated gold nanoparticles in healthy mice

This chapter represents an accepted article:

N. Daems, B. Verlinden, K. Van Hoecke, T. Cardinaels, S. Baatout,  
C. Michiels, S. Lucas, A. Aerts – 2020. Journal of Biomedical  
Nanotechnology

## 1. Abstract

Cetuximab-conjugated gold nanoparticles are known to target cancer cells, but display toxicity towards normal kidney, liver and endothelial cells *in vitro*. In this study, we investigated their pharmacokinetics, biodistribution and toxicity after intravenous administration in healthy mice. Our data showed that these nanoparticles were rapidly cleared from the blood and accumulated mainly in the liver and spleen with long-term retention. Acute liver injury, inflammatory activity and vascular damage were transient and negligible, as confirmed by the liver functionality tests and serum marker analysis. There was no sign of altered liver, kidney, lung and spleen morphology up to 4 weeks post-injection. After 6 months, kidney casts and splenic apoptosis appeared to be more prevalent than in the controls. Furthermore, occasional immune cell infiltration was observed in the lungs. Therefore, we recommend additional *in vivo* studies, in order to investigate the long-term toxicity and elimination of gold nanoparticles after multiple dosing in their preclinical validation as new targeted anti-cancer therapies.

## 2. Background

Over the last few decades, applications of gold nanoparticles (AuNPs) in nanomedicine have developed extensively due to their unique physicochemical properties. Furthermore, the possibility of modifying the surface of AuNPs with targeting agents strengthens their potential use in the diagnosis, monitoring and treatment of cancer<sup>19,543</sup>. Our previous studies have shown that AuNPs, coated with polyallylamine and conjugated to Cetuximab (AuNPs-PAA-Ctxb), successfully targeted cancer cells that were overexpressing the epidermal growth factor receptor (EGFR), both *in vitro* and *in vivo*<sup>360,474</sup>. Furthermore, AuNPs-PAA-Ctxb selectively radiosensitized EGFR-overexpressing cancer cells, thus increasing the efficacy of 25 keV/ $\mu$ m proton therapy (3.0 Gy) by 22%<sup>201,202</sup>. Several studies indicate that the physical interaction between AuNPs and radiation, leading to low-energy electron emission, is unlikely to be the only mechanism responsible for the radiosensitizing property of AuNPs<sup>210,214</sup>. In fact, it has been demonstrated that AuNPs also exert a direct biological effect on the cells. More specifically, AuNPs caused mitochondrial dysfunction, inhibition of the thioredoxin antioxidant defense system and oxidative stress in various cancer cells, which may predispose these cells to the damaging effects of ionizing radiation<sup>177,180,245,537</sup>. Moreover, we recently observed the same biological effects in non-cancerous, human kidney, liver and microvascular endothelial cells exposed to AuNPs-PAA-Ctxb *in vitro*. This indicates a general AuNP cytotoxicity mechanism, which is not cancer cell specific<sup>544</sup>.

When administered *in vivo*, the reticuloendothelial system (RES) is able to identify AuNPs as foreign substances that need to be sequestered and eliminated, while the renal system rapidly excretes AuNPs that are smaller than 5.5 nm. Therefore, the kidneys and RES organs, such as the liver, spleen and lungs can encounter a significant proportion of the administered AuNPs<sup>410</sup>. Therefore, although AuNPs hold promise to enhance the effectiveness of cancer radiotherapy, off-target accumulation and the cytotoxicity effects of AuNPs observed in normal cells warrant further investigation with respect to their potential toxicity and immunogenicity *in vivo*.

Several studies have reported on the toxicity of AuNPs *in vivo*, but with conflicting conclusions. Some reports have described how AuNPs can cause acute inflammation, changes in white blood cell levels, changes in liver and kidney functional parameters, emphysema of the lungs and damage to the liver, spleen and kidneys<sup>446,497,501,502,504,545</sup>. This is in contrast to other studies, which could not detect definite signs of *in vivo* toxicity<sup>451,453,455,546</sup>. This apparent discrepancy stems from differences in study set-up, with the administration route and dosage playing a pivotal role. In addition, the size, coating, surface charge and shape of the AuNPs also influenced the biodistribution and toxicity outcome<sup>453,461,511</sup>.



In this study, we investigated the pharmacokinetics, biodistribution and potential toxicity of our unique, in-house produced AuNPs-PAA-Ctxb in healthy BL6/57 male mice. As previously described, AuNPs-PAA-Ctxb are spherical and negatively charged ( $-7.04 \pm 0.22$  mV in cell culture medium, including 10% fetal bovine serum). These nanoparticles, including the gold core and coating, have a diameter of 4-5 nm, but the size increases to 26 nm if the antibody-functionalization is taken into account<sup>544</sup>. At specific time points after intravenous (IV) injection (5 min, 15 min, 30 min, 1h, 6h, 24h, 72h, 1 week, 4 weeks and 6 months), mice were sacrificed in order to collect their blood, lungs, kidneys, liver and spleen. The biodistribution of the AuNPs-PAA-Ctxb in these tissues was assessed using inductively coupled plasma mass spectrometry (ICP-MS). In addition, the *in vivo* toxicity was evaluated by monitoring the tissue morphology and functional parameters of the liver. Finally, we screened for certain cytokines that are involved in an immune response or specifically linked to cardiovascular damage because of the previously observed sensitivity of human microvascular endothelial cells to AuNPs-PAA-Ctxb<sup>544</sup>.

### 3. Methods

#### 3.1 Chemicals

Cetuximab (Erbix<sup>®</sup> 5 mg/ml) was kindly provided by the Sint-Dimpna Hospital (Geel, Belgium). Arabic gum (AG), the aspartate aminotransferase (AST) activity assay kit (MAK055), the alanine transaminase (ALT) activity assay kit (MAK052), the alkaline phosphatase (ALP) diethanolamine activity kit (AP0100), the gamma glutamyl transferase (GGT) activity colorimetric assay kit (MAK089), hematoxylin, eosin and formalin were purchased from Sigma-Aldrich (Diegem, Belgium). Paraplast Plus was obtained from Leica Microsystems (Diegem, Belgium) and Nembutal was purchased from Ceva Santé Animale N.V. (Brussels, Belgium). Nitric acid (HNO<sub>3</sub>), hydrochloric acid (HCl), hydrogen peroxide (H<sub>2</sub>O<sub>2</sub>) and hydrofluoric acid (HF) were of trace metal grade and purchased from Fisher Scientific (Merelbeke, Belgium). The external calibration and internal standards were prepared using SPEX Certiprep certified standard solutions (Boom B.V., Meppel, The Netherlands).

#### 3.2 Gold nanoparticles and antibody conjugation

AuNPs-PAA were produced and conjugated to Cetuximab as previously described<sup>201,471,544</sup>. Aliquots of 900 µg of gold were freeze-dried containing 3% AG. Before injection, the AuNPs-PAA-Ctxb were re-suspended in 1 ml of sterile 0.9% NaCl using pulsed sonication (50W, 30 kHz, 20% amplitude, 0.5 sec pulses).

#### 3.3 Animal study

Healthy adult (8-10 weeks) male C57/Bl6 mice were housed under standard laboratory conditions with a 12:12 hour light/dark cycle and 4-5 animals per cage. Food and water were available *ad libitum*. All animal experiments were approved by the Ethical Committee Animal

Studies of Medanex Clinic and conducted in compliance with the European Communities Council Directive of September 22, 2010. Ten groups of 5-6 animals received a single, non-lethal, IV injection of 100  $\mu$ l of AuNPs-PAA-Ctxb suspension (90  $\mu$ g of gold). The animals were anesthetized by intraperitoneal administration of 100  $\mu$ l Nembutal and euthanized by cardiac puncture, which enabled the collection of blood samples at 5 min, 15 min, 30 min, 1h, 6h, 24h, 72h and 1 week post-injection in EDTA-coated tubes. In addition, the liver, the spleen, the kidneys and the lungs were collected at 6h, 24h, 72h, 1 week, 4 weeks and 6 months post-injection. Control mice received 100  $\mu$ l of 0.9% NaCl or 3% AG and were euthanized at 6h, 24h or 6 months post-injection, as described above. All the animals were randomly assigned to each time point group.

### 3.4 Inductively coupled plasma mass spectrometry

The liver, spleen, right kidney and right lung intended for ICP-MS analysis were weighed and homogenized using the TissueLyser II (Qiagen, Antwerp, Belgium). Next, 25-75 mg of blood or homogenized tissue was digested in 3 ml concentrated  $\text{HNO}_3$  and 1 ml of  $\text{H}_2\text{O}_2$  for 4h at 110°C on a hotplate. The samples were evaporated to incipient dryness, followed by digestion with 4 ml of aqua regia overnight at 110°C. After evaporation, the dried samples were dissolved in 5-10 ml of 5% (v/v) aqua regia. Prior to a 2h UV digestion treatment in a 705 UV digester (Metrohm, Zwijndrecht, Belgium), the samples were spiked with 100  $\mu$ L of 30%  $\text{H}_2\text{O}_2$  to initiate radical formation. Finally, 0.05% HF was added to all samples in order to reduce Au memory effects in the ICP-MS introduction system. The gold concentration in the samples was quantified using an XSeriesII quadrupole ICP-MS instrument (ThermoFisher Scientific, Bremen, Germany) using external calibration standards containing 0.5, 1, 2 and 5 ng/mL of gold. Data was collected from 20 ms dwell time per isotope, 200 sweeps per reading, and 5 readings per sample. A rinsing time of 150 s with a solution containing 5% aqua regia and 0.05% HF was included between each sample. The elements Re, Ir, Tl were used as internal standards. The results are expressed as  $\mu$ g of gold per gram of tissue.

### 3.5 Histological examination

The right medial lobe of the liver, left kidney, left lung and 1/4<sup>th</sup> of the spleen intended for histological examination were fixed in 10% formalin for 24h, after which the samples were dehydrated and embedded in paraffin. Seven  $\mu$ m sections were then prepared and stained with hematoxylin and eosin (H&E) according to a standard protocol. Bright-field images were obtained using a Nikon Ti-Eclipse microscope.

### 3.6 Liver enzyme activity measurement and luminex analysis

Blood samples intended for liver enzyme activity measurements and luminex analysis were collected at 6h and 24h after injection in serum collection tubes. The blood samples were allowed to clot for 30 minutes at room temperature, after which serum was isolated by centrifugation at 10,000 g for 5 min, aliquoted and stored in Eppendorf tubes at -20°C until

analysis. In order to evaluate liver toxicity, the enzyme activity of AST, ALT, GGT and ALP in serum samples was measured. For this purpose, specific assay kits were used according to the manufacturer's instructions<sup>547-550</sup>. Samples were measured in duplicate and results were expressed as milliunits/ml (mU/ml). In order to evaluate immunotoxicity and cardiovascular damage, serum levels of CCL2, CCL5, CXCL10, EGF, FGF2, GDF-15, ICAM-1, IFN $\gamma$ , IL-1 $\beta$ , IL-2, IL-4, IL-6, IL-10, PCK9, P-Selectin, TNF $\alpha$ , uPAR were analyzed using a multiplex magnetic bead array (R&D systems). The luminex assay was performed according to manufacturer's instructions<sup>551</sup>. Samples were measured in duplicate using a Luminex 200 and analyzed with xPONENT 3.1 (Luminex Corporation).

### 3.7 Statistical analysis

Results were reported as a mean  $\pm$  standard error (SE). The treatment time is one variable and the dose remains constant. Therefore, a parametric one-way ANOVA was used to compare the multiple animal groups (more than two groups) that were treated for different time periods to the control groups (0.9% NaCl and arabic gum) for the enzyme activity assay and for the luminex assay, and to the 6 hours treatment groups for the ICP-MS assay. The Holm-Sidak test was chosen as post-hoc test, since it has a high power to identify significant pairs. The statistical analyses were performed using Prism 7.02 software. The level of statistical significance is indicated by the number of asterisks as follows: \* $p < 0.05$ , \*\* $p < 0.01$ , \*\*\* $p < 0.001$ , \*\*\*\* $p < 0.0001$ .

## 4. Results

### 4.1 Blood clearance

The AuNPs-PAA-Ctxb blood concentration-time curve was fitted by a three-phase exponential decay function, using Origin 2017 (**Figure 4.1**). The pharmacokinetic parameters are summarized in **Table 4.1**. The maximum Au concentration ( $C_{max}$ ) in the blood was reached immediately after IV injection ( $T_{max}$ ). Our data showed that AuNPs-PAA-Ctxb were rapidly eliminated from the blood circulation, leading to a rapid fall in the initial gold concentration. This explains the short initial half-life ( $T_{1/2\alpha}$ ) of 2.3 minutes (i.e. the time required for the Au concentration in the blood to decrease by 50% of its initial value at  $T_{max}$  (5 min post-injection)). This fast clearance was followed by a more gradual decline in Au concentration, which was associated with longer half-lives ( $T_{1/2\beta}$  and  $T_{1/2\gamma}$ ). After 6h, 97% of the initial Au concentration was removed from the blood. Since the gold content in the blood was detected until 1 week after injection, an area under the curve (AUC) of 22.3  $\mu\text{g.h.ml}^{-1}$  and an average blood clearance ( $C_{bl}$ ) of 4.0  $\text{ml.h}^{-1}$  were calculated.

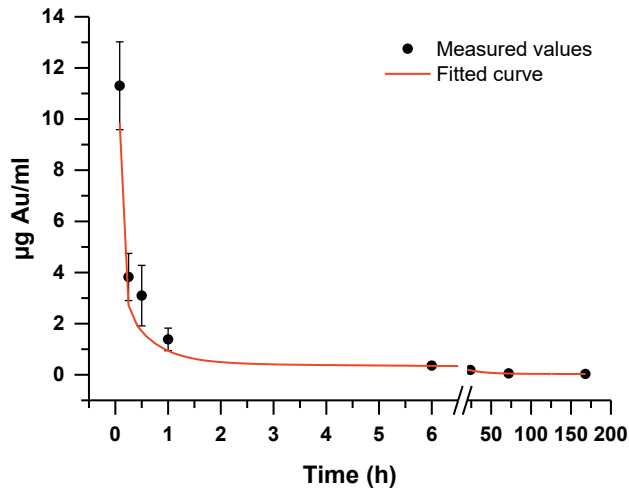


**Figure 4.1** Blood pharmacokinetic profile of AuNPs-PAA-Ctxb. Mean gold concentration ( $\mu\text{g/ml}$ ) in the blood at 5 min, 15 min, 30 min, 1h, 6h, 24h, 72h and 1 week after a single IV administration (90  $\mu\text{g}$  gold). Error bars represent SE ( $n = 5-6$ ).

**Abbreviations:** AuNPs-PAA-Ctxb: gold nanoparticles coated with poly-allylamine and conjugated to Cetuximab; IV: intravenous; SE: standard error.

**Table 4.1** Pharmacokinetic parameters based on the AuNPs-PAA-Ctxb blood concentration-time curve.

Parameter	AuNPs-PAA-Ctxb
$T_{\text{max}}$	5 min
$C_{\text{max}}$	$11.3 \mu\text{g} \cdot \text{ml}^{-1}$
$T_{1/2\alpha}$	2.3 min
$T_{1/2\beta}$	23.1 min
$T_{1/2\gamma}$	15.6 h
$\text{AUC}_{0\text{h} \rightarrow 1 \text{ week}}$	$22.3 \mu\text{g} \cdot \text{h} \cdot \text{ml}^{-1}$
$C_{\text{bl}}$	$4.0 \text{ ml} \cdot \text{h}^{-1}$

**Abbreviations:** AuNPs-PAA-Ctxb: gold nanoparticles coated with poly-allylamine and conjugated to Cetuximab;  $T_{\text{max}}$ : time point of maximal observed concentration;  $C_{\text{max}}$ : Maximal observed concentration;  $T_{1/2\alpha}$ : short half-life;  $T_{1/2\beta}$ : medium half-life;  $T_{1/2\gamma}$ : long half-life; AUC: area under the curve;  $C_{\text{bl}}$ : average blood clearance over 1 week.

## 4.2 Tissue distribution

In terms of pharmacokinetics, we observed a rapid clearance of the AuNPs-PAA-Ctxb from the blood to the tissues. Sequestration of AuNPs by the RES organs is a well-known phenomenon after IV administration<sup>426</sup>. Furthermore, the kidneys can eliminate AuNPs that are smaller than 5.5 nm<sup>410</sup>. Considering the above, we assessed the concentration of AuNPs-PAA-Ctxb using ICP-MS in several RES organs (i.e. liver, spleen, lungs) and the kidneys. Since 97% of the AuNPs-PAA-Ctxb were cleared from the blood circulation after 6h, AuNPs-PAA-Ctxb distribution was assessed at 6h, and further monitored at 24h, 72h, 1 week, 4 weeks

and 6 months post-administration. **Figure 4.2** indicates that AuNPs-PAA-Ctxb accumulated primarily in the liver and the spleen. The gold concentration ( $\mu\text{g gold/g tissue}$ ) was highest in the spleen, followed by the liver, lung and kidney. However, considering the different sizes of the organs, the percentage of injected dose (%ID) was higher in the liver than in the spleen (**Table 4.2**). In the liver, the gold concentration significantly increased over time, reaching a maximum value after 72h (67.24  $\mu\text{g/g}$ ). A similar increasing trend in gold concentration was observed in the spleen (maximum after 72h: 96.34  $\mu\text{g/g}$ ). In both liver and spleen, the increase in gold concentration was followed by a significant decline after 6 months (32.11  $\mu\text{g/g}$  liver and 41.76  $\mu\text{g/g}$  spleen). In the lung, the maximum gold concentration was observed after 6h (7.014  $\mu\text{g/g}$ ). This concentration then significantly decreased after 24h (2.749  $\mu\text{g/g}$ ). Finally, the lowest gold concentrations were observed in the kidney (maximum after 24h: 0.765  $\mu\text{g/g}$ ), which significantly decreased after 1 week (0.446  $\mu\text{g/g}$ ).

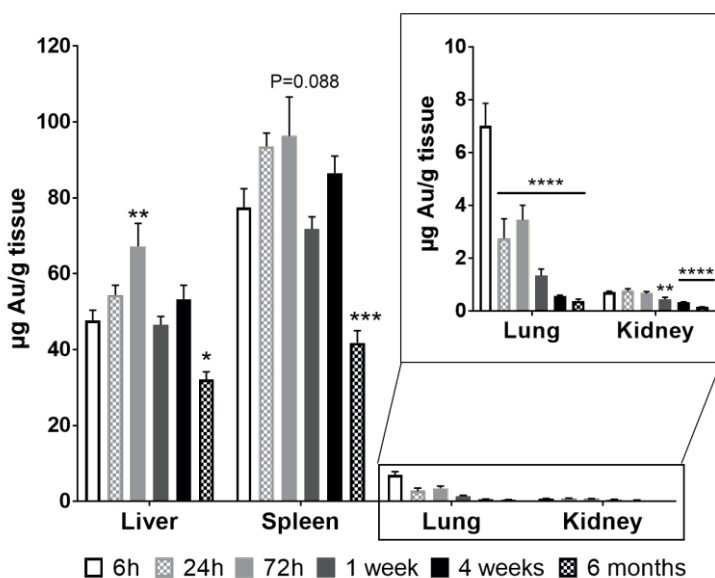


**Figure 4.2** Biodistribution of AuNPs-PAA-Ctxb. Mean gold concentration ( $\mu\text{g/g}$ ) in liver, spleen, kidney and lung at 6h, 24h, 72h, 1 week, 4 weeks and 6 months after a single IV injection (90  $\mu\text{g}$  gold). Error bars represent SE (n = 5-6). The statistical difference compared to 6h post-injection was calculated by a One-way ANOVA and a Holm-Sidak post-hoc test (\*p<0.05, \*\*p<0.01, \*\*\*p<0.001 \*\*\*\*p<0.0001).

**Abbreviations:** AuNPs-PAA-Ctxb: Gold nanoparticles coated with poly-allylamine and conjugated to Cetuximab; IV: intravenous; SE: standard error.

**Table 4.2** Biodistribution of AuNPs-PAA-Ctxb in liver, spleen, lung and kidney at 6h, 24h, 72h, 1 week, 4 weeks and 6 months after a single IV injection (90 µg gold) (n = 5-6). Results are expressed as mean %ID ± SE. Statistical difference as compared to 6h post-injection was calculated by a One-way ANOVA and a Holm-Sidak post-hoc test (\*p<0.05, \*\*p<0.01, \*\*\*p<0.001 \*\*\*\*p<0.0001).

Theoretically calculated percentage of injected dose (%ID) (mean±SE)					
	Liver	Spleen	Lung	Kidney	Other
6h	50±3	4.5±0.3	0.72±0.07	0.124±0.005	45
24h	48±5	5.5±0.4	0.30±0.08****	0.14±0.02	46
72h	62±2*	5.5±0.7	0.36±0.06****	0.106±0.009	32
1 week	52±1	3.9±0.3	0.15±0.02****	0.08±0.01*	44
4 weeks	47±2	5.5±0.5	0.069±0.007****	0.061±0.005**	47
6 months	40±3 (p = 0.058)	2.4±0.2**	0.045±0.008****	0.033±0.002****	58

**Abbreviations:** AuNPs-PAA-Ctxb: gold nanoparticles coated with poly-allylamine and conjugated to Cetuximab; IV: intravenous; %ID: percentage of the injected dose; SE: standard error.

### 4.3 Evaluation of liver toxicity

Our biodistribution results showed that a major proportion of the injected AuNPs-PAA-Ctxb accumulated in the liver. Therefore, we evaluated the effect of AuNPs-PAA-Ctxb on the liver by measuring the activity of serum ALT, ALP, AST and GGT. Since 97% of the AuNPs-PAA-Ctxb were distributed to the tissues after 6h, we assessed acute responses at 6h and 24h post-injection. AuNPs-PAA-Ctxb injection led to a small, but significant increase in ALT activity after 6h, as compared to the arabic gum control group (**Figure 4.3A**). Similarly, AST activity significantly increased 6h after AuNPs-PAA-Ctxb injection, compared to the 0.9% NaCl control group (**Figure 4.3B**). In both cases, the increase was transient and undetectable after 24h. In terms of ALP activity, no significant differences were observed (**Figure 4.3C**). Finally, GGT activity was undetectable in all serum samples.

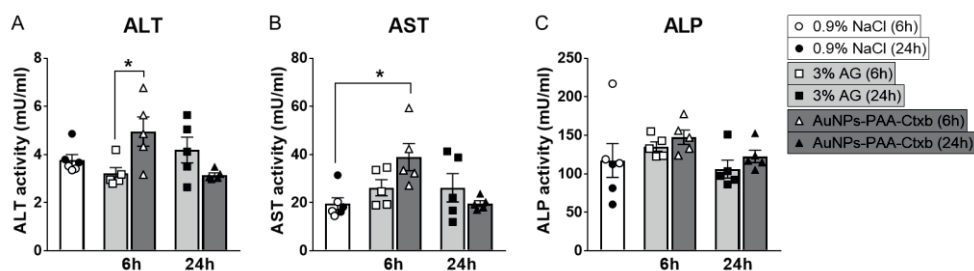


**Figure 4.3** Liver functionality tests. Liver enzyme activity of (A) ALT, (B) AST and (C) ALP in mouse serum at 6h and 24h after a single IV injection of AuNPs-PAA-Ctxb (90 µg Au), 0.9% NaCl or AG. Graphs show individual data points and the mean activity (mU/ml) represented by columns. Error bars represent SE (n = 5-6). The statistical difference between the treated groups and the 0.9% NaCl control group or the 3% AG control group was calculated by a One-way ANOVA and a Holm-Sidak post-hoc test (\*p<0.05).

**Abbreviations:** AG: Arabic gum; ALP: alkaline phosphatase; ALT: the alanine transaminase; AST: aspartate aminotransferase; AuNPs-PAA-Ctxb: gold nanoparticles coated with poly-allylamine and conjugated to Cetuximab; IV: intravenous; SE: standard error.

## 4.4 Evaluation of immunotoxicity and vascular damage

The liver and spleen are important lymphoid organs with resident immune cells that can mount a rapid immune response when they encounter antigenic particles. Furthermore, in our previous research, we demonstrated that microvascular endothelial cells were the most sensitive cells to AuNPs-PAA-Ctxb when compared to human kidney and liver cells<sup>544</sup>. Therefore, we measured the serum levels of several markers that are related to inflammatory activity and vascular damage (RANTES, IFN $\gamma$ , IL-1 $\beta$ , IL-2, IL-4, IL-6, IL-10, TNF $\alpha$ , GDF-15, ICAM-1, CCL2, CXCL-10, P-selectin, PCSK9, uPAR). Since the RES organs rapidly sequester the injected AuNPs-PAA-Ctxb, we assessed responses 6h and 24h post-injection. No significant increases in serum levels of TNF $\alpha$ , CCL2, IL-1 $\beta$ , IL-2, IL-4, IL-6, IL-10, IFN $\gamma$ , CXCL-10, PCSK9 and uPAR were observed after administration of AuNPs-PAA-Ctxb (**Supplemental Figure 4.1**). On the contrary, serum levels of GDF-15 and P-selectin significantly increased 6h after AuNPs-PAA-Ctxb injection, as compared to both the 0.9% NaCl and AG control groups. This response was transient and no longer detectable after 24h (**Figure 4.4A-B**). In addition, ICAM-1 levels significantly increased 6h after AuNPs-PAA-Ctxb injection, as compared to the 0.9% NaCl control group, and remained significantly elevated after 24h, as compared to both the 0.9% NaCl and AG control groups. It should be noted that a near-significant increase in the ICAM-1 level was also observed 6h after AG administration, compared to the 0.9% NaCl control group ( $p = 0.051$ ) (**Figure 4.4C**), which was not maintained after 24h. Finally, the serum level of RANTES significantly increased 6h after AG administration compared to the 0.9% NaCl control group, but was no longer detected after 24h (**Figure 4.4D**).

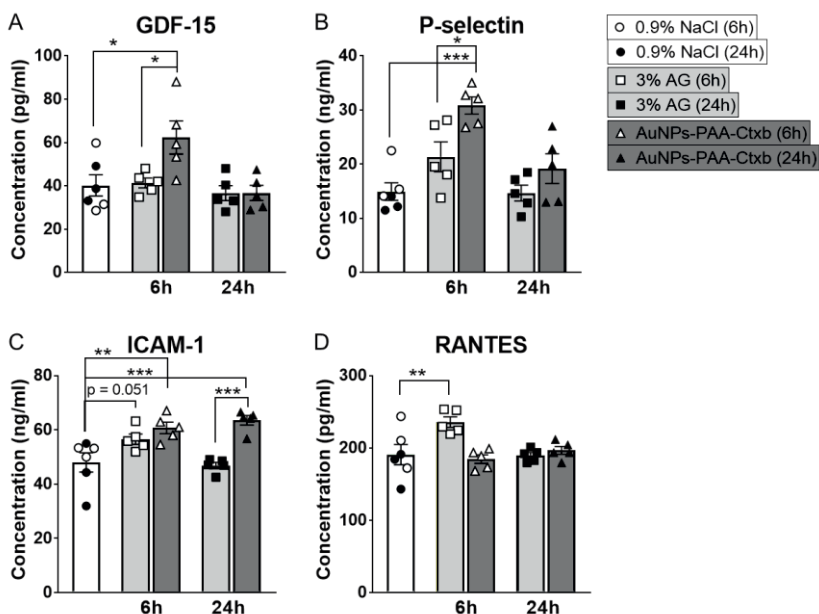


**Figure 4.4** Markers related to inflammatory activity and vascular damage. Serum levels of (A) GDF-15, (B) P-selectin, (C) ICAM-1 and (D) RANTES in mouse serum at 6h and 24h after a single IV injection of AuNPs-PAA-Ctxb (90 µg Au), 0.9% NaCl or AG. Graphs show individual data points and the mean concentration (pg or ng/ml) represented by columns. Error bars represent SE (n = 5-6). The statistical difference between the treated groups and the 0.9% NaCl control group or the 3% AG control group was calculated by a One-way ANOVA and a Holm-Sidak post-hoc test (\* $p < 0.05$ , \*\* $p < 0.01$ , \*\*\* $p < 0.001$ ). **Abbreviations:** AG: Arabic gum; AuNPs-PAA-Ctxb: gold nanoparticles coated with poly-allylamine and conjugated to Cetuximab; IV: intravenous; SE: standard error.

## 4.5 Histological examination

Our biodistribution studies showed that a major proportion of the AuNPs-PAA-Ctxb remained in the liver and spleen 6 months post-injection. Therefore, potential morphological effects of AuNPs-PAA-Ctxb in the organs due to long-term exposure should be considered. Hematoxylin and eosin staining demonstrated normal morphology of the liver (hepatocytes), spleen, kidney (glomeruli and tubules) and lungs (alveoli) 1 week and 4 weeks post-injection (

**Figure 4.5**). After 6 months, we observed a modest increase in the number of casts in the collecting tubules of the kidneys (5 out of 6 mice). Furthermore, apoptotic lesions in B-cell rich areas (germinal centers) in the white pulp of the spleen were more noticeable than in the control group (5 out of 6 animals). Finally, some immune cell infiltrations were found in the lungs (4 out of 6 animals). Although the liver accumulated a significant proportion of the injected AuNPs-PAA-Ctxb, no major morphological changes were observed after 6 months.



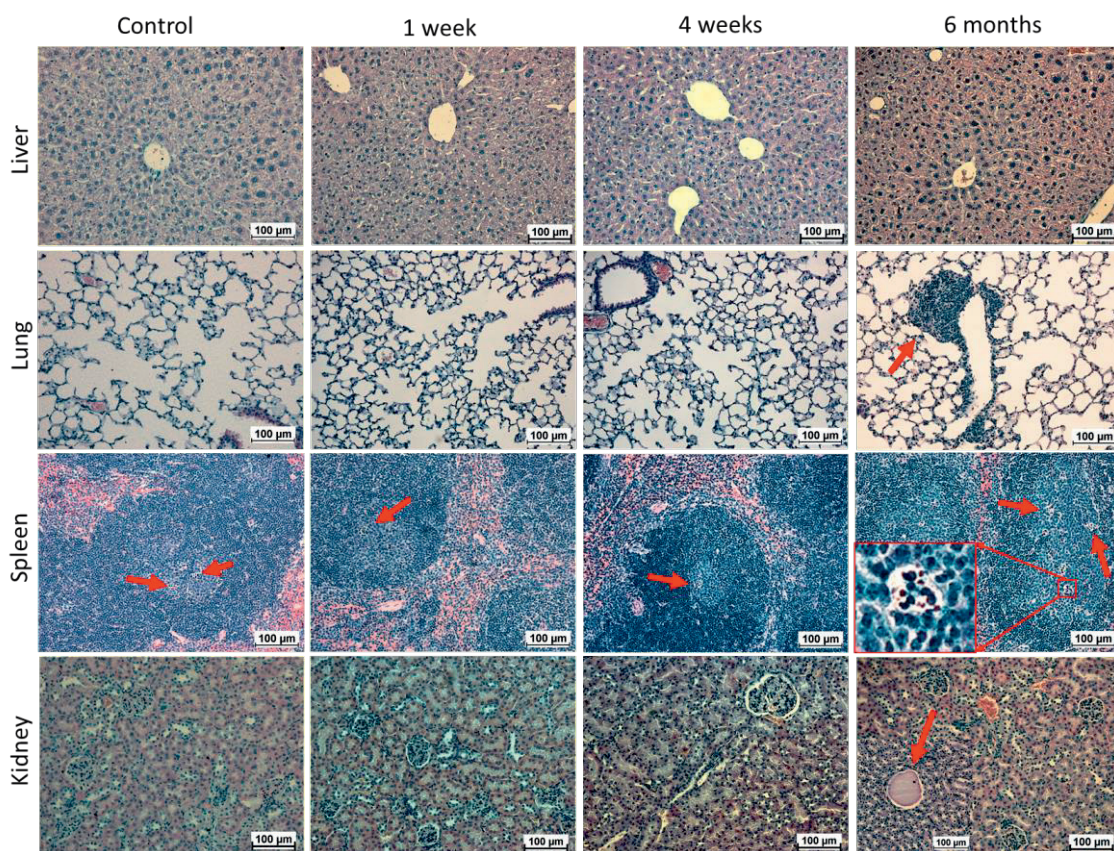


**Figure 4.5** Histological examination. Mouse liver, kidney, spleen and lung at 1 week, 4 weeks and 6 months after a single IV administration of AuNPs-PAA-Ctxb (90 µg Au), compared to the age-related control group, which did not receive AuNPs-PAA-Ctxb. Sections were stained with hematoxylin and eosin. Red arrows indicate immune cell infiltration in the lung, apoptotic cells in the spleen and cast in the collecting tubules of the kidney.

**Abbreviations:** AuNPs-PAA-Ctxb: gold nanoparticles coated with poly-allylamine and conjugated to Cetuximab; IV: intravenous.

## 5. Discussion

This study focused on the pharmacokinetics, biodistribution and toxicity of our unique in-house produced AuNPs-PAA-Ctxb. The dose was fixed at a single IV injection of 90 µg of gold ( $7.1 \times 10^{13}$  AuNPs-PAA-Ctxb). Based on a previous *in vitro* study, in theory, this dose would be sufficient to radiosensitize a small tumor of 11 cm<sup>3</sup> ( $1.1 \times 10^9$  cells) when (1) the dose is extrapolated to a person weighing 60 kg and (2) taking into account that 0.7% of the injected dose would reach the tumor <sup>201,360,410,474,552</sup>. In addition, this dose corresponds to the

standard dose range used in most studies, which allows us to compare our results with various *in vivo* studies<sup>461</sup>. The pharmacokinetic data indicated that the AuNPs-PAA-Ctxb were promptly eliminated from the blood stream with a short half-life of 2.3 minutes. This was followed by a predominant accumulation in the liver and spleen, and only a minor uptake in the kidneys and lungs. This observation is similar to the results of a recent study investigating laser-ablated, dextran-coated AuNPs, which had a diameter of 21 nm and were negatively charged. The authors demonstrated an initial blood half-life of 4.2 minutes and identified the liver and spleen as preferential sites for gold accumulation<sup>452</sup>. The pharmacokinetic results and biodistribution are partly related to the nanoparticle zeta potential and administration mode. Intravenous administration of nanoparticles is typically characterized by the fast adsorption of proteins to the nanoparticle surface, creating a biological identity that is presented to the cells. Charged AuNPs have been shown to adsorb more and a wider variety of proteins than neutral AuNPs. The formation of this protein corona strongly affects the AuNP biodistribution and biological impacts. For instance, adsorption of opsonins, such as complement factors, fibrinogen and IgG antibodies promotes the recognition of nanoparticles by the RES<sup>553</sup>. Since our AuNPs-PAA-Ctxb are negatively charged ( $-7.04 \pm 0.22$  mV in cell culture medium including 10% fetal bovine serum), opsonization is likely to occur, leading to the subsequent uptake by phagocytic cells that are in direct contact with the blood and present in the liver and spleen. Nevertheless, IV delivery is a realistic exposure scenario for AuNPs intended to be used in nanomedicine because it resists proteolytic degradation, achieves maximum bioavailability of the drug and allows fast onset of action<sup>554</sup>. Other administration routes investigated in literature are oral and intraperitoneal administration. Oral administration of AuNPs is usually associated with low systemic absorption and high gastro-intestinal elimination<sup>383,555-557</sup>, whereas intraperitoneal administration is followed by retention in the peritoneal cavity, delayed and reduced accumulation in the liver and spleen, and uptake in the pancreas, lungs, lymph nodes and intestine<sup>317,321,558,559</sup>. Subcutaneous administration of AuNPs has been used to visualize sentinel lymph nodes<sup>336</sup>.

The rapid sequestration by the RES after IV administration could potentially be delayed by modifying the surface of AuNPs with nonionic, sterically stabilizing hydrophilic polymers, such as polyethylene glycol (PEG). This would neutralize the surface charges of AuNPs, shield them from opsonization, and therefore prolong their blood circulation half-life<sup>426,429,446,487,493,494,560-564</sup>. Furthermore, predominant accumulation in the liver and spleen increases as the particle size increases, whereas small AuNPs (1.4-10 nm) have a wider organ distribution profile, with particles detected in the brain, heart, uterus, testis, thymus, kidneys and lungs<sup>426,490-492</sup>. It is possible that the size of our AuNPs-PAA-Ctxb (26 nm), together with a negative surface charge, favors their uptake by the liver and spleen after IV injection.

Interestingly, although 97% of the injected AuNPs-PAA-Ctxb were cleared from the blood after 6h, an increasing trend in gold concentration was observed in the liver and spleen for up to 72h post-injection. Comparable results were obtained with PEGylated AuNPs of

different sizes (6.2 nm – 61.2 nm) or with different shapes (rods and triangles) reaching maximum gold concentrations in the liver and spleen between 24h and 6 days post-injection<sup>457,565</sup>. This increase could potentially be attributed to a gradual redistribution of AuNPs-PAA-Ctxb from other tissues to the liver and spleen<sup>451</sup>. Furthermore, with a diameter of approximately 26 nm and a negative surface charge, AuNPs-PAA-Ctxb are less likely to be efficiently excreted by the negatively charged glomeruli, thus allowing redistribution to occur<sup>511</sup>. This is consistent with our biodistribution data illustrating the lowest amount of gold in the kidneys. In contrast to the liver and spleen, the gold concentration in the lungs and kidneys did not initially increase, but instead progressively decreased after 24h and 1 week, respectively.

After sequestration in the liver and spleen, AuNPs-PAA-Ctxb showed a long-term retention, with their concentration significantly decreasing only after 6 months. This indicates a slow elimination process, which has also been reported by several other long-term biodistribution studies<sup>453,462,511,565,566</sup>. In addition, it was reported that negatively charged particles were retained for slightly longer in the liver and spleen, and were eliminated more slowly compared to positively or neutrally charged particles<sup>491,511</sup>. The phagocytic cells in the RES system are responsible for recognizing and clearing AuNPs after IV administration<sup>426</sup>. Sadauskas et al (2009) investigated what happens to negatively charged 40 nm AuNPs in the liver and revealed that they were clustered inside endosome-like vesicles in long-living Kupffer cells, over a period of 6 months, and that damaged cells were cleared by new or nearby Kupffer cells<sup>462</sup>. The presence of PEGylated AuNPs in intracellular vesicles was also confirmed in splenic macrophages<sup>446,565</sup>. In addition, a recent study demonstrated that the depletion of Kupffer cells greatly improved the elimination efficiency of PEGylated AuNPs. Furthermore, ultra-small 4 nm AuNPs underwent a more efficient hepatobiliary elimination than larger particles, because they were less efficiently captured by the Kupffer cells and had a greater chance of moving from the liver endothelium to the hepatocytes<sup>362</sup>. According to our pharmacokinetic and biodistribution data and the above studies, we could assume that the characteristics of our AuNPs-PAA-Ctxb promote their rapid sequestration by the Kupffer cells and splenic macrophages after IV administration. The clearance of the AuNPs-PAA-Ctxb by these cells protects the organism from exposure to AuNPs-PAA-Ctxb and their related metabolites. However, it also prevents efficient nanoparticle elimination from the body, which explains their long-term retention. Although the elimination pathways are not assessed in this research, significant reduction of the gold concentration in the liver after 6 months could potentially result from occasional lysosomal damage and macrophage cell death, induced by the non-biodegradable AuNPs<sup>255</sup>. Subsequently, the hepatocytes could internalize some of the released AuNPs, thus leading to gradual and slow elimination via the hepatobiliary pathway<sup>426,462</sup>. Renal elimination of AuNPs-PAA-Ctxb is less likely, due to their size and negative surface charge, as mentioned earlier. The localization of a small amount of

AuNPs-PAA-Ctxb in lungs and kidneys is less clear, but resident alveolar and kidney macrophages could be involved.

Since the AuNPs-PAA-Ctxb were rapidly removed from the blood circulation and mainly sequestered by the liver, we were interested in the effects of AuNPs-PAA-Ctxb on the liver. Therefore, we investigated the activity of the liver enzymes ALT, ALP, AST and GGT in serum 6h and 24h post-injection. GGT activity was undetectable in all serum samples, and ALP activity was not significantly different from the control groups. This suggests that there was no obstruction of the biliary tract. However, AST and ALT activities (characteristic for hepatocellular injury) were significantly increased 6h after AuNPs-PAA-Ctxb injection, compared to the 0.9% NaCl or AG control groups, respectively. These increases were no longer detectable after 24h. Since the ALT and AST increases were minimal (1.5 and 2 times, respectively) we should question whether the statistically significant differences were also biologically and toxicologically relevant. In comparison, a toxic dose of acetaminophen, which results in severe liver injury, can increase the serum ALT and AST activities to several hundreds to thousands U/L in mice and rats, 4-12h after administration. These activities can increase further after 24h<sup>567,568</sup>. Therefore, if the AST and ALT activity increases in our study were indeed biologically relevant, then the AuNPs-PAA-Ctxb-induced stress to the liver was only mild and transient. Several other studies observed no significantly elevated liver enzyme activities up to 90 days after AuNPs administration compared to the controls<sup>451-455,511,563,569-571</sup>. Injection of 3% AG did not significantly affect the enzyme activities compared to the 0.9% NaCl controls, indicating that AG does not lead to hepatic injury.

In our previous *in vitro* study, microvascular endothelial cells were shown to be the most sensitive cells to AuNPs-PAA-Ctxb, compared to human kidney and liver cells. Therefore, we investigated the serum levels of specific cytokines related to vascular damage and inflammatory activity. Out of all the cytokines that we investigated (RANTES, IFN $\gamma$ , IL-1 $\beta$ , IL-2, IL-4, IL-6, IL-10, TNF $\alpha$ , GDF-15, ICAM-1, CCL2, CXCL-10, P-selectin, PCSK9, uPAR), only the serum levels of GDF-15, P-selectin and ICAM-1 significantly increased 6h after AuNPs-PAA-Ctxb administration, when compared to the 0.9% NaCl and AG control groups. For GDF-15 and P-selectin, the increases were transient and no longer detectable after 24h. The serum level of ICAM-1 remained elevated after 24h. It should be noted that ICAM-1 was also near-significantly elevated 6h after AG injection, when compared to the 0.9% NaCl control group. Unlike after AuNPs-PAA-Ctxb injection, ICAM-1 level was no longer increased 24h after AG injection. Therefore, we could suggest that AG might transiently increase ICAM-1 expression, which could be enhanced and prolonged by AuNPs-PAA-Ctxb. Finally, the chemokine RANTES was significantly elevated 6h after AG administration, compared to the 0.9% NaCl control group. However, this was not observed 6h after AuNPs-PAA-Ctxb administration, which questions the biological relevance of the increase or indicates that AuNPs-PAA-Ctxb eliminated the effect of AG on RANTES expression. GDF-15, P-selectin and ICAM-1 have been identified as biomarkers that reflect acute inflammation, endothelial cell activation and the

recruitment of leukocytes to the vessel wall<sup>572</sup>. However, the increases associated with these markers in this study were slight and mostly transient. Furthermore, levels of none of the other pro-inflammatory cytokines were significantly elevated. Based on these findings, we could propose that the risk of vascular damage and any acute immune response elicited by our AuNPs-PAA-Ctxb is limited. In the literature, different outcomes on immunoreactivity after AuNPs administration were identified. For example, liver mRNA levels of several adhesion molecules (ICAM-1, E-selectin and VCAM-1), chemokines (CCL-2, CCL-3, MIP-1 $\beta$  and RANTES) and inflammatory cytokines (IL-1 $\beta$ , IL-6, IL-10, IL-12 $\beta$  and TNF $\alpha$ ) were transiently elevated 30 min to 24h after administration of AuNPs, which suggests the presence of an acute immune response<sup>446,573</sup>. In contrast, various other studies observed no significant differences in hematological white blood cell indices and TNF- $\alpha$ , IL-1 $\beta$ , IL-6 and IL-10 levels after AuNPs administration<sup>451-453,455,563,569-571,574</sup>. Interestingly, a study focusing on the effects of antibody-conjugated AuNPs on the vascular system found that IV injection of AuNP-IgG even suppressed leukocyte adhesion to vessel walls. Furthermore, AuNPs-IgG prevented the expression of adhesion molecule PECAM-1, chemotaxis and oxidative stress activation on neutrophils after stimulation, which suggests an anti-inflammatory effect<sup>575</sup>.

Finally, since the AuNPs-PAA-Ctxb had a slow excretion rate from the body, we performed histological examinations at 1 week, 4 weeks and 6 months after injection. We did not observe any signs of toxicity until 4 weeks post-injection. Consistent with our results, other studies showed normal organ morphology without apoptosis, necrosis and fibrosis until 90 days after AuNPs administration<sup>451-453,455,511,563,565,570</sup>. However, at 6 months post-injection, we were able to observe a slightly increased presence of (1) immune cell infiltrations in the lung, (2) apoptotic lesions in the germinal center and white pulp of the spleen, and (3) casts in the collecting tubules of the kidney. Importantly, apoptotic lesions in the germinal center of the spleen and casts in the kidney were also occasionally observed in the control group, but from the qualitative images obtained, they seemed to be more noticeable 6 months after AuNPs-PAA-Ctxb injection. Comparable histological observations of the spleen and kidneys were reported previously. However, these results were obtained 1 week after injection<sup>448</sup>. The origin of the kidney casts in our study are unclear. In the spleen, the apoptotic lesions were mostly characterized by the presence of tangible body macrophages (TBMs), which are responsible for the clearance of apoptotic lymphocytes and required to down-regulate the germinal center reaction. This could suggest a potential activity of the adaptive immune response<sup>576</sup>. Interestingly, although a major proportion of the AuNPs-PAA-Ctxb accumulated in the liver, no histological abnormalities were observed until 6 months post-injection, which suggests organ-specific sensitivity to AuNPs-PAA-Ctxb. This is not consistent with another study, which shows increased apoptosis in the liver 1 week after IV injection of 4.26 mg/kg 13 nm PEG-coated AuNPs<sup>446</sup>.

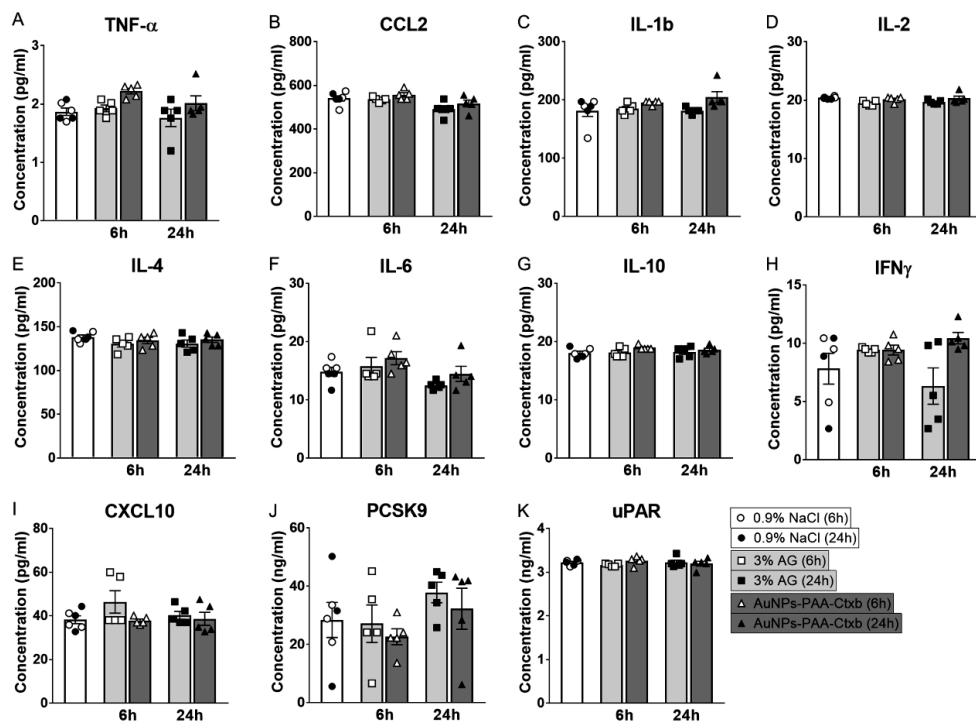
Overall, from our functional and morphological observations, and since all the mice survived, showing normal behavior and appearance over the course of the experiment, we consider

the toxicity of our AuNPs-PAA-Ctxb to be reasonably low. These results could be related to the surface charge and administration mode, which can affect the toxicity profile of the AuNPs. In fact, a study by Zhang et al demonstrated that intravenous injection of 13.5 nm AuNPs showed the lowest toxicity compared to the intraperitoneal and oral administration routes, which caused a significant decrease in body weight, spleen index and hematocrit<sup>577</sup>. Furthermore, in general, positively charged AuNPs exhibit a higher cytotoxicity profile than their negatively charged counterparts. Usually, this difference is associated with the electrostatic attraction and adhesion of the positively charged AuNPs to the negatively charged cell membrane, causing depolarization of the plasma membrane and disruption of the membrane integrity<sup>227,578</sup>. Wang, et al confirmed that the AuNP surface charge influences the toxicity in healthy mice, with 3 mM of positively charged gold nanoclusters (3.7 nm) inducing the most prominent effects on the peripheral blood system, compared to neutral and negatively charged gold nanoclusters<sup>511</sup>. Similarly, in zebrafish embryos, positively charged AuNPs (0.8-1.5-15 nm) were lethal at exposure concentrations higher than 400 ppb, whereas the negatively charged AuNPs induced sub-lethal toxic effects. Neutral AuNPs caused no adverse biological response up to a concentration of 50 ppm<sup>579</sup>. Nevertheless, we are not able to exclude long-term toxicity of AuNPs-PAA-Ctxb with certainty. Therefore, we recommend future research, which focuses on *in vivo* AuNPs toxicity, to consider long-term measurements beyond 6 months, including experiments assessing kidney functionality, liver functionality and immunoreactivity. Furthermore, this study was performed after a single IV injection. In a clinical setting, the use of AuNPs as radiosensitizing agents may require multiple injections. In fact, multiple intravenous injections resulted in a cumulative increase in AuNPs concentration at the tumor site in Swiss nude mice<sup>580</sup>. It should be noted that multiple dosing did not cause adverse effects in normal tissue, as demonstrated by several other studies<sup>448,563,581</sup>.

In conclusion, this study describes the pharmacokinetics, biodistribution and toxicity of our in-house produced AuNPs-PAA-Ctxb after a single IV injection. We demonstrated that the acute toxicity of AuNPs-PAA-Ctxb on the liver and vasculature, tested as increased serum AST and ALT activities, and elevated serum levels of GDF-15, P-selectin, ICAM-1 and RANTES, was limited and transient. However, the rapid clearance of the AuNPs-PAA-Ctxb from the blood, sequestration by the liver and spleen and long-term retention of the AuNPs-PAA-Ctxb in these organs could be limiting factors for the use of AuNPs-PAA-Ctxb as radiosensitizing agents *in vivo*. In order to evaluate the radiosensitizing potential of AuNPs-PAA-Ctxb, we labeled the nanoparticles with <sup>177</sup>Lu, which allows real-time assessment of the nanoparticle distribution and elimination in tumor-bearing animals. Since splenic apoptosis, kidney casts and immune cell infiltration in the lungs appeared to be more noticeable at 6 months post-injection compared to the controls, we could not exclude long-term toxicity with certainty. Therefore, we recommend that future *in vivo* studies consider long-term toxicity and the

elimination of AuNPs after multiple dosing, in their preclinical validation as new targeted anti-cancer therapies.

## 6. Supplemental information



**Supplemental Figure 4.1:** Serum levels of (A) TNF- $\alpha$ , (B) CCL2, (C) IL-1 $\beta$ , (D) IL-2, (E) IL-4, (F) IL-6, (G) IL-10, (H) IFN $\gamma$ , (I) CXCL10, (J) PCSK9, (K) uPAR in mouse serum at 6h and 24h after a single IV injection of AuNPs-PAA-Ctxb (90 µg Au), 0.9% NaCl or 3% AG. Graphs show individual data points and the mean concentration (pg or ng/ml) represented by columns. The error bars represent SE (n = 5-6).

**Abbreviations:** AG: Arabic gum; AuNPs-PAA-Ctxb: gold nanoparticles coated with poly-allylamine and conjugated to Cetuximab; IV: intravenous; SE: standard error



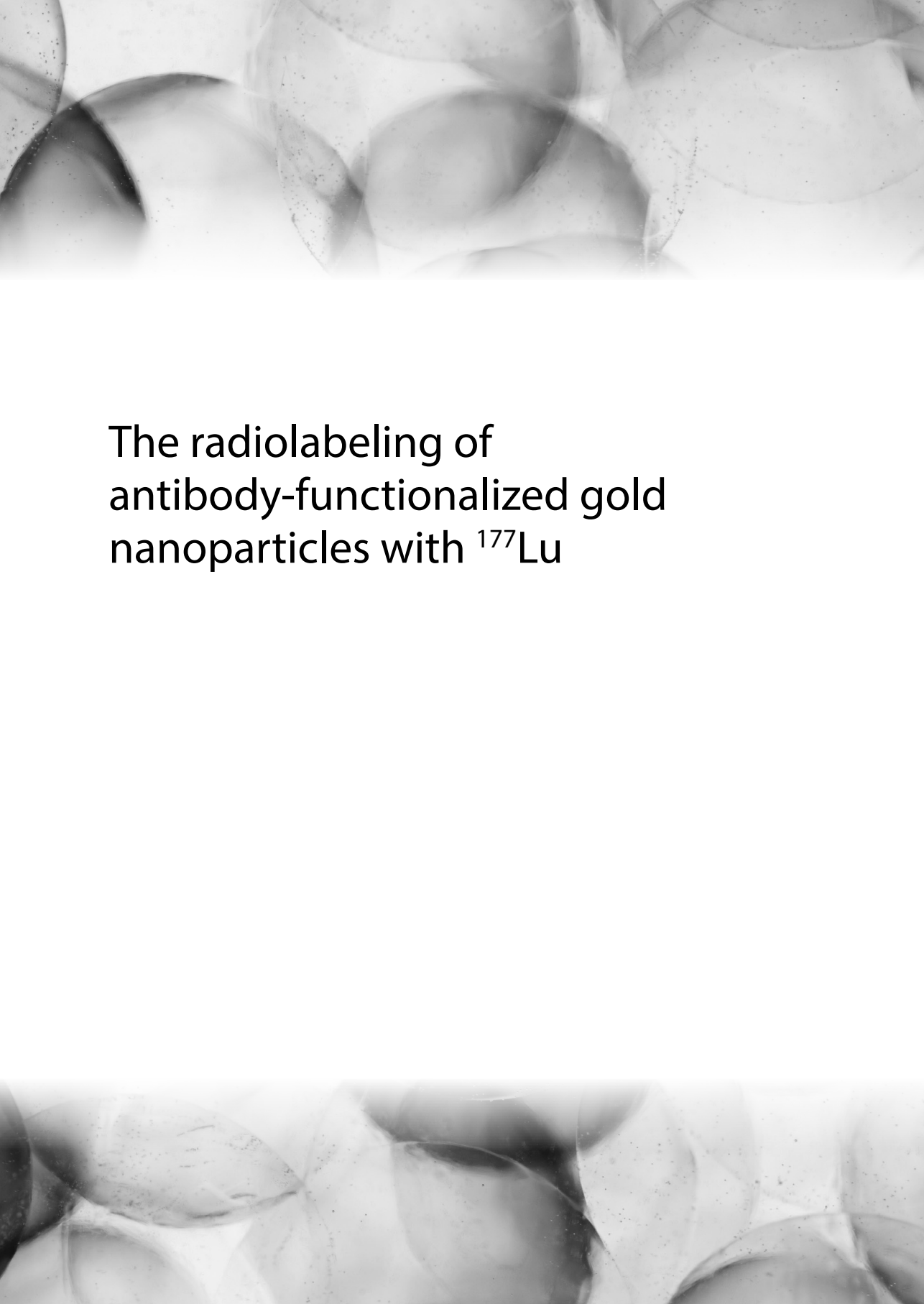




# 5

**CHAPTER**





# The radiolabeling of antibody-functionalized gold nanoparticles with $^{177}\text{Lu}$

## 1. Abstract

Poly-allylamine coated gold nanoparticles conjugated to Cetuximab (AuNPs-PAA-Ctxb) radiosensitize cancer cells to proton therapy and cause biological effects, such as mitochondrial dysfunction and inhibition of the antioxidant defense system, both systems play a role in cellular radiation response. Therefore, radiolabeled AuNPs-PAA-Ctxb might act as radiosensitizers in targeted radionuclide therapy. In this study, we radiolabeled AuNPs-PAA-Ctxb with  $^{177}\text{Lu}$ . The bifunctional chelator, diethylenetriaminepentaacetic acid (DTPA) was chosen because of the fast radiolabeling reaction under mild conditions and the minimal impact on the Ctxb binding capacity. After radiolabeling, a radiochemical stability of  $^{177}\text{Lu}$ -DTPA-Ctxb and  $^{177}\text{Lu}$ -DTPA-Ctxb-PAA-AuNPs of 86.1% and 79.5% was observed after 72 hours in serum. In addition,  $^{177}\text{Lu}$ -DTPA-Ctxb-PAA-AuNPs exhibited a larger internalization in cancer cells than  $^{177}\text{Lu}$ -DTPA-Ctxb. Blocking EGFR-overexpressing cancer cells with an excess of non-radioactive Ctxb reduced, but not abolished, the cell binding capacity of  $^{177}\text{Lu}$ -DTPA-Ctxb-PAA-AuNPs. On the other hand, EGFR-negative cancer cells demonstrated only a minimal reduction in  $^{177}\text{Lu}$ -DTPA-Ctxb-PAA-AuNPs binding after blocking. In conclusion, the capacity of Ctxb to recognize EGFR is preserved after radiolabeling with  $^{177}\text{Lu}$  using DTPA and conjugation with AuNPs-PAA. Future experiments will be conducted to investigate if  $^{177}\text{Lu}$ -DTPA-Ctxb-PAA-AuNPs may enhance cancer cell killing on EGFR-overexpressing A431 cells compared to  $^{177}\text{Lu}$ -DTPA-Ctxb. Furthermore, the biodistribution and elimination processes of  $^{177}\text{Lu}$ -DTPA-Ctxb-PAA-AuNPs will be assessed in tumor-bearing mice.

## 2. Introduction

Targeted radionuclide therapy (TRT) is based on the systemic administration of radionuclides conjugated to carrier molecules. The carrier molecules specifically target cancer cells and thus promote a favorable biodistribution of the radionuclide by increasing the tumor uptake and improving the tumor-to-background ratio. Depending on the type of radionuclide, the radiopharmaceutical can be used for molecular imaging, therapy or theranostic applications<sup>306</sup>. For instance,  $^{177}\text{Lu}$  has established a strong position as one of the best therapeutic agents for TRT. It emits  $\beta^-$  particles, which have an average energy of 0.498 MeV and a maximal tissue penetration range of approximately 2 mm, proficient to eradicate residual disease with a minimized damage to the surrounding healthy tissue. Furthermore, the emission of low-energy gamma photons (0.208 MeV) enables SPECT imaging, suitable for the assessment of tumoral uptake, biodistribution and elimination of the  $^{177}\text{Lu}$ -based radiopharmaceutical. Finally, the 6.65 days half-life of  $^{177}\text{Lu}$  offers the time to perform sophisticated radiolabeling and purification processes, and allows shipment of  $^{177}\text{Lu}$  or the processed radiopharmaceutical to nuclear medicine centers. The physical half-life of  $^{177}\text{Lu}$  also matches well with the biological half-life of antibodies, having a slow tissue distribution and long elimination half-life<sup>480</sup>. An example of a successful  $^{177}\text{Lu}$ -based radiopharmaceutical is the  $^{177}\text{Lu}$ -labeled somatostatin analog ( $^{177}\text{Lu}$ -DOTA-octreotate), Lutathera®, approved in January 2018. It is used for the treatment of gastro-enteropancreatic neuroendocrine tumors, reducing the risk on disease progression or death by 79% as compared to octreotate<sup>582-584</sup>. However, the conventional radiopharmaceuticals typically consist out of a single radionuclide conjugated to one carrier molecule. This could potentially result in a limited delivery of radioactivity to the tumor and a limited tumor response. In order to maximize the efficacy of TRT, gold nanoparticles (AuNPs) could act as a platform to carry multiple targeting ligands, each coupled to a radionuclide, and thus increasing the radionuclide cargo as well as the multivalent avidity, promoting the binding to the cancer cells. In addition, AuNPs exhibit a prolonged blood circulation half-life and accumulate in the tumor site by means of the enhanced permeability and retention (EPR) effect<sup>311,314</sup>. As a result, multiple studies demonstrated a higher uptake and retention of the targeted, radiolabeled AuNPs in tumors and micro-metastatic lesions after intravenous injection in mice, as compared to the monomeric, radiolabeled targeting ligands without AuNPs. This leads to enhanced therapeutic effects and a higher tumor-to-background ratio<sup>321,327,356,357,361,370</sup>.

Another advantage of introducing AuNPs in TRT is the ability of AuNPs to act as radiosensitizing agents. The rationale is based on the high Z number of Au, providing a higher mass energy absorption coefficient compared to soft tissue. Consequently, when AuNPs are internalized into tumors, they preferentially interact with the incoming radiation, releasing a burst of secondary electrons and increasing the dose deposition<sup>144</sup>. Indeed, *in silico* studies demonstrated strong radio-enhancement effects when AuNPs are irradiated with kilovoltage X-rays<sup>141,155,160,188,190</sup>. This is in contrast to the simulations considering AuNPs in combination

with clinically relevant megavoltage X-rays, indicating little or no increase in dose deposition<sup>134,154-157</sup>. Furthermore, in the case of radiotherapy with charged particles, the hit probability between AuNPs and the incoming radiation is low<sup>202,210</sup>. Nevertheless, multiple experimental *in vitro* and *in vivo* studies observed a higher cancer cell killing efficiency and a prolonged survival of tumor-bearing mice in the presence of AuNPs after irradiation with orthovoltage photons, megavoltage photons and protons, showing a stronger radiosensitizing effect than predicted<sup>133,134,143,181,201,202,215</sup>. This indicates that the radiosensitizing character of AuNPs should not be attributed exclusively to the physical interaction mechanisms between AuNPs and radiation. In fact, several studies suggested that AuNPs exert biological effects in cells. For instance, previous *in vitro* studies of our research group demonstrated that AuNPs inhibit the thiol-dependent antioxidant system, induce mitochondrial dysfunction and initiate apoptosis in several cancer cell lines and normal human cells. Furthermore, the role of oxidative stress was further highlighted by the protective effect of the anti-oxidant N-acetyl L-cysteine (NAC) abolishing the AuNPs-induced biological effects<sup>177,537,544</sup>. Our results are supported by other *in vitro* studies revealing that mitochondrial dysfunction, antioxidant inhibition and oxidative stress are related to AuNPs-induced apoptotic or necrotic cell death<sup>233,244,246,251-253,528,542</sup>. These effects are suggested to contribute to the radiosensitizing effects of AuNPs in cancer cells<sup>177,180,537</sup>.

The use of AuNPs as radiosensitizing agents is frequently focused on externally applied photon or proton radiotherapy. In case of targeted radionuclide therapy, radiolabeled AuNPs are usually exploited as alternative brachytherapeutic agents in order to achieve a homogeneously dispersed delivery of radioactivity after intratumoral injection, which is less invasive than the implantation of large seeds<sup>375,388,390</sup>. Several studies attributed the increased cancer cell death in the presence of the radiolabeled, targeted AuNPs to the high radionuclide payload and increased tumor uptake and retention of the radiopharmaceutical as compared to the monomeric targeting ligand<sup>370,384</sup>. However, no link was described between the radiosensitizing effects of AuNPs and their biological effects on cells. In this study, we describe the optimization of the radiolabeling process of Cetuximab-conjugated, polyallylamine-coated AuNPs (AuNPs-PAA-Ctxb) with <sup>177</sup>Lu, using bifunctional chelators, DTPA or DOTA. Furthermore, we assessed the binding and uptake of the radiolabeled <sup>177</sup>Lu-DTPA-Ctxb-PAA-AuNPs in EGFR-overexpressing A431 epidermoid cancer cells, EGFR-positive A549 lung cancer cells and EGFR-negative MCF-7 breast cancer cells. In our future perspectives, we will test the hypothesis that the biological effects of AuNPs-PAA-Ctxb contribute to the radiosensitization of cancer cells to the <sup>177</sup>Lu radionuclide therapy. Finally, we will assess the biodistribution of the <sup>177</sup>Lu-DTPA-Ctxb-PAA-AuNPs in mice, each bearing an EGFR-positive and an EGFR-negative tumor.

### 3. Materials and methods

#### 3.1. Chemicals

All cell lines were obtained from the American Type Culture Collection (Molsheim Cedex, France). Fetal bovine serum (FBS), Dulbecco's modified Eagle's medium (DMEM), Minimal Essential Medium (MEM), phosphate buffered saline (PBS) and penicillin-streptomycin were purchased from Gibco (Aalst, Belgium). Cetuximab was kindly provided by the Sint-Dimpna Hospital (Geel, Belgium). Vivaspin® centrifugal concentrators were obtained from Merck (Overijse, Belgium). PD10 desalting columns were obtained from GE healthcare (Machelen, Belgium). The bifunctional chelators S-2-(4-isothiocyanatobenzyl)-1,4,7,10-tetraazacyclododecane tetraacetic acid (p-SCN-Bn-DOTA) and [(R)-2-amino-3-(4-isothiocyanatophenyl)propyl]-trans-(S,S)-cyclohexane-1,2-diamine-pentaacetic acid (p-SCN-Bn-CHX-A''-DTPA) were purchased from Macrocyclics (Dallas, TX).  $^{177}\text{Lu}$  was provided by Global Morpho Pharma (La Chapelle-sur-Erdre, France) or was purchased from Isotopen Technologien München (Munich, Germany). Acetic acid was ordered from Alfa Aesar (Karlsruhe, Germany). Trace metal grade water was purchased from Honeywell (Charlotte, NC). All other chemicals were purchased from Sigma Aldrich (Diegem, Belgium). All buffers were prepared using trace-metal grade products and were treated with chelex to ensure a metal-free environment.

#### 3.2. Cell culture

The human EGFR-overexpressing, epidermoid cancer cell line A431 was cultured in DMEM growth medium. The human EGFR-negative, breast cancer cell line MCF-7 and the human EGFR-positive, lung cancer cell line A549 were grown in MEM. All media were supplemented with 10% FBS and 100 U/ml of penicillin-streptomycin. All cells were grown in a humidified atmosphere with 5%  $\text{CO}_2$  at 37°C. The EGFR expression of the different cell types is determined by Western blot, relative to the A431 cells (**Supplemental Figure 5.1**).

#### 3.3. DOTA and DTPA conjugation to Cetuximab

Cetuximab was purified in Class I water by filtration in a centrifugal filter unit with a molecular cut-off of 10 kDa, followed by lyophilization (LABCONCO, Osterode, Germany). Next, freeze-dried Ctxb was dissolved in 0.1 M sodium carbonate buffer (pH 8.5). The antibody concentration was measured by means of UV spectrophotometry at 280 nm (Nanodrop 2000, Thermo Scientific, Gent, Belgium). The Lambert-Beer equation (**Equation 5.1**) was used to correlate the absorbance with antibody concentration, in which A represent the absorbance in absorbance units (AU),  $\epsilon$  represents the extinction coefficient in  $\text{M}^{-1} \text{cm}^{-1}$ , c represents the molar protein concentration and l represents the optical path length in cm. To estimate the Ctxb concentration, the extinction coefficient was set at  $210\,000 \text{ M}^{-1} \text{cm}^{-1}$ . An example of the Ctxb absorbance spectrum is given in **Supplemental Figure 5.2**.

The bifunctional chelator, DTPA or DOTA (prepared as a 0.01 M stock solution in 0.1 M sodium bicarbonate buffer), was added to Ctxb in a 20-, 40- or 80-fold molar excess in a reaction volume of 1 ml. The mixture was incubated at 37°C, while shaking at 550 rpm for 1.5 hours. Next, purification of the conjugates and buffer exchange to 0.01 M PBS or 0.15 M ammonium acetate buffer (pH 5.5) was performed using a PD10 column. The extinction coefficient of DTPA and DOTA was estimated by measuring the A280 absorbance of DTPA and DOTA solutions ranging from 1.25 mM to 10 mM in 0.01 M PBS. Purified fractions were pooled and the concentration of the conjugate was measured by UV spectrophotometry (Nanodrop 2000, Thermo Scientific, Gent, Belgium) at 280 nm as described before by adjusting the molecular weight and extinction coefficient accordingly (**Table 5.1**). The number of bifunctional chelators conjugated to Ctxb was analyzed by GIGA Proteomics using MALDI-ToF-MS (Liège, Belgium). Finally, the conjugates were aliquoted and frozen at -20°C until further use.

$$A = \epsilon cl \quad (\text{Equation 5.1})$$

**Table 5.1:** The molecular weight and extinction coefficient of Cetuximab and Cetuximab conjugated to DTPA or DOTA.

Conjugate	Molecular weight	Extinction Coefficient
Cetuximab	152 kDa	210 000 M <sup>-1</sup> cm <sup>-1</sup>
Cetuximab + 20 molar excess DTPA	154 kDa	225 000 M <sup>-1</sup> cm <sup>-1</sup>
Cetuximab + 40 molar excess DTPA	155 kDa	260 000 M <sup>-1</sup> cm <sup>-1</sup>
Cetuximab + 80 molar excess DTPA	156 kDa	295 000 M <sup>-1</sup> cm <sup>-1</sup>
Cetuximab + 20 molar excess DOTA	154 kDa	226 000 M <sup>-1</sup> cm <sup>-1</sup>
Cetuximab + 40 molar excess DOTA	155 kDa	263 000 M <sup>-1</sup> cm <sup>-1</sup>
Cetuximab + 80 molar excess DOTA	156 kDa	299 000 M <sup>-1</sup> cm <sup>-1</sup>

### 3.4. Conjugation of Ctxb-DTPA to AuNPs-PAA

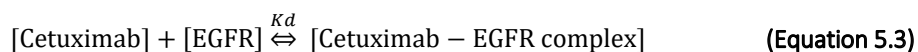
AuNPs-PAA production by means of plasma vapor deposition and the subsequent conjugation to Ctxb-DTPA was performed using the same method as previously described<sup>201,471,544</sup>. After purification of AuNPs-PAA-Ctxb-DTPA, the amount of Ctxb-DTPA conjugated to AuNPs-PAA was determined using a protein quantification assay (Pierce 660 nm protein assay, Thermo Scientific, Gent, Belgium). A defined amount of Au (7.5 µg Au/well) of AuNPs-PAA and AuNPs-PAA-Ctxb-DTPA was added to the wells, followed by the absorbance measurement before and after addition of 150 µl of the colorimetric reagent at 660 nm using a spectrophotometer (Nanodrop 2000, Therm Scientific, Gent, Belgium). The Ctxb content in the unknown samples was quantified by plotting a calibration curve using known concentrations of Ctxb-DTPA, and after subtraction of the AuNPs-PAA absorbance at 660 nm. Aliquots of the AuNPs-PAA-Ctxb-DTPA nanoconjugates containing 100 µg of Ctxb-DTPA were freeze-dried containing 3% arabic gum and stored at 4°C until radiolabeling.

### 3.5. ELISA

The target binding capacity of Ctxb-DTPA, Ctxb-DOTA and AuNPs-PAA-Ctxb-DTPA was evaluated using enzyme linked immunosorbent assay (ELISA). A431 cells were seeded in a 96 well plate (10 000 cells/well) and were incubated overnight in a humidified incubator at 37°C and 5%  $\text{CO}_2$ . Cells were rinsed twice with PBS and fixed with 4% paraformaldehyde. After rinsing twice with PBS, cells were blocked with 5% non-fat dry milk in PBS for 1 hour at room temperature. Next, cells were rinsed twice with PBS and once with 1% bovine serum albumin in PBS followed by incubation with Ctxb, Ctxb-DTPA, Ctxb-DOTA or AuNPs-PAA-Ctxb-DTPA at various concentrations. After rinsing three times with 1% BSA-PBS, cells were incubated with a mouse monoclonal anti-human IgG-biotin antibody for 1 hour at room temperature. Next, cells were rinsed twice with 1% BSA-PBS and once with PBS followed by incubation with streptavidin alkaline phosphatase for 30 min at room temperature. After rinsing twice with 1% BSA-PBS and once with PBS, alkaline phosphatase activity was revealed by incubation of the cells with 1 mg/ml p-nitrophenylphosphate and 1.5 mM tetramisole hydrochloride in 0.1 M diethanolamine for 45 minutes at 37°C. The reaction was stopped with 100  $\mu\text{l}$  of 2 N NaOH and the optical density was measured at 405 nm using a plate reader (Nanodrop 2000, Thermo Scientific, Gent, Belgium).

The binding affinity of the Ctxb and the Ctxb conjugates to EGFR is measured and reported by the dissociation constant ( $K_d$ ), which represents the concentration of the antibody that results in 50% of maximal EGFR binding. Therefore, the  $K_d$  value is inversely proportional to the affinity of the antibody for the receptor, meaning that the higher the  $K_d$  value, the lower the affinity of the antibody. The  $K_d$  values were estimated by GraphPad Prism 7 using **Equation 5.2**. In Equation 5.2,  $B_{\text{max}}$  represents the number of binding sites in the assay and  $K_d$  represents the dissociation constant. The dissociation reaction is represented in **Equation 5.3**

$$Y = \frac{B_{\text{max}} \times X}{K_d + X} \quad (\text{Equation 5.2})$$



### 3.6. $^{177}\text{Lu}$ labeling kinetics and stability of Ctxb-DOTA, Ctxb-DTPA and AuNPs-PAA-Ctxb-DTPA

For the radiolabeling, the aliquoted, freeze-dried AuNPs-PAA-Ctxb-DTPA were suspended in 0.15 M ammonium acetate buffer (pH 5.5). Next, 74-370 MBq of  $^{177}\text{Lu}$  was added to 100  $\mu\text{g}$  of Ctxb-DTPA (conjugated or not to AuNPs-PAA) or Ctxb-DOTA in 300  $\mu\text{l}$  of 0.15 M ammonium acetate buffer (pH 5.5). The reactions with Ctxb-DTPA, AuNPs-PAA-Ctxb-DTPA or Ctxb-DOTA conjugates were conducted while shaking on 550 rpm at room temperature or at 50°C,



respectively. The extent of complexation was analyzed by instant thin layer chromatography (iTLC) at 5, 10, 20, 30, 45, 60, 90 and 120 minutes after initiation of the reaction, with an extra time point at 180 min for the Ctxb-DOTA conjugate. iTLC was performed on silica gel impregnated thin layer sheets (iTLC-SG, Agilent Technologies) using a 0.1 M sodium citrate solution (pH 5) as mobile phase. After migration of the free  $^{177}\text{Lu}$ , the thin layer sheets were cut in half and the activity on each piece was measured using an automated gamma counter (Wizard 2 gamma counter, PerkinElmer, Groningen, The Netherlands). After the completion of the reaction,  $^{177}\text{Lu}$ -DTPA-Ctxb-PAA-AuNPs were purified from free  $^{177}\text{Lu}$  by centrifuging the nanoconjugates at 2700 rcf for 9 minutes. The nanoparticle pellet was resuspended in 300  $\mu\text{l}$  0.15 M ammonium acetate buffer. After purification, the radiochemical purity, which is the ratio of the DTPA-bound  $^{177}\text{Lu}$  to the total  $^{177}\text{Lu}$  in the final solution, of the reaction was again analyzed by iTLC. The radiochemical stability was evaluated by adding 50  $\mu\text{l}$  of  $^{177}\text{Lu}$ -DTPA-Ctxb-PAA-AuNPs or  $^{177}\text{Lu}$ -DTPA-Ctxb conjugates to 100  $\mu\text{l}$  PBS or 100  $\mu\text{l}$  serum incubated at 25°C and 37°C, respectively, during 72h. Aliquots were taken at 24h, 48h and 72h and were analyzed with iTLC.

### 3.7. Saturation binding of $^{177}\text{Lu}$ -DTPA-Ctxb and $^{177}\text{Lu}$ -DTPA-Ctxb-PAA-AuNPs

The target binding of the  $^{177}\text{Lu}$ -DTPA-Ctxb-PAA-AuNPs and  $^{177}\text{Lu}$ -DTPA-Ctxb conjugates was evaluated on A431 cells. A431 cells were seeded in a 24 well plate (60 000 cells/well). The next day, cells were incubated with 500  $\mu\text{l}$  of complete cell medium containing different concentrations of  $^{177}\text{Lu}$ -DTPA-Ctxb or  $^{177}\text{Lu}$ -DTPA-Ctxb-PAA-AuNPs during 1 hour at 37°C. In total, 8 different concentrations of  $^{177}\text{Lu}$ -DTPA-Ctxb (0.02 - 0.03 - 0.06 - 0.13 - 0.25 - 0.50 - 1.00 - 10.00  $\mu\text{g/ml}$  Ctxb) or  $^{177}\text{Lu}$ -DTPA-Ctxb-PAA-AuNPs (0.08 - 0.16 - 0.31 - 0.63 - 1.25 - 2.50 - 5.00 - 20.00  $\mu\text{g/ml}$  Ctxb) were tested. In addition, a 200-fold excess of unlabeled Ctxb was added to half of the wells to assess non-specific binding. After incubation, the unbound fraction was removed by rinsing the cells twice with 1 ml of complete cell medium. Next, the cells were lysed by addition of 500  $\mu\text{l}$  of 1 M NaOH during 30 min. The lysates were collected by two additional rinses and were counted for radioactivity in an automated  $\gamma$ -counter (Wizard 2 gamma counter, PerkinElmer, Groningen, The Netherlands). The  $K_d$  value represents of the radiolabeled conjugates was calculated with GraphPad Prism 7 using **Equation 5.2**.

### 3.8. Specificity of $^{177}\text{Lu}$ -DTPA-Ctxb and $^{177}\text{Lu}$ -DTPA-Ctxb-PAA-AuNPs

A431 cells, MCF-7 cells and A549 cells were seeded in a 24 well plate (60 000 cells/well). The next day, cells were incubated with 500  $\mu\text{l}$  of complete cell medium containing 0.17  $\mu\text{g/ml}$   $^{177}\text{Lu}$ -DTPA-Ctxb or 0.31  $\mu\text{g/ml}$   $^{177}\text{Lu}$ -DTPA-Ctxb-PAA-AuNPs during 1 hour at 37°C. In addition, a 200-fold excess of unlabeled Ctxb was added to half of the wells to assess non-

specific binding. After incubation, the unbound fraction was removed by rinsing the cells twice with 1 ml of complete cell medium. Next, the membrane-bound fraction was collected by incubating the cells with 500  $\mu\text{l}$  of 200 mM sodium acetate/500 mM NaCl (pH 2.5) for 10 min, followed by two well rinses. Then, the internalized fraction was collected by lysing the cells with 500  $\mu\text{L}$  of 1 M NaOH during 30 minutes, followed by two well rinses. The collected acid washes and lysates were counted for radioactivity in an automated  $\gamma$ -counter (Wizard 2 gamma counter, PerkinElmer, Groningen, The Netherlands).

## 4. Results

### 4.1. Immunoreactivity of Ctxb-DOTA and Ctxb-DTPA

Coupling multiple bifunctional chelators to each antibody is aimed to increase the radionuclide cargo and thus the therapeutic capacity of nano-radiopharmaceutical agents. In order to choose the best chelator for radiolabeling Ctxb, DTPA or DOTA was added to Ctxb in a 20-, 40- and 80-fold molar excess. According to the MALDI-ToF-MS analysis, this resulted in the conjugation of approximately two, four and six bifunctional chelators per antibody, respectively (**Supplemental Table 5.1**). However, a large number of chelator molecules conjugated to an antibody may impair its immunoreactivity. Therefore, we tested the capacity for binding of the Ctxb-DOTA and Ctxb-DTPA to the EGFR-overexpressing A431 cells by means of ELISA. According to the type of chelator attached to Ctxb, the immunoreactivity of Ctxb is different. **Figure 5.1** demonstrates that the addition of an 80-fold molar excess of DOTA or DTPA to Ctxb significantly reduced the immunoreactivity of Ctxb to EGFR. This effect was more pronounced with DOTA compared to DTPA. Moreover, a significantly reduced immunoreactivity was observed after addition of a 40-fold molar excess of DOTA, while a 20-fold molar excess of DOTA significantly reduced the immunoreactivity of Ctxb only at low antibody concentrations. On the other hand, a 20- and 40-fold molar excess of DTPA did not affect the binding capacity of Ctxb. Therefore, we chose a 20-fold excess of DTPA or DOTA for the following work. An illustration of the radiolabeled nanoconjugate is presented in **Figure 5.2**.

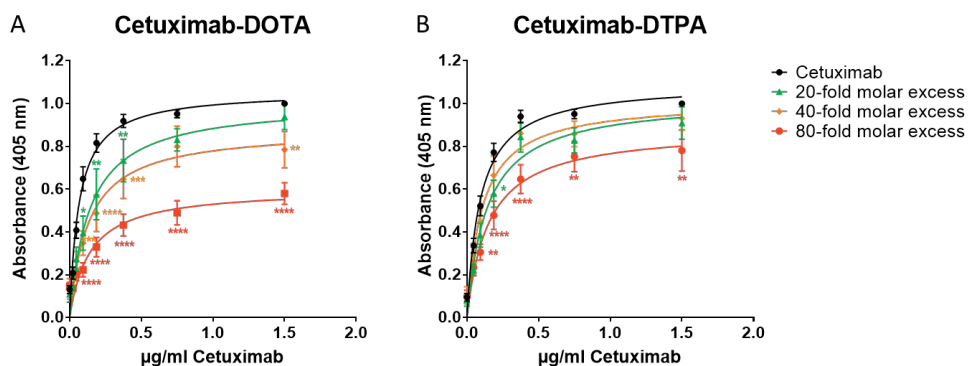


**Figure 5.1** ELISA analysis of (A) Ctxb-DOTA and (B) Ctxb-DTPA produced by the addition of a 20-, 40- or 80-fold excess of the bifunctional chelators to Ctxb. Data were obtained from 4-6 independent experiments with 2-3 replicates per concentration. Error bars represent SE. A non-linear fit was performed using GraphPad Prism 7. Statistical difference compared to free Ctxb was calculated by a two-way ANOVA and a Dunnett post-hoc test (\* $p < 0.05$ , \*\* $p < 0.01$ , \*\*\* $p < 0.001$ , \*\*\*\* $p < 0.0001$ ).

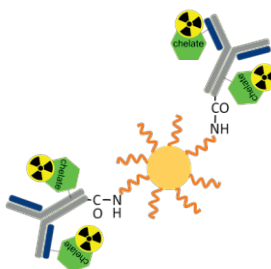


**Figure 5.2** Illustration of the  $^{177}\text{Lu}$ -radiolabeled AuNPs-PAA-Ctxb, including approximately two antibodies per AuNP and two chelators per Cetuximab molecule.

#### 4.2. $^{177}\text{Lu}$ -radiolabeling kinetics and stability

Radiolabeling of Ctxb-DTPA with  $^{177}\text{Lu}$  was performed at room temperature. It achieved a complexation of  $>95\%$  after 5 min (**Figure 5.3A**). On the other hand, radiolabeling of Ctxb-DOTA with  $^{177}\text{Lu}$  required an incubation temperature of  $50^\circ\text{C}$  during three hours before achieving a complexation  $>95\%$  (**Figure 5.3B**). Such high temperatures could potentially affect the antibody tertiary structure as well as the chemical bonds between AuNPs-PAA, Ctxb and the bifunctional chelator. Furthermore, as presented in **Figure 5.1**, conjugation of Ctxb to DTPA affected the antibody immunoreactivity to a lesser extent than the conjugation to DOTA. Therefore, radiolabeling and other experiments in this research were further limited to Ctxb-DTPA and AuNPs-PAA-Ctxb-DTPA. The radiolabeling of AuNPs-PAA-Ctxb-DTPA reached a maximal complexation of 90% at room temperature after 20 minutes of incubation

(Figure 5.3C). After the purification step, iTLC analysis demonstrated a radiochemical purity of >92%.

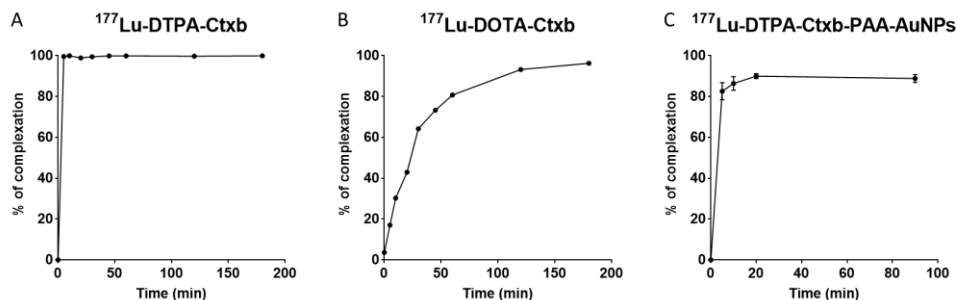


**Figure 5.3** The radiolabeling kinetics of (A) Ctxb-DTPA ( $n = 1$ ) at RT, (B) Ctxb-DOTA ( $n = 1$ ) at  $50^\circ\text{C}$  and (C) AuNPs-PAA-Ctxb-DTPA ( $n = 3$ ) at RT. Error bars represent SD.

The radiochemical stability of  $^{177}\text{Lu}$ -DTPA-Ctxb and  $^{177}\text{Lu}$ -DTPA-Ctxb-PAA-AuNPs was assessed in labeling buffer and PBS at room temperature, and in serum at  $37^\circ\text{C}$ . A high stability was observed for both conjugates. Indeed, after 72h, the radiochemical purity of  $^{177}\text{Lu}$ -DTPA-Ctxb slightly decreased from 89.2% to 83.3%, 77.9% and 86.1% in labeling buffer, PBS and serum, respectively (Figure 5.4A). In addition, after 72h, the radiochemical purity of  $^{177}\text{Lu}$ -DTPA-Ctxb-PAA-AuNPs decreased from 92.8% to 89.9% and 79.5% in PBS and serum, respectively. No decrease in the radiochemical purity of  $^{177}\text{Lu}$ -DTPA-Ctxb-PAA-AuNPs was observed when suspended in labeling buffer after 72h, indicating a high radiochemical stability (Figure 5.4B).

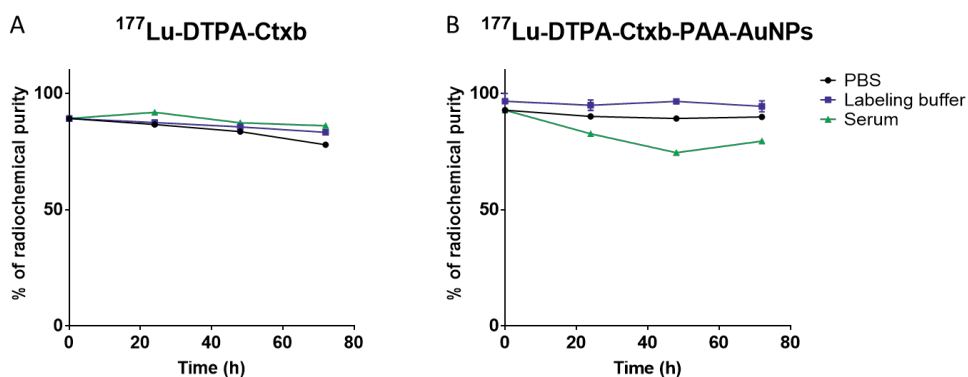


**Figure 5.4** The radiochemical stability of (A)  $^{177}\text{Lu}$ -DTPA-Ctxb and (B)  $^{177}\text{Lu}$ -DTPA-Ctxb-PAA-AuNPs in labeling buffer and PBS at  $25^\circ\text{C}$ , and in serum at  $37^\circ\text{C}$  for 72h.

### 4.3. Saturation binding of ( $^{177}\text{Lu}$ -)DTPA-Ctxb and ( $^{177}\text{Lu}$ -)DTPA-Ctxb-PAA-AuNPs

In order to assess the affinity of the Ctxb-DTPA, AuNPs-PAA-Ctxb-DTPA and their radiolabeled analogs, saturation binding assays on the EGFR-expressing A431 cells were performed by means of ELISA and radioactivity measurements, respectively (**Figure 5.5**). Radioactivity measurements allow the estimation of the non-specific binding by saturating the EGFR binding sites on the A431 cells with a 200-fold excess of cold Ctxb. Consequently, the specific binding could be calculated by subtracting the non-specific binding (after blocking) from the total binding (without blocking). An overview of the  $K_d$  values determined from the binding curves in **Figure 5.5** are represented in **Table 5.2**. The  $K_d$  value of  $^{177}\text{Lu}$ -DTPA-Ctxb and  $^{177}\text{Lu}$ -DTPA-Ctxb-PAA-AuNPs was determined from the specific saturation binding curves (green curves in **Figure 5.5A-C**) and had a value of 0.17  $\mu\text{g/ml}$  and 1.09  $\mu\text{g/ml}$ , respectively. Consistently, similar  $K_d$  values for non-radiolabeled Ctxb-DTPA ( $K_d$ : 0.09  $\mu\text{g/ml}$ ) and AuNPs-PAA-Ctxb-DTPA ( $K_d$ : 1.25  $\mu\text{g/ml}$ ) were calculated from the ELISA binding curve (**Figure 5.5D**). Importantly, the conjugation of DTPA to Ctxb ( $K_d$ : Ctxb 0.06 vs  $K_d$ : Ctxb-DTPA 0.09) or to AuNPs-PAA-Ctxb ( $K_d$ : AuNPs-PAA-Ctxb 1.36 vs  $K_d$ : AuNPs-PAA-Ctxb-DTPA 1.25) did not affect the affinity of Ctxb. However, the higher  $K_d$  values of the nanoconjugates compared to free ( $^{177}\text{Lu}$ -)DTPA-Ctxb reveals that the introduction of AuNP-PAA to ( $^{177}\text{Lu}$ -)DTPA-Ctxb reduced the Ctxb antibody affinity towards EGFR. Furthermore, in contrast to  $^{177}\text{Lu}$ -DTPA-Ctxb, which exhibits a high specificity for EGFR (**Figure 5.5A**), the total binding of  $^{177}\text{Lu}$ -DTPA-Ctxb-PAA-AuNPs (black curve) to A431 cells is much higher than the specific binding of  $^{177}\text{Lu}$ -DTPA-Ctxb-PAA-AuNPs (green curve) as the nanoconjugate concentration increased, indicating non-specific binding (**Figure 5.5B**). On the other hand, the ELISA analysis of AuNPs-PAA-Ctxb-DTPA, performed on fixed cells that were pre-blocked with 5% of non-fat dry milk, did not show an absorbance signal that reaches above the saturation plateau phase (**Figure 5.5D**).

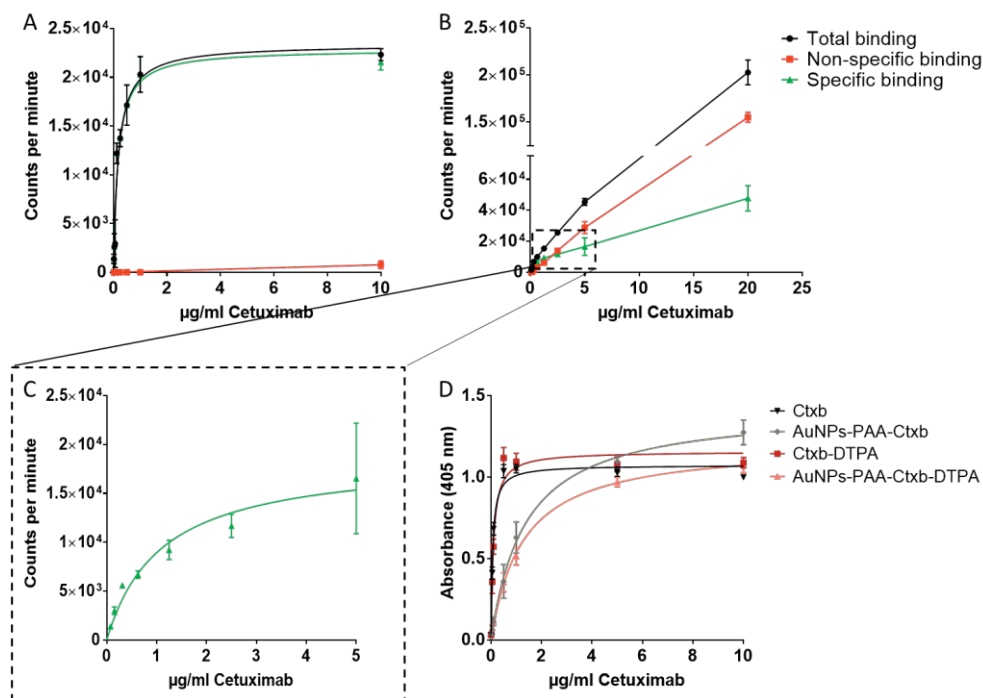


**Figure 5.5** Radioactivity analysis of the total binding (black), the non-specific binding after blocking EGFR (red curve) and the specific binding (green curve) of (A)  $^{177}\text{Lu}$ -DTPA-Ctxb, (B)  $^{177}\text{Lu}$ -DTPA-Ctxb-PAA-AuNPs and (C) a magnification of the specific binding of  $^{177}\text{Lu}$ -DTPA-Ctxb-PAA-AuNPs (green curve from B). Data were obtained from one experiment with three replicates per concentration. Error bars represent SD. (D) ELISA analysis of the binding of Ctxb-DTPA and AuNPs-PAA-Ctxb-DTPA. Data were obtained from 5-6 independent experiments with 2-3 replicates per concentration. Error bars represent SE. Non-linear fits and the calculations of the  $K_d$  values were performed using GraphPad Prism 7.

**Table 5.2** Overview of  $K_d$  values for antibody conjugates and nanoconjugates

Antibody conjugate	$K_d$ value ( $\mu\text{g/ml}$ )
Ctxb (Figure 5.5D)	0.06
Ctxb-DTPA (Figure 5.5D)	0.09
$^{177}\text{Lu}$ -DTPA-Ctxb (Figure 5.5A)	0.17
Nanoconjugate	$K_d$ value ( $\mu\text{g/ml}$ )
AuNPs-PAA-Ctxb (Figure 5.5D)	1.36
AuNPs-PAA-Ctxb-DTPA (Figure 5.5D)	1.25
$^{177}\text{Lu}$ -DTPA-Ctxb -PAA-AuNPs (Figure 5.5C)	1.09

#### 4.4. Specificity of $^{177}\text{Lu}$ -DTPA-Ctxb and $^{177}\text{Lu}$ -DTPA-Ctxb-PAA-AuNPs

The specific binding of  $^{177}\text{Lu}$ -DTPA-Ctxb (0.13  $\mu\text{g}/\text{ml}$  Ctxb,  $K_d$  value) and  $^{177}\text{Lu}$ -DTPA-Ctxb-PAA-AuNPs (0.31  $\mu\text{g}/\text{ml}$  Ctxb, 80% specific binding) towards EGFR-overexpressing A431 cells is presented in **Figure 5.6** as the total binding versus the binding after blocking EGFR with a 200-fold excess of cold Ctxb. Blocking EGFR fully abolished the binding of  $^{177}\text{Lu}$ -DTPA-Ctxb. Furthermore, the binding of  $^{177}\text{Lu}$ -DTPA-Ctxb-PAA-AuNPs was considerably reduced.

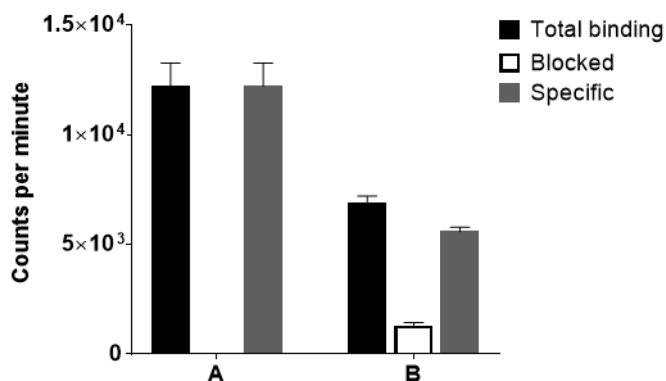


**Figure 5.6** Total binding, specific binding and non-specific binding to A431 cells after blocking with a 200-fold excess of cold Ctxb for (A)  $^{177}\text{Lu}$ -DTPA-Ctxb and (B)  $^{177}\text{Lu}$ -DTPA-Ctxb-PAA-AuNPs. Data were obtained from one experiment with three replicates per condition. Error bars represent SD.

In addition, we compared the membrane-bound and internalized fractions of  $^{177}\text{Lu}$ -DTPA-Ctxb (0.17  $\mu\text{g}/\text{ml}$  Ctxb,  $K_d$  value) and  $^{177}\text{Lu}$ -DTPA-Ctxb-PAA-AuNPs (0.31  $\mu\text{g}/\text{ml}$  Ctxb, 80% specific binding) in EGFR-overexpressing A431 cells, EGFR-positive A549 cells and EGFR-negative MCF-7 cells after 1 hour of incubation at 37°C (**Figure 5.7**).

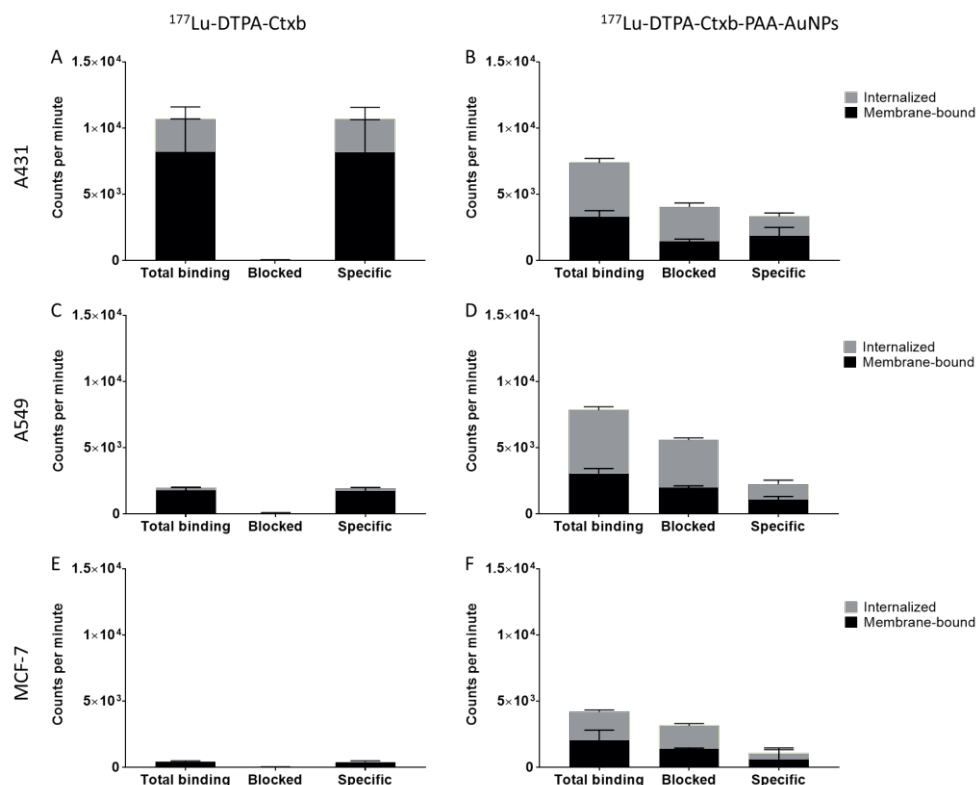


**Figure 5.7** The membrane-bound and internalized fractions of  $^{177}\text{Lu}$ -DTPA-Ctxb and  $^{177}\text{Lu}$ -DTPA-Ctxb-PAA-AuNPs in (A-B) EGFR-overexpressing A431 cells, (C-D) EGFR-positive A549 cells and (E-F) EGFR-negative MCF-7 cells. Data were obtained from one experiment with three replicates per condition. Error bars represent SD.

From the studied cell lines,  $^{177}\text{Lu}$ -DTPA-Ctxb showed the highest binding affinity to A431 cells, with reasonable proportion of  $^{177}\text{Lu}$ -DTPA-Ctxb internalized (23.0%). On the other hand, the binding of  $^{177}\text{Lu}$ -DTPA-Ctxb to A549 cells and MCF-7 was low, with a negligible uptake in A549 cells (10.1%) and no uptake in MCF-7 cells. Blocking EGFR fully abolished the binding of  $^{177}\text{Lu}$ -DTPA-Ctxb to all cell lines. Different results were obtained for  $^{177}\text{Lu}$ -DTPA-Ctxb-PAA-AuNPs. In fact, all cell lines internalized  $^{177}\text{Lu}$ -DTPA-Ctxb-PAA-AuNPs more extensively than  $^{177}\text{Lu}$ -DTPA-Ctxb (55.6%, 61.1%, 52.6% for A431 cells, A549 cells and MCF-7 cells, respectively). Nevertheless, the bound and internalized fractions of  $^{177}\text{Lu}$ -DTPA-Ctxb-PAA-AuNPs were higher for the EGFR-overexpressing A431 cells than for the EGFR-negative MCF-7 cells. There is little difference in the total binding and internalization of  $^{177}\text{Lu}$ -DTPA-Ctxb-PAA-AuNPs between A431 cells and A549 cells. Nevertheless, after blocking, the  $^{177}\text{Lu}$ -DTPA-Ctxb-PAA-AuNPs binding and uptake was reduced most in A431 cells, followed by A549 and MCF-7 cells.



## 5. Discussion

The goal of TRT is to provide a protracted and cytotoxic radiation exposure specifically to tumor cells, with a minimal exposure to non-targeted healthy tissues after systemic delivery. Radio-immunotherapy (RIT) is a form of TRT involving the use of antibodies as carriers of radionuclides, and is a strongly developing field in nuclear medicine <sup>586</sup>. However, it is not uncommon that radiolabeled antibodies show limited success in the treatment of solid tumors, despite promising pre-clinical evaluations <sup>587</sup>. Several reasons could explain these results, such as low tumor penetration and low uptake of the antibodies, a higher radio-resistance of solid tumors compared to hematological cancers, and the delivery of radiation doses, which are too low to promote tumor cell killing <sup>588,589</sup>. Thanks to their high area-to-volume ratio and the EPR effect, AuNPs are able to carry multiple radiolabeled antibodies and exhibit an increased accumulation at the tumor site compared to free antibodies. As a result, targeted, radiolabeled AuNPs have the potential to deliver a high radionuclide cargo to the tumor cells, increasing the efficacy of TRT <sup>311,314</sup>.

Acyclic and macrocyclic bifunctional chelators are suitable for the radiolabeling of biomolecules with <sup>177</sup>Lu <sup>590</sup>. In this study, we optimized the radiolabeling of Ctxb and AuNPs-PAA-Ctxb with <sup>177</sup>Lu using DOTA and DTPA as linkers. Importantly, the conjugation of multiple bifunctional chelators to a cancer-targeting ligand can affect its *in vitro* and *in vivo* behavior. In fact, the results of the ELISA immunoreactivity assay and the MALDI-ToF MS analysis suggest that the conjugation of more than two bifunctional chelators to each Ctxb reduced the antibody immunoreactivity to EGFR. Comparable results were obtained by other studies, in which antibody:bifunctional chelator molar ratios of 1:5, 1:10 and 1:50 achieved the conjugation of 1.62, 6.42 and 11.01 p-NCS-Bz-DOTA molecules per Rituximab antibody and diminished the antibody immunoreactivity by 28.8%, 46.95% and 80.63%, respectively <sup>591</sup>. On the other hand, Forrer, et al found that the immunoreactivity of Rituximab was still retained after conjugation of four p-NCS-Bz-DOTA chelators and diminished by 50% after conjugation of 8 chelator molecules <sup>592</sup>. In our study, the reduced Ctxb immunoreactivity was strongly pronounced when using DOTA as chelator. Another disadvantage of using DOTA as bifunctional chelator is the elevated temperature (up to 50°C) and the long duration of the reaction that are required for the radiolabeling reaction in order to achieve an adequate radiolabeling efficiency. Such high temperatures could be detrimental for the integrity of the antibody and the nanoconjugate. Therefore, we preferred to use the acyclic DTPA as bifunctional chelator, since it enabled a rapid and efficient radiolabeling of AuNPs-PAA-Ctxb under mild conditions, without affecting the antibody immunoreactivity.

Essential for TRT applications is the development of a radiochemically stable nanoconjugate, with limited release of free radionuclide when administered *in vivo*. Importantly, for the stability evaluation in **Figure 5.4**, a higher activity of <sup>177</sup>Lu (370 MBq) was added to Ctxb-DTPA and AuNPs-PAA-Ctxb-DTPA when compared to the activity that was added to the conjugates

to measure the radiolabeling kinetics, radiolabeling efficiency and radiochemical purity after centrifugation in **Figure 5.3** (147 MBq). This could be a possible reason that the initial radiochemical purity of  $^{177}\text{Lu}$ -DTPA-Ctxb (89.2%) and  $^{177}\text{Lu}$ -DTPA-Ctxb-PAA-AuNPs (92.8%) for the stability evaluation in **Figure 5.4** is lower than the radiochemical purity of  $^{177}\text{Lu}$ -DTPA-Ctxb in **Figure 5.3** (>95%) and of  $^{177}\text{Lu}$ -DTPA-Ctxb-PAA-AuNPs after centrifugation (>92%). Nevertheless, we observed a high radiochemical stability for both  $^{177}\text{Lu}$ -DTPA-Ctxb and  $^{177}\text{Lu}$ -DTPA-Ctxb-PAA-AuNPs in labeling buffer, with less than 5% release of free  $^{177}\text{Lu}$  after 72h post-radiolabeling. In contrast,  $^{177}\text{Lu}$  was slightly dissociated from  $^{177}\text{Lu}$ -DTPA-Ctxb-PAA-AuNPs and from  $^{177}\text{Lu}$ -DTPA-Ctxb after 72h by 13.3% in serum and by 11.3% in PBS, respectively. Nevertheless, this is still in line with the reported radiochemical purity of radiolabeled AuNPs, ranging from 80% to >95% after 24-72h in serum<sup>314,317-319,321-326</sup>. Furthermore, since the majority of the AuNPs-PAA-Ctxb are cleared from the blood circulation, 6h after intravenous injection, as demonstrated by our previous *in vivo* study,  $^{177}\text{Lu}$  release in the blood might be limited<sup>593</sup>.

The binding saturation assays of Ctxb-DTPA (ELISA) and  $^{177}\text{Lu}$ -DTPA-Ctxb (gamma detection) indicated that conjugation of DTPA to Ctxb and the radiolabeling with  $^{177}\text{Lu}$  did not alter the binding affinity of Ctxb towards EGFR. In contrast, the conjugation of AuNPs-PAA to ( $^{177}\text{Lu}$ -)DTPA-Ctxb increased the  $K_d$  value. This higher  $K_d$  value of ( $^{177}\text{Lu}$ -)DTPA-Ctxb-PAA-AuNPs compared to ( $^{177}\text{Lu}$ -)DTPA-Ctxb could be related to the multivalency of the Ctxb-functionalized AuNPs, where some antibodies on the AuNPs-PAA may not have the suitable orientation to interact with the EGFRs on the 2D cell monolayer<sup>474</sup>. Another consequence related to the conjugation of AuNPs-PAA to ( $^{177}\text{Lu}$ -)DTPA-Ctxb is the higher uptake of  $^{177}\text{Lu}$ -DTPA-Ctxb-PAA-AuNPs in cancer cells compared to  $^{177}\text{Lu}$ -DTPA-Ctxb. This could be explained by the internalization of AuNPs in cells via uptake mechanisms that are independent from the EGFR expression, such as macropinocytosis or receptor-independent endocytosis. Indeed, TEM images from our previous *in vitro* study (**Figure 3.2**) demonstrated the presence of AuNPs-PAA-Ctxb in intracellular vesicles in the perinuclear region of MDA-MB-453 cells, despite their low EGFR expression profile<sup>544</sup>. This considerable cellular uptake could partly explain the non-specific, cell-associated radioactivity behind the EGFR saturation level when the concentration of  $^{177}\text{Lu}$ -DTPA-Ctxb-PAA-AuNPs increased. Indeed, the total binding of  $^{177}\text{Lu}$ -DTPA-Ctxb-PAA-AuNPs to A431 cells is higher than the specific binding of  $^{177}\text{Lu}$ -DTPA-Ctxb-PAA-AuNPs. This was not observed in the ELISA assays using cells that were fixed and thus unable to internalize AuNPs-PAA-Ctxb. On the other hand, the suspension of  $^{177}\text{Lu}$ -DTPA-Ctxb-PAA-AuNPs in complete cell growth medium containing FBS could result in the formation of a protein corona, which might promote the non-specific interaction with cells.

Despite the non-specific cellular interaction of  $^{177}\text{Lu}$ -DTPA-Ctxb-PAA-AuNPs, it is important to note that the binding and the uptake of  $^{177}\text{Lu}$ -DTPA-Ctxb-PAA-AuNPs were higher in the EGFR-overexpressing A431 cells than in the EGFR-negative MCF-7 cells. Furthermore, blocking the EGFR with an excess of cold Ctxb reduced the binding and uptake of the  $^{177}\text{Lu}$ -

DTPA-Ctxb-PAA-AuNPs in A431 much more than in A549 cells, which have a low EGFR expression, and in EGFR-negative MCF-7 cells (**Supplemental Figure 5.1**). These results indicate that Ctxb enhanced the binding and uptake of  $^{177}\text{Lu}$ -DTPA-Ctxb-PAA-AuNPs in EGFR-overexpressing cancer cells. The presence of radioactive  $^{177}\text{Lu}$ -DTPA-Ctxb-PAA-AuNPs inside the cell is likely to generate more damage than membrane-bound  $^{177}\text{Lu}$ -DTPA-Ctxb. Furthermore, as shown previously, the AuNPs-PAA-Ctxb inhibit the cellular antioxidant defense system and induce mitochondrial dysfunction<sup>177,180,537,544</sup>. As a result,  $^{177}\text{Lu}$ -DTPA-Ctxb-PAA-AuNPs are expected to increase the efficacy of TRT.

## 6. Future perspectives

Further research on the potential of  $^{177}\text{Lu}$ -DTPA-Ctxb-PAA-AuNPs to enhance TRT efficacy is required. We aim to investigate whether  $^{177}\text{Lu}$ -DTPA-Ctxb-PAA-AuNPs enhance inhibition of the clonogenic potential and induce more cancer cell death than  $^{177}\text{Lu}$ -DTPA-Ctxb. Furthermore, we hypothesize that the mechanism of action of  $^{177}\text{Lu}$ -DTPA-Ctxb-PAA-AuNPs to sensitize the cancer cells to the radioactive  $^{177}\text{Lu}$  is the inhibition of the antioxidant thioredoxin reductase (TrxR)<sup>544</sup>. In order to investigate this, we will include three different cancer cell lines. A431 cells overexpress EGFR, but exhibit a low TrxR activity. A549 cells have a low EGFR expression and have a high TrxR activity. Finally, MCF-7 cells are EGFR-negative and exhibit a low TrxR activity (**Supplemental Figure 5.1**). Due to the TrxR inhibition by  $^{177}\text{Lu}$ -DTPA-Ctxb-PAA-AuNPs, it is expected that the treatment of A549 cells with  $^{177}\text{Lu}$ -DTPA-Ctxb-PAA-AuNPs will induce a stronger cell inhibitory effect than the  $^{177}\text{Lu}$ -DTPA-Ctxb treatment. On the other hand, the radiosensitizing effect in A431 and MCF-7 cells might be less pronounced. Nevertheless, the cell inhibitory effect will also depend on the internalization of  $^{177}\text{Lu}$ -DTPA-Ctxb-PAA-AuNPs in the different cancer cell types, which was shown to be higher in A431 cells than in MCF-7 cells. Furthermore, pre-exposure of A549 cells to N-acetyl L-cysteine (NAC) is expected to abolish the radiosensitizing effects of  $^{177}\text{Lu}$ -DTPA-Ctxb-PAA-AuNPs.

In addition, the *in vivo* specificity of the  $^{177}\text{Lu}$ -DTPA-Ctxb-PAA-AuNPs after intravenous injection will be assessed in mice, bearing EGFR-negative MCF-7 and EGFR-positive A431 tumor xenografts. SPECT-CT imaging, autoradiography and gamma-detection will be used to assess the biodistribution and elimination of  $^{177}\text{Lu}$ -DTPA-Ctxb-PAA-AuNPs compared to  $^{177}\text{Lu}$ -DTPA-Ctxb.

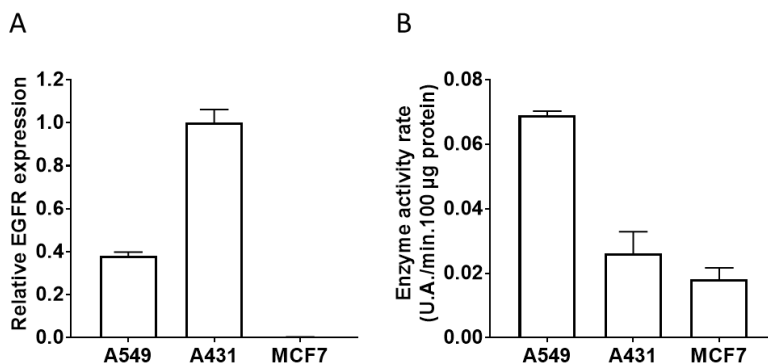
## 7. Supplemental information

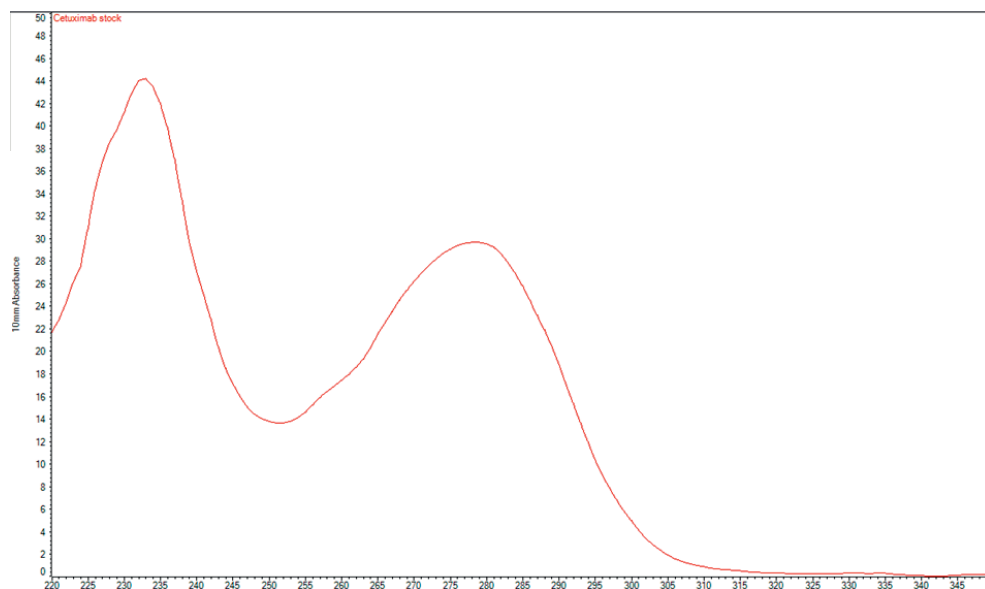
**MALDI-ToF-MS analysis:** The number of DTPA or DOTA chelators attached to Ctxb was assessed by MALDI-ToF-MS analysis. The number of bifunctional chelators per antibody was calculated by subtracting the weight of free Ctxb from the weight of the conjugate, divided by the estimated weight of the bifunctional chelator (**Supplemental Table 5.1**).

**Supplemental Table 5.1:** MALDI-ToF-MS analysis indicating the weight of the conjugates and the calculated number of bifunctional chelators per antibody.

Molar excess	Conjugate	Weight (kDa)	Chelator/Antibody
N.A.	DTPA	594.62	N.A.
N.A.	DOTA	551.61	N.A.
N.A.	Ctxb	152516	N.A.
20	Ctxb-DOTA	153966	2.629
	Ctxb-DTPA	153773	2.114
40	Ctxb-DOTA	154713	3.983
	Ctxb-DTPA	154858	3.939
80	Ctxb-DOTA	155695	5.763
	Ctxb-DTPA	156294	6.354

*Western blot analysis and Thioredoxin Reductase Activity measurement:* The Western blot analysis and the thioredoxin reductase activity measurement were performed as previously described<sup>544</sup>.

**Supplemental Figure 5.1:** (A) EGFR expression assessed with Western blot and (B) TrxR activity in A549, A431 and MCF-7 cells. EGFR expression data were obtained from one experiment with three replicates. Error bars represent SD. TrxR activity data were obtained from 2-3 independent experiments with three replicates. Error bars represent SE.



**Supplemental Figure 5.2:** The absorbance spectrum of Cetuximab with a concentration  $A_{280}$  of 29.5 and an extinction coefficient of  $210\,000\text{ M}^{-1}\text{ cm}^{-1}$ , which results in an estimated concentration of 21.5 mg/ml.

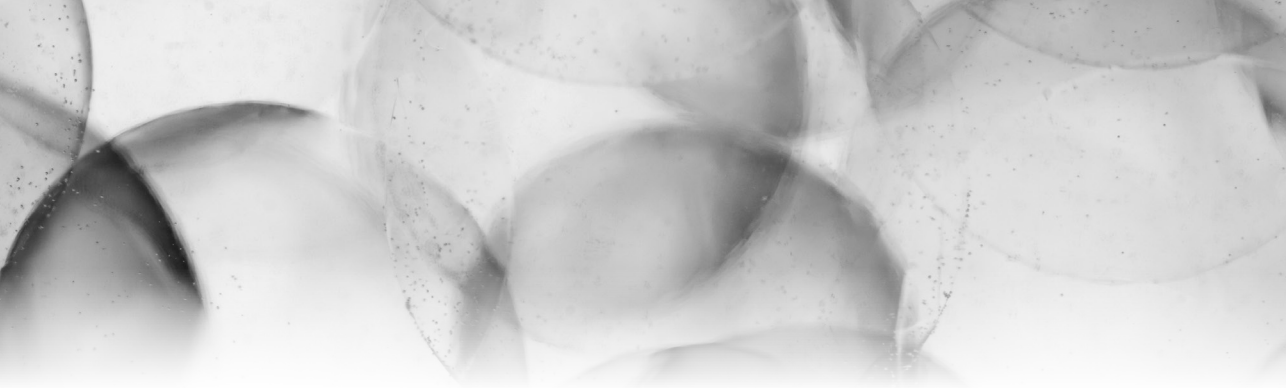




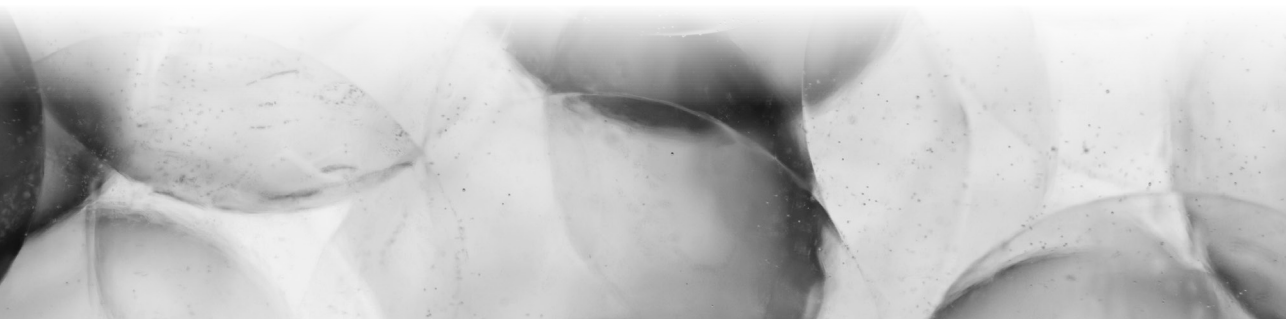
# 6

**CHAPTER**





## General discussion and conclusions





## 1. Study relevance

In the last few decades, gold nanoparticles (AuNPs) have rapidly emerged as promising tools in nanomedicine to improve the efficacy of cancer diagnosis, monitoring and treatment. In fact, the number of publications available on PubMed under the search queries ‘gold nanoparticles’ and ‘cancer’ strongly increased over the years since 2005 (**Figure 6.1**), with almost 800 hits in 2019. In this large body of literature, AuNPs were shown to be useful in targeted drug delivery, radiosensitization, photo-thermal therapy, medical imaging and nuclear medicine, enabling the development of complex multimodal, theranostic platforms<sup>16</sup>. As a result, the variety in AuNPs design regarding their size, shape, coating, charge, functionalization, etc. grew tremendously. Since these properties strongly influence the *in vitro* and *in vivo* effects and behavior of the AuNPs, it is useful to evaluate unique AuNPs for their diagnostic or therapeutic potentials, mode of action and/or toxicity.

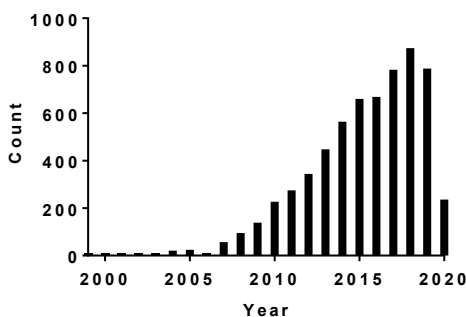


**Figure 6.1** The number of articles published each year from 2000-2020, available on PubMed under the search query ‘gold nanoparticles’ and ‘cancer’.

In this thesis, we used 5 nm-sized, poly-allylamine (PAA)-coated AuNPs, which were produced at the University of Namur<sup>4</sup>. In order to target cancer cells, the AuNPs-PAA were additionally conjugated to the antibody Cetuximab (Ctxb) that targets the epidermal growth factor receptor (EGFR). The conjugation leads to an increase in the size of the nanoparticles to 26 nm. In order to improve long-term storage and colloid stability, the AuNPs-PAA and AuNPs-PAA-Ctxb were freeze-dried before use. To prevent aggregation of the AuNPs-PAA(±Ctxb) during the freeze-drying process, arabic gum, a natural polysaccharide, was added as a stabilizer and cryoprotectant. Arabic gum might contribute to the observed negative surface charge (-30 mV in water) of the AuNPs-PAA(±Ctxb) by adsorbing onto the nanoparticle surface.

<sup>4</sup> AuNPs-PAA produced at l’Unité de Recherche Laboratoire d’Analyse par Reaction Nucléaire (LARN), University of Namur.

Previous research demonstrated that the AuNPs-PAA-Ctxb are able to selectively target EGFR-overexpressing A431 cancer cells *in vitro* and *in vivo*, and could prevent the phosphorylation of EGFR<sup>360,474</sup>. Furthermore, AuNPs-PAA-Ctxb enhance the efficacy of proton therapy in A431 cancer cells (SER of 1.22). This effect is associated with an increased ROS production<sup>201</sup>. These *in vitro* and *in vivo* results highlight the promising application of AuNPs-PAA-Ctxb as radiosensitizing agents. As thoroughly described in Chapter 1, the observed experimental radiosensitization effects of AuNPs are usually higher than predicted from the physical dose enhancement in Monte Carlo simulations. This strongly suggests that the physical interaction between AuNPs and ionizing radiation is not the only mechanism responsible for the radiosensitization properties of AuNPs<sup>133,134</sup>. For instance, there is emerging evidence that AuNPs can chemically catalyze the generation of ROS and can affect various cellular biological mechanisms involved in radiation responses, predisposing cells to cell death after irradiation<sup>238,537</sup>. However, despite the effective targeting of AuNPs to the tumor site, it is inevitable that also normal cells and tissues are exposed to AuNPs after administration *in vivo*. Since the majority of the studies are focused on the imaging and therapeutic potentials of the AuNPs in cancer cells, there is little research conducted on the effects of AuNPs in normal cells<sup>61,145,167,251,259,528,542,594-596</sup>.

Therefore, the first objective of this thesis was to assess the toxicity profile of AuNPs-PAA and AuNPs-PAA-Ctxb in several normal human cell types and to gain more insight into putative cytotoxicity mechanisms (Chapter 3). Since in Chapter 3, we showed that AuNPs-PAA and AuNPs-PAA-Ctxb cause various biological effects in normal human cells, such as antioxidant enzyme inhibition, mitochondrial dysfunction and induction of apoptosis, the second objective of this thesis was to investigate the *in vivo* pharmacokinetics, biodistribution and toxicity of AuNPs-PAA-Ctxb in healthy mice (Chapter 4). Finally, since antioxidant enzyme inhibition and mitochondrial dysfunction were previously identified as potential AuNPs-mediated radiosensitizing mechanisms, a third objective of this thesis was to radiolabel AuNPs-PAA-Ctxb with <sup>177</sup>Lu to assess the potential of <sup>177</sup>Lu-Ctxb-PAA-AuNPs to sensitize cancer cells to targeted radionuclide therapy (TRT) (Chapter 5)<sup>177,537</sup>.

## 2. The mechanism underlying the cytotoxicity of AuNPs-PAA-Ctxb

After intravenous administration, endothelial cells are the first cells to encounter the AuNPs, while the kidneys and liver are part of the renal and hepatobiliary excretion routes, respectively. Therefore, in chapter 3, human microvascular endothelial (TIME) cells, human proximal tubular kidney (HK-2) cells and human liver (THLE-2) cells were chosen as suitable cell models to estimate vascular toxicity, nephrotoxicity and hepatotoxicity, respectively. Although the cells are immortalized, they originated from primary human cells and retained their phenotypic and functional characteristics<sup>597-599</sup>. Besides these normal cells, we also

included the EGFR-overexpressing A431 cancer cell line and the EGFR-negative MDA-MB-453 cell line.

An overview of the EGFR expression, the TEM imaging, the ICP-MS data, the MTS viability, the thioredoxin reductase (TrxR) inhibition and the mitochondrial membrane depolarisation in the different cell types after exposure to AuNPs-PAA( $\pm$ Ctxb) is presented in **Table 3.2** of Chapter 3. TEM images demonstrated that AuNPs-PAA-Ctxb were internalized by all cell types and were present in intracellular vesicles indicating uptake via endocytosis. From the MTS viability assay data, we calculated the EC<sub>50</sub> values, which represented the nanoparticle concentration resulting in a 50% decrease of the cells' metabolic activity. Comparing these values demonstrated that the A431 cells and HK-2 cells were the least sensitive to the effects of AuNPs-PAA( $\pm$ Ctxb), despite their high EGFR expression and their considerable interaction with AuNPs-PAA-Ctxb according to quantitative ICP-MS data. On the contrary, TIME cells and THLE-2 cells, showing a low EGFR expression and an overall lower interaction with the AuNPs-PAA( $\pm$ Ctxb) according to ICP-MS data, were identified as the two most sensitive cell lines. However, although ICP-MS data suggest a low interaction between the TIME cells and the AuNPs-PAA-Ctxb, the TEM images show the uptake of remarkably large clusters of AuNPs-PAA-Ctxb, which could be related to a high rate of endocytosis in endothelial cells<sup>600</sup>.

Based on these *in vitro* observations, we hypothesize that the cytotoxicity of AuNPs-PAA and AuNPs-PAA-Ctxb strongly depends on the intrinsic properties of the specific cell line, rather than the antigen expression status of the cell and the extent of cellular-AuNPs interaction. In this view, we examined the mitochondrial function and the activity of the antioxidant enzyme TrxR, which both have been suggested as potential targets of AuNPs in order to radiosensitize cancer cells<sup>177,180,537</sup>. In line with the MTS data, the mitochondrial membrane depolarization caused by a non-lethal concentration of AuNPs-PAA( $\pm$ Ctxb) was most profound in TIME cells, followed by THLE-2 cells and HK-2 cells. As discussed in the introduction in Chapter 1, mitochondria are major endogenous sources of ROS generation and are important key regulators of autophagy and apoptosis<sup>260</sup>. Therefore, it is reasonable that the mitochondrial depolarization after exposure to a non-lethal concentration of AuNPs-PAA( $\pm$ Ctxb) activated an autophagic response in the cells. Autophagy can generate sufficient energy to cope with cellular stress and to restore the cellular homeostasis, which could explain why the mitochondrial membrane depolarization was observed as a transient response. In case of exposure to higher AuNPs-PAA( $\pm$ Ctxb) concentrations, excessive membrane depolarization might lead to mitochondrial membrane permeabilization, which is a hallmark of apoptosis initiation. Apoptosis was evidenced in the cell lines. Indeed, an increase in the apoptotic markers, cleaved caspase 3/7 and annexin V was observed.

In addition to mitochondrial depolarization, we also observed a significant inhibition of the activity of thioredoxin reductase (TrxR) in HK-2 cells, THLE-2 cells and TIME cells. Importantly, the basal TrxR activity in the TIME cells was remarkably higher and decreased more

extensively than in the THLE-2 cells and HK-2 cells. The Trx/TrxR system plays an important role in the cellular redox homeostasis and modulates a number of transcriptional pathways involved in inflammation, cell survival and angiogenesis<sup>538,601</sup>. The modulatory effect of the thioredoxin (Trx)/TrxR system on angiogenesis and thus vascular homeostasis is a potential reason for the high TrxR activity in TIME cells<sup>602</sup>. In various mammalian cells, reduced Trx indirectly prevents the degradation of hypoxia inducible factor-1 $\alpha$  (HIF-1 $\alpha$ ) and increases the DNA binding of the transcription factors activator protein-1 (AP-1) and nuclear factor- $\kappa$ B (NF- $\kappa$ B) on the promoter or enhancer regions of various target genes, including the VEGF gene<sup>538,602,603</sup>. This effect induces vascular endothelial growth factor (VEGF) expression, which in turn, activates several intracellular signaling pathways promoting cell survival, proliferation, migration and vascular permeability. In addition, reduced Trx interacts with the apoptosis signaling kinase-1 (ASK-1) and the growth suppressor phosphatase and tensin homolog (PTEN), preventing their pro-apoptotic and anti-proliferative functions, respectively<sup>538,602</sup>. Hence, inhibition of the TrxR activity, as we observed in the normal cells, diminishes the availability of reduced Trx, which may result in a pro-apoptotic status and a reduced cell proliferation and survival.

Glutathione reductase (GR) is closely related to TrxR and has a similar tertiary structure. GR maintains the supply of reduced glutathione, the most abundant thiol-containing compound in the cell<sup>604</sup>. The glutathione (GSH) and Trx antioxidant systems are the two major thiol-dependent pathways maintaining the redox balance in the cell. Importantly, the GSH and Trx systems have partially overlapping functions and can serve as a back-up for one another via cross-talk between both systems<sup>605-608</sup>. The activity of GR was significantly suppressed by AuNPs-PAA( $\pm$ Ctxb) in all three cell lines, but to a lesser extent compared to the inhibition of the TrxR activity. The reason for this difference is the faster and preferential reaction of gold with the selenocysteine residue in TrxR, as compared to the cysteine residue in GR<sup>243</sup>. Besides three thioredoxin reductases (TrxR1-3), the human selenoproteome (**Annex Table 3**) also includes five glutathione peroxidases (GPx1-4, 6) and one methionine sulfoxide reductase (MSRB1) providing efficient antioxidant defense. In addition, there are three iodothyronine deiodinases, which control the thyroid hormone metabolism, while selenoprotein P (SelP) and selenophosphate synthetase (SPS2) are involved in the transport of selenium and the synthesis of selenoproteins, respectively<sup>609-613</sup>. In contrast, little is known about 11 other selenoproteins (SelF, SelH, SelI, SelK, SelM, SelN, SelO, SelS, SelT, SelV, SelW). Based on their structure, one can hypothesize that the function of a major part of the selenoproteins is involved in maintaining the redox homeostasis. In addition, some selenoproteins present in the ER are proposed to be involved in protein folding or in the degradation process of misfolded proteins<sup>614</sup>. It might be of interest to investigate if TrxR is the only selenoprotein that is affected by AuNPs or if AuNPs are also able to interact with the selenocysteine residues of the other selenoproteins. Since many selenoproteins are proposed to play a role in the cellular redox homeostasis, inhibition of these proteins by

AuNPs might contribute to the oxidative stress and potentially result in an accumulation of misfolded proteins causing ER stress. For instance, several studies have reported the ability of auranofin and other gold-based compounds to form a stable complex with the selenocysteine residue in GPx1, blocking the active site of the enzyme<sup>615,616</sup>. Indeed, gold nanoclusters conjugated to negatively charged peptides inhibited the GPx activity in A549 cells in a dose-dependent manner, leading to an increased ROS level in the cells and to apoptosis<sup>617</sup>. Nevertheless, high concentrations of auranofin in the micro-molar range are needed to inhibit GPx activity, while TrxR activity was strongly suppressed at concentration in the nano-molar range. The difference in enzyme inhibition has been related to the position of the selenocysteine residue being more accessible in TrxR than in GPx.<sup>618,619</sup> Based on our *in vitro* results and the studies referred to above, we suggest that AuNPs-PAA( $\pm$ Ctxb) preferentially inhibit TrxR. However, TrxR is most likely not the only antioxidant target enzyme affected by AuNPs-PAA( $\pm$ Ctxb) as evidenced by the decreased GR activity.

The suppression of endogenous TrxR and GR antioxidant systems could significantly reduce the capacity of the normal cells to cope with ROS that can originate from the chemical enhancement and the biological enhancement of AuNPs (including mitochondrial dysfunction). In our study, the role of oxidative stress and the disturbance of the thiol-redox balance have been indirectly confirmed by the protective effect of N-acetyl L-cysteine, a thiol-containing antioxidant. Indeed, N-acetyl L-cysteine (NAC) prevents mitochondrial dysfunction and reduces apoptosis during exposure to AuNPs-PAA( $\pm$ Ctxb). The hypothesized cytotoxicity mechanism described above is illustrated in **Figure 6.2**.

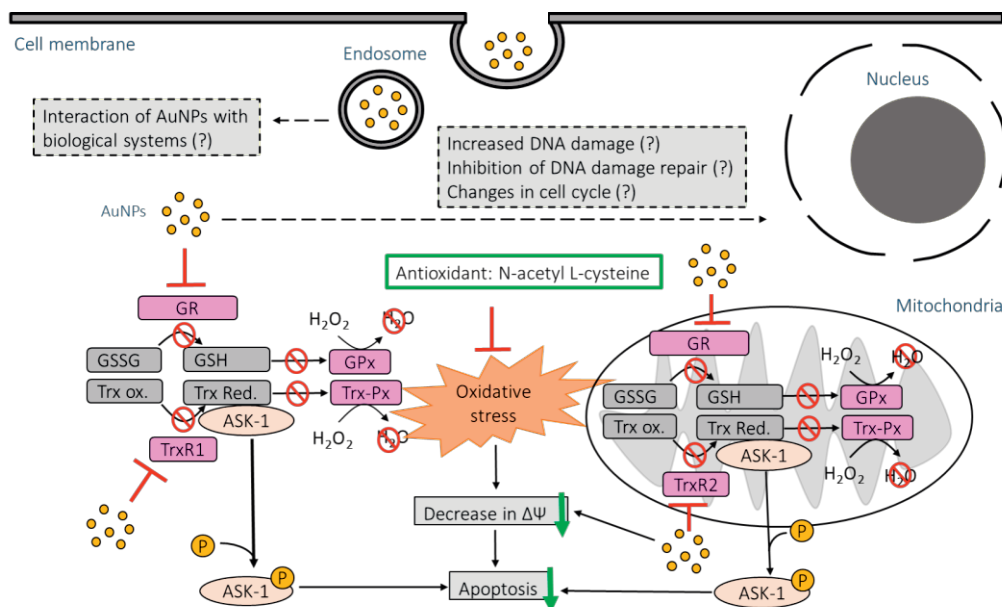


**Figure 6.2** The proposed cytotoxicity mechanism of AuNPs-PAA and AuNPs-PAA-Ctxb in normal cells based on the findings of our *in vitro* study. AuNPs-PAA( $\pm$ Ctxb) are internalized in the cells in intracellular vesicles. The uptake is followed by the inhibition of the antioxidant enzyme activities of GR and TrxR, which are both present in the cytosolic and mitochondrial compartments. As a result, glutathione disulfide and oxidized thioredoxin are not effectively reduced and thus are not able to detoxify hydrogen peroxide into water. The accumulation of hydrogen peroxide promotes the pro-oxidant status of the cell, leading to oxidative stress. Furthermore, the oxidation of thioredoxin results in the dissociation of its binding partner, ASK-1, which is activated by phosphorylation and activates the apoptosis signaling cascade. In addition, AuNPs-PAA( $\pm$ Ctxb) exposure causes depolarization of the mitochondrial membrane potential, either directly or indirectly via oxidative stress, which can initiate autophagy or apoptosis. Importantly, co-exposure of the cells with the antioxidant, N-acetyl L-cysteine, prevented the mitochondrial membrane depolarization and the induction of apoptosis.

**Abbreviations:** ASK-1: apoptosis signal-regulating kinase 1; AuNPs: gold nanoparticles; GR: glutathione reductase; GSSG: glutathione disulfide; GSH: glutathione; GPx: glutathione peroxidase; Trx ox: oxidized thioredoxin; Trx red: reduced thioredoxin; TrxR: thioredoxin reductase; Trx-Px: thioredoxin peroxidase; P: phosphate;  $\Delta\Psi$ : mitochondrial membrane potential.

Importantly, this cytotoxicity mechanism strongly resembles the radiosensitization mechanism of PEGylated AuNPs described by Penninckx, et al. These researchers evidenced a good correlation between the TrxR inhibition and the radiosensitization effect of PEGylated AuNPs combined with proton therapy in five different cancer cell types<sup>177,537</sup>. Furthermore, several studies demonstrated mitochondrial dysfunction in cancer cells after exposure to AuNPs, which has been suggested to contribute to biological radiosensitization<sup>180,251,252,528,620</sup>. Similarly, in our study, the basal TrxR activity, the extent of TrxR inhibition and the mitochondrial dysfunction were strongly correlated with the sensitivity of the normal

cells to AuNPs-PAA( $\pm$ Ctxb). It should be noted that the correlation was based on a limited data set of only three normal cell types and thus care should be taken to extrapolate these findings to other normal cell types. Nonetheless, our results clearly indicate that AuNPs-PAA-Ctxb strongly affect the biological systems in cells and thus have the potential to sensitize the cancer cells to ionizing radiation. The radiosensitizing effects of AuNPs are usually investigated considering radiation delivered by an external beam<sup>621</sup>. However, there are only a limited number of studies investigating the use of AuNPs as biological radiosensitizing agents in TRT (**Table 1.3** in Chapter 1). Therefore, in Chapter 5, we radiolabeled the AuNPs-PAA-Ctxb to <sup>177</sup>Lu in order to assess the radiosensitizing potential of the <sup>177</sup>Lu-DTPA-Ctxb-PAA-AuNPs in TRT, which is discussed in detail in, in this section, paragraph 4.

In normal cells, the TrxR and Trx mainly serve as antioxidants and redox regulators, while in aggressive and invasive cancers TrxR and Trx are commonly overexpressed to promote the tumor progression by providing a high proliferation capacity, a high metastatic potential and a low apoptosis rate. In fact, the overexpression of the TXNRD1 gene in tumors is even correlated with treatment resistance and poor patient outcomes<sup>537</sup>. Therefore, TrxR is a promising target for anti-cancer therapy<sup>622</sup>. Indeed, inhibition of TrxR by auranofin and other gold-based complexes has been linked with increased cancer cell apoptosis *in vitro* and reduced tumor growth *in vivo*<sup>623-625</sup>. However, the similarity between the results of our study in normal cells and the results in literature conducted in cancer cells indicate that the use of AuNPs-PAA-Ctxb as radiosensitizing agents might cause side effects after administration *in vivo*, related to the inhibition of TrxR and GR in normal cells.

In fact, certain side effects caused by chemotherapeutic drugs have been related to the inhibition of the TrxR and GR system in healthy tissues. For instance, nephrotoxicity is a common side effect of anti-cancer platinum-containing drugs and ifosfamide. Among the platinum-containing drugs, cisplatin (0.05 mM) was the most effective inhibitor of kidney TrxR1 activity in mice (60%), causing the severest increase in serum creatinine, blood urea nitrogen and renal injury<sup>626</sup>. Similarly, ifosfamide (350 mg/kg) specifically decreased the TrxR activity in the bladder and kidney by 74% and 37%, respectively<sup>627,628</sup>. Furthermore, increased blood urea nitrogen levels and renal injury were observed in the treated mice in a dose-dependent manner<sup>628</sup>. Next to nephrotoxicity, heart failure is a serious complication of high-dose cyclophosphamide. Cyclophosphamide (250 mg/kg) specifically diminished heart TrxR1 activity by 62% in treated mice, but only caused significant cardiac toxicity when the GSH content in the cells was compromised<sup>629</sup>. Consistently, depletion of the GSH content strongly exacerbated the ifosfamide-induced nephrotoxicity<sup>628</sup>. These observations confirm the cross-talk between the GR and TrxR antioxidant systems and the back-up ability of the GSH antioxidant system if the TrxR antioxidant system is compromised. Thus, bearing in mind that AuNPs-PAA( $\pm$ Ctxb) inhibit both TrxR and GR, it might be possible that administration of AuNPs-PAA-Ctxb could induce vascular dysfunction, nephrotoxicity or hepatotoxicity. Nevertheless, the potential of AuNPs-PAA-Ctxb to cause serious side effects strongly

depends on their *in vivo* pharmacokinetics and biodistribution. The aim of Chapter 4 was to assess these two parameters in healthy mice.

Another major finding of our *in vitro* study is the lower cytotoxicity of AuNPs-PAA-Ctxb compared to AuNPs-PAA without Ctxb, despite the trend of a higher uptake of AuNPs-PAA-Ctxb in the cells. Since conjugated Ctxb in AuNPs-PAA-Ctxb is able to target the EGFR *in vitro* and *in vivo*, the reduced cytotoxicity related to AuNPs-PAA-Ctxb exposure indicates that the inhibition of the EGFR pathway by the AuNPs-PAA-Ctxb, on its own, does not cause cytotoxic effects in an *in vitro* environment<sup>474,488</sup>. Nevertheless, *in vivo*, when AuNPs-PAA-Ctxb target the tumor site, the Fc region of Ctxb could attract immune effector cells, such as natural killer cells and cytotoxic T cells to eliminate the tumor cells. This process is known as antibody-dependent cell-mediated cytotoxicity, which is involved in the treatment of metastatic colorectal cancer<sup>630</sup>.

Notably, AuNPs-PAA-Ctxb appeared to inhibit TrxR and GR to a similar extent than AuNPs-PAA. However, AuNPs-PAA-Ctxb caused no mitochondrial dysfunction in HK-2 cells. In TIME cells, the mitochondrial dysfunction caused by AuNPs-PAA-Ctxb was significantly less severe than that induced by AuNPs-PAA. Thus, it might be possible that Ctxb shields the gold core from the surroundings, slightly reducing its biological and potentially also its chemical cytotoxicity. In addition, despite the suppression of the TrxR and GR antioxidant systems in all cell types after exposure to AuNPs-PAA-Ctxb, the HK-2 cells were the least sensitive cells. Thus, it might be possible that mitochondrial dysfunction and suppression of the antioxidant defense mechanism is a combined action that is required to induce sufficient oxidative stress and to initiate apoptotic signaling in the cells.

### 3. The fate and behavior of AuNPs-PAA-Ctxb *in vivo*

The second objective of this thesis was to investigate the pharmacokinetics, biodistribution and toxicity of intravenously injected AuNPs-PAA-Ctxb in healthy mice. The results demonstrated that, after a single intravenous administration, the AuNPs-PAA-Ctxb are rapidly cleared from the blood circulation, followed by their accumulation and long-term retention (> 6 months) in the liver and the spleen. Due to the size of the AuNPs-PAA-Ctxb and their negative surface charge, rapid renal elimination of AuNPs-PAA-Ctxb via the negatively charged glomerular filter is probably limited. Instead, the AuNPs are eliminated at a very slow pace, potentially via the hepatobiliary pathway. Although we observed significant cytotoxicity of the AuNPs-PAA-Ctxb in liver cells and endothelial cells *in vitro*, we found just a minimal and transient increase in a limited number of serum markers characteristic for liver toxicity and vascular damage. Furthermore, since AuNPs-PAA-Ctxb show a high sequestration by the reticuloendothelial system (RES), which is part of the immune system, we assessed the serum level of various cytokines that are related to the immune response<sup>631</sup>. We did not observe a significant change in the inflammatory serum markers. Furthermore, no signs of



altered liver, kidney, lung and spleen morphology were found on tissue slices up to 4 weeks post-injection. After 6 months, occasional kidney casts and splenic apoptosis appeared to be more prevalent in treated mice than in the control mice. However, it should be noted that, in our study, the hematoxylin/eosin staining was used as a qualitative assessment rather than a (semi)-quantitative method. Therefore, we are not able to exclude long-term toxicity of AuNPs-PAA-Ctxb.

The low toxicity profile of AuNPs-PAA-Ctxb *in vivo* can be explained by the rapid clearance of the AuNPs-PAA-Ctxb by the RES. Due to their negative surface charge, it is likely that AuNPs-PAA-Ctxb adsorb plasma proteins onto their surface when entering into the blood circulation, including opsonins, such as complement components and immunoglobulins, forming the biocorona<sup>411,425,426</sup>. The phagocytic cells of the RES may effectively recognize and rapidly internalize the opsonized AuNPs-PAA-Ctxb in order to protect the organism against the potential harmful effects of the AuNPs<sup>462</sup>. Indeed, the blood circulation half-life of the AuNPs-PAA-Ctxb is very short (2.3 minutes), which minimizes the exposure concentration and time of healthy cells and tissues to AuNPs-PAA-Ctxb *in vivo*. However, in order to increase the probability for the AuNPs-PAA-Ctxb to encounter and accumulate into the tumor and thus increase their therapeutic potential, a long blood circulation time is desirable. Furthermore, their long-term retention in the liver and spleen could be a concern regarding the safety and approval of the nanomedicine.

How could we adapt the AuNPs-PAA-Ctxb to improve the pharmacokinetics and biodistribution, while minimizing toxicity in normal tissues?

First, rapid sequestration of the AuNPs-PAA-Ctxb by phagocytic cells should be prevented in order to prolong the blood circulation time and to prevent their long-term retention in liver and spleen. There are several factors that could affect the uptake of AuNPs-PAA-Ctxb by the RES. For instance, it has been reported that nanoparticles with sizes larger than 40 nm show a high uptake by the phagocytic cells, which prevents them to be eliminated via the hepatobiliary excretion pathway<sup>632,633</sup>. The AuNPs-PAA-Ctxb are generally stable in cell culture medium containing 10% FBS. However, whole blood has a complex composition containing cells and certain factors that are absent in serum. Therefore, the biocorona formation and the interactions between certain components and AuNPs-PAA-Ctxb in whole blood are most likely different than in cell culture media containing 10% FBS. This could potentially reduce the colloid stability, resulting in nanoparticle aggregation and enhancing the uptake by the RES. The colloid stability strongly depends on the coating of the AuNPs. Poly-allylamine is a weak polyelectrolyte, providing a hydrophilic nature and a strong charge to AuNPs, which supports the electrosteric stabilization of the colloid suspension<sup>25,634</sup>. However, the charged polymer coating might also promote adsorption of arabic gum and proteins onto the AuNPs-PAA-Ctxb surface. Furthermore, due to the electrical double layer formed around the charged particle, the stability of the AuNPs-PAA-Ctxb colloid depends on

the pH and ionic strength of the incubation medium. This was observed by the considerable reduction of the zeta potential magnitude of the AuNPs-PAA-Ctxb when suspended in cell medium compared to water (from -30 mV in water to -7.59 mV and -7.04 mV, in cell medium without 10% FBS and in medium containing 10% FBS, respectively). In order to minimize potential aggregation of the AuNPs-PAA-Ctxb after administration into the blood stream, it might be of interest to increase the thickness of the poly-allylamine coating to investigate the steric stabilization. However, increasing the coating thickness could reduce the dose enhancement efficiency after irradiation due to energy deposition of the secondary electrons inside the coating. Another option to improve colloid stability and reduce protein adsorption after administration into the blood stream would be to replace the charged poly-allylamine coating of the AuNPs-PAA-Ctxb by a hydrophilic, neutral polymer coating, such as PEG. As described in the introduction Chapter 1, PEGylation of AuNPs is frequently used to increase the colloid stability, to decrease the extent of protein adsorption and to prolong the circulation half-life *in vivo* by reducing the RES uptake. The prolonged circulation half-life could increase the probability for the AuNPs to accumulate at the tumor site. Furthermore, PEG is a biocompatible polymer minimizing the toxicity to normal cells.

Second, in order to facilitate the AuNPs-PAA-Ctxb accumulation and retention in the tumor, active targeting of AuNPs-PAA-Ctxb is mediated by the antibody Ctxb. The main advantage of using Ctxb as a targeting molecule is its availability and its high affinity and specificity toward EGFR. However, using a full-length antibody as targeting molecule has certain disadvantages. For instance, the conjugation of Ctxb to AuNPs-PAA is based on a commonly used, but unspecific reaction method, which covalently links the amino groups of the PAA coating to the surface-exposed carboxyl groups of Ctxb. Since an antibody may contain multiple carboxylic acid side chains along its structure, this chemical reaction might lead to a suboptimal orientation of the antibody onto the nanoparticle surface<sup>635-637</sup>. Nevertheless, the conjugated Ctxb in AuNPs-PAA-Ctxb is able to specifically target EGFR-overexpressing A431 cells *in vitro* and *in vivo*, indicating that the antigen recognizing regions of Ctxb are accessible to bind EGFR<sup>323,474</sup>. In addition, Fc receptors on the surface of macrophages in the liver and the spleen might recognize the Fc portion of the full-length antibody, resulting in Fc receptor-mediated clearance and thus a reduced blood circulation time. Finally, the large size of a full-length antibody limits the number of antibody molecules that can be accommodated onto the AuNPs surface and considerably increases the total size of the nanoparticle<sup>34,638</sup>. According to thermogravimetric analyses, the AuNPs-PAA-Ctxb used in this thesis are loaded with, on average, two to three Ctxb molecules per nanoparticle. This loading increases the total particle size from 5 nm to 26 nm<sup>544</sup>.

The total size of the nanoparticle has a considerable impact on its biodistribution and elimination profile. Since AuNPs-PAA-Ctxb are not biodegradable, researchers prefer their elimination from the body. In fact, degradation or elimination of nanomedicine from the body after its intended medical use is an important requirement to obtain approval of

regulatory agencies such as the European Medicine Agency (EMA) and the United States Food and Drug Administration (FDA) <sup>362,506,639,640</sup>. Due to the molecular size of Ctxb, the AuNPs-PAA-Ctxb are too large (> 5.5 nm) to be filtered and eliminated by the kidneys. Therefore, phagocytic uptake of AuNPs-PAA-Ctxb by the RES should be prevented in order for the AuNPs-PAA-Ctxb to be cleared via the hepatobiliary pathway. The size of the liver sinusoidal endothelial cell fenestrae allows passage of AuNPs smaller than 200 nm. The hepatobiliary excretion efficiency exponentially increases as the size of the AuNPs decreases <sup>362,491</sup>. For instance, Poon, et al demonstrated that next to renal elimination, 4 nm PEGylated AuNPs exhibited a cumulative elimination of 6.1% of the injected dose over a period of 14 days, while 15 nm PEGylated AuNPs showed a cumulative elimination of 1.7 % of the injected dose or lower. Gold nanoparticles with a total size smaller than 10-15 nm can easily penetrate through the various physiological structures of the liver, having a greater opportunity to interact with the hepatocytes, while macrophages are less effective in removing these small AuNPs from the liver sinusoidal circulation <sup>362,491</sup>. Other studies showed similar results <sup>641-643</sup>. Generally, as the total size of AuNPs increases further, then the excretion via the hepatobiliary pathway becomes considerably slower, ranging from multiple months to even more than one year <sup>405,462</sup>. Besides a more efficient renal and hepatobiliary elimination, small sized AuNPs of 2 nm-6 nm show a longer blood circulation time and an increased tumor uptake as compared to 15 nm AuNPs. Furthermore, their small size enables them to freely diffuse into the tumor tissue, promoting a homogenous intratumoral distribution <sup>493,644</sup>. However, small AuNPs are also able to exit the tumor tissue, exhibiting a shorter tumor retention. Moreover, small AuNPs show a more widespread distribution within the normal tissues, increasing the probability of normal tissue toxicity. In contrast, large AuNPs remain around the blood vessels at the periphery of the tumor, which limits their tumor accumulation, but promotes a longer tumor retention. In addition, AuNPs with a large size are predominantly accumulated in the liver and spleen <sup>491,493,553</sup>.

Thus, in order to benefit from the small size of the AuNPs-PAA and to prevent a considerable increase in the total size after conjugation of full-length Ctxb, it might be of interest to consider the use of small antibody fragments as targeting ligands. Small antibody fragments maintain a high antigen specificity and affinity, could allow a higher loading density on the AuNPs surface, which increases the multivalence effect, and could reduce the immunogenicity due to the removal of the Fc region <sup>34,645</sup>. For instance, Cheng, et al demonstrated that liposomes targeted with full-length antibodies targeting B-cell antigen CD19 had a shorter blood circulation half-life and an increased uptake in liver and spleen compared to the liposomes targeted with the antibody Fab' fragment. Furthermore, the Fab'-antibody fragment conjugated liposomes were slightly more effective in prolonging the survival time of mice with CD19-positive lymphoma compared to the liposomes conjugated with the full-length antibody <sup>646</sup>. In this view, the use of small antibody fragments as targeting molecules instead of full-length antibodies might change the biodistribution profile of the

AuNPs-PAA with a longer blood circulation time and a more efficient elimination from the body.

Taken all together, it is important to bear in mind that the fate of AuNPs after administration *in vivo* will be determined by multiple factors related to the AuNPs properties, including the total size, the coating, the charge, the targeting molecules, and the shape. Tuning the properties of the AuNPs is a required process to obtain the most favorable balance in the pharmacokinetics, biodistribution, normal tissue toxicity and efficiency of the intended applications.

#### 4. The feasibility of radiolabeled $^{177}\text{Lu}$ -DTPA-Ctxb-PAA-AuNPs as therapeutic agent

A third objective of this thesis was to radiolabel the AuNPs-PAA-Ctxb with the radionuclide  $^{177}\text{Lu}$  in order to investigate if the biological effects caused by AuNPs-PAA-Ctxb can sensitize cancer cells to the radiation effects of  $^{177}\text{Lu}$ , compared to  $^{177}\text{Lu}$ -DTPA-Ctxb without AuNPs. The rationale for this objective was derived from results indicating that AuNPs-PAA-Ctxb can sensitize cancer cells to proton radiotherapy<sup>201</sup>. Furthermore, in Chapter 3, we demonstrated that AuNPs-PAA-Ctxb caused biological effects in cells, such as mitochondrial dysfunction and inhibition of GR and TrxR. Mitochondria and the antioxidant enzymes play an important role in the regulation of apoptotic and autophagic pathways, and the defense against oxidative stress, respectively, which are important mechanisms involved in the cellular radiation response<sup>647</sup>. Furthermore, TrxR inhibition was identified by Penninckx, et al. as considerable factor contributing to the radiosensitizing mechanism of PEGylated AuNPs<sup>177,537,544</sup>. Therefore, we hypothesize that the biological effects caused by AuNPs-PAA-Ctxb can also sensitize cells to other types of radiation therapy, such as internal targeted radiotherapy (TRT).

In Chapter 5, we optimized the radiolabeling strategy of AuNPs-PAA-Ctxb using bifunctional chelators conjugated to Ctxb, and investigated the binding and internalization of the radiolabeled  $^{177}\text{Lu}$ -DTPA-Ctxb-PAA-AuNPs in EGFR-overexpressing A431 epidermoid cancer cells, EGFR-positive A549 lung cancer cells and EGFR-negative MCF-7 breast cancer cells. In short, according to MALDI-ToF MS and ELISA, approximately two DTPA molecules can be coupled to Ctxb without affecting the antibody binding capacity to EGFR. Furthermore, fast radiolabeling of AuNPs-PAA-Ctxb-DTPA was achieved under mild conditions. We demonstrated that Ctxb of the  $^{177}\text{Lu}$ -DTPA-Ctxb-PAA-AuNPs conjugate recognized EGFR on A431 cancer cells. However, the amount of non-specific binding gradually increased as the concentration of  $^{177}\text{Lu}$ -DTPA-Ctxb-PAA-AuNPs added to the cells increased. This could partly be explained by  $^{177}\text{Lu}$ -DTPA-Ctxb-PAA-AuNPs activating endocytosis mechanisms, which are independent from EGFR expression (e.g. macropinocytosis or receptor-independent endocytosis)<sup>221</sup>. Indeed, there was a considerable internalization of  $^{177}\text{Lu}$ -DTPA-Ctxb-PAA-

AuNPs in EGFR-negative MCF-7 cells, which could not be blocked with an excess of cold Ctxb, and which was not observed after exposure to free  $^{177}\text{Lu}$ -DTPA-Ctxb. In addition, TEM images also demonstrated uptake of AuNPs-PAA-Ctxb in EGFR-negative MDA-MB-453 cells (**Figure 3.2**, Chapter 3)<sup>544</sup>. Another potential reason could be the formation of a biocorona when  $^{177}\text{Lu}$ -DTPA-Ctxb-PAA-AuNPs are suspended in cell culture medium containing 10% FBS, which could promote non-specific binding of the nanoparticles to the cell surface.

What is the rationale to study  $^{177}\text{Lu}$ -DTPA-Ctxb-PAA-AuNPs as potential cancer drugs for TRT? Clinically, radio-immunotherapy is used to treat the most radiosensitive tumors, such as leukemia and lymphoma. Extending the successful use of radio-immunotherapy to treat solid tumors has proven to be more difficult. Solid tumors are in general more radioresistant than hematopoietic cancers and need a 10 times higher radiation dose deposition to obtain a meaningful tumor response<sup>648,649</sup>. Since  $^{177}\text{Lu}$  is a low-energy  $\beta^-$  emitting radionuclide, a high number of  $^{177}\text{Lu}$  atoms needs to be delivered to the tumor. However, antibodies are usually conjugated to a single radionuclide. Furthermore, the low tumor uptake of antibodies restricts the deposited radiation dose in tumors and thus the effectiveness of radio-immunotherapy<sup>311</sup>. In this regard,  $^{177}\text{Lu}$ -DTPA-Ctxb-PAA-AuNPs could exhibit an improved therapeutic potential compared to  $^{177}\text{Lu}$ -DTPA-Ctxb. First, multiple Ctxb molecules are coupled to  $^{177}\text{Lu}$ -DTPA-Ctxb-PAA-AuNPs, which could offer a multivalent targeting avidity. Furthermore, the Fc region of the Ctxb molecules could cause antibody-dependent cell-mediated cytotoxicity, as explained before. Second,  $^{177}\text{Lu}$ -DTPA-Ctxb-PAA-AuNPs can biologically radiosensitize the cancer cells. Third,  $^{177}\text{Lu}$ -DTPA-Ctxb-PAA-AuNPs show an enhanced internalization in cancer cells compared to  $^{177}\text{Lu}$ -DTPA-Ctxb and delivers multiple  $^{177}\text{Lu}$  atoms per nanoparticle to the perinuclear region of the cells.

In theory, one AuNP-PAA-Ctxb-DTPA nanoconjugate contains approximately two antibodies and each antibody is coupled to two DTPA molecules. As a result, each AuNP-PAA-Ctxb-DTPA can carry four  $^{177}\text{Lu}$  atoms (**Figure 5.2**, Chapter 5). Since our *in vitro* results demonstrate that EGFR-overexpressing A431 cells internalize approximately 1 pg of gold per cell, then a tumor with a radius of 0.5 cm containing  $5.24 \times 10^7$  cells is expected to take up approximately 52.4  $\mu\text{g}$  of Au, which equals  $4.2 \times 10^{13}$  AuNPs-PAA-Ctxb and thus  $1.67 \times 10^{14}$   $^{177}\text{Lu}$  atoms. The absorbed dose delivered to the 0.5 cm-radius tumor is estimated to be in the range of 22-45 Gy, assuming that the  $^{177}\text{Lu}$ -DTPA-Ctxb-PAA-AuNPs have a tumor half-life of 2-6 days, are internalized in the tumor instantaneously and exhibit a uniform intratumoral distribution. The tumor half-life of the  $^{177}\text{Lu}$ -DTPA-Ctxb-PAA-AuNPs is based on previous *in vivo* studies demonstrating that  $^{131}\text{I}$ -Ctxb-PAA-AuNPs and  $^{89}\text{Zr}$ -Ctxb-PAA-AuNPs activity in the tumor reduced by half after approximately two days or was still present after 6 days, respectively<sup>323,474</sup>. The absorbed dose calculations were based on a publication of Lucas, et al, who simulated the potential of nanoparticles to fully eradicate a solid lung tumor with a 0.5 cm or 1 cm radius when containing several  $\beta$ -emitters<sup>311</sup>. They demonstrated that the number of radionuclides per nanoparticle required for a 100% tumor control probability (TCP)

depends on the type of radionuclide and its physical properties, the tumor size, the biological half-life of the nanoparticle and the spatial distribution of the nanoparticles in the tumor tissue. A considerable larger number of radionuclides is required to maintain the treatment efficacy when considering a realistic nanoparticle distribution at which the nanoparticle concentration decreases exponentially from the surface of the tumor towards the center, compared to a uniform distribution or a linear decrease in concentration. In case of an exponential distribution, a nanoparticle should contain 188 and 996  $^{177}\text{Lu}$  atoms to achieve 100% TCP of a tumor with a 0.5 cm and 1 cm radius, respectively, assuming a tumor half-life of 6 days, an instantaneous uptake and a covering fraction of  $10^9$  nanoparticles/cm<sup>2</sup>. The reason for this high number is the low energy and the short penetration range of the  $\beta^-$  particles. The inclusion of such a high number of radionuclides per nanoparticle also dramatically increases the dose deposition in healthy lung tissue. Therefore, the authors concluded that the high-energy  $\beta^-$  emitters  $^{90}\text{Y}$  and  $^{188}\text{Re}$ , rather than  $^{177}\text{Lu}$ , were suitable candidates to obtain 100% TCP of a small tumor, because of the limited number of radionuclides required per nanoparticle (between 3-21), while a larger tumor was best treated with  $^{124}\text{I}$ -nanoparticles to limit the healthy tissue toxicity<sup>311</sup>. In this view, although  $^{177}\text{Lu}$  might not be the best suitable radionuclide regarding radio-immunotherapy according to the Monte Carlo simulation, assessment of the radiosensitizing potential of  $^{177}\text{Lu}$ -DTPA-Ctxb-PAA-AuNPs in TRT is still relevant. Indeed, the mitochondrial dysfunction and antioxidant inhibition caused by AuNPs-PAA-Ctxb could sensitize the cancer cells to the radionuclides, an effect which is not taken into account in the Monte Carlo simulation, and thus might reduce the number of radionuclides required per nanoparticle to obtain a meaningful tumor response. This would reduce the probability on healthy tissue toxicity and might increase the opportunity to use other radionuclides.

In order to investigate the radiosensitizing properties of  $^{177}\text{Lu}$ -DTPA-Ctxb-PAA-AuNPs, future experiments will be conducted, including assessment of the clonogenic potential and viability of various cancer cell types after exposure to  $^{177}\text{Lu}$ -DTPA-Ctxb-PAA-AuNPs or  $^{177}\text{Lu}$ -DTPA-Ctxb. The various cancer cell types will exhibit different expression levels of EGFR and activity levels of TrxR. Importantly, the binding and uptake of the  $^{177}\text{Lu}$ -DTPA-Ctxb-PAA-AuNPs and  $^{177}\text{Lu}$ -DTPA-Ctxb to each cancer cell type will have to be taken into account during the interpretation of the results. In addition, the protective effect of NAC will be investigated to potentially abolish the radiosensitization effect of  $^{177}\text{Lu}$ -DTPA-Ctxb-PAA-AuNPs. Finally, the biodistribution, the tumor uptake and the elimination of  $^{177}\text{Lu}$ -DTPA-Ctxb-PAA-AuNPs and  $^{177}\text{Lu}$ -DTPA-Ctxb in mice bearing an EGFR-negative and EGFR-positive tumor xenograft will be compared.

## 5. General conclusions and future perspectives

In conclusion, in this thesis, we provided insight into the cytotoxicity mechanism of AuNPs-PAA and AuNPs-PAA-Ctxb in normal cells. AuNPs-PAA and AuNPs-PAA-Ctxb induced

biological effects, with mitochondrial dysfunction, oxidative stress and inhibition of the thiol-dependent antioxidant system, playing an important role. These effects resemble the biological radiosensitization mechanism previously established for PEGylated AuNPs in 5 different cancer cell types<sup>177,537</sup>. As a result, AuNPs-PAA-Ctxb have the potential to act as a radiosensitizing agent and help to reduce the radiation dose needed to treat a tumor, without compromising the treatment efficacy. Conversely, the biological radiosensitizing properties of AuNPs-PAA-Ctxb could improve the tumor response of radioresistant tumors at the conventional radiation doses. However, due to the similarity with the biological radiosensitizing mechanism of AuNPs in cancer cells, AuNPs-PAA-Ctxb could potentially cause side effects *in vivo* when used as radiosensitizing agents if they reside in normal tissues. Nevertheless, AuNPs-PAA-Ctxb showed a fast blood clearance by the RES, without causing major toxicity to the liver, spleen, lungs and kidneys. Furthermore, AuNPs-PAA-Ctxb did not increase in serum cytokine levels related to the immune response. On the other hand, the short blood circulation time and the long-term retention of AuNPs-PAA-Ctxb in liver and spleen might restrict the therapeutic potential and approval of AuNPs-PAA-Ctxb as nanomedicine. Fine-tuning the characteristics of AuNPs-PAA-Ctxb, such as the surface coating, surface charge, targeting molecule and total size, might be set as a future goal to optimize their pharmacokinetics and biodistribution profile. In addition, there are still many aspects linked to the toxicity of AuNPs-PAA-Ctxb that are useful to investigate, such as repeated-dose toxicity, genotoxicity, carcinotoxicity, reproductive toxicity and developmental toxicity. These are topics, which are recommended by the EMA to include in nonclinical safety studies to support the proceeding of pharmaceuticals to human clinical trials and marketing authorization. Furthermore, it would be of interest to investigate if other transition metal NPs next to AuNPs could also selectively inhibit the thioredoxin reductase enzyme and show similar biological radiosensitizing effects as AuNPs.

Finally, we successfully radiolabeled AuNPs-PAA-Ctxb with <sup>177</sup>Lu using the bifunctional chelator DTPA. The obtained conjugate <sup>177</sup>Lu-DTPA-Ctxb-PAA-AuNPs was still capable to bind EGFR and showed an enhanced uptake in cancer cells. Therefore, it would be of interest to perform additional studies on the potential of <sup>177</sup>Lu-DTPA-Ctxb-PAA-AuNPs to sensitize cancer cells to the delivered <sup>177</sup>Lu compared to <sup>177</sup>Lu-DTPA-Ctxb, such as the *in vitro* assessment of cancer cell viability and clonogenic potential, and the *in vivo* assessment of the biodistribution and elimination in tumor-bearing mice after exposure. The radiolabeling of AuNPs-PAA-Ctxb with <sup>177</sup>Lu and future experiments will help to pave the way to the development of new, promising radiopharmaceuticals at SCK CEN.

# Annex

**Annex Table 1:** List of useful radioisotopes for diagnosis and treatment of cancer-related diseases.

Isotope	Decay	Daughter nuclide	Half-life	Max tissue depth (mm)	Particle Energy (MeV)	Photon energy MeV (%)	Clinical indication
<sup>99m</sup> Tc	γ	<sup>99</sup> Ru	6h	/	/	0.141 (98.6%)	Used for common diagnostic procedures
<sup>123</sup> I	EC	<sup>123</sup> Te	13.2h	/	/	0.159 (83.3%)	Scintigraphy of thyroid
<sup>211</sup> At	α EC	<sup>207</sup> Bi (unstable) <sup>211</sup> Po (unstable)	7.2h	<0.01	5.87 (41.8%)	/	Under investigation for targeted alpha therapy
<sup>223</sup> Ra	α	<sup>219</sup> Rn (unstable)	11.4d	<0.01	5.78	0.267 (13.7%)	Treatment of bone metastasis
<sup>90</sup> Y	β <sup>-</sup>	<sup>90</sup> Zr	64.1h	12	2.28 (100%)	/	Microspheres for SIRT of liver cancer
<sup>166</sup> Ho	β <sup>-</sup>	<sup>166</sup> Er	1.12d	8	1.85 (51%)	0.081 (6.6%)	
<sup>131</sup> I	β <sup>-</sup>	<sup>131</sup> Xe	8.02d	2.4	0.607 (89.6%)	0.365 (81.5%)	Treatment of hyperthyroidism, thyroid carcinoma and NETs
<sup>177</sup> Lu	β <sup>-</sup>	<sup>177</sup> Hf	6.73d	1.7	0.498 (79%)	0.208 (11%)	Treatment of prostate cancer and NETs
<sup>89</sup> Sr	β <sup>-</sup>	<sup>89</sup> Y	50.5d	7.5	1.46 (100%)	/	Treatment of bone metastasis associated pain
<sup>153</sup> Sm	β <sup>-</sup>	<sup>153</sup> Eu	46.5h	3.1	0.704 (49.4%)	0.103 (29.8%)	
<sup>186</sup> Re	β <sup>-</sup> EC	<sup>186</sup> Os <sup>186</sup> W	3.72d	3.6	1.07 (71%)	0.137 (9.2%)	
<sup>188</sup> Re	β <sup>-</sup>	<sup>188</sup> Os	17.0h	11	2.12 (71%)	0.155 (15%)	
<sup>192</sup> Ir	β <sup>-</sup> EC	<sup>192</sup> Pt <sup>192</sup> Os	73.8d	No data	0.672 (47.9%)	0.468 (47.8%)	High-dose rate brachytherapy
<sup>198</sup> Au	β <sup>-</sup>	<sup>198</sup> Hg	2.69d	3.66	0.960 (99%)	0.412 (96%)	Brachytherapy
<sup>125</sup> I	EC	<sup>125</sup> Te	59.5d	/	/	0.035 (7%)	Low-dose rate brachytherapy
<sup>111</sup> In	EC	<sup>111</sup> Cd	2.8d	/	/	0.245 (94%)	Scintigraphy of NETs

A



## Annex

$^{89}\text{Zr}$	$\beta^+$	$^{89}\text{Y}$	3.27d	3.8	0.897 (23%)	0.909 (99.9%)	Under investigation for PET imaging
$^{68}\text{Ga}$	$\beta^+$ EC	$^{68}\text{Zn}$	1.13h	8.9	1.899 (89%)	/	PET-CT imaging of neuroendocrine tumours
$^{18}\text{F}$	$\beta^+$ EC	$^{18}\text{O}$	1.83h	2.4	0.634 (97%)	/	Routinely used in the form of $^{18}\text{F}$ -FDG as PET-CT imaging in cardiology, neurology and oncology
$^{64}\text{Cu}$	$\beta^+$ /EC $\beta^-$	$^{64}\text{Ni}$ $^{64}\text{Zn}$	12.7h	2.5	0.653 $_{\beta^+}$ (17.5%) 0.579 $_{\beta^-}$ (38.5%)	1.346 (0.47%)	Under investigation for PET imaging
$^{124}\text{I}$	$\beta^+$	$^{124}\text{Te}$	4.2d	No data	2.137 (23%)	0.603 (63%)	PET/CT in thyroid cancer

**Abbreviations:** CT: computed tomography; EC: electron conversion; FDG: fluorodeoxyglucose; NET: neuroendocrine tumor; PET: positron emission tomography; SIRT: selective internal radiation therapy; SPECT: single-photon emission tomography

Annex Table 2: An overview of radiolabeled gold nanoparticles under investigation for their imaging and diagnostic potentials

Isotope	Particle	Size (nm)	Functionalization	Labeling method	Cell model, administration	Function	Effect	Author
<sup>131</sup> I	<sup>131</sup> I-AuNPs-PEG-cRGD	93.4 x 24.8	Cyclic RGD	adsorption	B16F10 (pos)	Targeted SPECT-CT, <i>in vivo</i>	%ID/g (pos): 3.6 - 4.0 - 5.1   T/M: 7.1 - 6.9 - 10.0   T/Bi: 1.0 - 0.8 - 1.6 (1h - 3h - 6h)	Zhang, et al <sup>350</sup>
					MCF-7 (neg) IV, 1.5-7.4 MBq, 100 µl		%ID/g (blocked): 2.2   T/M: 3.9   T/B: 0.6 (6h) %ID/g (neg): 1.3 - 1.8 - 1.6   T/M: 2.2 - 3.3 - 3.7   T/Bi: 0.5 - 0.6 - 0.6 (1h - 3h - 6h)	
<sup>124</sup> I	<sup>124</sup> I-PEG-Au@AuCBs	87.1	PEG	Covalent and encapsulation	4T1	Combining PET and CLI	%ID/g: 5.4 (1h) - 3.4 (6h) - 1.8 (24h) T/M: ≈4-5 (1h - 24h)	Lee, et al <sup>348</sup>
					Sentinel lymph nodes (SLNs), subcutaneous	PET-CLI detection of sentinel lymph nodes	SLNs visible 1h p.i., strongest signal observed 6h p.i. Signal decreased, but still evident at 24h p.i.	
<sup>125</sup> I	<sup>125</sup> I-cRP-AuNPs	31	Cyclic RGD	Adsorption	U87MG IV, 11 MBq	targeted SPECT-CT	%ID/g: ≈30 (1h) - ≈10 (24h) <sup>125</sup> I-cRP-AuNPs were localized inside αvβ3-positive U87MG cells, and were found in a negligible amount inside αvβ3-negative MCF7 cells. <sup>125</sup> I-cRP-AuNPs targeted the tumor site effectively (10 min) - ≈1 %ID/g (1h). After blocking: tumor was almost undetectable.	Kim, et al <sup>349</sup>
<sup>125</sup> I <sup>111</sup> In	dual-radiolabeled AuNPs	10	PEG pMMP9	Covalent Chelation	A431 (high) 4T1Luc (low) IV	Characterize MMP activity, biodistribution and tumor uptake using SPECT-CT	<sup>125</sup> I signal was isolated to the thyroid, stomach, and bladder (4h) <sup>111</sup> In chelation by DTPA stable <i>in vivo</i> (4h) %ID/g (A431): 7.25 (24h) - 6.23 (48h) %ID/g (4T1Luc): 6.41 (24h) - 10.2 (48h) T/M (both tumors):-8 (48h)	Black, et al <sup>340</sup>
					33.3 MBq <sup>111</sup> In 22.2 MBq <sup>125</sup> I			
<sup>111</sup> In	<sup>111</sup> In-AuNP-Trastuzumab	54.2 42.1	Trastuzumab (T) Untargeted	Chelation	MDA-MB-361 IT and IV 10-12 MBq	SPECT-CT to track the <i>in vivo</i> fate of Trastuzumab-	%ID/g (T-IV): 1.23 (48h) %ID/g (T-IT): 29.59 (48h) %ID/g (UT-IV): 2.20 (48h)	Chattopadhyay, et al <sup>365</sup>

A

<sup>111</sup> In-HAuNS-C225	37	Cetuximab (C225) (T) Untargeted (UT)	Chelation		A431 IV, 0.37 MBq, 130 µl	AuNP- <sup>111</sup> In after IV and IT injection. Targeted SPECT-CT to evaluate biodistribution	%ID/g (UT-IT): 23.58 (48h)	Melancon, et al <sup>371</sup>
RGD-modified indium-111 labeled gold nanoparticles	7	RGD (T) Untargeted (UT)	Incorporation		M21 (high) M21-L (low) U87-MG (high) IV, 1 MBq	Targeted SPECT-CT to evaluate the imaging platform based on AuNPs	Uptake %ID/g (M21): 0.52 Uptake %ID/g (M21-L): 0.39 Uptake %ID/g (U87): 0.93 (T) – 0.37 (UT)	Ng, et al <sup>650</sup>
<sup>111</sup> In-EGF-Au-PEG	32.5	EGF	Chelation		MDA-MB-468, (pos) 231-H2N (neg) IV, 8 MBq	SPECT to evaluate tumor uptake of <sup>111</sup> In-EGF-Au-PEG in co-administration of EGF	Internalization: 11–15% in MDA-MB-468 cells, <2% in 231-H2N cells (4h). %ID/g (pos): 2.81   %ID/g (co-EGF): 3.91 (72h) %ID/g (neg): 1.43   %ID/g (co-EGF): 1.29 (72h)	Song, et al <sup>368</sup>
<sup>111</sup> In-Au@HSANP	213	Albumin	Chelation		CT-26 IV, IP, 1.7 MBq	SPECT to investigate the biodistribution and tumor uptake.	%ID/g (IV): 0.29 - 0.33 - 0.19 - 0.21   T/M: 9.5 - 11.1 - 9.3 - 7 (1h - 24h - 48h - 96h) %ID/g (IP): 7.77 - 8.89 - 3.40 - 1.45   T/M: 89.4 - 217.4 - 128.8 - 28.3 (1h - 24h - 48h - 96h)	Chen, et al <sup>317</sup>
<sup>111</sup> In-DTX-PEG3000-AuNPs-TIONts	10x170	PEG	Chelation		PC-3 IT, 5.7-8.7 MBq	SPECT-CT to evaluate biodistribution	%ID/g: 60-80 (1h - 6d) – 40-50 (10d - 20d)	Loiseau, et al <sup>651</sup>
<sup>99m</sup> Tc-AuNP-RGD	21.7	Cyclic RGD	Chelation		C6 IV and IP, 3.7 MBq, 50 µl	RyB <sub>3</sub> expression imaging using targeted SPECT-CT	%ID/g (IV): 3.48 - 3.65 - 2.49 - 1.94 (0.5h - 1h - 3h - 24h); blocked: 1.46 (1h) %ID/g (IP): 2.09 - 3.28 - 8.18 - 3.20 (0.5h - 1h - 3h - 24h); blocked: 1.18 (1h) T/BI (IV): 7.4   T/M: 10.0   T/Li: 0.2   T/S: 0.7 (1h)	Morales-Avila, et al <sup>321</sup>

							T/BI (IP): 20.5   T/M: 27.3   T/Li: 2.1   T/S: 3.4 (1h) Tumor uptake is higher than that of UT form or <sup>99m</sup> Tc-RGD (1h, IV)			Ocampo-Garcia, et al <sup>322</sup>
<sup>99m</sup> Tc-AuNP-mannose	23.3 20	Mannose (T) Untargeted (UT)	Chelation	Sentinel lymph nodes Subcutaneous, 1.85 MBq	Sentinel lymph node detection using targeted SPECT-CT		%ID (T) : 12.99 (1h) and 21.02 (24h) %ID (UT): 5.41 (1h) and 13.85 (24h)			Ocampo-Garcia, et al <sup>322</sup>
<sup>99m</sup> Tc-AuNP-RGD	22	cRGD	Chelation	4T1-luc IV, 1.85 MBq, 200 µl	Targeted SPECT-CT to evaluate micrometastasis		%ID lung metastasis (1h): 14. <sup>99m</sup> Tc-AuNP-RGD achieved a 5.2x higher signal in lung metastases than the <sup>99m</sup> Tc-RGD (1h).			Peiris, et al <sup>356</sup>
Gd/ <sup>99m</sup> Tc-AuNPs-RGD	29 51 80	cRGD Untargeted	Chelation	H1299 IV, 7.4 MBq, 100 µl	Combining MRI and SPECT-CT for image-guided radiosensitization		MRI rSIE (29): (T) 2.4 - (UT) 1.5 - (block) 1.5 (4h) MRI rSIE (51): (T) 1.6 - (UT) 1.3 - (block) 1.4 (4h) MRI rSIE (80): (T) 1.5 - (UT) 1.3 - (block) 1.4 (4h) %ID/g (29): (T) 14.6 - (UT) 4.0 - (Block) 6.2 (6h) %ID/g (51): (T) 9.4 - (UT) 4.4 - (block) 5.1 (6h) %ID/g (80): (T) 8.4 - (UT) 3.3 - (block) 4.9 (6h)			Yang, et al <sup>325</sup>
{(Au <sub>0</sub> ) <sub>6</sub> -G2-NOTA ( <sup>99m</sup> Tc)-PEG-RGD} DENPs	1.9	RGD (T) Untargeted (UT)	Chelation	C6 IV, 21 MBq, 150 µl	targeted SPECT/CT to evaluate α <sub>3</sub> integrin expressing tumors		T treatment: Increased signal SPECT (24x) and CT (>2x) intensities 30 minutes after injection compared to UT treatment.			Xu, et al <sup>324</sup>
{(Au <sub>0</sub> ) <sub>6</sub> -G2-DTPA ( <sup>99m</sup> Tc)-PEG-FA} DENPs	1.3-1.6	Folic acid (T) Untargeted (UT)	Chelation	HeLa IV , 37 MBq, 100 µl	SPECT-CT imaging, <i>in vivo</i>		T treatment: CT intensity 1.3x higher than after UT treatment SPECT intensity 2x higher than after UT treatment, 90 minutes after injection			Li, et al <sup>379</sup>
<sup>99m</sup> Tc-APAS-Au-PENPs	3.3	pH responsive APAS (T) Untargeted (UT)	Chelation	HT1080	SPECT-CT imaging of cancer cells <i>in vitro</i>		Increased acidity (pH 6.5-5.5), sharply increases the cellular uptake and the CT and SPECT intensities of the T form compared to UT form.			Zhu, et al <sup>376</sup>

<sup>99m</sup> Tc-Au-Ac-PENPs <sup>99m</sup> Tc-Au-Gly-PENPs	3.3	Acetylated or hydroxylated surface	Chelation	Sentinel lymph node (SLNs), subcutaneous 185 MBq, 0.5 ml	Sentinel lymph node (SLNs) detection by SPECT-CT	The SLNs can be detected in CT-SPECT imaging at 0.5h p.i. The accumulation becomes brighter with time. At 4 h p.i. the SLNs show accurate delineation. HU values: 6 (1h) – 101 (4h).	Zhao, et al <sup>652</sup> and Wen, et al <sup>653</sup>
<sup>99m</sup> Tc-RGD-AuNPs-PENPs	2.6 2.2	RGD (UT) Untargeted (UT)	Chelation	Orthotopic HCC-LM3 IV, 22.2 MBq, 150 µl	SPECT-CT imaging of αvβ3 integrin-overexpressing tumors	SPECT-CT signal intensities are much higher in the normal liver than in the cancer tissue. HU (T): 47.1 – SPECT: 1.86 Mbq/mm <sup>3</sup> (0.5h) HU (UT): 32.6 – SPECT: 1.65 Mbq/mm <sup>3</sup> (0.5h)	Zhou, et al <sup>380</sup>
<sup>99m</sup> Tc-AuNP-Lys3-bombesin	20.6	Bombesin (T)	Chelation	PC3 IV, 1.85 MBq, 50 µl	SPECT-CT for <i>in vivo</i> GRP-receptor imaging	%ID/g (T): 4.30 – 6.39 – 0.44 (0.5h - 1h - 24h) T/BI (T): 5.8 (1h) – Pacreas/BI: 36 T/BI (Monomer): 3.75 – Pancreas/BI: 16	Mendoza-Sanchez, et al <sup>358</sup>
<sup>99m</sup> Tc-duramycin-Au DENPs	5.9 2.2	Duramycin (T) Untargeted (UT)	Chelation	C6 IV, 74 MBq, 100 µl	SPECT-CT to evaluate apoptosis in tumors induced by chemotherapy	T treatment: increased SPECT (>3x) and CT (1.56x) signal intensities 2h-12h p.i. compared to UT.	Xing, et al <sup>378</sup>
<sup>198</sup> Au <sup>199</sup> Au	41.6 36.2	Chitosan Untargeted	Incorporation	MCF-7	Cell internalization for future TRT	UT treatment: no signal intensity changes. % internalization (T): 4.12 - 4.99 - 7.12 - 25.34 - 12.62 - 14.23% (2h - 4h - 6h - 24h - 48h - 72h) % internalization (UT): 0.30 - 0.19 - 0.33 - 1.0 - 3.02 - 4.89% (2h - 4h - 6h - 24h - 48h - 72h)	Rovais, et al <sup>333</sup>
<sup>199</sup> Au-AuNPs	5 (S) 18 (L)	D-Ala1-peptide T-amide (DAPTA) (T) Untargeted (UT)	Incorporation	4T1 IV, 185 kBq (biodistribution) 29.6 MBq (SPECT)	SPECT imaging	T (S): %D/g: 7.13 - T/M: 18.7 (24h) UT (S): %D/g: 3.45 - T/M: 10.1 (24h) UT (L): %D/g: 3 - T/M: 11.9 (24h) heterogeneous intratumoral distribution	Zhao, et al <sup>329</sup>
<sup>64</sup> Cu <sup>64</sup> Cu	4.5	AMD3100 (T) Untargeted (UT)	Incorporation	Orthotopic 4T1, IV, 3.7 MBq, 100 µl	PET imaging of orthotopic lung tumor and metastasis	Primary tumor (1 week post implantation): %ID (monomer): 2.13 – T/M: 3.55 (24h) %ID (T): 7.15 – T/M: 18.9 (24h) %ID (UT): 3.08 – T/M: 3.79 (24h) Metastasis (4 weeks post implantation): %ID (monomer): 0.65 (24h)	Zhao, et al <sup>327</sup>

<sup>64</sup> Cu-cRGD-DOX-AuNPs	10x45	cRGD (T) Untargeted (UT)	Chelation	U87MG IV, 5-10 MBq	PET imaging of biodistribution and tumor-targeting efficacy	%ID (T): 7.36 - L/M: 24.1 (24h) %ID (UT): 0.79 (24h) %ID (T): 6.4 - 4.6 - 3.3 - 2.2 (1h - 5h - 24h - 48h) %ID (UT): 6.4 - 5.3 - 3.1 - 1.8 (1h - 5h - 24h - 48h) T/M (T): 16.6 (5h) - 3.6 (48h)	Xiao, et al <sup>654</sup>
<sup>64</sup> Cu-NS	140	PEG	Chelation	SCC-4 IV, 17-18 MBq, 500 µl	PET imaging of biodistribution and tumor accumulation of <sup>64</sup> Cu-NS for future image-guided PTT.	Tumor uptake was not significant after 1h, but increased over time and plateaued after 20 h. The majority of accumulated particles still at the tumor site after 44h. %ID/g <sup>64</sup> Cu-NS: 0.77 (46h) %ID/g <sup>64</sup> Cu-DOTA(PEG): 0.1-0.15 (46h)	Xie, et al <sup>357</sup>
<sup>64</sup> Cu-DOTA-PEG-AuNCs	55 (L) 30 (S)	PEG	Chelation	EMT-6 IV, 3.7 MBq, 100 µl	PET-CT imaging: biodistribution and EPR tumor targeting of two differently sized AuNCs	%ID/g (L): <2 (1h-24h) T/M (L): 4.13 - 11.9 - 12.8 (1h-4h-24h) T/BI (L): 0.30 - 1.20 (1h-24h) %ID/g (S): 2.68 - 7.2 - 7.9 (1h-4h-24h) T/M (S): 25.7 (24h) T/BI (S): 0.14 - 5.15 (1h-24h)	Wang, et al <sup>319</sup>
<sup>64</sup> Cu-NS	170	PEG	Chelation	SCC-4, IV, 10.8-14.2 MBq IT, 17-18 MBq	PET-CT to assess biodistribution for future PTT	IT: high tumor concentrations up to 44h %ID/g: 6.28 (46h) IV: much lower amount of nanoshells in tumor, slow increase over time %ID/g: 0.77 (46h)	Xie, et al <sup>393</sup>
<sup>64</sup> Cu-RGD-PEG-HAuNS	44.7	Cyclic RGD (T) iodized oil Untargeted (UT)	Chelation	VX4 IV, 25 MBq, 1 ml IA, 23 MBq, 1.4 ml	PET-CT to compare tumor uptake of HAuNS after IV and IA administration	%ID/g (IV-T): 0.16 - 0.15 (1h-24h)   T/Li: 0.79 - T/M: 13.54 (1h) %ID/g (IV-UT): 0.22 - 0.13 (1h-24h)   T/Li: 1.11 - T/M: 17.37 (1h) %ID/g (IA-T): 0.20 (1h-24h)   T/Li: 0.81 - T/M: 12.74 (1h)	Tian, et al <sup>374</sup>

								%ID/g (IA-UT): 0.13 - 0.10 (1h-24h)   T/Li: 0.81 - T/M: 14.16 (1h) %ID/g (IA-UT+oil): 0.51 - 0.33 (1h-24h)   T/Li: 4.17 - T/M: 48.01 (1h)			Yang, et al <sup>287</sup>
<sup>64</sup> Cu-NOTA-Au-IONP-Affibody	24.4	Anti-EGFR affibody	Chelation	A431 IV, 3.7 MBq, 150 $\mu$ l	Targeted PET and MRI imaging			%ID/g: 3.5 (4h) - 4.6 (24h)   T/M: 6 (4-48h) %ID/g (blocked): 1.9 (24h)   T/M: 2 (4-48h) 44% decrease in MRI signal intensity 48h after injection of T. No decrease in MRI signal intensity after blocking.			Yang, et al <sup>287</sup>
<sup>64</sup> CuAuNCs	4.3 6.9	PEG 350 Da PEG 1000 Da	Incorporation	PC-3 IV, 3.7 MBq, 100 $\mu$ l	PET imaging			%ID/g: ~0.8 (1h) - ~3 (24h) for both T/M: ~0.5 (1h) - ~2.5 (24h) for both heterogeneous distribution of radioactivity across the tumor mass			Zhao, et al <sup>367</sup>
<sup>64</sup> CuAuNPs	27	PEG	Incorporation	EMT6 IV, 3.7 MBq, 100 $\mu$ l	Improving PET-CT accuracy and radiolabeling stability			Stable in mouse serum without degradation up to 48h ID%/g: 4.93 (1h) - 16.8 (48h) T/M: 3.99 (1h) - 11.9 (24h) - 16.2 (48h)			Zhao, et al <sup>330</sup>
[ <sup>64</sup> Cu]AuNR-RGD	25x8	RGD (T) Untargeted (UT)	Incorporation	U87MG IV, 5.55 MBq	Targeted PET-CT for future image guided PTT			%ID/g (T): 5 - 8 - 8.37 - 7.6 (4h - 16h - 24h - 45h) %ID/g (blocked): 6.17 (24h) %ID/g (UT): 6.19 (24h)			Sun, et al <sup>332</sup>
<sup>64</sup> Cu-AuNPs	25 73 40	NDM/Tw20 PEG S/QA	Incorporation	FaDu IV, 1.24-2.28 MBq	PET-CT to investigate biodistribution of AuNPs			%ID/g (NDM/Tw20): 1.29 (24h) %ID/g (PEG): 3.89 (24h) %ID/g (S/QA): negligible			Frellsen, et al <sup>328</sup>
<sup>64</sup> Cu-PEG-HAUS-DOX	42.5	DOX	Chelation	VX2, Embolization (E)	PET-CT to visualize NP uptake in tumors after ablation			SUV tumor (E): 13.9-14.1 (1h-18h)   T/Li: 1.1-1.7 (1h-18h) SUV tumor (E+RFA): 21.5-13.6 (1h-18h)   T/Li: 4.7-1.4 (1h-18h)			Tam, et al <sup>318</sup>

						SUV tumor (E+IRE): 12.6-12.3 (1h-18h)   T/Li: 0.81-2 (1h-18h) SUV tumor (E+LITT): 4.8-17.9 (1h-18h)   T/Li: 2-1.5 (1h-18h)		
<sup>89</sup> Zr	<sup>89</sup> Zr-anti-CD105-AuNPs-PPAA	103 4.8	Anti-endoglin Ab (CD105) (T) Untargeted (UT)	Chelation	B16F10-luc IV, 2.9-4.1 MBq	PET-CT to evaluate the impact of AuNP conjugation on the targeting of CD105	%D/ml (T): 4.6 (24h) %D/ml (blocked): 1.9 (6h) %D/ml (CD105- <sup>89</sup> Zr): 6.5 (24h) T/B: >4 (24h)	Karmani, et al <sup>488</sup>
	<sup>89</sup> Zr-Cetuximab-PPAA-AuNPs	31 4.8	Cetuximab (Ctxb)	Chelation	A431 IV, 2.2-4.6 MBq	PET to evaluate the impact of AuNP conjugation on the targeting of Ctxb	%D/ml (T): 3.3 (48h) %D/ml (Blocked): 1.5 (48h) %D/ml (Ctxb- <sup>89</sup> Zr): 3.9 (48h) T/B (T): 12 (48h), >20 (168h) T/B (blocked): 3.4 (48h) T/B (Ctxb- <sup>89</sup> Zr): < 10 (48h), <20 (168h)	Karmani, et al <sup>360</sup>

**Abbreviations:** Ac: acetylated; Au@AuCB: crushed gold shell gold core nanoballs; AuNC: Gold nanocluster; AuNP: Gold nanoparticle; AuNR: gold nanorod; Au-PENPs: polyethylenimine-entrapped gold nanoparticles; APAS: alkoxyphenyl acylsulfonamide; cRP: cRGD-PEG; CLI: Cerenkov luminescent imaging; CT: computed tomography; DAPTA: D-Ala1-peptide T-amide; Au-DENPs: dendrimer-entrapped gold nanoparticles; DOX: doxorubicin; DOTA: 1,4,7,10-Tetraazacyclododecane-1,4,7,10-tetraacetic acid; DTPA: diethylenetriaminepentaacetic acid; DTX: docetaxel; E: embolization; EGF: epidermal growth factor; EGFR: epidermal growth factor receptor; gly: glycol monomethyl; FA: folic acid; HAuNS: hollow gold nanoshell; Au@HSANP: gold nanocore-encapsulated human serum albumin nanoparticle; HU: Hounsfield unit; IA: intra-arterial; IONP: iron oxide nanoparticle; IP: intraperitoneal; IRE: irreversible electroporation; IT: intratumoral; IV: intravenous; L: large; LITT: laser induced thermal therapy; L/M: lung-to-muscle ratio; MRI: magnetic resonance imaging; NDM/Tw20: 1-Dodecanethiol/Tween 20; NOTA: 2-S-(4-isothiocyanatobenzyl)-1, 4, 7-triazacyclononane-1, 4, 7-triacetic acid; NS: nanoshell; PEG: Polyethylene glycol; PET: positron emission tomography; p.i.: post-injection; PTT: photo-thermal therapy; pMMP9: matrix metalloproteinase-9 cleavable peptide; PPAA: plasma-polymerized allylamine; RFA: radiofrequency ablation; rSIE: relative signal intensity enhancement; S: small; SLN: sentinel lymph node; SPECT: single photon emission computed tomography; SUV: standardized uptake value; S/QA: Sulphonate/quaternary ammonium; T: targeted; T/B: tumor-to-background ratio; T/Bi: tumor-to-blood ratio; TIONTs: titanate nanotubes; T/L: tumor-to-lung ratio; T/Li: Tumor-to-liver ratio; T/M: tumor-to-muscle ratio; T/S: tumor-to-spleen ratio; TRT: targeted radionuclide therapy; UT: untargeted; %ID: percentage of injected dose.



**Annex Table 3:** An overview of the human selenoproteome (adapted from <sup>609-613</sup>)

Selenoprotein	Abbrev.	Localization	Function
Cytosolic glutathione peroxidase	GPx1	Cytosol	Reduction of cellular H <sub>2</sub> O <sub>2</sub>
Gastrointestinal glutathione peroxidase	GPx2	Cytosol	Reduction of peroxide in gut
Plasma glutathione peroxidase	GPx3	Plasma	Reduction of peroxide in blood
Phospholipid hydroperoxide glutathione peroxidase	GPx4	Cytosol, mitochondria, nucleus	Reduction of phospholipid peroxide
Olfactory glutathione peroxidase	GPx6	Cytosol	Reduction of cellular H <sub>2</sub> O <sub>2</sub> in the olfactory epithelium
Thioredoxin reductase 1	TrxR1	Cytosol	Reduction of the oxidized form of cytosolic thioredoxin
Thioredoxin reductase 2	TrxR2	Mitochondria	Reduction of the oxidized form of mitochondrial thioredoxin
Thioredoxin reductase 3	TrxR3	Cytosol	Reduction of the oxidized form of thioredoxin in the testes
Iodothyronine deiodinase 1	DIO1	Plasma membrane	Activation of the thyroid pro-hormone T <sub>4</sub> to T <sub>3</sub>
Iodothyronine deiodinase 2	DIO2	ER	Activation of the thyroid pro-hormone T <sub>4</sub> to T <sub>3</sub>
Iodothyronine deiodinase 3	DIO3	Plasma membrane	Inactivation of the thyroid pro-hormone T <sub>4</sub> to reverse T <sub>3</sub>
Methionine sulfoxide reductase B1	MSRB1, SelR	Cytosol	Reduces methionine-R-sulfoxide residues in proteins to methionine
Selenophosphate synthetase	SPS2	Cytosol	Synthesis of selenophosphate (selenium donor for the selenocysteine in selenoproteins)
Selenoprotein P	SelP	Plasma	Se transport from plasma to peripheral tissues and antioxidant function
Selenoprotein F	SelF, Sep 15	ER	Trx-like fold, thiol-disulfide oxidoreductase, possibly involved in protein folding
Selenoprotein H	SelH	Nucleus	Trx-like fold, redox homeostasis, mitochondrial biogenesis; de novo GSH synthesis, inflammation, tumor suppression
Selenoprotein I	SelI	Plasma membrane	Phospholipid biosynthesis
Selenoprotein K	SelK	ER membrane	Redox homeostasis in cardiomyocytes, member of the ERAD <sup>5</sup> , required for Ca <sup>2+</sup> flux in immune

<sup>5</sup> Responsible for targeting misfolded proteins in the ER for cytosolic degradation.

			cells and immune cell activation, proliferation and migration.
Selenoprotein M	SeIM	ER	Trx-like fold, highly expressed in brain, neuroprotective function, intracellular $\text{Ca}^{2+}$ homeostasis, redox homeostasis, regulation of body weight and energy metabolism
Selenoprotein N	SeIN	ER membrane	Redox homeostasis, regulation of redox-related calcium homeostasis (ryanodine receptor activity), plays a role skeletal muscle regeneration (deficiency leads to myopathy)
Selenoprotein O	SeIO	Mitochondria	Unknown function
Selenoprotein S	SeIS	ER membrane	Member of the ERAD, redox homeostasis, regulation of inflammation, glucose homeostasis
Selenoprotein T	SeIT	ER, golgi	Trx-like fold, redox homeostasis, glucose homeostasis, cell adhesion, $\text{Ca}^{2+}$ homeostasis, neuroendocrine secretion.
Selenoprotein V	SeIV	Cytosol	Trx-like fold, unknown function, testes specific
Selenoprotein W	SeIW	Cytosol	Trx-like fold, unknown function, expressed in skeletal muscle and other tissues

A

**Abbreviations:** ER: endoplasmatic reticulum; ERAD: Endoplasmic Reticulum Associated Protein Degradation; GSH: glutathione;  $\text{H}_2\text{O}_2$ : hydrogen peroxide;  $\text{T}_3$ : triiodothyronine;  $\text{T}_4$ : thyroxine; Trx: thioredoxin.



# References

1. Pothukuchi S, Li Y, Wong CP. *Formulation of different shapes of nanoparticles and their incorporation into polymers*. 2004.
2. Dykman LA, Khlebtsov NG. Gold nanoparticles in biology and medicine: recent advances and prospects. *Acta Naturae*. 2011;3(2):34-55.
3. Mingos DMP. Historical Introduction to Gold Colloids, Clusters and Nanoparticles. In: Mingos DMP, ed. *Gold Clusters, Colloids and Nanoparticles I*. Cham: Springer International Publishing; 2014:1-47.
4. Zsigmondy R. *Colloids and the Ultramicroscope*. NY, USA: J.Wiley and Sons; 1914.
5. Thompson D. Michael Faraday's recognition of ruby gold: the birth of modern nanotechnology. *Gold Bulletin*. 2007;40(4):267-269.
6. Edwards PP, Thomas JM. Gold in a metallic divided state--from Faraday to present-day nanoscience. *Angewandte Chemie (International ed in English)*. 2007;46(29):5480-5486.
7. Zhang Y, Hu J, Xiao X. The Application of STM and AFM in Nanoprocess and Fabrication. In: Zhou Z, Wang Z, Lin L, eds. *Microsystems and Nanotechnology*. Berlin, Heidelberg: Springer Berlin Heidelberg; 2012:495-511.
8. Ganguly S, Mukhopadhyay S. Nano Science and Nanotechnology: Journey from Past to Present and Prospect in Veterinary Science and Medicine. *International Journal of Nanoscience and Nanotechnology (International Research Publication House, Delhi, India)*. 2011;2:79-83.
9. Pricker SPJGB. Medical uses of gold compounds: Past, present and future. 1996;29(2):53-60.
10. Thakor AS, Jokerst J, Zavaleta C, Massoud TF, Gambhir SS. Gold nanoparticles: a revival in precious metal administration to patients. *Nano letters*. 2011;11(10):4029-4036.
11. Faulk WP, Taylor GM. An immunocolloid method for the electron microscope. *Immunochemistry*. 1971;8(11):1081-1083.
12. Kudgus RA, Bhattacharya R, Mukherjee P. Cancer nanotechnology: emerging role of gold nanoconjugates. *Anticancer Agents Med Chem*. 2011;11(10):965-973.
13. Govindaraju S, Yun K. Synthesis of gold nanomaterials and their cancer-related biomedical applications: an update. *3 Biotech*. 2018;8(2):113.
14. WHO. Cancer. 2018; <https://www.who.int/news-room/fact-sheets/detail/cancer>.
15. World Health O. *Guide to cancer early diagnosis*. Geneva: World Health Organization; 2017.
16. Singh P, Pandit S, Mokkapati V, Garg A, Ravikumar V, Mijakovic I. Gold Nanoparticles in Diagnostics and Therapeutics for Human Cancer. *International journal of molecular sciences*. 2018;19(7).
17. Haume K, Rosa S, Grellet S, et al. Gold nanoparticles for cancer radiotherapy: a review. *Cancer Nanotechnol*. 2016;7(1):8.
18. Chang DS, Lasley FD, Das IJ, Mendonca MS, Dynlacht JR. Therapeutic Ratio. In: Chang DS, Lasley FD, Das IJ, Mendonca MS, Dynlacht JR, eds. *Basic Radiotherapy Physics and Biology*. Cham: Springer International Publishing; 2014:277-282.
19. Sztandera K, Gorzkiewicz M, Klajnert-Maculewicz B. Gold Nanoparticles in Cancer Treatment. *Mol Pharm*. 2019;16(1):1-23.
20. Yang W, Liang H, Ma S, Wang D, Huang J. Gold nanoparticle based photothermal therapy: Development and application for effective cancer treatment. *Sustainable Materials and Technologies*. 2019;22:e00109.
21. Vines JB, Yoon JH, Ryu NE, Lim DJ, Park H. Gold Nanoparticles for Photothermal Cancer Therapy. *Front Chem*. 2019;7:167.
22. Hainfeld JF, Slatkin DN, Focella TM, Smilowitz HM. Gold nanoparticles: a new X-ray contrast agent. *The British journal of radiology*. 2006;79(939):248-253.
23. Guerrini L, Alvarez-Puebla RA, Pazos-Perez N. Surface Modifications of Nanoparticles for Stability in Biological Fluids. *Materials (Basel)*. 2018;11(7).
24. Yang C. Measuring Zeta Potential, Methods. In: Li D, ed. *Encyclopedia of Microfluidics and Nanofluidics*. Boston, MA: Springer US; 2008:1068-1076.
25. Moore TL, Rodriguez-Lorenzo L, Hirsch V, et al. Nanoparticle colloidal stability in cell culture media and impact on cellular interactions. *Chemical Society Reviews*. 2015;44(17):6287-6305.
26. Delong RK, Reynolds CM, Malcolm Y, Schaeffer A, Severs T, Wanekaya A. Functionalized gold nanoparticles for the binding, stabilization, and delivery of therapeutic DNA, RNA, and other biological macromolecules. *Nanotechnology, science and applications*. 2010;3:53-63.

## References

27. Riley RS, Day ES. Gold nanoparticle-mediated photothermal therapy: applications and opportunities for multimodal cancer treatment. *Wiley interdisciplinary reviews Nanomedicine and nanobiotechnology*. 2017;9(4).
28. Pate K, Safier P. 12 - Chemical metrology methods for CMP quality. In: Babu S, ed. *Advances in Chemical Mechanical Planarization (CMP)*. Woodhead Publishing; 2016:299-325.
29. Navya PN, Daima HK. Rational engineering of physicochemical properties of nanomaterials for biomedical applications with nanotoxicological perspectives. *Nano Converg*. 2016;3(1):1.
30. Arvizo RR, Bhattacharyya S, Kudgus RA, Giri K, Bhattacharya R, Mukherjee P. Intrinsic therapeutic applications of noble metal nanoparticles: past, present and future. *Chem Soc Rev*. 2012;41(7):2943-2970.
31. Henriksen-Lacey M, Carregal-Romero S, Liz-Marzan LM. Current Challenges toward In Vitro Cellular Validation of Inorganic Nanoparticles. *Bioconjugate chemistry*. 2017;28(1):212-221.
32. Bertrand N, Wu J, Xu X, Kamaly N, Farokhzad OC. Cancer nanotechnology: the impact of passive and active targeting in the era of modern cancer biology. *Adv Drug Deliv Rev*. 2014;66:2-25.
33. Fang J, Nakamura H, Maeda H. The EPR effect: Unique features of tumor blood vessels for drug delivery, factors involved, and limitations and augmentation of the effect. *Adv Drug Deliv Rev*. 2011;63(3):136-151.
34. Friedman AD, Claypool SE, Liu R. The smart targeting of nanoparticles. *Curr Pharm Des*. 2013;19(35):6315-6329.
35. Samadian H, Hosseini-Nami S, Kamrava SK, Ghaznavi H, Shakeri-Zadeh A. Folate-conjugated gold nanoparticle as a new nanoplatform for targeted cancer therapy. *J Cancer Res Clin Oncol*. 2016;142(11):2217-2229.
36. Rizk N, Christoforou N, Lee S. Optimization of anti-cancer drugs and a targeting molecule on multifunctional gold nanoparticles. *Nanotechnology*. 2016;27(18):185704.
37. Wu X, Liu J, Yang L, Wang F. Photothermally controlled drug release system with high dose loading for synergistic chemo-photothermal therapy of multidrug resistance cancer. *Colloids Surf B Biointerfaces*. 2019;175:239-247.
38. Saber MM, Bahrainian S, Dinarvand R, Atyabi F. Targeted drug delivery of Sunitinib Malate to tumor blood vessels by cRGD-chitosan-gold nanoparticles. *International journal of pharmaceutics*. 2017;517(1-2):269-278.
39. S R, M P. Multi-functional FITC-silica@gold nanoparticles conjugated with guar gum succinate, folic acid and doxorubicin for CT/fluorescence dual imaging and combined chemo/PTT of cancer. *Colloids Surf B Biointerfaces*. 2019;186:110701.
40. Mahalunkar S, Yadav AS, Gorain M, et al. Functional design of pH-responsive folate-targeted polymer-coated gold nanoparticles for drug delivery and in vivo therapy in breast cancer. *International journal of nanomedicine*. 2019;14:8285-8302.
41. Feng Q, Shen Y, Fu Y, et al. Self-Assembly of Gold Nanoparticles Shows Microenvironment-Mediated Dynamic Switching and Enhanced Brain Tumor Targeting. *Theranostics*. 2017;7(7):1875-1889.
42. Paris JL, Villaverde G, Gomez-Grana S, Vallet-Regi M. Nanoparticles for multimodal antivascular therapeutics: Dual drug release, photothermal and photodynamic therapy. *Acta Biomater*. 2020;101:459-468.
43. Kunjachan S, Kotb S, Pola R, et al. Selective Priming of Tumor Blood Vessels by Radiation Therapy Enhances Nanodrug Delivery. *Scientific reports*. 2019;9(1):15844.
44. Liszbinski RB, Romagnoli GG, Gorgulho CM, Basso CR, Pedrosa VA, Kaneno R. Anti-EGFR-Coated Gold Nanoparticles In Vitro Carry 5-Fluorouracil to Colorectal Cancer Cells. *Materials (Basel)*. 2020;13(2).
45. Huang H, Yang DP, Liu M, et al. pH-sensitive Au-BSA-DOX-FA nanocomposites for combined CT imaging and targeted drug delivery. *International journal of nanomedicine*. 2017;12:2829-2843.
46. Nunes T, Pons T, Hou X, et al. Pulsed-laser irradiation of multifunctional gold nanoshells to overcome trastuzumab resistance in HER2-overexpressing breast cancer. *J Exp Clin Cancer Res*. 2019;38(1):306.
47. Nichols JW, Bae YH. Odyssey of a cancer nanoparticle: from injection site to site of action. *Nano Today*. 2012;7(6):606-618.
48. Xie X, Zhang Y, Li F, et al. Challenges and Opportunities from Basic Cancer Biology for Nanomedicine for Targeted Drug Delivery. *Current cancer drug targets*. 2019;19(4):257-276.
49. Mo R, Gu Z. Tumor microenvironment and intracellular signal-activated nanomaterials for anticancer drug delivery. *Materials Today*. 2016;19(5):274-283.
50. Issels RD. Hyperthermia adds to chemotherapy. *European journal of cancer (Oxford, England : 1990)*. 2008;44(17):2546-2554.

51. Moyer HR, Delman KA. The role of hyperthermia in optimizing tumor response to regional therapy. *Int J Hyperthermia*. 2008;24(3):251-261.
52. Kim HS, Lee DY. Near-Infrared-Responsive Cancer Photothermal and Photodynamic Therapy Using Gold Nanoparticles. *Polymers (Basel)*. 2018;10(9).
53. Sharifi M, Attar F, Saboury AA, et al. Plasmonic gold nanoparticles: Optical manipulation, imaging, drug delivery and therapy. *Journal of controlled release : official journal of the Controlled Release Society*. 2019;311-312:170-189.
54. Jain PK, Lee KS, El-Sayed IH, El-Sayed MA. Calculated absorption and scattering properties of gold nanoparticles of different size, shape, and composition: applications in biological imaging and biomedicine. *J Phys Chem B*. 2006;110(14):7238-7248.
55. Xia H, Gao Y, Yin L, et al. Light-Triggered Covalent Coupling of Gold Nanoparticles for Photothermal Cancer Therapy. *Chembiochem*. 2019;20(5):667-671.
56. Yang S, Yao D, Wang Y, Yang W, Zhang B, Wang D. Enzyme-triggered self-assembly of gold nanoparticles for enhanced retention effects and photothermal therapy of prostate cancer. *Chem Commun (Camb)*. 2018;54(70):9841-9844.
57. Cheng M, Zhang Y, Zhang X, Wang W, Yuan Z. One-pot synthesis of acid-induced in situ aggregating theranostic gold nanoparticles with enhanced retention in tumor cells. *Biomater Sci*. 2019;7(5):2009-2022.
58. Park S, Lee WJ, Park S, Choi D, Kim S, Park N. Reversibly pH-responsive gold nanoparticles and their applications for photothermal cancer therapy. *Scientific reports*. 2019;9(1):20180.
59. Qin Z, Du T, Zheng Y, et al. Glutathione Induced Transformation of Partially Hollow Gold-Silver Nanocages for Cancer Diagnosis and Photothermal Therapy. *Small (Weinheim an der Bergstrasse, Germany)*. 2019;15(35):e1902755.
60. Nouri S, Mohammadi E, Mehravi B, et al. NIR triggered glycosylated gold nanoshell as a photothermal agent on melanoma cancer cells. *Artif Cells Nanomed Biotechnol*. 2019;47(1):2316-2324.
61. Wang P, Wu Q, Wang F, et al. Evaluating cellular uptake of gold nanoparticles in HL-7702 and HepG2 cells for plasmonic photothermal therapy. *Nanomedicine (London, England)*. 2018;13(18):2245-2259.
62. Huang X, Jain PK, El-Sayed IH, El-Sayed MA. Determination of the minimum temperature required for selective photothermal destruction of cancer cells with the use of immunotargeted gold nanoparticles. *Photochem Photobiol*. 2006;82(2):412-417.
63. Yang H, He H, Tong Z, Xia H, Mao Z, Gao C. The impact of size and surface ligand of gold nanorods on liver cancer accumulation and photothermal therapy in the second near-infrared window. *J Colloid Interface Sci*. 2020;565:186-196.
64. Liu T, Jin R, Yuan P, Bai Y, Cai B, Chen X. Intracellular Enzyme-Triggered Assembly of Amino Acid-Modified Gold Nanoparticles for Accurate Cancer Therapy with Multimode. *ACS applied materials & interfaces*. 2019;11(32):28621-28630.
65. Zeng J, Shi D, Gu Y, et al. Injectable and Near-Infrared-Responsive Hydrogels Encapsulating Dopamine-Stabilized Gold Nanorods with Long Photothermal Activity Controlled for Tumor Therapy. *Biomacromolecules*. 2019;20(9):3375-3384.
66. Liu P, Yang W, Shi L, et al. Concurrent photothermal therapy and photodynamic therapy for cutaneous squamous cell carcinoma by gold nanoclusters under a single NIR laser irradiation. *J Mater Chem B*. 2019;7(44):6924-6933.
67. Beik J, Asadi M, Khoei S, et al. Simulation-guided photothermal therapy using MRI-traceable iron oxide-gold nanoparticle. *J Photochem Photobiol B*. 2019;199:111599.
68. Liu B, Cao W, Qiao G, et al. Effects of gold nanoprism-assisted human PD-L1 siRNA on both gene down-regulation and photothermal therapy on lung cancer. *Acta Biomater*. 2019;99:307-319.
69. Zhang L, Yang XQ, Wei JS, Li X, Wang H, Zhao YD. Intelligent gold nanostars for in vivo CT imaging and catalase-enhanced synergistic photodynamic & photothermal tumor therapy. *Theranostics*. 2019;9(19):5424-5442.
70. Huang P, Lin J, Wang S, et al. Photosensitizer-conjugated silica-coated gold nanoclusters for fluorescence imaging-guided photodynamic therapy. *Biomaterials*. 2013;34(19):4643-4654.
71. Wang J, Potocny AM, Rosenthal J, Day ES. Gold Nanoshell-Linear Tetrapyrrole Conjugates for Near Infrared-Activated Dual Photodynamic and Photothermal Therapies. *ACS Omega*. 2020;5(1):926-940.
72. Yang Y, Hu Y, Du H, Ren L, Wang H. Colloidal plasmonic gold nanoparticles and gold nanorings: shape-dependent generation of singlet oxygen and their performance in enhanced photodynamic cancer therapy. *International journal of nanomedicine*. 2018;13:2065-2078.
73. Garcia Calavia P, Bruce G, Perez-Garcia L, Russell DA. Photosensitizer-gold nanoparticle conjugates for photodynamic therapy of cancer. *Photochem Photobiol Sci*. 2018;17(11):1534-1552.

## References

74. Sivasubramanian M, Chuang YC, Lo LW. Evolution of Nanoparticle-Mediated Photodynamic Therapy: From Superficial to Deep-Seated Cancers. *Molecules*. 2019;24(3).
75. Chen NT, Tang KC, Chung MF, et al. Enhanced plasmonic resonance energy transfer in mesoporous silica-encased gold nanorod for two-photon-activated photodynamic therapy. *Theranostics*. 2014;4(8):798-807.
76. Zhao T, Shen X, Li L, et al. Gold nanorods as dual photo-sensitizing and imaging agents for two-photon photodynamic therapy. *Nanoscale*. 2012;4(24):7712-7719.
77. Xia F, Niu J, Hong Y, et al. Matrix metalloproteinase 2 targeted delivery of gold nanostars decorated with IR-780 iodide for dual-modal imaging and enhanced photothermal/photodynamic therapy. *Acta Biomater*. 2019;89:289-299.
78. Liu L, Xie HJ, Mu LM, et al. Functional chlorin gold nanorods enable to treat breast cancer by photothermal/photodynamic therapy. *International journal of nanomedicine*. 2018;13:8119-8135.
79. Nagy-Simon T, Potara M, Craciun AM, Licarete E, Astilean S. IR780-dye loaded gold nanoparticles as new near infrared activatable nanotheranostic agents for simultaneous photodynamic and photothermal therapy and intracellular tracking by surface enhanced resonant Raman scattering imaging. *J Colloid Interface Sci*. 2018;517:239-250.
80. Tham HP, Chen H, Tan YH, et al. Photosensitizer anchored gold nanorods for targeted combinational photothermal and photodynamic therapy. *Chem Commun (Camb)*. 2016;52(57):8854-8857.
81. Bhana S, O'Connor R, Johnson J, Ziebarth JD, Henderson L, Huang X. Photosensitizer-loaded gold nanorods for near infrared photodynamic and photothermal cancer therapy. *J Colloid Interface Sci*. 2016;469:8-16.
82. Yu M, Guo F, Wang J, Tan F, Li N. Photosensitizer-Loaded pH-Responsive Hollow Gold Nanospheres for Single Light-Induced Photothermal/Photodynamic Therapy. *ACS applied materials & interfaces*. 2015;7(32):17592-17597.
83. Zhang C, Cheng X, Chen M, et al. Fluorescence guided photothermal/photodynamic ablation of tumours using pH-responsive chlorin e6-conjugated gold nanorods. *Colloids Surf B Biointerfaces*. 2017;160:345-354.
84. Li H, Wang P, Deng Y, et al. Combination of active targeting, enzyme-triggered release and fluorescent dye into gold nanoclusters for endomicroscopy-guided photothermal/photodynamic therapy to pancreatic ductal adenocarcinoma. *Biomaterials*. 2017;139:30-38.
85. Xu W, Qian J, Hou G, et al. PEGylated hydrazided gold nanorods for pH-triggered chemo/photodynamic/photothermal triple therapy of breast cancer. *Acta Biomater*. 2018;82:171-183.
86. Jiang Y, Liu Y, Fang S, Ji M. Gold Nanoshells Coated 5-Aminolevulinic Liposomes for Photothermal-Photodynamic Antitumor Therapy. *Journal of nanoscience and nanotechnology*. 2020;20(1):1-14.
87. Zhang A, Pan S, Zhang Y, et al. Carbon-gold hybrid nanoprobe for real-time imaging, photothermal/photodynamic and nanozyme oxidative therapy. *Theranostics*. 2019;9(12):3443-3458.
88. Liu Y, Zhi X, Yang M, et al. Tumor-triggered drug release from calcium carbonate-encapsulated gold nanostars for near-infrared photodynamic/photothermal combination antitumor therapy. *Theranostics*. 2017;7(6):1650-1662.
89. Choi J, Lee SE, Park JS, Kim SY. Gold nanorod-photosensitizer conjugates with glutathione-sensitive linkages for synergistic cancer photodynamic/photothermal therapy. *Biotechnol Bioeng*. 2018;115(5):1340-1354.
90. Liu B, Cao W, Cheng J, et al. Human natural killer cells for targeting delivery of gold nanostars and bimodal imaging directed photothermal/photodynamic therapy and immunotherapy. *Cancer Biol Med*. 2019;16(4):756-770.
91. Xu W, Qian J, Hou G, et al. A dual-targeted hyaluronic acid-gold nanorod platform with triple-stimuli responsiveness for photodynamic/photothermal therapy of breast cancer. *Acta Biomater*. 2019;83:400-413.
92. Woods D, Turchi JJ. Chemotherapy induced DNA damage response: convergence of drugs and pathways. *Cancer biology & therapy*. 2013;14(5):379-389.
93. Thambiraj S, Hema S, Shankaran DR. An Overview on Applications of Gold Nanoparticle for Early Diagnosis and Targeted Drug Delivery to Prostate Cancer. *Recent Pat Nanotechnol*. 2018;12(2):110-131.
94. Ghosh P, Han G, De M, Kim CK, Rotello VM. Gold nanoparticles in delivery applications. *Adv Drug Deliv Rev*. 2008;60(11):1307-1315.
95. Theodosiou M, Boukos N, Sakellis E, Zachariadis M, Efthimiadou EK. Gold nanoparticle decorated pH-sensitive polymeric nanocontainers as a potential theranostic agent. *Colloids and Surfaces B: Biointerfaces*. 2019;183:110420.

96. Taghdisi SM, Danesh NM, Lavaee P, et al. Double targeting, controlled release and reversible delivery of daunorubicin to cancer cells by polyvalent aptamers-modified gold nanoparticles. *Mater Sci Eng C Mater Biol Appl*. 2016;61:753-761.
97. Kumar K, Moitra P, Bashir M, Kondaiah P, Bhattacharya S. Natural tripeptide capped pH-sensitive gold nanoparticles for efficacious doxorubicin delivery both in vitro and in vivo. *Nanoscale*. 2020;12(2):1067-1074.
98. Hou Z, Wang Z, Liu R, et al. The effect of phospho-peptide on the stability of gold nanoparticles and drug delivery. *J Nanobiotechnology*. 2019;17(1):88.
99. Ruan S, Yuan M, Zhang L, et al. Tumor microenvironment sensitive doxorubicin delivery and release to glioma using angiopep-2 decorated gold nanoparticles. *Biomaterials*. 2015;37:425-435.
100. Chandran PR, Sandhyarani N. An electric field responsive drug delivery system based on chitosan-gold nanocomposites for site specific and controlled delivery of 5-fluorouracil. *RSC Advances*. 2014;4(85):44922-44929.
101. Li J, Cai C, Li J, et al. Chitosan-Based Nanomaterials for Drug Delivery. *Molecules (Basel, Switzerland)*. 2018;23(10):2661.
102. Elgadir MA, Uddin MS, Ferdosh S, Adam A, Chowdhury AJK, Sarker MZI. Impact of chitosan composites and chitosan nanoparticle composites on various drug delivery systems: A review. *Journal of Food and Drug Analysis*. 2015;23(4):619-629.
103. Banihashem S, Nezhati MN, Panahi HA. Synthesis of chitosan-grafted-poly(N-vinylcaprolactam) coated on the thiolated gold nanoparticles surface for controlled release of cisplatin. *Carbohydr Polym*. 2020;227:115333.
104. Maney V, Singh M. The Synergism of Platinum-Gold Bimetallic Nanoconjugates Enhances 5-Fluorouracil Delivery In Vitro. *Pharmaceutics*. 2019;11(9).
105. Ruan S, Cao X, Cun X, et al. Matrix metalloproteinase-sensitive size-shrinkable nanoparticles for deep tumor penetration and pH triggered doxorubicin release. *Biomaterials*. 2015;60:100-110.
106. Yang K, Liu Y, Wang Y, et al. Enzyme-induced in vivo assembly of gold nanoparticles for imaging-guided synergistic chemo-photothermal therapy of tumor. *Biomaterials*. 2019;223:119460.
107. Li L, Fu S, Chen C, et al. Microenvironment-Driven Bioelimination of Magnetoplasmonic Nanoassemblies and Their Multimodal Imaging-Guided Tumor Photothermal Therapy. *ACS nano*. 2016;10(7):7094-7105.
108. Gotov O, Battogtokh G, Ko YT. Docetaxel-Loaded Hyaluronic Acid-Cathepsin B-Cleavable-Peptide-Gold Nanoparticles for the Treatment of Cancer. *Mol Pharm*. 2018;15(10):4668-4676.
109. Encinas-Basurto D, Ibarra J, Juarez J, et al. Hybrid folic acid-conjugated gold nanorods-loaded human serum albumin nanoparticles for simultaneous photothermal and chemotherapeutic therapy. *Mater Sci Eng C Mater Biol Appl*. 2018;91:669-678.
110. Chen J, Li X, Zhao X, et al. Doxorubicin-conjugated pH-responsive gold nanorods for combined photothermal therapy and chemotherapy of cancer. *Bioact Mater*. 2018;3(3):347-354.
111. Li B, Xu Q, Li X, Zhang P, Zhao X, Wang Y. Redox-responsive hyaluronic acid nanogels for hyperthermia-assisted chemotherapy to overcome multidrug resistance. *Carbohydr Polym*. 2019;203:378-385.
112. Huang W, Zhao H, Wan J, et al. pH- and photothermal-driven multistage delivery nanoplatfrom for overcoming cancer drug resistance. *Theranostics*. 2019;9(13):3825-3839.
113. Wang B, Wu S, Lin Z, et al. A personalized and long-acting local therapeutic platform combining photothermal therapy and chemotherapy for the treatment of multidrug-resistant colon tumor. *International journal of nanomedicine*. 2018;13:8411-8427.
114. Li B, Wang Y, He J. Gold Nanorods-Based Smart Nanoplatforms for Synergic Thermotherapy and Chemotherapy of Tumor Metastasis. *ACS applied materials & interfaces*. 2019;11(8):7800-7811.
115. Hou G, Qian J, Xu W, et al. A novel pH-sensitive targeting polysaccharide-gold nanorod conjugate for combined photothermal-chemotherapy of breast cancer. *Carbohydr Polym*. 2019;212:334-344.
116. Emami F, Banstola A, Vatanara A, et al. Doxorubicin and Anti-PD-L1 Antibody Conjugated Gold Nanoparticles for Colorectal Cancer Photochemotherapy. *Mol Pharm*. 2019;16(3):1184-1199.
117. Yin T, Zhang X, Luo L, et al. Multistimuli-responsive drug vehicles based on gold nanoflowers for chemophotothermal synergistic cancer therapy. *Nanomedicine (London, England)*. 2018;13(16):1967-1983.
118. Elbialy NS, Fathy MM, Al-Wafi R, et al. Multifunctional magnetic-gold nanoparticles for efficient combined targeted drug delivery and interstitial photothermal therapy. *International journal of pharmaceutics*. 2019;554:256-263.
119. Cheng H, Huo D, Zhu C, et al. Combination cancer treatment through photothermally controlled release of selenous acid from gold nanocages. *Biomaterials*. 2018;178:517-526.



## References

120. Noh MS, Lee S, Kang H, et al. Target-specific near-IR induced drug release and photothermal therapy with accumulated Au/Ag hollow nanoshells on pulmonary cancer cell membranes. *Biomaterials*. 2015;45:81-92.
121. Zhu F, Tan G, Zhong Y, et al. Smart nanoplatform for sequential drug release and enhanced chemothermal effect of dual drug loaded gold nanorod vesicles for cancer therapy. *J Nanobiotechnology*. 2019;17(1):44.
122. Wang J, Ma K, Wang H, Hu Z, Fu Y, Li F. Peptide Multifunctionalized Gold Nanorods with Dual pH/NIR Responsive Release of Doxorubicin for High-Efficiency Cancer Treatment. *J Biomed Nanotechnol*. 2019;15(11):2164-2178.
123. Liu J, Ma W, Kou W, Shang L, Huang R, Zhao J. Poly-amino acids coated gold nanorod and doxorubicin for synergistic photodynamic therapy and chemotherapy in ovarian cancer cells. *Biosci Rep*. 2019;39(12).
124. Xu W, Wang J, Qian J, et al. NIR/pH dual-responsive polysaccharide-encapsulated gold nanorods for enhanced chemo-photothermal therapy of breast cancer. *Mater Sci Eng C Mater Biol Appl*. 2019;103:109854.
125. Li H, Li H, Yu W, et al. PEGylated hyaluronidase/NIR induced drug controlled release system for synergetic chemo-photothermal therapy of hepatocellular carcinoma. *Eur J Pharm Sci*. 2019;133:127-136.
126. Tu TY, Yang SJ, Tsai MH, et al. Dual-triggered drug-release vehicles for synergistic cancer therapy. *Colloids Surf B Biointerfaces*. 2019;173:788-797.
127. Baskar R, Lee KA, Yeo R, Yeoh KW. Cancer and radiation therapy: current advances and future directions. *Int J Med Sci*. 2012;9(3):193-199.
128. Bucci MK, Bevan A, Roach M, 3rd. Advances in radiation therapy: conventional to 3D, to IMRT, to 4D, and beyond. *CA: a cancer journal for clinicians*. 2005;55(2):117-134.
129. Statkiewicz Sherer MA, Visconti PJ, Ritenour ER, Haynes K. *Radiation Protection in Medical Radiography*. 7th ed. Elsevier Mosby; 2015.
130. Reisz JA, Bansal N, Qian J, Zhao W, Furdul CM. Effects of ionizing radiation on biological molecules--mechanisms of damage and emerging methods of detection. *Antioxidants & redox signaling*. 2014;21(2):260-292.
131. Liu Y, Zhang P, Li F, et al. Metal-based NanoEnhancers for Future Radiotherapy: Radiosensitizing and Synergistic Effects on Tumor Cells. *Theranostics*. 2018;8(7):1824-1849.
132. Hainfeld JF, Dilmanian FA, Slatkin DN, Smilowitz HM. Radiotherapy enhancement with gold nanoparticles. *J Pharm Pharmacol*. 2008;60(8):977-985.
133. Rosa S, Connolly C, Schettino G, Butterworth KT, Prise KM. Biological mechanisms of gold nanoparticle radiosensitization. *Cancer Nanotechnol*. 2017;8(1):2.
134. Butterworth KT, McMahon SJ, Currell FJ, Prise KM. Physical basis and biological mechanisms of gold nanoparticle radiosensitization. *Nanoscale*. 2012;4(16):4830-4838.
135. Hainfeld JF, Slatkin DN, Smilowitz HM. The use of gold nanoparticles to enhance radiotherapy in mice. *Physics in medicine and biology*. 2004;49(18):N309-315.
136. Laprise-Pelletier M, Simao T, Fortin MA. Gold Nanoparticles in Radiotherapy and Recent Progress in Nanobrachytherapy. *Adv Healthc Mater*. 2018;7(16):e1701460.
137. Her S, Jaffray DA, Allen C. Gold nanoparticles for applications in cancer radiotherapy: Mechanisms and recent advancements. *Adv Drug Deliv Rev*. 2017;109:84-101.
138. Cui L, Her S, Borst GR, Bristow RG, Jaffray DA, Allen C. Radiosensitization by gold nanoparticles: Will they ever make it to the clinic? *Radiother Oncol*. 2017;124(3):344-356.
139. Berger MJ, Hubbell JH, Seltzer SM, et al. XCOM: Photon Cross Sections Database. In: National Institute of Standards and Technology P, Radiation Physics Division, ed. Gaithersburg, Maryland, USA2010.
140. Mesbahi A. A review on gold nanoparticles radiosensitization effect in radiation therapy of cancer. *Reports of practical oncology and radiotherapy : journal of Greatpoland Cancer Center in Poznan and Polish Society of Radiation Oncology*. 2010;15(6):176-180.
141. Lin Y, McMahon SJ, Scarpelli M, Paganetti H, Schuemann J. Comparing gold nano-particle enhanced radiotherapy with protons, megavoltage photons and kilovoltage photons: a Monte Carlo simulation. *Physics in medicine and biology*. 2014;59(24):7675-7689.
142. Schuemann J, Berbeco R, Chithrani DB, et al. Roadmap to Clinical Use of Gold Nanoparticles for Radiation Sensitization. *International journal of radiation oncology, biology, physics*. 2016;94(1):189-205.
143. Wolfe T, Chatterjee D, Lee J, et al. Targeted gold nanoparticles enhance sensitization of prostate tumors to megavoltage radiation therapy in vivo. *Nanomedicine : nanotechnology, biology, and medicine*. 2015;11(5):1277-1283.

144. Chithrani DB, Jelveh S, Jalali F, et al. Gold nanoparticles as radiation sensitizers in cancer therapy. *Radiation research*. 2010;173(6):719-728.
145. Jain S, Coulter JA, Hounsell AR, et al. Cell-specific radiosensitization by gold nanoparticles at megavoltage radiation energies. *International journal of radiation oncology, biology, physics*. 2011;79(2):531-539.
146. Liu CJ, Wang CH, Chen ST, et al. Enhancement of cell radiation sensitivity by pegylated gold nanoparticles. *Physics in medicine and biology*. 2010;55(4):931-945.
147. Kazmi F, Vallis KA, Vellayappan BA, Bandla A, Yukun D, Carlisle R. Megavoltage Radiosensitization of Gold Nanoparticles on a Glioblastoma Cancer Cell Line Using a Clinical Platform. 2020;21(2):429.
148. Saberi A, Shahbazi-Gahreuei D, Abbasian M, Fesharaki M, Baharlouei A, Arab-Bafrani Z. Gold nanoparticles in combination with megavoltage radiation energy increased radiosensitization and apoptosis in colon cancer HT-29 cells. *International Journal of Radiation Biology*. 2017;93(3):315-323.
149. Hau H, Khanal D, Rogers L, et al. Dose enhancement and cytotoxicity of gold nanoparticles in colon cancer cells when irradiated with kilo- and mega-voltage radiation. *Bioeng Transl Med*. 2016;1(1):94-102.
150. Zhao N, Yang Z, Li B, et al. RGD-conjugated mesoporous silica-encapsulated gold nanorods enhance the sensitization of triple-negative breast cancer to megavoltage radiation therapy. *International journal of nanomedicine*. 2016;11:5595-5610.
151. Zhang X, Wang H, Coulter JA, Yang R. Octaarginine-modified gold nanoparticles enhance the radiosensitivity of human colorectal cancer cell line LS180 to megavoltage radiation. *International journal of nanomedicine*. 2018;13:3541-3552.
152. Khoshgard K, Hashemi B, Arbabi A, Rasaei MJ, Soleimani M. Radiosensitization effect of folate-conjugated gold nanoparticles on HeLa cancer cells under orthovoltage superficial radiotherapy techniques. *Physics in medicine and biology*. 2014;59(9):2249-2263.
153. Kong T, Zeng J, Wang X, et al. Enhancement of radiation cytotoxicity in breast-cancer cells by localized attachment of gold nanoparticles. *Small (Weinheim an der Bergstrasse, Germany)*. 2008;4(9):1537-1543.
154. Roeske JC, Nunez L, Hoggarth M, Labay E, Weichselbaum RR. Characterization of the theoretical radiation dose enhancement from nanoparticles. *Technol Cancer Res Treat*. 2007;6(5):395-401.
155. Lin Y, Paganetti H, McMahon SJ, Schuemann J. Gold nanoparticle induced vasculature damage in radiotherapy: Comparing protons, megavoltage photons, and kilovoltage photons. *Med Phys*. 2015;42(10):5890-5902.
156. Mesbahi A, Jamali F, Garehaghaji N. Effect of photon beam energy, gold nanoparticle size and concentration on the dose enhancement in radiation therapy. *Bioimpacts*. 2013;3(1):29-35.
157. Liu Y, Liu X, Jin X, et al. The dependence of radiation enhancement effect on the concentration of gold nanoparticles exposed to low- and high-LET radiations. *Phys Med*. 2015;31(3):210-218.
158. Rudek B, McNamara A, Ramos-Mendez J, Byrne H, Kuncic Z, Schuemann J. Radio-enhancement by gold nanoparticles and their impact on water radiolysis for x-ray, proton and carbon-ion beams. *Physics in medicine and biology*. 2019;64(17):175005.
159. Gadoue SM, Zygmanski P, Sajo E. The dichotomous nature of dose enhancement by gold nanoparticle aggregates in radiotherapy. *Nanomedicine (London, England)*. 2018;13(8):809-823.
160. Zabihzadeh M, Moshirian T, Ghorbani M, Knaup C, Behrooz MA. A Monte Carlo Study on Dose Enhancement by Homogeneous and Inhomogeneous Distributions of Gold Nanoparticles in Radiotherapy with Low Energy X-rays. *J Biomed Phys Eng*. 2018;8(1):13-28.
161. McMahon SJ, Hyland WB, Muir MF, et al. Biological consequences of nanoscale energy deposition near irradiated heavy atom nanoparticles. *Scientific reports*. 2011;1:18.
162. McMahon SJ, Hyland WB, Muir MF, et al. Nanodosimetric effects of gold nanoparticles in megavoltage radiation therapy. *Radiother Oncol*. 2011;100(3):412-416.
163. Bobyk L, Edouard M, Deman P, et al. Photoactivation of gold nanoparticles for glioma treatment. *Nanomedicine : nanotechnology, biology, and medicine*. 2013;9(7):1089-1097.
164. Butterworth KT, Coulter JA, Jain S, et al. Evaluation of cytotoxicity and radiation enhancement using 1.9 nm gold particles: potential application for cancer therapy. *Nanotechnology*. 2010;21(29):295101.
165. Chattopadhyay N, Cai Z, Kwon YL, Lechtman E, Pignol JP, Reilly RM. Molecularly targeted gold nanoparticles enhance the radiation response of breast cancer cells and tumor xenografts to X-radiation. *Breast Cancer Res Treat*. 2013;137(1):81-91.
166. tu y, Chen N, Yang W, Bao Y, Xu H, Qin S. BSA Capped Au Nanoparticle as An Efficient Sensitizer for Glioblastoma Tumor Radiation Therapy. *RSC Adv*. 2015;5.
167. Coulter JA, Jain S, Butterworth KT, et al. Cell type-dependent uptake, localization, and cytotoxicity of 1.9 nm gold nanoparticles. *International journal of nanomedicine*. 2012;7:2673-2685.
168. Cui L, Tse K, Zahedi P, et al. Hypoxia and cellular localization influence the radiosensitizing effect of gold nanoparticles (AuNPs) in breast cancer cells. *Radiation research*. 2014;182(5):475-488.

## References

169. Geng F, Song K, Xing JZ, et al. Thio-glucose bound gold nanoparticles enhance radio-cytotoxic targeting of ovarian cancer. *Nanotechnology*. 2011;22(28):285101.
170. Guo M, Sun Y, Zhang X-D. Enhanced Radiation Therapy of Gold Nanoparticles in Liver Cancer. 2017;7(3):232.
171. Jain S, Coulter JA, Butterworth KT, et al. Gold nanoparticle cellular uptake, toxicity and radiosensitisation in hypoxic conditions. *Radiother Oncol*. 2014;110(2):342-347.
172. Jeynes JC, Merchant MJ, Spindler A, Wera AC, Kirkby KJ. Investigation of gold nanoparticle radiosensitization mechanisms using a free radical scavenger and protons of different energies. *Physics in medicine and biology*. 2014;59(21):6431-6443.
173. Joh DY, Sun L, Stangl M, et al. Selective targeting of brain tumors with gold nanoparticle-induced radiosensitization. *PloS one*. 2013;8(4):e62425.
174. Kaur H, Pujari G, Semwal MK, Sarma A, Avasthi DK. In vitro studies on radiosensitization effect of glucose capped gold nanoparticles in photon and ion irradiation of HeLa cells. *Nuclear Instruments and Methods in Physics Research Section B: Beam Interactions with Materials and Atoms*. 2013;301:7-11.
175. Liu CJ, Wang CH, Chien CC, et al. Enhanced x-ray irradiation-induced cancer cell damage by gold nanoparticles treated by a new synthesis method of polyethylene glycol modification. *Nanotechnology*. 2008;19(29):295104.
176. Liu X, Liu Y, Zhang P, et al. The synergistic radiosensitizing effect of tirapazamine-conjugated gold nanoparticles on human hepatoma HepG2 cells under X-ray irradiation. *International journal of nanomedicine*. 2016;11:3517-3531.
177. Penninckx S, Heuskin AC, Michiels C, Lucas S. The role of thioredoxin reductase in gold nanoparticle radiosensitization effects. *Nanomedicine (London, England)*. 2018.
178. Roa W, Zhang X, Guo L, et al. Gold nanoparticle sensitize radiotherapy of prostate cancer cells by regulation of the cell cycle. *Nanotechnology*. 2009;20(37):375101.
179. Shi M, Paquette B, Thippayamontri T, Gendron L, Guerin B, Sanche L. Increased radiosensitivity of colorectal tumors with intra-tumoral injection of low dose of gold nanoparticles. *International journal of nanomedicine*. 2016;11:5323-5333.
180. Taggart LE, McMahon SJ, Currell FJ, Prise KM, Butterworth KT. The role of mitochondrial function in gold nanoparticle mediated radiosensitisation. *Cancer Nanotechnol*. 2014;5(1):5.
181. Wang C, Li X, Wang Y, Liu Z, Fu L, Hu L. Enhancement of radiation effect and increase of apoptosis in lung cancer cells by thio-glucose-bound gold nanoparticles at megavoltage radiation energies. *Journal of Nanoparticle Research*. 2013;15(5):1642.
182. Wang C, Jiang Y, Li X, Hu L. Thioglucose-bound gold nanoparticles increase the radiosensitivity of a triple-negative breast cancer cell line (MDA-MB-231). *Breast Cancer*. 2015;22(4):413-420.
183. Zhang XD, Wu D, Shen X, et al. Size-dependent radiosensitization of PEG-coated gold nanoparticles for cancer radiation therapy. *Biomaterials*. 2012;33(27):6408-6419.
184. Zhang XD, Chen J, Luo Z, et al. Enhanced tumor accumulation of sub-2 nm gold nanoclusters for cancer radiation therapy. *Adv Healthc Mater*. 2014;3(1):133-141.
185. Chen N, Yang W, Bao Y, Xu H, Qin S, Tu Y. BSA capped Au nanoparticle as an efficient sensitizer for glioblastoma tumor radiation therapy. *RSC Advances*. 2015;5(51):40514-40520.
186. Hainfeld JF, Dilmanian FA, Zhong Z, Slatkin DN, Kalef-Ezra JA, Smilowitz HM. Gold nanoparticles enhance the radiation therapy of a murine squamous cell carcinoma. *Physics in medicine and biology*. 2010;55(11):3045-3059.
187. Hainfeld JF, Smilowitz HM, O'Connor MJ, Dilmanian FA, Slatkin DN. Gold nanoparticle imaging and radiotherapy of brain tumors in mice. *Nanomedicine (London, England)*. 2013;8(10):1601-1609.
188. Cho SH. Estimation of tumour dose enhancement due to gold nanoparticles during typical radiation treatments: a preliminary Monte Carlo study. *Physics in medicine and biology*. 2005;50(15):N163-173.
189. Hwang C, Kim JM, Kim J. Influence of concentration, nanoparticle size, beam energy, and material on dose enhancement in radiation therapy. *Journal of radiation research*. 2017;58(4):405-411.
190. Zheng XJ, Chow JC. Radiation dose enhancement in skin therapy with nanoparticle addition: A Monte Carlo study on kilovoltage photon and megavoltage electron beams. *World J Radiol*. 2017;9(2):63-71.
191. Khodadadi A, Nedaie HA, Sadeghi M, Ghassemi MR, Mesbahi A, Banaee N. Determination of the dose enhancement exclusively in tumor tissue due to the presence of GNPs. *Appl Radiat Isot*. 2019;145:39-46.
192. Changizi O, Khoei S, Mahdavian A, Shirvalilou S, Mahdavi SR, Keyvan Rad J. Enhanced radiosensitivity of LNCaP prostate cancer cell line by gold-photoactive nanoparticles modified with folic acid. *Photodiagnosis and Photodynamic Therapy*. 2020;29:101602.

193. Liang G, Jin X, Zhang S, Xing D. RGD peptide-modified fluorescent gold nanoclusters as highly efficient tumor-targeted radiotherapy sensitizers. *Biomaterials*. 2017;144:95-104.
194. Ma N, Liu P, He N, Gu N, Wu FG, Chen Z. Action of Gold Nanospikes-Based Nanoradiosensitizers: Cellular Internalization, Radiotherapy, and Autophagy. *ACS applied materials & interfaces*. 2017;9(37):31526-31542.
195. Sung W, Schuemann J. Energy optimization in gold nanoparticle enhanced radiation therapy. *Physics in medicine and biology*. 2018;63(13):135001.
196. Hossain M, Su M. Nanoparticle location and material dependent dose enhancement in X-ray radiation therapy. *The journal of physical chemistry C, Nanomaterials and interfaces*. 2012;116(43):23047-23052.
197. Bannister AH, Bromma K, Sung W, et al. Modulation of nanoparticle uptake, intracellular distribution, and retention with docetaxel to enhance radiotherapy. *The British journal of radiology*. 2020;93(1106):20190742.
198. Lechtman E, Pignol J-P. Interplay between the gold nanoparticle sub-cellular localization, size, and the photon energy for radiosensitization. *Scientific reports*. 2017;7(1):13268.
199. Sung W, Ye SJ, McNamara AL, et al. Dependence of gold nanoparticle radiosensitization on cell geometry. *Nanoscale*. 2017;9(18):5843-5853.
200. Enferadi M, Fu SY, Hong JH, et al. Radiosensitization of ultrasmall GNP-PEG-cRGDFk in ALTS1C1 exposed to therapeutic protons and kilovoltage and megavoltage photons. *Int J Radiat Biol*. 2018;94(2):124-136.
201. Li S, Bouchy S, Penninckx S, et al. Antibody-functionalized gold nanoparticles as tumor-targeting radiosensitizers for proton therapy. *Nanomedicine (London, England)*. 2019;14(3):317-333.
202. Li S, Penninckx S, Karmani L, et al. LET-dependent radiosensitization effects of gold nanoparticles for proton irradiation. *Nanotechnology*. 2016;27(45):455101.
203. Ma N, Wu FG, Zhang X, et al. Shape-Dependent Radiosensitization Effect of Gold Nanostructures in Cancer Radiotherapy: Comparison of Gold Nanoparticles, Nanospikes, and Nanorods. *ACS applied materials & interfaces*. 2017;9(15):13037-13048.
204. Luo D, Wang X, Zeng S, Ramamurthy G, Burda C, Basilion JP. Prostate-specific membrane antigen targeted gold nanoparticles for prostate cancer radiotherapy: does size matter for targeted particles? *Chem Sci*. 2019;10(35):8119-8128.
205. Gilles M, Brun E, Sicard-Roselli C. Gold nanoparticles functionalization notably decreases radiosensitization through hydroxyl radical production under ionizing radiation. *Colloids Surf B Biointerfaces*. 2014;123:770-777.
206. Spaas C, Dok R, Deschaume O, et al. Dependence of Gold Nanoparticle Radiosensitization on Functionalizing Layer Thickness. *Radiation research*. 2016;185(4):384-392.
207. Cho J, Gonzalez-Lepera C, Manohar N, Kerr M, Krishnan S, Cho SH. Quantitative investigation of physical factors contributing to gold nanoparticle-mediated proton dose enhancement. *Physics in medicine and biology*. 2016;61(6):2562-2581.
208. Martinez-Rovira I, Prezado Y. Evaluation of the local dose enhancement in the combination of proton therapy and nanoparticles. *Med Phys*. 2015;42(11):6703-6710.
209. Walzlein C, Scifoni E, Kramer M, Durante M. Simulations of dose enhancement for heavy atom nanoparticles irradiated by protons. *Physics in medicine and biology*. 2014;59(6):1441-1458.
210. Heuskin AC, Gallez B, Feron O, Martinive P, Michiels C, Lucas S. Metallic nanoparticles irradiated by low-energy protons for radiation therapy: Are there significant physical effects to enhance the dose delivery? *Med Phys*. 2017;44(8):4299-4312.
211. Peukert D, Kempson I, Douglass M, Bezak E. Gold nanoparticle enhanced proton therapy: A Monte Carlo simulation of the effects of proton energy, nanoparticle size, coating material, and coating thickness on dose and radiolysis yield. *Med Phys*. 2020;47(2):651-661.
212. Hespeels F, Lucas S, Tabarrant T, et al. Experimental measurements validate the use of the binary encounter approximation model to accurately compute proton induced dose and radiolysis enhancement from gold nanoparticles. *Physics in medicine and biology*. 2019;64(6):065014.
213. Lin Y, McMahon SJ, Paganetti H, Schuemann J. Biological modeling of gold nanoparticle enhanced radiotherapy for proton therapy. *Physics in medicine and biology*. 2015;60(10):4149-4168.
214. Sotiropoulos M, Henthorn NT, Warmenhoven JW, Mackay RI, Kirkby KJ, Merchant MJ. Modelling direct DNA damage for gold nanoparticle enhanced proton therapy. *Nanoscale*. 2017;9(46):18413-18422.
215. Kim JK, Seo SJ, Kim HT, et al. Enhanced proton treatment in mouse tumors through proton irradiated nanoradiator effects on metallic nanoparticles. *Physics in medicine and biology*. 2012;57(24):8309-8323.
216. Kim JK, Seo SJ, Kim KH, et al. Therapeutic application of metallic nanoparticles combined with particle-induced x-ray emission effect. *Nanotechnology*. 2010;21(42):425102.

## References

217. Polf JC, Bronk LF, Driessen WH, Arap W, Pasqualini R, Gillin M. Enhanced relative biological effectiveness of proton radiotherapy in tumor cells with internalized gold nanoparticles. *Appl Phys Lett*. 2011;98(19):193702.
218. Abdul Rashid R, Zainal Abidin S, Khairil Anuar MA, et al. Radiosensitization effects and ROS generation by high Z metallic nanoparticles on human colon carcinoma cell (HCT116) irradiated under 150 MeV proton beam. *OpenNano*. 2019;4:100027.
219. Liu Y, Liu X, Jin X, et al. The Radiation Enhancement of 15 nm Citrate-Capped Gold Nanoparticles Exposed to 70 keV/956m Carbon Ions. *Journal of nanoscience and nanotechnology*. 2016;16(3):2365-2370.
220. Foroozandeh P, Aziz AA. Insight into Cellular Uptake and Intracellular Trafficking of Nanoparticles. *Nanoscale Res Lett*. 2018;13(1):339.
221. Behzadi S, Serpooshan V, Tao W, et al. Cellular uptake of nanoparticles: journey inside the cell. *Chem Soc Rev*. 2017;46(14):4218-4244.
222. Chithrani BD, Chan WC. Elucidating the mechanism of cellular uptake and removal of protein-coated gold nanoparticles of different sizes and shapes. *Nano letters*. 2007;7(6):1542-1550.
223. Zhao J, Stenzel MH. Entry of nanoparticles into cells: the importance of nanoparticle properties. *Polymer Chemistry*. 2018;9(3):259-272.
224. Bartneck M, Keul HA, Singh S, et al. Rapid uptake of gold nanorods by primary human blood phagocytes and immunomodulatory effects of surface chemistry. *ACS nano*. 2010;4(6):3073-3086.
225. Banerjee A, Qi J, Gogoi R, Wong J, Mitragotri S. Role of nanoparticle size, shape and surface chemistry in oral drug delivery. *Journal of controlled release : official journal of the Controlled Release Society*. 2016;238:176-185.
226. Cho EC, Xie J, Wurm PA, Xia Y. Understanding the role of surface charges in cellular adsorption versus internalization by selectively removing gold nanoparticles on the cell surface with a I2/KI etchant. *Nano letters*. 2009;9(3):1080-1084.
227. Arvizo RR, Miranda OR, Thompson MA, et al. Effect of nanoparticle surface charge at the plasma membrane and beyond. *Nano letters*. 2010;10(7):2543-2548.
228. Lin J, Zhang H, Chen Z, Zheng Y. Penetration of lipid membranes by gold nanoparticles: insights into cellular uptake, cytotoxicity, and their relationship. *ACS nano*. 2010;4(9):5421-5429.
229. Qiu Y, Liu Y, Wang L, et al. Surface chemistry and aspect ratio mediated cellular uptake of Au nanorods. *Biomaterials*. 2010;31(30):7606-7619.
230. Naslavsky N, Caplan S. The enigmatic endosome - sorting the ins and outs of endocytic trafficking. *J Cell Sci*. 2018;131(13).
231. Martens T, Remaut K, Demeester J, De Smedt S, Braeckmans K. Intracellular delivery of nanomaterials: How to catch endosomal escape in the act. *Nano Today*. 2014;9:344-364.
232. Smith SA, Selby LI, Johnston APR, Such GK. The Endosomal Escape of Nanoparticles: Toward More Efficient Cellular Delivery. *Bioconjugate chemistry*. 2019;30(2):263-272.
233. Sabella S, Carney RP, Brunetti V, et al. A general mechanism for intracellular toxicity of metal-containing nanoparticles. *Nanoscale*. 2014;6(12):7052-7061.
234. Tang Y, Shen Y, Huang L, et al. In vitro cytotoxicity of gold nanorods in A549 cells. *Environ Toxicol Pharmacol*. 2015;39(2):871-878.
235. Mateo D, Morales P, Avalos A, Haza AI. Oxidative stress contributes to gold nanoparticle-induced cytotoxicity in human tumor cells. *Toxicol Mech Methods*. 2014;24(3):161-172.
236. Zhang X, Guo X, Kang X, et al. Surface Functionalization of Pegylated Gold Nanoparticles with Antioxidants Suppresses Nanoparticle-Induced Oxidative Stress and Neurotoxicity. *Chemical research in toxicology*. 2020.
237. Akbarzadeh Khiavi M, Safary A, Barar J, et al. PEGylated gold nanoparticles-ribonuclease induced oxidative stress and apoptosis in colorectal cancer cells. *Bioimpacts*. 2020;10(1):27-36.
238. Hvolbæk B, Janssens TVW, Clausen BS, Falsig H, Christensen CH, Nørskov JK. Catalytic activity of Au nanoparticles. *Nano Today*. 2007;2(4):14-18.
239. Nel A, Xia T, Madler L, Li N. Toxic potential of materials at the nanolevel. *Science (New York, NY)*. 2006;311(5761):622-627.
240. Turner M, Golovko VB, Vaughan OP, et al. Selective oxidation with dioxygen by gold nanoparticle catalysts derived from 55-atom clusters. *Nature*. 2008;454(7207):981-983.
241. Cheng NN, Starkewolf Z, Davidson RA, et al. Chemical enhancement by nanomaterials under X-ray irradiation. *J Am Chem Soc*. 2012;134(4):1950-1953.
242. Misawa M, Takahashi J. Generation of reactive oxygen species induced by gold nanoparticles under x-ray and UV Irradiations. *Nanomedicine : nanotechnology, biology, and medicine*. 2011;7(5):604-614.

243. Saccoccia F, Angelucci F, Boumis G, et al. On the mechanism and rate of gold incorporation into thiol-dependent flavoreductases. *J Inorg Biochem.* 2012;108:105-111.
244. Liu R, Wang Y, Yuan Q, An D, Li J, Gao X. The Au clusters induce tumor cell apoptosis via specifically targeting thioredoxin reductase 1 (TrxR1) and suppressing its activity. *Chem Commun (Camb).* 2014;50(73):10687-10690.
245. Wang H, Bouzakoura S, de Mey S, et al. Auranofin radiosensitizes tumor cells through targeting thioredoxin reductase and resulting overproduction of reactive oxygen species. *Oncotarget.* 2017;8(22):35728-35742.
246. Hwang-Bo H, Jeong JW, Han MH, et al. Auranofin, an inhibitor of thioredoxin reductase, induces apoptosis in hepatocellular carcinoma Hep3B cells by generation of reactive oxygen species. *Gen Physiol Biophys.* 2017;36(2):117-128.
247. Taggart LE, McMahon SJ, Butterworth KT, Currell FJ, Schettino G, Prise KM. Protein disulphide isomerase as a target for nanoparticle-mediated sensitisation of cancer cells to radiation. *Nanotechnology.* 2016;27(21):215101.
248. Zhao RZ, Jiang S, Zhang L, Yu ZB. Mitochondrial electron transport chain, ROS generation and uncoupling (Review). *Int J Mol Med.* 2019;44(1):3-15.
249. Gallud A, Klöditz K, Ytterberg J, et al. Cationic gold nanoparticles elicit mitochondrial dysfunction: a multi-omics study. *Scientific reports.* 2019;9(1):4366.
250. Salnikov V, Lukanenko YO, Frederick CA, Lederer WJ, Lukanenko V. Probing the outer mitochondrial membrane in cardiac mitochondria with nanoparticles. *Biophys J.* 2007;92(3):1058-1071.
251. Wang L, Liu Y, Li W, et al. Selective targeting of gold nanorods at the mitochondria of cancer cells: implications for cancer therapy. *Nano letters.* 2011;11(2):772-780.
252. Ramalingam V, Revathidevi S, Shanmuganayagam TS, Muthulakshmi L, Rajaram R. Gold nanoparticle induces mitochondria-mediated apoptosis and cell cycle arrest in nonsmall cell lung cancer cells. *Gold Bulletin.* 2017;50(2):177-189.
253. Pan Y, Leifert A, Ruau D, et al. Gold nanoparticles of diameter 1.4 nm trigger necrosis by oxidative stress and mitochondrial damage. *Small (Weinheim an der Bergstrasse, Germany).* 2009;5(18):2067-2076.
254. Schaeublin NM, Braydich-Stolle LK, Schrand AM, et al. Surface charge of gold nanoparticles mediates mechanism of toxicity. *Nanoscale.* 2011;3(2):410-420.
255. Manshian BB, Pokhrel S, Madler L, Soenen SJ. The impact of nanoparticle-driven lysosomal alkalization on cellular functionality. *J Nanobiotechnology.* 2018;16(1):85.
256. Yuan L, Zhang F, Qi X, et al. Chiral polymer modified nanoparticles selectively induce autophagy of cancer cells for tumor ablation. *J Nanobiotechnology.* 2018;16(1):55.
257. Ma X, Wu Y, Jin S, et al. Gold nanoparticles induce autophagosome accumulation through size-dependent nanoparticle uptake and lysosome impairment. *ACS nano.* 2011;5(11):8629-8639.
258. Maysinger D, Gran ER, Bertorelle F, et al. Gold nanoclusters elicit homeostatic perturbations in glioblastoma cells and adaptive changes of lysosomes. *Theranostics.* 2020;10(4):1633-1648.
259. Zhao P, Chen X, Wang Q, et al. Differential toxicity mechanism of gold nanoparticles in HK-2 renal proximal tubular cells and 786-O carcinoma cells. *Nanomedicine (London, England).* 2020.
260. Rambold AS, Lippincott-Schwartz J. Mechanisms of mitochondria and autophagy crosstalk. *Cell Cycle.* 2011;10(23):4032-4038.
261. Ding F, Li Y, Liu J, et al. Overendocytosis of gold nanoparticles increases autophagy and apoptosis in hypoxic human renal proximal tubular cells. *International journal of nanomedicine.* 2014;9:4317-4330.
262. Barnum KJ, O'Connell MJ. Cell cycle regulation by checkpoints. *Methods Mol Biol.* 2014;1170:29-40.
263. Dewey WC, Noel JS, Dettor CM. Changes in Radiosensitivity and Dispersion of Chromatin during the Cell Cycle of Synchronous Chinese Hamster Cells. *Radiation research.* 1972;52(2):373-394.
264. Mao Z, Bozzella M, Seluanov A, Gorbunova V. DNA repair by nonhomologous end joining and homologous recombination during cell cycle in human cells. *Cell Cycle.* 2008;7(18):2902-2906.
265. Abdel-Ghany S, Mahfouz M, Ashraf N, Sabit H, Cevik E, El-Zawahri M. Gold nanoparticles induce G2/M cell cycle arrest and enhance the expression of E-cadherin in breast cancer cells. *Inorganic and Nano-Metal Chemistry.* 2020:1-7.
266. Mackey MA, Saira F, Mahmoud MA, El-Sayed MA. Inducing cancer cell death by targeting its nucleus: solid gold nanospheres versus hollow gold nanocages. *Bioconjugate chemistry.* 2013;24(6):897-906.
267. Zhang Q, Ma Y, Yang S, Xu B, Fei X. Small-sized gold nanoparticles inhibit the proliferation and invasion of SW579 cells. *Mol Med Rep.* 2015;12(6):8313-8319.
268. Li Q, Huang C, Liu L, Hu R, Qu J. Effect of Surface Coating of Gold Nanoparticles on Cytotoxicity and Cell Cycle Progression. *Nanomaterials (Basel).* 2018;8(12).

## References

269. Choudhury D, Xavier PL, Chaudhari K, et al. Unprecedented inhibition of tubulin polymerization directed by gold nanoparticles inducing cell cycle arrest and apoptosis. *Nanoscale*. 2013;5(10):4476-4489.
270. Jiang J, Mao Q, Li H, Lou J. Apigenin stabilized gold nanoparticles increased radiation therapy efficiency in lung cancer cells. *International Journal of Clinical and Experimental Medicine*. 2017;10:13298-13305.
271. Mackey MA, El-Sayed MA. Chemosensitization of cancer cells via gold nanoparticle-induced cell cycle regulation. *Photochem Photobiol*. 2014;90(2):306-312.
272. Hanzic N, Horvat A, Bibic J, et al. Syntheses of gold nanoparticles and their impact on the cell cycle in breast cancer cells subjected to megavoltage X-ray irradiation. *Mater Sci Eng C Mater Biol Appl*. 2018;91:486-495.
273. Zheng Q, Yang H, Wei J, Tong JL, Shu YQ. The role and mechanisms of nanoparticles to enhance radiosensitivity in hepatocellular cell. *Biomed Pharmacother*. 2013;67(7):569-575.
274. Martinez-Torres AC, Lorenzo-Anota HY, Garcia-Juarez MG, Zarate-Trivino DG, Rodriguez-Padilla C. Chitosan gold nanoparticles induce different ROS-dependent cell death modalities in leukemic cells. *International journal of nanomedicine*. 2019;14:7173-7190.
275. Yasui H, Takeuchi R, Nagane M, et al. Radiosensitization of tumor cells through endoplasmic reticulum stress induced by PEGylated nanogel containing gold nanoparticles. *Cancer Lett*. 2014;347(1):151-158.
276. Tsai YY, Huang YH, Chao YL, et al. Identification of the nanogold particle-induced endoplasmic reticulum stress by omic techniques and systems biology analysis. *ACS nano*. 2011;5(12):9354-9369.
277. Ma X, Sun J, Zhong L, et al. Evaluation of Turning-Sized Gold Nanoparticles on Cellular Adhesion by Golgi Disruption in Vitro and in Vivo. *Nano letters*. 2019;19(12):8476-8487.
278. Hashimoto M, Sasaki JI, Yamaguchi S, et al. Gold Nanoparticles Inhibit Matrix Metalloproteases without Cytotoxicity. *J Dent Res*. 2015;94(8):1085-1091.
279. Hashimoto M, Kawai K, Kawakami H, Imazato S. Matrix metalloproteases inhibition and biocompatibility of gold and platinum nanoparticles. *J Biomed Mater Res A*. 2016;104(1):209-217.
280. Cormode DP, Naha PC, Fayad ZA. Nanoparticle contrast agents for computed tomography: a focus on micelles. *Contrast media & molecular imaging*. 2014;9(1):37-52.
281. Khademi S, Sarkar S, Shakeri-Zadeh A, et al. Targeted gold nanoparticles enable molecular CT imaging of head and neck cancer: An in vivo study. *Int J Biochem Cell Biol*. 2019;114:105554.
282. Kim D, Park S, Lee JH, Jeong YY, Jon S. Antibiofouling polymer-coated gold nanoparticles as a contrast agent for in vivo X-ray computed tomography imaging. *J Am Chem Soc*. 2007;129(24):7661-7665.
283. Cai QY, Kim SH, Choi KS, et al. Colloidal gold nanoparticles as a blood-pool contrast agent for X-ray computed tomography in mice. *Invest Radiol*. 2007;42(12):797-806.
284. Li J, You J, Wu C, et al. T1-T2 molecular magnetic resonance imaging of renal carcinoma cells based on nano-contrast agents. *International journal of nanomedicine*. 2018;13:4607-4625.
285. Abed Z, Beik J, Laurent S, et al. Iron oxide-gold core-shell nano-theranostic for magnetically targeted photothermal therapy under magnetic resonance imaging guidance. *J Cancer Res Clin Oncol*. 2019;145(5):1213-1219.
286. Zhong D, Zhao J, Li Y, et al. Laser-triggered aggregated cubic  $\alpha\text{-Fe}_2\text{O}_3\text{@Au}$  nanocomposites for magnetic resonance imaging and photothermal/enhanced radiation synergistic therapy. *Biomaterials*. 2019;219:119369.
287. Yang M, Cheng K, Qi S, et al. Affibody modified and radiolabeled gold-iron oxide hetero-nanostructures for tumor PET, optical and MR imaging. *Biomaterials*. 2013;34(11):2796-2806.
288. Hebert EM, Debouttiere PJ, Lepage M, Sanche L, Hunting DJ. Preferential tumour accumulation of gold nanoparticles, visualised by Magnetic Resonance Imaging: radiosensitisation studies in vivo and in vitro. *Int J Radiat Biol*. 2010;86(8):692-700.
289. Liu J, Xiong Z, Zhang J, et al. Zwitterionic Gadolinium(III)-Complexed Dendrimer-Entrapped Gold Nanoparticles for Enhanced Computed Tomography/Magnetic Resonance Imaging of Lung Cancer Metastasis. *ACS applied materials & interfaces*. 2019;11(17):15212-15221.
290. Zhou B, Xiong Z, Wang P, et al. Targeted tumor dual mode CT/MR imaging using multifunctional polyethylenimine-entrapped gold nanoparticles loaded with gadolinium. *Drug Deliv*. 2018;25(1):178-186.
291. Xu C, Wang Y, Zhang C, Jia Y, Luo Y, Gao X. AuGd integrated nanoprobe for optical/MRI/CT triple-modal in vivo tumor imaging. *Nanoscale*. 2017;9(13):4620-4628.
292. Coughlin AJ, Ananta JS, Deng N, Larina IV, Decuzzi P, West JL. Gadolinium-conjugated gold nanoshells for multimodal diagnostic imaging and photothermal cancer therapy. *Small (Weinheim an der Bergstrasse, Germany)*. 2014;10(3):556-565.
293. Pitchaimani A, Duong T, Nguyen T, et al. Gd(3)(+) Tethered Gold Nanorods for Combined Magnetic Resonance Imaging and Photo-Thermal Therapy. *J Biomed Nanotechnol*. 2017;13(4):417-426.

294. Huang X, El-Sayed MA. Gold nanoparticles: Optical properties and implementations in cancer diagnosis and photothermal therapy. *Journal of Advanced Research*. 2010;1(1):13-28.
295. Li M, Qiu Y, Fan C, Cui K, Zhang Y, Xiao Z. Design of SERS nanoprobes for Raman imaging: materials, critical factors and architectures. *Acta Pharm Sin B*. 2018;8(3):381-389.
296. Wang S, Fu L, Xin J, et al. Photoacoustic response induced by nanoparticle-mediated photothermal bubbles beyond the thermal expansion for potential theranostics. 2018;23 %J Journal of Biomedical Optics(12):125002.
297. Gao F, Bai L, Liu S, et al. Rationally encapsulated gold nanorods improving both linear and nonlinear photoacoustic imaging contrast in vivo. *Nanoscale*. 2017;9(1):79-86.
298. Zagaynova EV, Shirmanova MV, Kirillin MY, et al. Contrasting properties of gold nanoparticles for optical coherence tomography: phantom, in vivo studies and Monte Carlo simulation. *Physics in medicine and biology*. 2008;53(18):4995-5009.
299. Alamzadeh Z, Beik J, Mirrahimi M, et al. Gold nanoparticles promote a multimodal synergistic cancer therapy strategy by co-delivery of thermo-chemo-radio therapy. *Eur J Pharm Sci*. 2020;145:105235.
300. Xu X, Chong Y, Liu X, et al. Multifunctional nanotheranostic gold nanocages for photoacoustic imaging guided radio/photodynamic/photothermal synergistic therapy. *Acta Biomater*. 2019;84:328-338.
301. Kim S, Chen YS, Luke GP, Emelianov SY. In-vivo ultrasound and photoacoustic image- guided photothermal cancer therapy using silica-coated gold nanorods. *IEEE Trans Ultrason Ferroelectr Freq Control*. 2014;61(5):891-897.
302. Curry T, Kopelman R, Shilo M, Popovtzer R. Multifunctional theranostic gold nanoparticles for targeted CT imaging and photothermal therapy. *Contrast media & molecular imaging*. 2014;9(1):53-61.
303. Liu Y, Ashton JR, Moding EJ, et al. A Plasmonic Gold Nanostar Theranostic Probe for In Vivo Tumor Imaging and Photothermal Therapy. *Theranostics*. 2015;5(9):946-960.
304. Zhong J, Yang S, Wen L, Xing D. Imaging-guided photoacoustic drug release and synergistic chemo-photoacoustic therapy with paclitaxel-containing nanoparticles. *Journal of controlled release : official journal of the Controlled Release Society*. 2016;226:77-87.
305. Yan D, Liu X, Deng G, et al. Facile assembling of novel polypyrrole nanocomposites theranostic agent for magnetic resonance and computed tomography imaging guided efficient photothermal ablation of tumors. *J Colloid Interface Sci*. 2018;530:547-555.
306. Bhattacharyya S, Dixit M. Metallic radionuclides in the development of diagnostic and therapeutic radiopharmaceuticals. *Dalton Trans*. 2011;40(23):6112-6128.
307. National Research C, Institute of Medicine Committee on State of the Science of Nuclear M. The National Academies Collection: Reports funded by National Institutes of Health. In: *Advancing Nuclear Medicine Through Innovation*. Washington (DC): National Academies Press (US) National Academy of Sciences.; 2007.
308. Maccora D, Dini V, Battocchio C, et al. Gold Nanoparticles and Nanorods in Nuclear Medicine: A Mini Review. 2019;9(16):3232.
309. Sugiura G, Kuhn H, Sauter M, Haberkorn U, Mier W. Radiolabeling strategies for tumor-targeting proteinaceous drugs. *Molecules*. 2014;19(2):2135-2165.
310. Liu S. Bifunctional coupling agents for radiolabeling of biomolecules and target-specific delivery of metallic radionuclides. *Adv Drug Deliv Rev*. 2008;60(12):1347-1370.
311. Lucas S, Feron O, Gallez B, Masereel B, Michiels C, Vander Borgh T. Monte Carlo Calculation of Radioimmunotherapy with (90)Y-, (177)Lu-, (131)I-, (124)I-, and (188)Re-Nanoobjects: Choice of the Best Radionuclide for Solid Tumour Treatment by Using TCP and NTCP Concepts. *Comput Math Methods Med*. 2015;2015:284360.
312. Bouchat V, Nuttens VE, Michiels C, et al. Radioimmunotherapy with radioactive nanoparticles: biological doses and treatment efficiency for vascularized tumors with or without a central hypoxic area. *Med Phys*. 2010;37(4):1826-1839.
313. Bouchat V, Nuttens VE, Lucas S, et al. Radioimmunotherapy with radioactive nanoparticles: first results of dosimetry for vascularized and necrosed solid tumors. *Med Phys*. 2007;34(11):4504-4513.
314. Song L, Falzone N, Vallis KA. EGF-coated gold nanoparticles provide an efficient nano-scale delivery system for the molecular radiotherapy of EGFR-positive cancer. *Int J Radiat Biol*. 2016;92(11):716-723.
315. Jeon J. Review of Therapeutic Applications of Radiolabeled Functional Nanomaterials. *International journal of molecular sciences*. 2019;20(9).
316. Byegård J, Skarnemark G, Skålberg M. The stability of some metal EDTA, DTPA and DOTA complexes: Application as tracers in groundwater studies. *Journal of Radioanalytical and Nuclear Chemistry*. 1999;241(2):281-290.



## References

317. Chen CC, Li JJ, Guo NH, et al. Evaluation of the Biological Behavior of a Gold Nanocore-Encapsulated Human Serum Albumin Nanoparticle (Au@HSANP) in a CT-26 Tumor/Ascites Mouse Model after Intravenous/Intraperitoneal Administration. *International journal of molecular sciences*. 2019;20(1).
318. Tam AL, Melancon MP, Abdelsalam M, et al. Imaging Intratumoral Nanoparticle Uptake After Combining Nanoembolization with Various Ablative Therapies in Hepatic VX2 Rabbit Tumors. *J Biomed Nanotechnol*. 2016;12(2):296-307.
319. Wang Y, Liu Y, Luehmann H, et al. Evaluating the pharmacokinetics and in vivo cancer targeting capability of Au nanocages by positron emission tomography imaging. *ACS nano*. 2012;6(7):5880-5888.
320. Yook S, Cai Z, Lu Y, Winnik MA, Pignol JP, Reilly RM. Radiation Nanomedicine for EGFR-Positive Breast Cancer: Panitumumab-Modified Gold Nanoparticles Complexed to the beta-Particle-Emitter, (177)Lu. *Mol Pharm*. 2015;12(11):3963-3972.
321. Morales-Avila E, Ferro-Flores G, Ocampo-Garcia BE, et al. Multimeric system of 99mTc-labeled gold nanoparticles conjugated to c[RGDFK(C)] for molecular imaging of tumor alpha(v)beta(3) expression. *Bioconjugate chemistry*. 2011;22(5):913-922.
322. Ocampo-Garcia BE, Ramirez Fde M, Ferro-Flores G, et al. (99m)Tc-labelled gold nanoparticles capped with HYNIC-peptide/mannose for sentinel lymph node detection. *Nucl Med Biol*. 2011;38(1):1-11.
323. Karmani L, Bouchat V, Bouzin C, et al. (89)Zr-labeled anti-endoglin antibody-targeted gold nanoparticles for imaging cancer: implications for future cancer therapy. *Nanomedicine (London, England)*. 2014;9(13):1923-1937.
324. Xu X, Zhao L, Li X, et al. Targeted tumor SPECT/CT dual mode imaging using multifunctional RGD-modified low generation dendrimer-entrapped gold nanoparticles. *Biomater Sci*. 2017;5(12):2393-2397.
325. Yang Y, Zhang L, Cai J, et al. Tumor Angiogenesis Targeted Radiosensitization Therapy Using Gold Nanoprobes Guided by MRI/SPECT Imaging. *ACS applied materials & interfaces*. 2016;8(3):1718-1732.
326. Pretze M, van der Meulen NP, Wangler C, Schibli R, Wangler B. Targeted (64) Cu-labeled gold nanoparticles for dual imaging with positron emission tomography and optical imaging. *J Labelled Comp Radiopharm*. 2019;62(8):471-482.
327. Zhao Y, Detering L, Sultan D, et al. Gold Nanoclusters Doped with (64)Cu for CXCR4 Positron Emission Tomography Imaging of Breast Cancer and Metastasis. *ACS nano*. 2016;10(6):5959-5970.
328. Frellsen AF, Hansen AE, Jolck RI, et al. Mouse Positron Emission Tomography Study of the Biodistribution of Gold Nanoparticles with Different Surface Coatings Using Embedded Copper-64. *ACS nano*. 2016;10(11):9887-9898.
329. Zhao Y, Pang B, Luehmann H, et al. Gold Nanoparticles Doped with (199) Au Atoms and Their Use for Targeted Cancer Imaging by SPECT. *Adv Healthc Mater*. 2016;5(8):928-935.
330. Zhao Y, Sultan D, Detering L, et al. Copper-64-alloyed gold nanoparticles for cancer imaging: improved radiolabel stability and diagnostic accuracy. *Angewandte Chemie (International ed in English)*. 2014;53(1):156-159.
331. Wang J, Zhang G, Li Q, et al. In vivo self-bio-imaging of tumors through in situ biosynthesized fluorescent gold nanoclusters. *Scientific reports*. 2013;3:1157.
332. Sun X, Huang X, Yan X, et al. Chelator-free (64)Cu-integrated gold nanomaterials for positron emission tomography imaging guided photothermal cancer therapy. *ACS nano*. 2014;8(8):8438-8446.
333. Rovais MRA, Alirezapour B, Moassesi ME, Amiri M, Novin FB, Maadi E. Internalization capabilities of gold-198 nanoparticles: Comparative evaluation of effects of chitosan agent on cellular uptake into MCF-7. *Appl Radiat Isot*. 2018;142:85-91.
334. Black KC, Wang Y, Luehmann HP, et al. Radioactive 198Au-doped nanostructures with different shapes for in vivo analyses of their biodistribution, tumor uptake, and intratumoral distribution. *ACS nano*. 2014;8(5):4385-4394.
335. Wang Y, Liu Y, Luehmann H, et al. Radioluminescent gold nanocages with controlled radioactivity for real-time in vivo imaging. *Nano letters*. 2013;13(2):581-585.
336. Lee SB, Yoon G, Lee SW, et al. Combined Positron Emission Tomography and Cerenkov Luminescence Imaging of Sentinel Lymph Nodes Using PEGylated Radionuclide-Embedded Gold Nanoparticles. *Small (Weinheim an der Bergstrasse, Germany)*. 2016;12(35):4894-4901.
337. Lee SB, Lee HW, Singh TD, et al. Visualization of Macrophage Recruitment to Inflammation Lesions using Highly Sensitive and Stable Radionuclide-Embedded Gold Nanoparticles as a Nuclear Bio-Imaging Platform. *Theranostics*. 2017;7(4):926-934.
338. Lee SB, Lee YJ, Cho SJ, et al. Antigen-Free Radionuclide-Embedded Gold Nanoparticles for Dendritic Cell Maturation, Tracking, and Strong Antitumor Immunity. *Adv Healthc Mater*. 2018;7(9):e1701369.

339. Sun N, Zhao L, Zhu J, et al. (131)I-labeled polyethylenimine-entrapped gold nanoparticles for targeted tumor SPECT/CT imaging and radionuclide therapy. *International journal of nanomedicine*. 2019;14:4367-4381.
340. Black KCL, Akers WJ, Sudlow G, Xu B, Laforest R, Achilefu S. Dual-radiolabeled nanoparticle SPECT probes for bioimaging. *Nanoscale*. 2015;7(2):440-444.
341. Su N, Dang Y, Liang G, Liu G. Iodine-125-labeled cRGD-gold nanoparticles as tumor-targeted radiosensitizer and imaging agent. *Nanoscale Res Lett*. 2015;10:160.
342. Kao HW, Lin YY, Chen CC, et al. Evaluation of EGFR-targeted radioimmuno-gold-nanoparticles as a theranostic agent in a tumor animal model. *Bioorg Med Chem Lett*. 2013;23(11):3180-3185.
343. Jeon J, Shim HE, Mushtaq S, et al. An Optimized Protocol for the Efficient Radiolabeling of Gold Nanoparticles by Using a 125I-labeled Azide Prosthetic Group. *J Vis Exp*. 2016(116).
344. Guerrero S, Herance JR, Rojas S, et al. Synthesis and in vivo evaluation of the biodistribution of a 18F-labeled conjugate gold-nanoparticle-peptide with potential biomedical application. *Bioconjugate chemistry*. 2012;23(3):399-408.
345. Ghiassian S, Yu L, Gobbo P, et al. Nitrone-Modified Gold Nanoparticles: Synthesis, Characterization, and Their Potential as (18)F-Labeled Positron Emission Tomography Probes via I-SPANC. *ACS Omega*. 2019;4(21):19106-19115.
346. Zhu J, Chin J, Wangler C, Wangler B, Lennox RB, Schirrmacher R. Rapid (18)F-labeling and loading of PEGylated gold nanoparticles for in vivo applications. *Bioconjugate chemistry*. 2014;25(6):1143-1150.
347. Lee SB, Lee SW, Jeong SY, et al. Engineering of Radioiodine-Labeled Gold Core-Shell Nanoparticles As Efficient Nuclear Medicine Imaging Agents for Trafficking of Dendritic Cells. *ACS applied materials & interfaces*. 2017;9(10):8480-8489.
348. Lee SB, Kumar D, Li Y, et al. PEGylated crushed gold shell-radiolabeled core nanoballs for in vivo tumor imaging with dual positron emission tomography and Cerenkov luminescent imaging. *J Nanobiotechnology*. 2018;16(1):41.
349. Kim YH, Jeon J, Hong SH, et al. Tumor targeting and imaging using cyclic RGD-PEGylated gold nanoparticle probes with directly conjugated iodine-125. *Small (Weinheim an der Bergstrasse, Germany)*. 2011;7(14):2052-2060.
350. Zhang Y, Zhang Y, Yin L, et al. Synthesis and Bioevaluation of Iodine-131 Directly Labeled Cyclic RGD-PEGylated Gold Nanorods for Tumor-Targeted Imaging. *Contrast media & molecular imaging*. 2017;2017:6081724.
351. Eskandari N, Yavari K, Outokesh M, Sadjadi S, Ahmadi SJ. Iodine-131 radiolabeling of poly ethylene glycol-coated gold nanorods for in vivo imaging. *J Labelled Comp Radiopharm*. 2013;56(1):12-16.
352. Dziawer L, Koźmiński P, Męczyńska-Wielgosz S, et al. Gold nanoparticle bioconjugates labelled with 211At for targeted alpha therapy. *RSC Advances*. 2017;7(65):41024-41032.
353. Dziawer L, Majkowska-Pilip A, Gawel D, et al. Trastuzumab-Modified Gold Nanoparticles Labeled with (211)At as a Prospective Tool for Local Treatment of HER2-Positive Breast Cancer. *Nanomaterials (Basel)*. 2019;9(4).
354. Walsh AA. Chemisorption of iodine-125 to gold nanoparticles allows for real-time quantitation and potential use in nanomedicine. *Journal of Nanoparticle Research*. 2017;19(4):152.
355. Wang P, Sun W, Wang Q, et al. Iodine-Labeled Au Nanorods with High Radiochemical Stability for Imaging-Guided Radiotherapy and Photothermal Therapy. *ACS Applied Nano Materials*. 2019;2(3):1374-1381.
356. Peiris PM, Deb P, Doolittle E, et al. Vascular Targeting of a Gold Nanoparticle to Breast Cancer Metastasis. *J Pharm Sci*. 2015;104(8):2600-2610.
357. Xie H, Wang ZJ, Bao A, Goins B, Phillips WT. In vivo PET imaging and biodistribution of radiolabeled gold nanoshells in rats with tumor xenografts. *International journal of pharmaceuticals*. 2010;395(1-2):324-330.
358. Mendoza-Sanchez AN, Ferro-Flores G, Ocampo-García BE, et al. Lys3-bombesin conjugated to 99mTc-labelled gold nanoparticles for in vivo gastrin releasing peptide-receptor imaging. *J Biomed Nanotechnol*. 2010;6(4):375-384.
359. Yook S, Lu Y, Jeong JJ, et al. Stability and Biodistribution of Thiol-Functionalized and (177)Lu-Labeled Metal Chelating Polymers Bound to Gold Nanoparticles. *Biomacromolecules*. 2016;17(4):1292-1302.
360. Karmani L, Labar D, Valembois V, et al. Antibody-functionalized nanoparticles for imaging cancer: influence of conjugation to gold nanoparticles on the biodistribution of 89Zr-labeled cetuximab in mice. *Contrast media & molecular imaging*. 2013;8(5):402-408.
361. Orocio-Rodriguez E, Ferro-Flores G, Santos-Cuevas CL, et al. Two Novel Nanosized Radiolabeled Analogues of Somatostatin for Neuroendocrine Tumor Imaging. *Journal of nanoscience and nanotechnology*. 2015;15(6):4159-4169.

## References

362. Poon W, Zhang YN, Ouyang B, et al. Elimination Pathways of Nanoparticles. *ACS nano*. 2019;13(5):5785-5798.
363. Silva F, Zambre A, Campello MP, et al. Interrogating the Role of Receptor-Mediated Mechanisms: Biological Fate of Peptide-Functionalized Radiolabeled Gold Nanoparticles in Tumor Mice. *Bioconjugate chemistry*. 2016;27(4):1153-1164.
364. Chanda N, Kattumuri V, Shukla R, et al. Bombesin functionalized gold nanoparticles show in vitro and in vivo cancer receptor specificity. *Proceedings of the National Academy of Sciences of the United States of America*. 2010;107(19):8760-8765.
365. Chattopadhyay N, Fonge H, Cai Z, et al. Role of antibody-mediated tumor targeting and route of administration in nanoparticle tumor accumulation in vivo. *Mol Pharm*. 2012;9(8):2168-2179.
366. Zhang G, Yang Z, Lu W, et al. Influence of anchoring ligands and particle size on the colloidal stability and in vivo biodistribution of polyethylene glycol-coated gold nanoparticles in tumor-xenografted mice. *Biomaterials*. 2009;30(10):1928-1936.
367. Zhao Y, Sultan D, Detering L, Luehmann H, Liu Y. Facile synthesis, pharmacokinetic and systemic clearance evaluation, and positron emission tomography cancer imaging of (6)(4)Cu-Au alloy nanoclusters. *Nanoscale*. 2014;6(22):13501-13509.
368. Song L, Able S, Johnson E, Vallis KA. Accumulation of (111)In-Labelled EGF-Au-PEG Nanoparticles in EGFR-Positive Tumours is Enhanced by Coadministration of Targeting Ligand. *Nanotheranostics*. 2017;1(3):232-243.
369. Azorín-Vega EP, Zambrano-Ramírez OD, Rojas-Calderón EL, Ocampo-García BE, Ferro-Flores G. Tumoral fibrosis effect on the radiation absorbed dose of <sup>177</sup>Lu-Tyr3-octreotate and <sup>177</sup>Lu-Tyr3-octreotate conjugated to gold nanoparticles. *Applied Radiation and Isotopes*. 2015;100:96-100.
370. Vilchis-Juarez A, Ferro-Flores G, Santos-Cuevas C, et al. Molecular targeting radiotherapy with cyclo-RGDFK(C) peptides conjugated to <sup>177</sup>Lu-labeled gold nanoparticles in tumor-bearing mice. *J Biomed Nanotechnol*. 2014;10(3):393-404.
371. Melancon MP, Lu W, Yang Z, et al. In vitro and in vivo targeting of hollow gold nanoshells directed at epidermal growth factor receptor for photothermal ablation therapy. *Mol Cancer Ther*. 2008;7(6):1730-1739.
372. Chen CH, Lin FS, Liao WN, et al. Establishment of a trimodality analytical platform for tracing, imaging and quantification of gold nanoparticles in animals by radiotracer techniques. *Anal Chem*. 2015;87(1):601-608.
373. Adams GP, Schier R, McCall AM, et al. High affinity restricts the localization and tumor penetration of single-chain fv antibody molecules. *Cancer research*. 2001;61(12):4750-4755.
374. Tian M, Lu W, Zhang R, et al. Tumor uptake of hollow gold nanospheres after intravenous and intra-arterial injection: PET/CT study in a rabbit VX2 liver cancer model. *Mol Imaging Biol*. 2013;15(5):614-624.
375. Laprise-Pelletier M, Lagueux J, Cote MF, LaGrange T, Fortin MA. Low-Dose Prostate Cancer Brachytherapy with Radioactive Palladium-Gold Nanoparticles. *Adv Healthc Mater*. 2017;6(4).
376. Zhu J, Zhao L, Yang J, et al. (99m)Tc-Labeled Polyethylenimine-Entrapped Gold Nanoparticles with pH-Responsive Charge Conversion Property for Enhanced Dual Mode SPECT/CT Imaging of Cancer Cells. *Langmuir*. 2019;35(41):13405-13412.
377. Zhao L, Li Y, Zhu J, et al. Chlorotoxin peptide-functionalized polyethylenimine-entrapped gold nanoparticles for glioma SPECT/CT imaging and radionuclide therapy. *J Nanobiotechnology*. 2019;17(1):30.
378. Xing Y, Zhu J, Zhao L, et al. SPECT/CT imaging of chemotherapy-induced tumor apoptosis using (99m)Tc-labeled dendrimer-entrapped gold nanoparticles. *Drug Deliv*. 2018;25(1):1384-1393.
379. Li X, Xiong Z, Xu X, et al. (99m)Tc-Labeled Multifunctional Low-Generation Dendrimer-Entrapped Gold Nanoparticles for Targeted SPECT/CT Dual-Mode Imaging of Tumors. *ACS applied materials & interfaces*. 2016;8(31):19883-19891.
380. Zhou B, Wang R, Chen F, et al. (99m)Tc-Labeled RGD-Polyethylenimine Conjugates with Entrapped Gold Nanoparticles in the Cavities for Dual-Mode SPECT/CT Imaging of Hepatic Carcinoma. *ACS applied materials & interfaces*. 2018;10(7):6146-6154.
381. Cheng Y, Zhu J, Zhao L, et al. (131)I-labeled multifunctional dendrimers modified with BmK CT for targeted SPECT imaging and radiotherapy of gliomas. *Nanomedicine (London, England)*. 2016;11(10):1253-1266.
382. Grootendorst MR, Cariati M, Kothari A, Tuch DS, Purushotham A. Cerenkov luminescence imaging (CLI) for image-guided cancer surgery. *Clin Transl Imaging*. 2016;4(5):353-366.
383. Rambanapasi C, Barnard N, Grobler A, et al. Dual radiolabeling as a technique to track nanocarriers: the case of gold nanoparticles. *Molecules*. 2015;20(7):12863-12879.

384. Jimenez-Mancilla N, Ferro-Flores G, Santos-Cuevas C, et al. Multifunctional targeted therapy system based on (99m) Tc/(177) Lu-labeled gold nanoparticles-Tat(49-57)-Lys(3) -bombesin internalized in nuclei of prostate cancer cells. *J Labelled Comp Radiopharm*. 2013;56(13):663-671.
385. Cai Z, Chattopadhyay N, Yang K, et al. (111)In-labeled trastuzumab-modified gold nanoparticles are cytotoxic in vitro to HER2-positive breast cancer cells and arrest tumor growth in vivo in athymic mice after intratumoral injection. *Nucl Med Biol*. 2016;43(12):818-826.
386. Cai Z, Yook S, Lu Y, et al. Local Radiation Treatment of HER2-Positive Breast Cancer Using Trastuzumab-Modified Gold Nanoparticles Labeled with (177)Lu. *Pharm Res*. 2017;34(3):579-590.
387. Mendoza-Nava H, Ferro-Flores G, Ramirez FM, et al. Fluorescent, Plasmonic, and Radiotherapeutic Properties of the (177)Lu-Dendrimer-AuNP-Folate-Bombesin Nanoprobe Located Inside Cancer Cells. *Mol Imaging*. 2017;16:1536012117704768.
388. Chanda N, Kan P, Watkinson LD, et al. Radioactive gold nanoparticles in cancer therapy: therapeutic efficacy studies of GA-198AuNP nanoconstruct in prostate tumor-bearing mice. *Nanomedicine : nanotechnology, biology, and medicine*. 2010;6(2):201-209.
389. Shukla R, Chanda N, Zambre A, et al. Laminin receptor specific therapeutic gold nanoparticles (198AuNP-EGCg) show efficacy in treating prostate cancer. *Proceedings of the National Academy of Sciences of the United States of America*. 2012;109(31):12426-12431.
390. Axiak-Bechtel SM, Upendran A, Lattimer JC, et al. Gum arabic-coated radioactive gold nanoparticles cause no short-term local or systemic toxicity in the clinically relevant canine model of prostate cancer. *International journal of nanomedicine*. 2014;9:5001-5011.
391. Al-Yasiri AY, Khoobchandani M, Cutler CS, et al. Mangiferin functionalized radioactive gold nanoparticles (MGF-(198)AuNPs) in prostate tumor therapy: green nanotechnology for production, in vivo tumor retention and evaluation of therapeutic efficacy. *Dalton Trans*. 2017;46(42):14561-14571.
392. Moeendarbari S, Tekade R, Mulgaonkar A, et al. Theranostic Nanoseeds for Efficacious Internal Radiation Therapy of Unresectable Solid Tumors. *Scientific reports*. 2016;6:20614.
393. Xie H, Goins B, Bao A, Wang ZJ, Phillips WT. Effect of intratumoral administration on biodistribution of 64Cu-labeled nanoshells. *International journal of nanomedicine*. 2012;7:2227-2238.
394. Yook S, Cai Z, Lu Y, Winnik MA, Pignol JP, Reilly RM. Intratumorally Injected 177Lu-Labeled Gold Nanoparticles: Gold Nanoseed Brachytherapy with Application for Neoadjuvant Treatment of Locally Advanced Breast Cancer. *J Nucl Med*. 2016;57(6):936-942.
395. Le Goas M, Paquet M, Paquirissamy A, et al. Improving (131)I Radioiodine Therapy By Hybrid Polymer-Grafted Gold Nanoparticles. *International journal of nanomedicine*. 2019;14:7933-7946.
396. Ngwa W, Korideck H, Kassis AI, et al. In vitro radiosensitization by gold nanoparticles during continuous low-dose-rate gamma irradiation with I-125 brachytherapy seeds. *Nanomedicine : nanotechnology, biology, and medicine*. 2013;9(1):25-27.
397. Wojtowicz A, Krug P, Glowala P, et al. Nano-radiogold-decorated composite bioparticles. *Mater Sci Eng C Mater Biol Appl*. 2019;97:768-775.
398. E. Abraham Peter B. Himmel GUY. Management of Rheumatoid Arthritis: Rationale for the Use of Colloidal Metallic Gold. *Journal of Nutritional & Environmental Medicine*. 1997;7(4):295-305.
399. ten Hagen TL, Eggermont AM. Solid tumor therapy: manipulation of the vasculature with TNF. *Technol Cancer Res Treat*. 2003;2(3):195-203.
400. van Harsen R, Ten Hagen TL, Eggermont AM. TNF-alpha in cancer treatment: molecular insights, antitumor effects, and clinical utility. *Oncologist*. 2006;11(4):397-408.
401. Kimura K, Taguchi T, Urushizaki I, et al. Phase I study of recombinant human tumor necrosis factor. *Cancer Chemother Pharmacol*. 1987;20(3):223-229.
402. Taguchi T. Phase I study of recombinant human tumor necrosis factor (rHu-TNF:PT-050). *Cancer Detect Prev*. 1988;12(1-6):561-572.
403. Libutti SK, Paciotti GF, Byrnes AA, et al. Phase I and pharmacokinetic studies of CYT-6091, a novel PEGylated colloidal gold-rhTNF nanomedicine. *Clinical cancer research : an official journal of the American Association for Cancer Research*. 2010;16(24):6139-6149.
404. Stern JM, Kibanov Solomonov VV, Sazykina E, Schwartz JA, Gad SC, Goodrich GP. Initial Evaluation of the Safety of Nanoshell-Directed Photothermal Therapy in the Treatment of Prostate Disease. *Int J Toxicol*. 2016;35(1):38-46.
405. Gad SC, Sharp KL, Montgomery C, Payne JD, Goodrich GP. Evaluation of the toxicity of intravenous delivery of auroshell particles (gold-silica nanoshells). *Int J Toxicol*. 2012;31(6):584-594.
406. Rastinehad AR, Anastos H, Wajswol E, et al. Gold nanoshell-localized photothermal ablation of prostate tumors in a clinical pilot device study. 2019;116(37):18590-18596.

## References

407. Kumthekar P, Rademaker A, Ko C, et al. A phase 0 first-in-human study using NU-0129: A gold base spherical nucleic acid (SNA) nanoconjugate targeting BCL2L12 in recurrent glioblastoma patients. 2019;37(15\_suppl):3012-3012.
408. Kharlamov AN, Tyurnina AE, Veselova VS, Kovtun OP, Shur VY, Gabinsky JL. Silica-gold nanoparticles for atheroprotective management of plaques: results of the NANOM-FIM trial. *Nanoscale*. 2015;7(17):8003-8015.
409. Kharlamov AN, Feinstein JA, Cramer JA, Boothroyd JA, Shishkina EV, Shur V. Plasmonic photothermal therapy of atherosclerosis with nanoparticles: long-term outcomes and safety in NANOM-FIM trial. *Future Cardiol*. 2017;13(4):345-363.
410. Wilhelm S, Tavares AJ, Dai Q, et al. Analysis of nanoparticle delivery to tumours. *Nature Reviews Materials*. 2016;1:16014.
411. Ma Y, Hong J, Ding Y. Biological Behavior Regulation of Gold Nanoparticles via the Protein Corona. *Adv Healthc Mater*. 2020;9(6):e1901448.
412. Garcia-Alvarez R, Hadjidemetriou M, Sanchez-Iglesias A, Liz-Marzan LM, Kostarelos K. In vivo formation of protein corona on gold nanoparticles. The effect of their size and shape. *Nanoscale*. 2018;10(3):1256-1264.
413. Piella J, Bastus NG, Puentes V. Size-Dependent Protein-Nanoparticle Interactions in Citrate-Stabilized Gold Nanoparticles: The Emergence of the Protein Corona. *Bioconjugate chemistry*. 2017;28(1):88-97.
414. Gebauer JS, Malissek M, Simon S, et al. Impact of the nanoparticle-protein corona on colloidal stability and protein structure. *Langmuir*. 2012;28(25):9673-9679.
415. Deng ZJ, Liang M, Monteiro M, Toth I, Minchin RF. Nanoparticle-induced unfolding of fibrinogen promotes Mac-1 receptor activation and inflammation. *Nature nanotechnology*. 2011;6(1):39-44.
416. Kuschnerus I, Lau M, Giri K, et al. Effect of a protein corona on the fibrinogen induced cellular oxidative stress of gold nanoparticles. *Nanoscale*. 2020;12(10):5898-5905.
417. Wang G, Yan C, Gao S, Liu Y. Surface chemistry of gold nanoparticles determines interactions with bovine serum albumin. *Mater Sci Eng C Mater Biol Appl*. 2019;103:109856.
418. Sepand MR, Ghavami M, Zanganeh S, et al. Impact of plasma concentration of transferrin on targeting capacity of nanoparticles. *Nanoscale*. 2020;12(8):4935-4944.
419. Su G, Jiang H, Xu B, Yu Y, Chen X. Effects of Protein Corona on Active and Passive Targeting of Cyclic RGD Peptide-Functionalized PEGylation Nanoparticles. *Mol Pharm*. 2018;15(11):5019-5030.
420. Xiao W, Xiong J, Zhang S, Xiong Y, Zhang H, Gao H. Influence of ligands property and particle size of gold nanoparticles on the protein adsorption and corresponding targeting ability. *International journal of pharmaceutics*. 2018;538(1-2):105-111.
421. Su G, Zhou X, Zhou H, et al. Size-Dependent Facilitation of Cancer Cell Targeting by Proteins Adsorbed on Nanoparticles. *ACS applied materials & interfaces*. 2016;8(44):30037-30047.
422. Dai Q, Yan Y, Ang CS, et al. Monoclonal antibody-functionalized multilayered particles: targeting cancer cells in the presence of protein coronas. *ACS nano*. 2015;9(3):2876-2885.
423. Yeo ELL, Thong PSP, Soo KC, Kah JCY. Protein corona in drug delivery for multimodal cancer therapy in vivo. *Nanoscale*. 2018;10(5):2461-2472.
424. Corbo C, Molinaro R, Parodi A, Toledano Furman NE, Salvatore F, Tasciotti E. The impact of nanoparticle protein corona on cytotoxicity, immunotoxicity and target drug delivery. *Nanomedicine (London, England)*. 2016;11(1):81-100.
425. Quach QH, Kah JCY. Non-specific adsorption of complement proteins affects complement activation pathways of gold nanomaterials. *Nanotoxicology*. 2017;11(3):382-394.
426. Haute DV, Berlin JM. Challenges in realizing selectivity for nanoparticle biodistribution and clearance: lessons from gold nanoparticles. *Ther Deliv*. 2017;8(9):763-774.
427. Dai Q, Walkey C, Chan WCW. Polyethylene Glycol Backfilling Mitigates the Negative Impact of the Protein Corona on Nanoparticle Cell Targeting. 2014;53(20):5093-5096.
428. Walkey CD, Olsen JB, Guo H, Emili A, Chan WC. Nanoparticle size and surface chemistry determine serum protein adsorption and macrophage uptake. *J Am Chem Soc*. 2012;134(4):2139-2147.
429. Akiyama Y, Mori T, Katayama Y, Niidome T. The effects of PEG grafting level and injection dose on gold nanorod biodistribution in the tumor-bearing mice. *Journal of controlled release : official journal of the Controlled Release Society*. 2009;139(1):81-84.
430. Hatakeyama H, Akita H, Harashima H. The polyethyleneglycol dilemma: advantage and disadvantage of PEGylation of liposomes for systemic genes and nucleic acids delivery to tumors. *Biol Pharm Bull*. 2013;36(6):892-899.
431. Champion JA, Mitragotri S. Shape induced inhibition of phagocytosis of polymer particles. *Pharm Res*. 2009;26(1):244-249.

432. Geng Y, Dalhaimer P, Cai S, et al. Shape effects of filaments versus spherical particles in flow and drug delivery. *Nature nanotechnology*. 2007;2(4):249-255.
433. Christian DA, Cai S, Garbuzenko OB, et al. Flexible filaments for in vivo imaging and delivery: persistent circulation of filomicelles opens the dosage window for sustained tumor shrinkage. *Mol Pharm*. 2009;6(5):1343-1352.
434. Park JH, von Maltzahn G, Zhang L, et al. Systematic surface engineering of magnetic nanoworms for in vivo tumor targeting. *Small (Weinheim an der Bergstrasse, Germany)*. 2009;5(6):694-700.
435. Beningo KA, Wang Y-I. Fc-receptor-mediated phagocytosis is regulated by mechanical properties of the target. 2002;115(4):849-856.
436. Ting L, Hoon C, Rong Z, I-Wei C. RES blockade: A strategy for boosting efficiency of nanoparticle drug. *Nano Today*. 2015;10(1):11-21.
437. Sun X, Yan X, Jacobson O, et al. Improved Tumor Uptake by Optimizing Liposome Based RES Blockade Strategy. *Theranostics*. 2017;7(2):319-328.
438. Liu L, Ye Q, Lu M, et al. A New Approach to Deliver Anti-cancer Nanodrugs with Reduced Off-target Toxicities and Improved Efficiency by Temporarily Blunting the Reticuloendothelial System with Intralipid. *Scientific reports*. 2017;7(1):16106.
439. van Rooijen N. Liposomes for targeting of antigens and drugs: immunoadjuvant activity and liposome-mediated depletion of macrophages. *Journal of drug targeting*. 2008;16(7):529-534.
440. Hu Q, van Rooijen N, Liu D. Effect of Macrophage Elimination Using Liposome-Encapsulated Dichloromethylene Diphosphonate on Tissue Distribution of Liposomes. *Journal of Liposome Research*. 1996;6(4):681-698.
441. Ohara Y, Oda T, Yamada K, et al. Effective delivery of chemotherapeutic nanoparticles by depleting host Kupffer cells. *International journal of cancer Journal international du cancer*. 2012;131(10):2402-2410.
442. Diagaradjane P, Deorukhkar A, Gelovani JG, Maru DM, Krishnan S. Gadolinium chloride augments tumor-specific imaging of targeted quantum dots in vivo. *ACS nano*. 2010;4(7):4131-4141.
443. Zhang YN, Poon W, Tavares AJ, McGilvray ID, Chan WCW. Nanoparticle-liver interactions: Cellular uptake and hepatobiliary elimination. *Journal of controlled release : official journal of the Controlled Release Society*. 2016;240:332-348.
444. Wicki A, Witzigmann D, Balasubramanian V, Huwyler J. Nanomedicine in cancer therapy: challenges, opportunities, and clinical applications. *Journal of controlled release : official journal of the Controlled Release Society*. 2015;200:138-157.
445. Sengupta J, Datta P, Patra HK, Dasgupta AK, Gomes A. In vivo interaction of gold nanoparticles after acute and chronic exposures in experimental animal models. *Journal of nanoscience and nanotechnology*. 2013;13(3):1660-1670.
446. Cho WS, Cho M, Jeong J, et al. Acute toxicity and pharmacokinetics of 13 nm-sized PEG-coated gold nanoparticles. *Toxicol Appl Pharmacol*. 2009;236(1):16-24.
447. Khan HA, Ibrahim KE, Khan A, Alrokayan SH, Alhomida AS. Immunostaining of proinflammatory cytokines in renal cortex and medulla of rats exposed to gold nanoparticles. *Histology and histopathology*. 2017;32(6):597-607.
448. Ibrahim KE, Al-Mutary MG, Bakhiet AO, Khan HA. Histopathology of the Liver, Kidney, and Spleen of Mice Exposed to Gold Nanoparticles. *Molecules*. 2018;23(8).
449. Khan HA, Abdelhalim MA, Alhomida AS, Al-Ayed MS. Effects of naked gold nanoparticles on proinflammatory cytokines mRNA expression in rat liver and kidney. *BioMed research international*. 2013;2013:590730.
450. Khan HA, Ibrahim KE, Khan A, Alrokayan SH, Alhomida AS, Lee YK. Comparative evaluation of immunohistochemistry and real-time PCR for measuring proinflammatory cytokines gene expression in livers of rats treated with gold nanoparticles. *Exp Toxicol Pathol*. 2016;68(7):381-390.
451. Naz F, Koul V, Srivastava A, Gupta YK, Dinda AK. Biokinetics of ultrafine gold nanoparticles (AuNPs) relating to redistribution and urinary excretion: a long-term in vivo study. *Journal of drug targeting*. 2016;24(8):720-729.
452. Bailly AL, Correard F, Popov A, et al. In vivo evaluation of safety, biodistribution and pharmacokinetics of laser-synthesized gold nanoparticles. *Scientific reports*. 2019;9(1):12890.
453. Yang L, Kuang H, Zhang W, Aguilar ZP, Wei H, Xu H. Comparisons of the biodistribution and toxicological examinations after repeated intravenous administration of silver and gold nanoparticles in mice. *Scientific reports*. 2017;7(1):3303.
454. Rambanapasi C, Zeevaert JR, Bunting H, et al. Bioaccumulation and Subchronic Toxicity of 14 nm Gold Nanoparticles in Rats. *Molecules*. 2016;21(6).

## References

455. Lasagna-Reeves C, Gonzalez-Romero D, Barria MA, et al. Bioaccumulation and toxicity of gold nanoparticles after repeated administration in mice. *Biochem Biophys Res Commun*. 2010;393(4):649-655.
456. Senut MC, Zhang Y, Liu F, Sen A, Ruden DM, Mao G. Size-Dependent Toxicity of Gold Nanoparticles on Human Embryonic Stem Cells and Their Neural Derivatives. *Small (Weinheim an der Bergstrasse, Germany)*. 2016;12(5):631-646.
457. Li X, Hu Z, Ma J, et al. The systematic evaluation of size-dependent toxicity and multi-time biodistribution of gold nanoparticles. *Colloids Surf B Biointerfaces*. 2018;167:260-266.
458. Coradeghini R, Gioria S, Garcia CP, et al. Size-dependent toxicity and cell interaction mechanisms of gold nanoparticles on mouse fibroblasts. *Toxicol Lett*. 2013;217(3):205-216.
459. Soenen SJ, Rivera-Gil P, Montenegro J-M, Parak WJ, De Smedt SC, Braeckmans K. Cellular toxicity of inorganic nanoparticles: Common aspects and guidelines for improved nanotoxicity evaluation. *Nano Today*. 2011;6(5):446-465.
460. Wan J, Wang J-H, Liu T, Xie Z, Yu X-F, Li W. Surface chemistry but not aspect ratio mediates the biological toxicity of gold nanorods in vitro and in vivo. *Scientific reports*. 2015;5(1):11398.
461. Khlebtsov N, Dykman L. Biodistribution and toxicity of engineered gold nanoparticles: a review of in vitro and in vivo studies. *Chem Soc Rev*. 2011;40(3):1647-1671.
462. Sadauskas E, Danscher G, Stoltenberg M, Vogel U, Larsen A, Wallin H. Protracted elimination of gold nanoparticles from mouse liver. *Nanomedicine : nanotechnology, biology, and medicine*. 2009;5(2):162-169.
463. Fraga S, Brandao A, Soares ME, et al. Short- and long-term distribution and toxicity of gold nanoparticles in the rat after a single-dose intravenous administration. *Nanomedicine : nanotechnology, biology, and medicine*. 2014;10(8):1757-1766.
464. Stohrer M, Boucher Y, Stangassinger M, Jain RK. Oncotic Pressure in Solid Tumors Is Elevated. 2000;60(15):4251-4255.
465. Hua S, de Matos MBC, Metselaar JM, Storm G. Current Trends and Challenges in the Clinical Translation of Nanoparticulate Nanomedicines: Pathways for Translational Development and Commercialization. *Front Pharmacol*. 2018;9:790.
466. Soares S, Sousa J, Pais A, Vitorino C. Nanomedicine: Principles, Properties, and Regulatory Issues. *Front Chem*. 2018;6:360.
467. Agency EM. *Reflection paper on the data requirements for intravenous iron-based nano-colloidal products developed with reference to an innovator medicinal product*. London, United Kingdom 2015.
468. Agency EM. *Reflection paper on the data requirements for intravenous liposomal products developed with reference to an innovator liposomal product*. London, United Kingdom 2013. EMA/CHMP/806058/2009/Rev. 02.
469. Agency EM. *Joint MHLW/EMA reflection paper on the development of block copolymer micelle medicinal products*. London, United Kingdom 2013.
470. Agency EM. *Reflection paper on surface coatings: general issues for consideration regarding parenteral administration of coated nanomedicine products*. London, United Kingdom 2013.
471. Moreau N, Michiels C, Masereel B, et al. PVD Synthesis and Transfer into Water-Based Solutions of Functionalized Gold Nanoparticles. *Plasma Processes and Polymers*. 2009;6:S888-892.
472. Masereel B, Dinguizli M, Bouzin C, et al. Antibody immobilization on gold nanoparticles coated layer-by-layer with polyelectrolytes. *Journal of Nanoparticle Research*. 2011;13(4):1573-1580.
473. Koçak A. *MATERIALS SCIENCE AND ENGINEERING #Thin Film Preparation, Particle Size and Thickness Analysis Experimental Report*. 2018.
474. Marega R, Karmani L, Flamant L. Antibody-functionalized polymer-coated gold nanoparticles targeting cancer cells: an in vitro and in vivo study. *J Mater Chem*. 2012;22(21305):21305-21312.
475. Chidharla A, Parsi M, Kasi A. Cetuximab. In: *StatPearls*. Treasure Island (FL) 2020.
476. Galizia G, Lieto E, De Vita F, et al. Cetuximab, a chimeric human mouse anti-epidermal growth factor receptor monoclonal antibody, in the treatment of human colorectal cancer. *Oncogene*. 2007;26(25):3654-3660.
477. Wieduwilt MJ, Moasser MM. The epidermal growth factor receptor family: biology driving targeted therapeutics. *Cellular and molecular life sciences : CMLS*. 2008;65(10):1566-1584.
478. Mendelsohn J, Baselga J. Status of epidermal growth factor receptor antagonists in the biology and treatment of cancer. *Journal of clinical oncology : official journal of the American Society of Clinical Oncology*. 2003;21(14):2787-2799.
479. Blick SK, Scott LJ. Cetuximab: a review of its use in squamous cell carcinoma of the head and neck and metastatic colorectal cancer. *Drugs*. 2007;67(17):2585-2607.

480. Dash A, Pillai MR, Knapp FF, Jr. Production of (177)Lu for Targeted Radionuclide Therapy: Available Options. *Nucl Med Mol Imaging*. 2015;49(2):85-107.
481. Zhang X. Gold Nanoparticles: Recent Advances in the Biomedical Applications. *Cell biochemistry and biophysics*. 2015;72(3):771-775.
482. Chang MY, Shiau AL, Chen YH, Chang CJ, Chen HH, Wu CL. Increased apoptotic potential and dose-enhancing effect of gold nanoparticles in combination with single-dose clinical electron beams on tumor-bearing mice. *Cancer science*. 2008;99(7):1479-1484.
483. de Barros AB, Tsourkas A, Saboury B, Cardoso VN, Alavi A. Emerging role of radiolabeled nanoparticles as an effective diagnostic technique. *EJNMMI research*. 2012;2(1):39.
484. Popovtzer R, Agrawal A, Kotov NA, et al. Targeted gold nanoparticles enable molecular CT imaging of cancer. *Nano letters*. 2008;8(12):4593-4596.
485. Reuveni T, Motiei M, Romman Z, Popovtzer A, Popovtzer R. Targeted gold nanoparticles enable molecular CT imaging of cancer: an in vivo study. *International journal of nanomedicine*. 2011;6:2859-2864.
486. Bhattacharyya S, Bhattacharya R, Curley S, McNiven MA, Mukherjee P. Nanoconjugation modulates the trafficking and mechanism of antibody induced receptor endocytosis. *Proceedings of the National Academy of Sciences of the United States of America*. 2010;107(33):14541-14546.
487. Kudgus RA, Walden CA, McGovern RM, Reid JM, Robertson JD, Mukherjee P. Tuning pharmacokinetics and biodistribution of a targeted drug delivery system through incorporation of a passive targeting component. *Scientific reports*. 2014;4:5669.
488. Karmani L, Bouchat V, Bouzin C, et al. (89)Zr-labeled anti-endoglin antibody-targeted gold nanoparticles for imaging cancer: implications for future cancer therapy. *Nanomedicine (London, England)*. 2014;9(13):1923-1937.
489. Qian Y, Qiu M, Wu Q, et al. Enhanced cytotoxic activity of cetuximab in EGFR-positive lung cancer by conjugating with gold nanoparticles. *Scientific reports*. 2014;4:7490.
490. Sonavane G, Tomoda K, Makino K. Biodistribution of colloidal gold nanoparticles after intravenous administration: effect of particle size. *Colloids Surf B Biointerfaces*. 2008;66(2):274-280.
491. Hirn S, Semmler-Behnke M, Schleh C, et al. Particle size-dependent and surface charge-dependent biodistribution of gold nanoparticles after intravenous administration. *Eur J Pharm Biopharm*. 2011;77(3):407-416.
492. De Jong WH, Hagens WI, Krystek P, Burger MC, Sips AJ, Geertsma RE. Particle size-dependent organ distribution of gold nanoparticles after intravenous administration. *Biomaterials*. 2008;29(12):1912-1919.
493. Huang K, Ma H, Liu J, et al. Size-dependent localization and penetration of ultrasmall gold nanoparticles in cancer cells, multicellular spheroids, and tumors in vivo. *ACS nano*. 2012;6(5):4483-4493.
494. Huo S, Ma H, Huang K, et al. Superior penetration and retention behavior of 50 nm gold nanoparticles in tumors. *Cancer research*. 2013;73(1):319-330.
495. England CG, Huang JS, James KT, Zhang G, Gobin AM, Frieboes HB. Detection of Phosphatidylcholine-Coated Gold Nanoparticles in Orthotopic Pancreatic Adenocarcinoma using Hyperspectral Imaging. *PLoS one*. 2015;10(6):e0129172.
496. Abdelhalim MA, Jarrar BM. The appearance of renal cells cytoplasmic degeneration and nuclear destruction might be an indication of GNPs toxicity. *Lipids Health Dis*. 2011;10:147.
497. Abdelhalim MA, Jarrar BM. Renal tissue alterations were size-dependent with smaller ones induced more effects and related with time exposure of gold nanoparticles. *Lipids Health Dis*. 2011;10:163.
498. Gharatape A, Salehi R. Recent progress in theranostic applications of hybrid gold nanoparticles. *Eur J Med Chem*. 2017;138:221-233.
499. Ng CT, Li JJ, Gurung RL, et al. Toxicological profile of small airway epithelial cells exposed to gold nanoparticles. *Exp Biol Med (Maywood)*. 2013;238(12):1355-1361.
500. Li JJ, Hartono D, Ong CN, Bay BH, Yung LY. Autophagy and oxidative stress associated with gold nanoparticles. *Biomaterials*. 2010;31(23):5996-6003.
501. Chen YS, Hung YC, Liao I, Huang GS. Assessment of the In Vivo Toxicity of Gold Nanoparticles. *Nanoscale Res Lett*. 2009;4(8):858-864.
502. Terentyuk GS, Maslyakova GN, Suleymanova LV, et al. Circulation and distribution of gold nanoparticles and induced alterations of tissue morphology at intravenous particle delivery. *J Biophotonics*. 2009;2(5):292-302.
503. Gosens I, Post JA, de la Fonteyne LJ, et al. Impact of agglomeration state of nano- and submicron sized gold particles on pulmonary inflammation. *Particle and fibre toxicology*. 2010;7(1):37.



## References

504. Abdelhalim MA, Jarrar BM. Gold nanoparticles induced cloudy swelling to hydropic degeneration, cytoplasmic hyaline vacuolation, polymorphism, binucleation, karyopyknosis, karyolysis, karyorrhexis and necrosis in the liver. *Lipids Health Dis.* 2011;10:166.
505. Shukla R, Bansal V, Chaudhary M, Basu A, Bhonde RR, Sastry M. Biocompatibility of gold nanoparticles and their endocytotic fate inside the cellular compartment: a microscopic overview. *Langmuir.* 2005;21(23):10644-10654.
506. Alkilany AM, Murphy CJ. Toxicity and cellular uptake of gold nanoparticles: what we have learned so far? *Journal of nanoparticle research : an interdisciplinary forum for nanoscale science and technology.* 2010;12(7):2313-2333.
507. Connor EE, Mwamuka J, Gole A, Murphy CJ, Wyatt MD. Gold nanoparticles are taken up by human cells but do not cause acute cytotoxicity. *Small (Weinheim an der Bergstrasse, Germany).* 2005;1(3):325-327.
508. Ortega MT, Riviere JE, Choi K, Monteiro-Riviere NA. Biocorona formation on gold nanoparticles modulates human proximal tubule kidney cell uptake, cytotoxicity and gene expression. *Toxicology in vitro : an international journal published in association with BIBRA.* 2017;42:150-160.
509. Choi K, Riviere JE, Monteiro-Riviere NA. Protein corona modulation of hepatocyte uptake and molecular mechanisms of gold nanoparticle toxicity. *Nanotoxicology.* 2017;11(1):64-75.
510. Freese C, Gibson MI, Klok HA, Unger RE, Kirkpatrick CJ. Size- and coating-dependent uptake of polymer-coated gold nanoparticles in primary human dermal microvascular endothelial cells. *Biomacromolecules.* 2012;13(5):1533-1543.
511. Wang JY, Chen J, Yang J, et al. Effects of surface charges of gold nanoclusters on long-term in vivo biodistribution, toxicity, and cancer radiation therapy. *International journal of nanomedicine.* 2016;11:3475-3485.
512. Gunduz N, Ceylan H, Guler MO, Tekinay AB. Intracellular Accumulation of Gold Nanoparticles Leads to Inhibition of Macropinocytosis to Reduce the Endoplasmic Reticulum Stress. *Scientific reports.* 2017;7:40493.
513. Longmire M, Choyke PL, Kobayashi H. Clearance properties of nano-sized particles and molecules as imaging agents: considerations and caveats. *Nanomedicine (London, England).* 2008;3(5):703-717.
514. Satorius. Product Guide: Incucyte® Annexin V Reagents. 2020; <https://www.essenbioscience.com/media/uploads/files/Incucyte-Annexin-V-Reagents-Product-Guide-en-8000-0730-A00.pdf>.
515. Satorius. Product Guide: Incucyte® Caspase-3/ 7 Reagents. 2020; <https://www.essenbioscience.com/media/uploads/files/Incucyte-Caspase-3-7-Reagents-en-8000-0729-A00.pdf>.
516. Sigma-Aldrich. Technical Bulletin: Thiorodoxin Reductase Assay Kit (CS0170). 2019; <https://www.sigmaaldrich.com/content/dam/sigma-aldrich/docs/Sigma/Bulletin/1/cs0170bul.pdf>.
517. Abcam. Glutathione Reductase (GR) Assay Kit: Instructions for Use (ab83461). 2019; [https://www.abcam.com/ps/products/83/ab83461/documents/ab83461%20Glutathione%20Reductas%20GR%20Assay%20Kit%20Protocol%20v5a%20\(website\).pdf](https://www.abcam.com/ps/products/83/ab83461/documents/ab83461%20Glutathione%20Reductas%20GR%20Assay%20Kit%20Protocol%20v5a%20(website).pdf).
518. Zafarullah M, Li WQ, Sylvester J, Ahmad M. Molecular mechanisms of N-acetylcysteine actions. *Cellular and molecular life sciences : CMLS.* 2003;60(1):6-20.
519. Aruoma OI, Halliwell B, Hoey BM, Butler J. The antioxidant action of N-acetylcysteine: its reaction with hydrogen peroxide, hydroxyl radical, superoxide, and hypochlorous acid. *Free radical biology & medicine.* 1989;6(6):593-597.
520. Garcia-Fernandez L, Garcia-Pardo J, Tort O, et al. Conserved effects and altered trafficking of Cetuximab antibodies conjugated to gold nanoparticles with precise control of their number and orientation. *Nanoscale.* 2017;9(18):6111-6121.
521. Chithrani BD, Ghazani AA, Chan WC. Determining the size and shape dependence of gold nanoparticle uptake into mammalian cells. *Nano letters.* 2006;6(4):662-668.
522. Hewlett LJ, Prescott AR, Watts C. The coated pit and macropinocytic pathways serve distinct endosome populations. *J Cell Biol.* 1994;124(5):689-703.
523. Hamasaki M, Araki N, Hatae T. Association of early endosomal autoantigen 1 with macropinocytosis in EGF-stimulated A431 cells. *Anat Rec A Discov Mol Cell Evol Biol.* 2004;277(2):298-306.
524. Fede C, Fortunati I, Weber V, et al. Evaluation of gold nanoparticles toxicity towards human endothelial cells under static and flow conditions. *Microvascular research.* 2015;97:147-155.
525. Cheng MJ, Kumar R, Sridhar S, Webster TJ, Ebong EE. Endothelial glycocalyx conditions influence nanoparticle uptake for passive targeting. *International journal of nanomedicine.* 2016;11:3305-3315.
526. Wang Z, Tiruppathi C, Cho J, Minshall RD, Malik AB. Delivery of nanoparticle: complexed drugs across the vascular endothelial barrier via caveolae. *IUBMB Life.* 2011;63(8):659-667.

527. Martinez-Torres AC, Zarate-Trivino DG, Lorenzo-Anota HY, Avila-Avila A, Rodriguez-Abrego C, Rodriguez-Padilla C. Chitosan gold nanoparticles induce cell death in HeLa and MCF-7 cells through reactive oxygen species production. *International journal of nanomedicine*. 2018;13:3235-3250.
528. Zhang F, Zhu X, Gong J, et al. Lysosome-mitochondria-mediated apoptosis specifically evoked in cancer cells induced by gold nanorods. *Nanomedicine (London, England)*. 2016;11(15):1993-2006.
529. Kondath S, Srinivas Raghavan B, Anantanarayanan R, Rajaram R. Synthesis and characterisation of morin reduced gold nanoparticles and its cytotoxicity in MCF-7 cells. *Chem Biol Interact*. 2014;224:78-88.
530. Alex SA, Rajiv S, Chakravarty S, Chandrasekaran N, Mukherjee A. Significance of surface functionalization of Gold Nanorods for reduced effect on IgG stability and minimization of cytotoxicity. *Mater Sci Eng C Mater Biol Appl*. 2017;71:744-754.
531. Choi SY, Jeong S, Jang SH, et al. In vitro toxicity of serum protein-adsorbed citrate-reduced gold nanoparticles in human lung adenocarcinoma cells. *Toxicology in vitro : an international journal published in association with BIBRA*. 2012;26(2):229-237.
532. Dragoni S, Franco G, Regoli M, et al. Gold nanoparticles uptake and cytotoxicity assessed on rat liver precision-cut slices. *Toxicol Sci*. 2012;128(1):186-197.
533. Yang Y, Nan J, Hou J, et al. Cytotoxicity of gold nanoclusters in human liver cancer cells. *International journal of nanomedicine*. 2014;9:5441-5448.
534. Brown DM, Johnston H, Gubbins E, Stone V. Cytotoxicity and cytokine release in rat hepatocytes, C3A cells and macrophages exposed to gold nanoparticles--effect of biological dispersion media or corona. *J Biomed Nanotechnol*. 2014;10(11):3416-3429.
535. Zhang XQ, Xu X, Bertrand N, Pridgen E, Swami A, Farokhzad OC. Interactions of nanomaterials and biological systems: Implications to personalized nanomedicine. *Adv Drug Deliv Rev*. 2012;64(13):1363-1384.
536. Yang Y, Ren L, Wang H. Strategies in the design of gold nanoparticles for intracellular targeting: opportunities and challenges. *Ther Deliv*. 2017;8(10):879-897.
537. Penninckx S, Heuskin AC, Michiels C, Lucas S. Thioredoxin Reductase Activity Predicts Gold Nanoparticle Radiosensitization Effect. *Nanomaterials (Basel)*. 2019;9(2).
538. Dunn LL, Buckle AM, Cooke JP, Ng MK. The emerging role of the thioredoxin system in angiogenesis. *Arterioscler Thromb Vasc Biol*. 2010;30(11):2089-2098.
539. Huang Q, Zhou HJ, Zhang H, et al. Thioredoxin-2 inhibits mitochondrial reactive oxygen species generation and apoptosis stress kinase-1 activity to maintain cardiac function. *Circulation*. 2015;131(12):1082-1097.
540. Zorov DB, Juhaszova M, Sollott SJ. Mitochondrial ROS-induced ROS release: an update and review. *Biochimica et biophysica acta*. 2006;1757(5-6):509-517.
541. Mateo D, Morales P, Avalos A, Haza AI. Comparative cytotoxicity evaluation of different size gold nanoparticles in human dermal fibroblasts. *Journal of Experimental Nanoscience*. 2015;10(18):1401-1417.
542. Ghita M, McMahon SJ, Taggart LE, Butterworth KT, Schettino G, Prise KM. A mechanistic study of gold nanoparticle radiosensitisation using targeted microbeam irradiation. *Scientific reports*. 2017;7:44752.
543. Popovtzer R. Foreword. Biomedical applications of gold nanomaterials. *Nanomedicine (London, England)*. 2014;9(13):1903-1904.
544. Daems N, Penninckx S, Nelissen I, et al. Gold nanoparticles affect the antioxidant status in selected normal human cells. *International journal of nanomedicine*. 2019;14:4991-5015.
545. Zhang XD, Wu D, Shen X, et al. Size-dependent in vivo toxicity of PEG-coated gold nanoparticles. *International journal of nanomedicine*. 2011;6:2071-2081.
546. Lopez-Chaves C, Soto-Alvaredo J, Montes-Bayon M, Bettmer J, Llopis J, Sanchez-Gonzalez C. Gold nanoparticles: Distribution, bioaccumulation and toxicity. In vitro and in vivo studies. *Nanomedicine : nanotechnology, biology, and medicine*. 2018;14(1):1-12.
547. Sigma-Aldrich. Technical Bulletin: Aspartate Aminotransferase (AST) Activity Assay (MAK055). 2017; <https://www.sigmaaldrich.com/content/dam/sigma-aldrich/docs/Sigma/Bulletin/1/mak055bul.pdf>.
548. Sigma-Aldrich. Technical Bulletin: Alanine Aminotransferase Activity Assay Kit (MAK052). 2017; <https://www.sigmaaldrich.com/content/dam/sigma-aldrich/docs/Sigma/Bulletin/1/mak052bul.pdf>.
549. Sigma-Aldrich. Technical Bulletin: g-Glutamyltransferase (GGT) Activity Colorimetric Assay Kit (MAK089). 2017; <https://www.sigmaaldrich.com/content/dam/sigma-aldrich/docs/Sigma/Bulletin/1/mak089bul.pdf>.
550. Sigma-Aldrich. Technical Bulletin: Alkaline Phosphatase, Diethanolamine Detection Kit (AP0100). 2017; <https://www.sigmaaldrich.com/content/dam/sigma-aldrich/docs/Sigma/Bulletin/1/ap0100bul.pdf>.

## References

551. R&Dsystems. How to Run an R&D Systems Luminex® Assay. *Magnetic Luminex Assay: Mouse Premixed Multi-analyte Kit* 2019; <https://www.rndsystems.com/resources/protocols/how-run-rd-systems-luminex-assay>.
552. Del Monte U. Does the cell number 109 still really fit one gram of tumor tissue? *Cell Cycle*. 2009;8(3):505-506.
553. Li B, Lane LA. Probing the biological obstacles of nanomedicine with gold nanoparticles. *Wiley interdisciplinary reviews Nanomedicine and nanobiotechnology*. 2019;11(3):e1542.
554. Taylor U, Rehbock C, Streich C, Rath D, Barcikowski S. Rational design of gold nanoparticle toxicology assays: a question of exposure scenario, dose and experimental setup. *Nanomedicine (London, England)*. 2014;9(13):1971-1989.
555. Bednarski M, Dudek M, Knutelska J, et al. The influence of the route of administration of gold nanoparticles on their tissue distribution and basic biochemical parameters: In vivo studies. *Pharmacol Rep*. 2015;67(3):405-409.
556. Alalaiwe A, Roberts G, Carpinone P, Munson J, Roberts S. Influence of PEG coating on the oral bioavailability of gold nanoparticles in rats. *Drug Deliv*. 2017;24(1):591-598.
557. Campbell JL, SoRelle ED, Ilovich O, et al. Multimodal assessment of SERS nanoparticle biodistribution post ingestion reveals new potential for clinical translation of Raman imaging. *Biomaterials*. 2017;135:42-52.
558. Arvizo RR, Miranda OR, Moyano DF, et al. Modulating pharmacokinetics, tumor uptake and biodistribution by engineered nanoparticles. *PloS one*. 2011;6(9):e24374.
559. Sadauskas E, Wallin H, Stoltenberg M, et al. Kupffer cells are central in the removal of nanoparticles from the organism. *Particle and fibre toxicology*. 2007;4:10.
560. Kao HW, Lin YY, Chen CC, et al. Biological characterization of cetuximab-conjugated gold nanoparticles in a tumor animal model. *Nanotechnology*. 2014;25(29):295102.
561. Niidome T, Yamagata M, Okamoto Y, et al. PEG-modified gold nanorods with a stealth character for in vivo applications. *Journal of controlled release : official journal of the Controlled Release Society*. 2006;114(3):343-347.
562. Lipka J, Semmler-Behnke M, Sperling RA, et al. Biodistribution of PEG-modified gold nanoparticles following intratracheal instillation and intravenous injection. *Biomaterials*. 2010;31(25):6574-6581.
563. You J, Zhou J, Zhou M, et al. Pharmacokinetics, clearance, and biosafety of polyethylene glycol-coated hollow gold nanospheres. *Particle and fibre toxicology*. 2014;11:26.
564. Bogdanov AA, Jr., Gupta S, Koshkina N, et al. Gold nanoparticles stabilized with MPEG-grafted poly(l-lysine): in vitro and in vivo evaluation of a potential theranostic agent. *Bioconjugate chemistry*. 2015;26(1):39-50.
565. Alfranca G, Beola L, Liu Y, et al. In vivo comparison of the biodistribution and long-term fate of colloids - gold nanoprisms and nanorods - with minimum surface modification. *Nanomedicine (London, England)*. 2019.
566. Aborig M, Malik PRV, Nambiar S, et al. Biodistribution and Physiologically-Based Pharmacokinetic Modeling of Gold Nanoparticles in Mice with Interspecies Extrapolation. *Pharmaceutics*. 2019;11(4).
567. McGill MR, Williams CD, Xie Y, Ramachandran A, Jaeschke H. Acetaminophen-induced liver injury in rats and mice: comparison of protein adducts, mitochondrial dysfunction, and oxidative stress in the mechanism of toxicity. *Toxicol Appl Pharmacol*. 2012;264(3):387-394.
568. James LP, McCullough SS, Lamps LW, Hinson JA. Effect of N-acetylcysteine on acetaminophen toxicity in mice: relationship to reactive nitrogen and cytokine formation. *Toxicol Sci*. 2003;75(2):458-467.
569. Lopez-Chaves C, Soto-Alvaredo J, Montes-Bayon M, Bettmer J, Llopis J, Sanchez-Gonzalez C. Gold nanoparticles: Distribution, bioaccumulation and toxicity. In vitro and in vivo studies. *Nanomedicine : nanotechnology, biology, and medicine*. 2017.
570. Dam DH, Culver KS, Kandela I, et al. Biodistribution and in vivo toxicity of aptamer-loaded gold nanostars. *Nanomedicine : nanotechnology, biology, and medicine*. 2015;11(3):671-679.
571. Le QL, Linh Do TP, Nguyen HPU, Dang VP, Nguyen QH. Biodistribution of gold nanoparticles synthesized by  $\gamma$ -irradiation after intravenous administration in mice. *Advances in Natural Sciences: Nanoscience and Nanotechnology*. 2014;5(2):025009.
572. Eggers KM, Kempf T, Lind L, et al. Relations of growth-differentiation factor-15 to biomarkers reflecting vascular pathologies in a population-based sample of elderly subjects. *Scand J Clin Lab Invest*. 2012;72(1):45-51.
573. Ibrahim KE, Bakhiet AO, Awadalla ME, Khan HA. A priming dose protects against gold nanoparticles-induced proinflammatory cytokines mRNA expression in mice. *Nanomedicine (London, England)*. 2018;13(3):313-323.

574. Simpson CA, Salleng KJ, Cliffl DE, Feldheim DL. In vivo toxicity, biodistribution, and clearance of glutathione-coated gold nanoparticles. *Nanomedicine : nanotechnology, biology, and medicine*. 2013;9(2):257-263.
575. Uchiyama MK, Deda DK, Rodrigues SF, et al. In vivo and in vitro toxicity and anti-inflammatory properties of gold nanoparticle bioconjugates to the vascular system. *Toxicol Sci*. 2014;142(2):497-507.
576. Victora GD. SnapShot: the germinal center reaction. *Cell*. 2014;159(3):700-700 e701.
577. Zhang XD, Wu HY, Wu D, et al. Toxicologic effects of gold nanoparticles in vivo by different administration routes. *International journal of nanomedicine*. 2010;5:771-781.
578. Adewale OB, Davids H, Cairncross L, Roux S. Toxicological Behavior of Gold Nanoparticles on Various Models: Influence of Physicochemical Properties and Other Factors. *Int J Toxicol*. 2019;38(5):357-384.
579. Harper SL, Carriere JL, Miller JM, Hutchison JE, Maddux BL, Tanguay RL. Systematic evaluation of nanomaterial toxicity: utility of standardized materials and rapid assays. *ACS nano*. 2011;5(6):4688-4697.
580. Puvanakrishnan P, Park J, Chatterjee D, Krishnan S, Tunnell JW. In vivo tumor targeting of gold nanoparticles: effect of particle type and dosing strategy. *International journal of nanomedicine*. 2012;7:1251-1258.
581. Weaver JL, Tobin GA, Ingle T, et al. Evaluating the potential of gold, silver, and silica nanoparticles to saturate mononuclear phagocytic system tissues under repeat dosing conditions. *Particle and fibre toxicology*. 2017;14(1):25.
582. EMA/506460/2017 EMA. LUTATHERA International non-proprietary name: lutetium (177lu) oxodotreotide. 2017; [https://www.ema.europa.eu/en/documents/assessment-report/lutathera-epar-public-assessment-report\\_en.pdf](https://www.ema.europa.eu/en/documents/assessment-report/lutathera-epar-public-assessment-report_en.pdf). Accessed 14-04-2020.
583. Strosberg J, El-Haddad G, Wolin E, et al. Phase 3 Trial of (177)Lu-Dotatate for Midgut Neuroendocrine Tumors. *The New England journal of medicine*. 2017;376(2):125-135.
584. Strosberg J, Wolin E, Chasen B, et al. Health-Related Quality of Life in Patients With Progressive Midgut Neuroendocrine Tumors Treated With (177)Lu-Dotatate in the Phase III NETTER-1 Trial. *Journal of clinical oncology : official journal of the American Society of Clinical Oncology*. 2018;36(25):2578-2584.
585. Hein P, Michel MC, Leineweber K, Wieland T, Wettschureck N, Offermanns S. Receptor and Binding Studies. In: Dhein S, Mohr FW, Delmar M, eds. *Practical Methods in Cardiovascular Research*. Berlin, Heidelberg: Springer Berlin Heidelberg; 2005:723-783.
586. Jurcic JG, Wong JYC, Knox SJ, Wahl DR, Rosenblat TL, Meredith RF. Chapter 22 - Targeted Radionuclide Therapy. In: Gunderson LL, Tepper JE, eds. *Clinical Radiation Oncology (Fourth Edition)*. Philadelphia: Elsevier; 2016:399-418.e314.
587. Boswell CA, Brechbiel MW. Development of radioimmunotherapeutic and diagnostic antibodies: an inside-out view. *Nucl Med Biol*. 2007;34(7):757-778.
588. Navarro-Teulon I, Lozza C, Pelegrin A, Vives E, Pouget JP. General overview of radioimmunotherapy of solid tumors. *Immunotherapy*. 2013;5(5):467-487.
589. Martins CD, Kramer-Marek G, Oyen WJG. Radioimmunotherapy for delivery of cytotoxic radioisotopes: current status and challenges. *Expert Opin Drug Deliv*. 2018;15(2):185-196.
590. D'Huyvetter M, Aerts A, Xavier C, et al. Development of 177Lu-nanobodies for radioimmunotherapy of HER2-positive breast cancer: evaluation of different bifunctional chelators. *Contrast media & molecular imaging*. 2012;7(2):254-264.
591. Guleria M, Das T, Kumar C, et al. Effect of Number of Bifunctional Chelating Agents on the Pharmacokinetics and Immunoreactivity of 177Lu-labeled Rituximab: A Systemic Study. *Anticancer Agents Med Chem*. 2018;18(1):146-153.
592. Forrer F, Chen J, Fani M, et al. In vitro characterization of (177)Lu-radiolabelled chimeric anti-CD20 monoclonal antibody and a preliminary dosimetry study. *European journal of nuclear medicine and molecular imaging*. 2009;36(9):1443-1452.
593. Daems N, Verlinden B, Van Hoecke K, et al. In vivo pharmacokinetics, biodistribution and toxicity of antibody-conjugated gold nanoparticles in healthy mice. *Journal of Biomedical Nanotechnology (Accepted)*. 2020.
594. Xia Q, Huang J, Feng Q, et al. Size- and cell type-dependent cellular uptake, cytotoxicity and in vivo distribution of gold nanoparticles. *International journal of nanomedicine*. 2019;14:6957-6970.
595. Nicol JR, Harrison E, O'Neill SM, Dixon D, McCarthy HO, Coulter JA. Unraveling the cell-type dependent radiosensitizing effects of gold through the development of a multifunctional gold nanoparticle. *Nanomedicine: Nanotechnology, Biology and Medicine*. 2018;14(2):439-449.
596. Patra CR, Bhattacharya R, Mukherjee P. Fabrication and functional characterization of goldnanoconjugates for potential application in ovarian cancer. *Journal of materials chemistry*. 2010;20(3):547-554.

## References

597. Ryan MJ, Johnson G, Kirk J, Fuerstenberg SM, Zager RA, Torok-Storb B. HK-2: an immortalized proximal tubule epithelial cell line from normal adult human kidney. *Kidney Int.* 1994;45(1):48-57.
598. Venetsanakos E, Mirza A, Fanton C, Romanov SR, Tlsty T, McMahon M. Induction of tubulogenesis in telomerase-immortalized human microvascular endothelial cells by glioblastoma cells. *Experimental cell research.* 2002;273(1):21-33.
599. Pfeifer AM, Cole KE, Smoot DT, et al. Simian virus 40 large tumor antigen-immortalized normal human liver epithelial cells express hepatocyte characteristics and metabolize chemical carcinogens. *Proceedings of the National Academy of Sciences of the United States of America.* 1993;90(11):5123-5127.
600. Gromnicova R, Kaya M, Romero IA, et al. Transport of Gold Nanoparticles by Vascular Endothelium from Different Human Tissues. *PLoS one.* 2016;11(8):e0161610.
601. Nakamura H, Masutani H, Yodoi J. Extracellular thioredoxin and thioredoxin-binding protein 2 in control of cancer. *Seminars in cancer biology.* 2007;16:444-451.
602. Ebrahimi T, Touyz RM. Thioredoxin in vascular biology: role in hypertension. *Antioxidants & redox signaling.* 2008;10(6):1127-1136.
603. Schmidt D, Textor B, Pein OT, et al. Critical role for NF-kappaB-induced JunB in VEGF regulation and tumor angiogenesis. *EMBO J.* 2007;26(3):710-719.
604. Forman HJ, Zhang H, Rinna A. Glutathione: overview of its protective roles, measurement, and biosynthesis. *Mol Aspects Med.* 2009;30(1-2):1-12.
605. Du Y, Zhang H, Lu J, Holmgren A. Glutathione and glutaredoxin act as a backup of human thioredoxin reductase 1 to reduce thioredoxin 1 preventing cell death by aurothioglucose. *J Biol Chem.* 2012;287(45):38210-38219.
606. Lu J, Holmgren A. The thioredoxin antioxidant system. *Free Radical Biology and Medicine.* 2014;66:75-87.
607. Branco V, Coppo L, Solá S, et al. Impaired cross-talk between the thioredoxin and glutathione systems is related to ASK-1 mediated apoptosis in neuronal cells exposed to mercury. *Redox Biology.* 2017;13:278-287.
608. Ouyang Y, Peng Y, Li J, Holmgren A, Lu J. Modulation of thiol-dependent redox system by metal ions via thioredoxin and glutaredoxin systems. *Metallomics.* 2018;10(2):218-228.
609. Kasaikina MV, Hatfield DL, Gladyshev VN. Understanding selenoprotein function and regulation through the use of rodent models. *Biochimica et biophysica acta.* 2012;1823(9):1633-1642.
610. Shchedrina VA, Zhang Y, Labunskyy VM, Hatfield DL, Gladyshev VN. Structure-function relations, physiological roles, and evolution of mammalian ER-resident selenoproteins. *Antioxidants & redox signaling.* 2010;12(7):839-849.
611. Pitts MW, Hoffmann PR. Endoplasmic reticulum-resident selenoproteins as regulators of calcium signaling and homeostasis. *Cell Calcium.* 2018;70:76-86.
612. Liu H, Xu H, Huang K. Selenium in the prevention of atherosclerosis and its underlying mechanisms. *Metallomics.* 2017;9(1):21-37.
613. Mangiapane E, Pessione A, Pessione E. Selenium and Selenoproteins: An Overview on Different Biological Systems. *Current protein & peptide science.* 2014;15.
614. Labunskyy VM, Hatfield DL, Gladyshev VN. Selenoproteins: molecular pathways and physiological roles. *Physiol Rev.* 2014;94(3):739-777.
615. Bhabak KP, Muges G. A Synthetic Model for the Inhibition of Glutathione Peroxidase by Antiarthritic Gold Compounds. *Inorganic Chemistry.* 2009;48(6):2449-2455.
616. Chaudiere J, Tappel AL. Interaction of gold(I) with the active site of selenium-glutathione peroxidase. *J Inorg Biochem.* 1984;20(4):313-325.
617. Liu M, Gao L, Zhao L, et al. Peptide-Au Clusters Induced Tumor Cells Apoptosis via Targeting Glutathione Peroxidase-1: The Molecular Dynamics Assisted Experimental Studies. *Scientific reports.* 2017;7(1):131.
618. Radenkovic F, Holland O, Vanderlelie JJ, Perkins AV. Selective inhibition of endogenous antioxidants with Auranofin causes mitochondrial oxidative stress which can be countered by selenium supplementation. *Biochemical pharmacology.* 2017;146:42-52.
619. Gandin V, Fernandes AP. Metal- and Semimetal-Containing Inhibitors of Thioredoxin Reductase as Anticancer Agents. 2015;20(7):12732-12756.
620. Ghita M, McMahon B, Taggart LE, Butterworth KT, Schettino G, Prise KM. A mechanistic study of gold nanoparticle radiosensitisation using targeted microbeam irradiation. *Scientific reports.* 2017;7( 44752).
621. Gholami YH, Maschmeyer R, Kuncic Z. Radio-enhancement effects by radiolabeled nanoparticles. *Scientific reports.* 2019;9(1):14346.

622. Lincoln DT, Ali Emadi EM, Tonissen KF, Clarke FM. The thioredoxin-thioredoxin reductase system: over-expression in human cancer. *Anticancer research*. 2003;23(3b):2425-2433.
623. Powis G, Wipf P, Lynch SM, Birmingham A, Kirkpatrick DL. Molecular pharmacology and antitumor activity of palmarumycin-based inhibitors of thioredoxin reductase. *Molecular cancer therapeutics*. 2006;5(3):630-636.
624. Topkas E, Cai N, Cumming A, et al. Auranofin is a potent suppressor of osteosarcoma metastasis. *Oncotarget*. 2016;7(1):831-844.
625. Cheng X, Holenya P, Can S, et al. A TrxR inhibiting gold(I) NHC complex induces apoptosis through ASK1-p38-MAPK signaling in pancreatic cancer cells. *Molecular Cancer*. 2014;13(1):221.
626. Cheng P, Liu H, Li Y, et al. Inhibition of thioredoxin reductase 1 correlates with platinum-based chemotherapeutic induced tissue injury. *Biochemical pharmacology*. 2020;175:113873.
627. Wang X, Zhang J, Xu T. Thioredoxin reductase inactivation as a pivotal mechanism of ifosfamide in cancer therapy. *Eur J Pharmacol*. 2008;579(1-3):66-73.
628. Zhang J, Lu H. Ifosfamide induces acute renal failure via inhibition of the thioredoxin reductase activity. *Free radical biology & medicine*. 2007;43(12):1574-1583.
629. Wang X, Zhang J, Xu T. Cyclophosphamide-evoked heart failure involves pronounced co-suppression of cytoplasmic thioredoxin reductase activity and non-protein free thiol level. *European journal of heart failure*. 2009;11(2):154-162.
630. Wang L, Wei Y, Fang W, et al. Cetuximab Enhanced the Cytotoxic Activity of Immune Cells during Treatment of Colorectal Cancer. *Cellular Physiology and Biochemistry*. 2017;44(3):1038-1050.
631. Tarantino G, Scalera A, Finelli C. Liver-spleen axis: intersection between immunity, infections and metabolism. *World J Gastroenterol*. 2013;19(23):3534-3542.
632. Hoshyar N, Gray S, Han H, Bao G. The effect of nanoparticle size on in vivo pharmacokinetics and cellular interaction. *Nanomedicine (London, England)*. 2016;11(6):673-692.
633. Gustafson HH, Holt-Casper D, Grainger DW, Ghandehari H. Nanoparticle uptake: The phagocyte problem. *Nano Today*. 2015;10(4):487-510.
634. Jachimska B, Jasiński T, Warszyński P, Adamczyk Z. Conformations of poly (allylamine hydrochloride) in electrolyte solutions: Experimental measurements and theoretical modeling. *Colloids and Surfaces A-physicochemical and Engineering Aspects - COLLOID SURFACE A*. 2010;355:7-15.
635. Oliveira JP, Prado AR, Keijok WJ, Antunes PWP, Yapuchura ER, Guimarães MCC. Impact of conjugation strategies for targeting of antibodies in gold nanoparticles for ultrasensitive detection of 17 $\beta$ -estradiol. *Scientific reports*. 2019;9(1):13859.
636. Puertas S, Batalla P, Moros M, et al. Taking Advantage of Unspecific Interactions to Produce Highly Active Magnetic Nanoparticle-Antibody Conjugates. *ACS nano*. 2011;5(6):4521-4528.
637. Welch NG, Scoble JA, Muir BW, Pigram PJ. Orientation and characterization of immobilized antibodies for improved immunoassays (Review). 2017;12(2):02D301.
638. Pietersz GA, Wang X, Yap ML, Lim B, Peter K. Therapeutic targeting in nanomedicine: the future lies in recombinant antibodies. 2017;12(15):1873-1889.
639. Choi HS, Frangioni JV. Nanoparticles for biomedical imaging: fundamentals of clinical translation. *Molecular imaging*. 2010;9(6):291-310.
640. Vilches C, Quidant R. Chapter 12 - Targeted hyperthermia with plasmonic nanoparticles. In: Parak WJ, Feliu N, eds. *Frontiers of Nanoscience*. Vol 16. Elsevier; 2020:307-352.
641. Semmler-Behnke M, Kreyling WG, Lipka J, et al. Biodistribution of 1.4- and 18-nm Gold Particles in Rats. 2008;4(12):2108-2111.
642. Balogh L, Nigavekar SS, Nair BM, et al. Significant effect of size on the in vivo biodistribution of gold composite nanodevices in mouse tumor models. *Nanomedicine: Nanotechnology, Biology and Medicine*. 2007;3(4):281-296.
643. Zhao Y, Sultan D, Detering L, Luehmann H, Liu Y. Facile synthesis, pharmacokinetic and systemic clearance evaluation, and positron emission tomography cancer imaging of <sup>64</sup>Cu-Au alloy nanoclusters. *Nanoscale*. 2014;6(22):13501-13509.
644. Huo S, Ma H, Huang K, et al. Superior Penetration and Retention Behavior of 50 nm Gold Nanoparticles in Tumors. *Cancer research*. 2012.
645. Richards DA, Maruani A, Chudasama V. Antibody fragments as nanoparticle targeting ligands: a step in the right direction. *Chemical science*. 2017;8(1):63-77.
646. Cheng WW, Allen TM. Targeted delivery of anti-CD19 liposomal doxorubicin in B-cell lymphoma: a comparison of whole monoclonal antibody, Fab' fragments and single chain Fv. *Journal of controlled release : official journal of the Controlled Release Society*. 2008;126(1):50-58.

## References

- 647. Kawamura K, Qi F, Kobayashi J. Potential relationship between the biological effects of low-dose irradiation and mitochondrial ROS production. *Journal of radiation research*. 2018;59(suppl\_2):ii91-ii97.
- 648. Larson SM, Carrasquillo JA, Cheung NK, Press OW. Radioimmunotherapy of human tumours. *Nature reviews Cancer*. 2015;15(6):347-360.
- 649. Aghevlian S, Boyle AJ, Reilly RM. Radioimmunotherapy of cancer with high linear energy transfer (LET) radiation delivered by radionuclides emitting alpha-particles or Auger electrons. *Adv Drug Deliv Rev*. 2017;109:102-118.
- 650. Ng QK, Olariu CI, Yaffee M, et al. Indium-111 labeled gold nanoparticles for in-vivo molecular targeting. *Biomaterials*. 2014;35(25):7050-7057.
- 651. Loiseau A, Boudon J, Oudot A, et al. Titanate Nanotubes Engineered with Gold Nanoparticles and Docetaxel to Enhance Radiotherapy on Xenografted Prostate Tumors. *Cancers*. 2019;11(12).
- 652. Zhao L, Wen S, Zhu M, et al. 99mTc-labelled multifunctional polyethylenimine-entrapped gold nanoparticles for dual mode SPECT and CT imaging. *Artificial Cells, Nanomedicine, and Biotechnology*. 2018;46(sup1):488-498.
- 653. Wen S, Zhao L, Zhao Q, et al. A promising dual mode SPECT/CT imaging platform based on (99m)Tc-labeled multifunctional dendrimer-entrapped gold nanoparticles. *J Mater Chem B*. 2017;5(21):3810-3815.
- 654. Xiao Y, Hong H, Matson VZ, et al. Gold Nanorods Conjugated with Doxorubicin and cRGD for Combined Anticancer Drug Delivery and PET Imaging. *Theranostics*. 2012;2(8):757-768.

# List of publications

## Journal articles

Daems N, Verlinden B, Van Hoecke K, Cardinaels T, Baatout S, Michiels C, Lucas S, Aerts A. In vivo pharmacokinetics, biodistribution and toxicity of antibody-conjugated gold nanoparticles in healthy mice. *Journal of Biomedical Nanotechnology*. 2020 (Accepted).

Daems N, Penninckx S, Nelissen I, Van Hoecke K, Cardinaels T, Baatout S, Michiels C, Lucas S, Aerts A. Gold nanoparticles affect the antioxidant status in selected normal human cells. *International journal of nanomedicine*. 2019;14:4991-5015.

Genbrugge C, Eertmans W, Meex I, Van Kerrebroeck M, Daems N, Creemers A, Jans F, Boer W, Dens J, De Deyne C. What is the value of regional cerebral saturation in post-cardiac arrest patients? A prospective observational study, *Crit Care*. 2016, 20 (1), 327.

## Articles under preparation

Verlinden B, Van Hoecke K, Aerts A, Daems N, Dobney A, Janssens K, Cardinaels T. Quantification of Boron in Cells for evaluation of drug agents used in Boron Neutron Capture Therapy. (Submitted in *Journal of Analytical Atomic Spectrometry*).

Daems N, Ooms M, Van Hoecke K, Baatout S, Lucas S, Michiels C, Aerts A. Radiolabeled antibody-functionalized gold nanoparticles radiosensitize cancer cells to <sup>177</sup>Lu. Experiments ongoing.

Daems N, Van Hoecke K, Baatout S, Lucas S, Michiels C, Aerts A. Radiolabeling of gold nanoparticles and their potential use in cancer diagnostics and therapy. Review article.

Daems N, Van Hoecke K, Baatout S, Lucas S, Michiels C, Aerts A. The biological effects of gold nanoparticles, and their challenges to proceed to clinical trials. Review article.

## Oral presentations

N. Daems. Gold nanoparticles and their toxicity in non-cancerous human cell lines. Narilis Research Day. 2018. Namur. Belgium.

N.Daems. Gold nanoparticles for cancer theranostics: Their toxicity in non-targeted cells. SCK CEN PhD Day. 2018. Mol. Belgium.

N Daems. Radiolabeling of antibody-functionalized gold nanoparticles. NURA PhD Day. 2018. Mol. Belgium.



## List of publications

N. Daems. Toxicity of gold nanoparticles and their radiolabeling with  $^{177}\text{Lu}$ . Seminar. 2019. Namur. Belgium.

N.Daems. Radiolabeling of gold nanoparticles with  $^{177}\text{Lu}$ . Seminar. 2019. Mol. Belgium.

N.Daems. Radiolabeling of gold nanoparticles with  $^{177}\text{Lu}$ . NURA PhD day. 2019. Mol. Belgium

N.Daems. Gold nanoparticles: a tiny treasure to improve cancer radiotherapy? Day of Radiation Biology and Medicine. 2019. Mol. Belgium

## Poster presentations

N. Daems, J. Buset, A. Micheaux, P. Vandormael, L. Peeters, S. Baatout, H. Derradji. The Cellular and Molecular Effects of Ionizing Radiation and Iodine Deficiency on Non-Cancerous Thyroid Cells. Mosa Conference. 2016. Maastricht. The Netherlands.

N. Daems, R. Marega, O. Fichera, S. Cagno, K. Van Hoecke, S. Baatout, T. Cardinaels, C. Michiels, S. Lucas, A. Aerts. Cytotoxicity assessment of gold nanoparticles on non-cancerous cell lines. Kick-off meeting of NARILIS Cancer Research Pole. 2017. Namur. Belgium.

N. Daems, R. Marega, O. Fichera, S. Cagno, K. Van Hoecke, S. Baatout, T. Cardinaels, C. Michiels, S. Lucas, A. Aerts. Cytotoxicity assessment of gold nanoparticles on non-cancerous cell lines. Interuniversity PhD Day. 2017. Liège. Belgium.

N. Daems, R. Marega, O. Fichera, S. Cagno, K. Van Hoecke, S. Baatout, T. Cardinaels, C. Michiels, S. Lucas, A. Aerts. Cytotoxicity assessment of gold nanoparticles on non-cancerous cell lines. 6th symposium on medical radioisotopes. 2017. Mechelen. Belgium.

N. Daems, R. Marega, O. Fichera, S. Cagno, K. Van Hoecke, S. Baatout, T. Cardinaels, C. Michiels, S. Lucas, A. Aerts. Cytotoxicity assessment of gold nanoparticles on non-cancerous cell lines. Knowledge for Growth. 2017. Gent. Belgium.

N. Daems, R. Marega, O. Fichera, S. Cagno, K. Van Hoecke, S. Baatout, T. Cardinaels, C. Michiels, S. Lucas, A. Aerts. Cytotoxicity assessment of gold nanoparticles on non-cancerous cell lines. RBSM2017 Meeting. 2017. Antwerp. Belgium.

N. Daems, R. Marega, O. Fichera, S. Cagno, K. Van Hoecke, S. Baatout, T. Cardinaels, C. Michiels, S. Lucas, A. Aerts. Cytotoxicity assessment of gold nanoparticles on non-cancerous cell lines. European Radiation Research Society (ERRS-GBS) Conference. 2017. Essen. Germany.

N. Daems, R. Marega, O. Fichera, S. Cagno, K. Van Hoecke, S. Baatout, T. Cardinaels, C. Michiels, S. Lucas, A. Aerts. Cytotoxicity assessment of gold nanoparticles on non-cancerous cell lines. ICRP. 2017. Paris. France.

N. Daems, R. Marega, O. Fichera, K. Van Hoecke, S. Baatout, T. Cardinaels, C. Michiels, S. Lucas, A. Aerts. Cytotoxicity assessment of gold nanoparticles on non-cancerous cell lines. SCK CEN PhD day. 2017. Mol. Belgium.

N. Daems, O. Fichera, K. Van Hoecke, S. Baatout, T. Cardinaels, C. Michiels, S. Lucas, A. Aerts. Gold nanoparticles induce oxidative stress-dependent apoptosis in vascular endothelial cells. Knowledge for Growth. 2018. Gent. Belgium.

N. Daems, O. Fichera, K. Van Hoecke, S. Baatout, T. Cardinaels, C. Michiels, S. Lucas, A. Aerts. Gold nanoparticles coated with antibodies lead to ROS-dependent apoptotic cell death in non-cancerous human cell lines (E-poster). EANM. 2018. Dusseldorf. Germany.

N. Daems, M. Ooms, T. Cardinaels, S. Baatout, C. Michiels, S. Lucas, K. Van Hoecke, A. Aerts. Radiolabeling of gold nanoparticles with  $^{177}\text{Lu}$  as platform for cancer theranostics. 7th symposium on medical radioisotopes. 2019. Liège. Belgium.

N. Daems, M. Ooms, T. Cardinaels, S. Baatout, C. Michiels, S. Lucas, K. Van Hoecke, A. Aerts. The radiolabeling of antibody-conjugated gold nanoparticles with  $^{177}\text{Lu}$ . SCK CEN PhD day. 2019. Mol. Belgium.

N. Daems, M. Ooms, T. Cardinaels, S. Baatout, C. Michiels, S. Lucas, K. Van Hoecke, A. Aerts. Radiolabeling of gold nanoparticles with Lu-177 as a platform for cancer theranostics (E-poster). EANM 2019. Barcelona. Spain.

N. Daems, S. Penninckx, I. Nelissen, K. Van Hoecke, T. Cardinaels, S. Baatout, C. Michiels, S. Lucas, A. Aerts. Gold nanoparticles affect the antioxidant status in selected normal human cells. BNS-YG 2019. Mol. Belgium



